Cosmological evolution of the galaxy merger rate from MUSE deep fields

Emmy Ventou

Université Fédérale
Toulouse Midi-Pyrénées

THÈSE

En vue de l'obtention du

DOCTORAT DE L'UNIVERSITÉ DE TOULOUSE

Délivré par l'Université Toulouse 3 - Paul Sabatier

Présentée et soutenue par

Emmy VENTOU

Le 21 décembre 2018

Evolution cosmologique du taux de fusion des galaxies à partir des champs profonds MUSE

Ecole doctorale : **SDU2E - Sciences de l'Univers, de l'Environnement et de l'Espace**

Spécialité : **Astrophysique, Sciences de l'Espace, Planétologie**

Unité de recherche :
IRAP - Institut de Recherche en Astrophysique et Planetologie

Thèse dirigée par
Thierry CONTINI et Benoît EPINAT

Jury

M. Olivier LE FèVRE, Rapporteur
M. Christopher CONSELICE, Rapporteur
Mme Anne VERHAMME, Examinatrice
M. Nicolas BOUCHE, Examinateur
Mme Genevieve SOUCAIL, Examinatrice
M. Carlos LOPEZ SAN JUAN, Examinateur
M. Thierry CONTINI, Directeur de thèse
M. Benoit EPINAT, Co-directeur de thèse

Cosmological evolution of the galaxy merger rate from MUSE deep fields

Emmy Ventou

Toulouse III, Paul Sabatier University

December 21, 2018

À mes parents.

"Tout parle dans l'univers,
il n'est rien qui n'ait son langage."

Jean de la Fontaine

Acknowledgements/Remerciements

Ces trois années, passées au sein du laboratoire de l'IRAP à Toulouse, ont été riches d'apprentissages et de nouvelles expériences. Avant tout, je tiens à remercier toutes les personnes qui ont contribué à ce travail, et qui m'ont apporté leur soutien tout au long de cette thèse. En premier, je voudrais remercier mon directeur de thèse Thierry Contini de m'avoir donné l'opportunité d'intégrer un projet tel que MUSE et m'avoir prise sous son aile et cela dès le stage en master. J'ai énormément appris à ses côtés. Merci pour tous tes conseils, ta patience, ta compréhension et ta bonne humeur. Je me souviendrais longtemps de tous ces bons moments passé lors de tous ces voyages notamment au Chili et en Corse (j'ai encore en tête le goût de cette côte de bœuf et la musique de radio Contini).

Je tiens particulièrement à remercier l'équipe MUSE de l'IRAP, pour m'avoir accueilli et épaulé durant cette thèse. Ce fut un réel plaisir de travailler avec eux merci donc à Geneviève, Nicolas, Roser, Ilane (pour ton humour et ton café) et enfin Hayley (pour ta joie de vivre et ton amitié si précieuse à mes yeux).

Je voudrais également exprimer ma gratitude à tous les membres du consortium pour tous ces bons moments passés lors des Busy weeks, ce sont vraiment des personnes incroyables. Benoit et Anne, vos commentaires et vos idées ont toujours été précieux et ont grandement amélioré la qualité de mon travail. Merci à Olivier Le Fèvre et Christopher Conselice pour avoir rapporté mon manuscrit et pour leurs commentaires positifs, ainsi qu'à Carlos Lopez San Juan d'avoir accepté de faire partie de mon jury.

Merci également à tous les postdocs et doctorants de Toulouse, Lyon, Zurich et Leiden. En particulier Florianne et Sofia pour ce merveilleux voyage au Japon, «Arigatōgozaimashita». Une petite pensée pour mes camarades de bureau David et Tristan pour m'avoir supporté tout ce temps.

Enfin, je veux remercier ici ceux qui me sont chers : À la bande des pins (Yasmina et les autres, merci pour votre soutien et votre amitié sans faille); à Cécile, Charles, Jeremy, Marc, Fil et compagnie pour toutes ces soirées de jeux (merci pour tous ces

fous rires et de me laisser gagner à terraforming et game of thrones). J'adresse un merci particulier à Célia sans qui je n'aurais tout simplement pas fini cette thèse (ma licornasse merci pour ton soutien si précieux).

En dernier, je remercie ma famille et plus particulièrement mes parents qui ont toujours été mes premiers supporteurs.

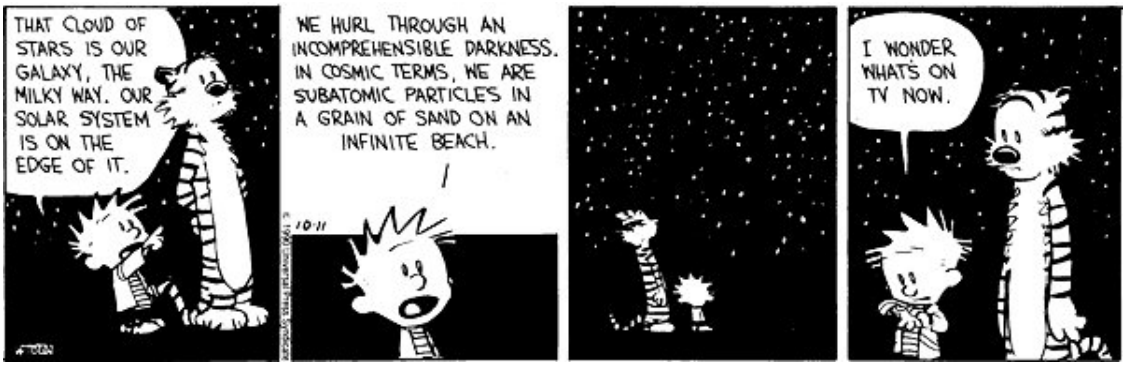

Abstract

Over the past two decades, strong evidence that galaxies have undergone a significant evolution over cosmic time were found. Do galaxy mergers, one of the main driving mechanisms behind the growth of galaxies, played a key role in their evolution at significant look-back time? Due to the difficulty to identify these interactions between galaxies at high redshifts, the major merger rate, involving two galaxies of similar masses, was constrained so far up to redshift $z \approx 3$ from previous studies of spectroscopic pair counts. Thanks to MUSE, which is perfectly suited to identify close pairs of galaxies with secure spectroscopic redshifts, we are now able to extend such studies up to $z \approx 6$. During my thesis, my research focused mainly on providing new constraints on the growth of galaxies over the last 12 billion years, by studying the evolution of the galaxy merger fraction.

I present the results obtained from the analysis of deep MUSE observations, first in the Hubble Ultra Deep Field and Hubble Deep Field South. Within this spectroscopic sample 23 major close pairs are identified at high redshift ($z > 3$) through their Lyman alpha emission. For these galaxies, key potential biases such as Lyman alpha offsets were taken into account. I give the first estimate of the major merger fraction for $z \sim 4 - 6$ from spectroscopic close pairs counts.

In a second part, I expand this analysis to two other regions deeply observed with MUSE, Abell 2744 and COSMOS-GR30. Close pair selection criteria were improved with an analysis of the phase-space distance of galaxy pairs from ILLUSTRIS simulations. Around 372 secure close pairs of galaxies were identified among a large spectroscopic parent sample of 2483 galaxies spread over a large redshift range ($0.2 < z < 6$) and over a broad range of stellar masses, thus providing the first constraints on the galaxy major and minor merger evolution over 12 Gyrs.

Our results show that the major merger fraction reaches a maximum around $z \approx 2 - 3$ then slowly decreases from $z \sim 3$ to $z \approx 6$. The minor merger fraction seems to follow a more constant evolutionary trend with redshift, around 20% for $z < 1.5$ with a slight decrease to 8-13% for $z \geq 3$. Lastly, estimates of the galaxy major and minor merger rates along cosmic time were derived from these fractions. This study illustrates the potential of using blind spectroscopy from IFU surveys to study pair counts and derive merger fractions/rates at high redshift.

Résumé

Au cours des dernières décennies, de nombreuses preuves que les galaxies ont subit une profonde évolution depuis leur formation s'accumulent. Les fusions de galaxies, un des principaux mecanismes à l'origine de la croissance des galaxies, ont-elles joué un rôle dans leur évolution lorsque l'univers était encore jeune? En raison de la difficulté à détecter des interactions entre galaxies à grand redshifts, le taux de fusions majeures de galaxies, qui impliquent la fusion de deux galaxies de masses et de tailles similaires, était seulement contraint jusqu'à un redshift de 3, grâce aux études précédentes portant sur des sondages spectroscopiques.

Grace à sa technologie innovante, le spectrographe integral de champ MUSE, un nouvel instrument installé sur le VLT au Chili, convient parfaitement à l'identification de paires proches de galaxies. Ses mesures de redshift spectroscopique ont permis d'étendre l'étude de l'évolution du taux de fusion jusqu'à $z = 6$. Ainsi durant ma thèse, j'ai tenté d'apporter de nouvelles contraintes sur la croissance des galaxies depuis les 12 derniers milliard d'années, en étudiant l'évolution du taux de fusion des galaxies.

Je présente ici les résultats obtenus sur l'analyse des champs les plus profonds obtenus jusqu'alors avec MUSE, tout d'abord dans le Hubble Ultra Deep Field et dans le Hubble Deep Field South. En tout 23 paires proches de galaxies ont été identifiées à grand redshift ($z > 3$) à travers leur émissions Lyα. Pour ces galaxies, certains biais ont été pris en compte. J'ai ainsi pu donner une première estimation du taux de fusions majeures entre $z > 4$ et $z \sim 6$.

Dans une seconde étude, j'ai étendu cette analyse à deux autres régions observées par MUSE : Abell 2744 et COSMOS-GR30. Les critères de sélection des paires proches de galaxies ont été améliorés avec une étude sur la distance de séparation et différence de vitesse de paires de galaxies et sa probabilité de fusionner plus tard, dans les simulations Illustris. Près de 372 paires proches ont pu être identifiées à partir d'un échantillon parent de 2483 galaxies distribuées sur un grand domaine de redshift ($0.2 < z < 6$) et de masses stellaires. Ceci nous fournit les premières contraintes sur la fusion de galaxies majeures et mineures sur prés de 12 milliard d'années d'évolution.

Nos résultats montrent que les fusions majeures atteignent un maximum autour $z = 2 - 3$ pour ensuite lentement décroître de $z > 3$ à $z = 6$. Les fusions mineures quant à elles semblent suivre une évolution moins marquée en fonction

du temps, avec une fraction autour de 20% à $z = 1.5$ et une légère décroissance jusqu'à 8-13% pour $z > 3$.

Dans un dernier temps, le taux de fusions majeures et mineures de galaxies au cours du temps cosmique est estimé à partir de ces fractions. Cette étude illustre bien le potentiel de MUSE pour étudier les fusions de galaxies à grand redshift.

Contents

List of Figures **17**

List of Tables **19**

1 Introduction **21**

2 Introduction (French) **23**

3 How do galaxies grow over cosmic time ? **25**

3.1 Galaxy evolution since the early universe 26

3.1.1 Some fundamental properties of galaxies 26

3.1.2 Evolution of the star formation rate 28

3.1.3 Evolution of the stellar mass density of galaxies 30

3.2 Galaxy mergers versus cold gas accretion 31

3.2.1 The role of cold gas flows in feeding galaxies 31

3.2.2 The role of galaxy mergers in galaxy evolution 34

3.3 How can we detect galaxy mergers ? 38

3.3.1 Morphological studies 39

3.3.2 Close pair counts of galaxies 40

3.4 The galaxy merger fraction and rate up to z $\approx$ 3 41

3.5 Organization of the thesis 44

4 MUSE observations **47**

4.1 The project 47

4.2 The instrument 49

4.3 MUSE deep fields 52

4.3.1 Hubble Deep Field South 52
4.3.2 Hubble Ultra Deep Field 55
4.3.3 Abell 2744 60
4.3.4 COSMOS-Gr30 63

5 Evolution of the major merger fraction since $z \approx 6$ 69
5.1 The MUSE Hubble Ultra Deep Field Survey IX: Evolution of galaxy major merger fraction since $z \approx 6$ 69

6 Using new selection criteria from Illustris simulations to investigate the evolution of the major and minor merger fraction 87
6.1 New criteria for the selection of galaxy close pairs from cosmological simulations: evolution of the major and minor merger fraction in MUSE deep fields 87

7 Evolution of the major and minor merger rates since $z \approx 6$ 107
7.1 The galaxy merger timescale 107
7.2 Results 110

8 Conclusion and perspective 115

9 Conclusion et perspective (French) 119

Bibliography 123

List of Figures

3.1 The Hubble sequence at three different cosmological epochs 26
3.2 The history of cosmic star formation 28
3.3 The integrated stellar mass density estimated from various studies over a large redshift range 30
3.4 An artist's view of a galaxy in the process of pulling in cool gas from its environments 32
3.5 A disk galaxy accreting gas along cosmic web filaments at $z \approx 3$ from numerical simulations 33
3.6 Hubble images of galaxies in the merging process 34
3.7 Time sequence of a galaxy merger event 35
3.8 A galaxy merger history from numerical simulation 36
3.9 Evolution of the major merger fraction from spectroscopic close pair counts studies 42
3.10 Comparison of the major merger rate derived from CANDELS and SDSS surveys for mass-ratio and flux-ratio selected samples 43

4.1 Photographs of MUSE on the Nasmyth focus of Yepun at the Cerro Paranal Observatory in Chile 48
4.2 Illustration of MUSE optical schematic system and data acquisition 50
4.3 Illustration of a MUSE data cube, showing the three-dimensional view of the Pillars of Creation nebula in the Messier 16 region . . . 51
4.4 View of the HDF-S in the WFPC2 F814W image 53
4.5 One of the Lyα emitters (MUSE ID 553) identified by MUSE without any HST counterpart at $z \approx 5.08$ 54

4.6 Orientation and position of the UDF-Mosaic and UDF10 MUSE fields in the HST F775W image of the HUDF region 56
4.7 Reconstructed white-light images for the UDF-Mosaic and UDF10 . 58
4.8 Redshift distribution of all objects detected in the combined UDF-Mosaic and UDF10 surveys 60
4.9 Magnitude vs redshift diagram for all objects with secure redshifts of the combined MUSE data set over UDF-Mosaic and UDF10 . . 61
4.10 View of A2744 in the RGB HST image, delimited by the MUSE mosaic field of view 64
4.11 An example of a multiple image system identified in A2744 65
4.12 View of the galaxy group COSMOS-Gr30 in the MUSE reconstructed white light and HST RGB images 66

7.1 The major merger rate from MUSE data compared to previous spectroscopic studies and numerical simulations 112
7.2 Evolution of the minor merger rate from MUSE combined samples analyzed in this thesis 113

List of Tables

7.1 Major merger rates from MUSE observations over the HUDF, HDF-S, A2744 and COSMOS-GR30 regions 111
7.2 Minor merger rates from MUSE observations 111

1 Introduction

Galaxies are complex systems of gravitationally bound stars, gas, dust, and dark matter. Ever since their discovery, astronomers have been intrigued by these objects and understanding the processes behind the formation and evolution of galaxies remains one of the most outstanding issues of astrophysics. Thanks to technology development, more and more sophisticated instruments came on line, and thus much progress has been made in the last decade on both observational and numerical side of galactic evolution. Morphology and other fundamental galaxy properties such as the star formation rate or the stellar mass density of galaxies are used to trace the evolution of galaxies across cosmic time.

How do galaxies grow ? The processes that govern their evolution are still unclear. Two main processes contribute to the build-up of galaxies since the early universe, cold gas accretion and galaxy mergers. In the first scenario, galaxies are supplied in gas trough cold filaments following the cosmic web of large-scale structures. The second mechanism involves the collision of two galaxies resulting in a single one, the so-called galaxy mergers. In order to know the contribution of each processes to the growth of galaxies, we need to quantify them.

The purpose of this thesis is to provide new constraints on the growth of galaxies over the last 12 billion years, with an estimate of the minor and major galaxy merger rate. During these three years, I had the chance to use the last data obtained

from the Multi Unit Spectroscopic Explorer observations. This new instrument installed at the Paranal Observatory in Chile, saw its first light on January 31, 2014, 9 months before the beginning of this thesis. I thus had the pleasure to work with completely new data provided by blind spectroscopy from IFU surveys. As a member, I also participated to the consortium group meetings, the so called "MUSE busy week", where everyone discuss their science projects. In the first year of my PhD, my work focused on the detection of satellite galaxies orbiting around another in MUSE Hubble Ultra Deep Field Survey. This leaded to the publication of my first article where I estimated the major merger fractions in the the Hubble Ultra Deep Field and Hubble Deep Field South up to $z \sim 6$. In the last year of my PhD, I tried to expand this analysis to other deep regions observed with MUSE, like Abell 2744 and COSMOS-GR30. Using Illustris simulations, I investigated the relation between close pair selection criteria, the separation distance and relative velocity, and the probability of the two galaxy to merge in order to trace more accurately the galaxy merger fraction. This analysis resulted in a second paper, where I provide constraints on the galaxy major and minor merger evolution over a large redshift range ($0.2 < z < 6$) and over a broad range of stellar masses. In the last months, I tried to derived major and minor merger rates from my estimated merger fractions. This manuscript summarized all of my works and illustrates the potential of instruments such as MUSE for assessing the role of mergers in the growth of galaxies or probing the environments of high-redshift galaxies.

2
Introduction (French)

Les galaxies sont des systèmes complexes d'étoiles, de gaz, de poussières et de matière noire liées gravitationnellement. Depuis leur découverte, les astronomes ont été intrigués par ces objets, comprendre comment elles se forment et évoluent reste à ce jour l'un des problèmes les plus importants de l'astrophysique. Grâce au développements technologiques, à la construction d'instruments de plus en plus sophistiqués, et aux nombreux progrès réalisés en modélisation numérique, d'énormes progrès ont pu être réalisés sur ce sujet au cours de la dernière décennie, tant du côté observation que modélisation. La morphologie des galaxies et d'autres propriétés fondamentales, telles que le taux de formation d'étoiles ou la densité de masse stellaire des galaxies, permettent de suivre l'évolution des galaxies au cours du temps cosmique.

Comment les galaxies grandissent-elles? Les processus qui régissent leur évolution nous sont encore inconnus. Deux phénomènes semblent jouer un rôle important dans l'évolution des galaxies depuis le début de l'univers: l'accretion de gaz froid et la fusion de galaxies. Dans le premier scénario, les galaxies sont alimentées en gaz par des filaments qui suivent les hyper structures cosmiques de notre univers. Un autre mécanisme implique la collision de deux galaxies pour n'en former qu'une seule, une fusion de galaxies. Afin de connaître la contribution de chaque processus à la croissance des galaxies, nous devons les quantifier.

Le but de cette thèse est de fournir des nouvelle contraintes sur l'évolution des galaxies au cours des 12 derniers milliards d'années, avec une estimation des taux de fusions mineures et majeures des galaxies.

Au cours de ces trois dernières années, j'ai eu la chance d'utiliser les dernières données obtenues à partir des observations du Multi Unit Spectroscopic Explorer (MUSE). Ce nouvel instrument installé à l'Observatoire Paranal au Chili a vu sa première lumière le 31 janvier 2014, 9 mois avant le début de cette thèse. J'ai donc eu le plaisir de travailler avec des données d'une richesse exceptionnelle fournies par MUSE. En tant que membre, j'ai également participé aux réunions du consortium, les fameuses "MUSE busy week", au cours desquelles chacun discute ses projets scientifiques, une expérience particulièrement enrichissante. Au cours de la première année de ma thèse, mon travail était axé sur la détection de petites galaxies satellites en orbite autour d'une autre, dans le champ profond du Hubble Ultra Deep Field observé par MUSE. Ceci a conduit à la publication de mon premier article où je donne une estimation de la fraction de fusions majeures des galaxies jusqu'à $z \sim 6$. Au cours de la dernière année de mon doctorat, j'ai étendu cette analyse à d'autres régions observées avec MUSE, comme l'amas de galaxies Abell 2744 et le groupe de galaxies GR30 dans le champ COSMOS. À l'aide de simulations Illustris, j'ai étudié la relation entre les critères de sélection des paires proches de galaxies et leur probabilité de fusionner après un certain temps. Cette analyse a abouti à un deuxième article, dans lequel je présente l'évolution de la fraction de fusions majeures et mineures des galaxies sur un large domaine de redshift (0,2 <z <6) et de masses stellaires. Au cours des derniers mois, j'ai tenté d'estimer les taux de fusions majeures et mineures à partir de mes fractions. Dans ce manuscrit je résumé ces trois années de travail qui montre le potentiel d'instruments comme MUSE pour évaluer le rôle des fusions dans la croissance des galaxies ou pour sonder l'environnement des galaxies à grand redshift

3

How do galaxies grow over cosmic time ?

Contents

3.1 Galaxy evolution since the early universe 26
3.1.1 Some fundamental properties of galaxies 26
3.1.2 Evolution of the star formation rate 28
3.1.3 Evolution of the stellar mass density of galaxies 30
3.2 Galaxy mergers versus cold gas accretion 31
3.2.1 The role of cold gas flows in feeding galaxies 31
3.2.2 The role of galaxy mergers in galaxy evolution 34
3.3 How can we detect galaxy mergers ? 38
3.3.1 Morphological studies 39
3.3.2 Close pair counts of galaxies 40
3.4 The galaxy merger fraction and rate up to z $\approx$ 3 41
3.5 Organization of the thesis 44

In the early 20th century Edwin Hubble managed to estimate the distance of Andromeda using Cepheids variables stars, proving for the first time that Andromeda was not a nearby galactic nebula but rather another galaxy beyond the Milky way. In the following years it was acknowledged that the observable universe harbors not one or two but billion of billion of galaxies. Since then understanding the processes behind their formation and evolution remains one of the most outstanding issues of astrophysics. Thanks to technology development, more and more sophisticated instruments came on line, and thus much progress has been made in the domain

of galactic evolution in the last decade.

3.1 Galaxy evolution since the early universe

3.1.1 Some fundamental properties of galaxies

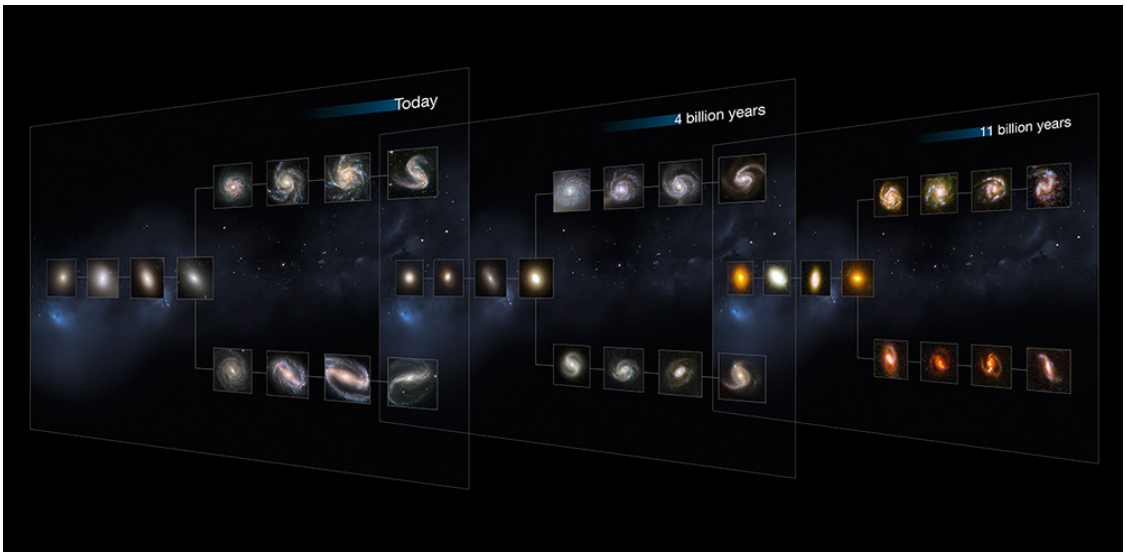

Figure 3.1: This image illustrates the Hubble sequence for galaxy classification at three different cosmological epochs. It shows the evolution of each galaxy type along cosmic time up to the present-day universe where galaxies are fully formed with various shapes. These images come from the Hubble Space Telescope Cosmic Assembly Near-infrared Deep Extragalactic Legacy Survey (CANDELS). *Credit: NASA, ESA, and M. Kornmesser (ESO)*

After the discovery of galaxies, astronomers began to observe them, trying first to classify these objects according to their structure and morphology. After years of science, this led to the well known Hubble sequence or "Hubble tuning fork" diagram which separates galaxies according to their morphology. First published by E. Hubble in 1926, it has been extended by de Vaucouleurs in 1959 and Sandage in 1961. Two main types of galaxies dominate this diagram: ellipticals and spirals. Figure 3.1 (left side, present-day diagram) shows the ellipticals on the left branch of the diagram and the spirals galaxies on the right. The spirals galaxies are further divided into spirals with (bottom branch) or without (top branch) bars in their central regions. The lenticular galaxies, S0, are placed at the center of the fork between the ellipticals and the spirals galaxies. These galaxies tend to

have a bright central bulge surrounded by disk-like structure but with no visible real spiral arm structures like in spiral galaxies.

The de Vaucouleurs classification system complements Hubble sequence with a more elaborated division of the spiral galaxies type, taking into account the presence of bars and rings. This was followed by many other works each trying to improve the sequence by enhancing for example the classification of spiral arms (eg. Elmegreen & Elmegreen 1982, 1987). Other classification systems exist like the Yerkes scheme developed by Morgan (1962), which is based on the shape and the central concentration of light in a galaxy image. However the morphological classification method introduced by E. Hubble is still the most commonly used.

This allowed scientists to classify galaxies in the nearby universe visually through structural features. However when we go further back in time these galaxies are still in their formation process. In Fig. 3.1 we can see that these galaxies, if we go back to 4 and 11 billion years ago, are smaller and more peculiars. It illustrates that galaxies have indeed evolved along cosmic time.

Another result brought by Hubble is the relation between the apparent velocity of galaxies (V) and their distance (D), expressed by the following equation :

$$V = H \times D \tag{3.1}$$

This relation is called Hubble's law (Hubble 1929), where H corresponds to the Hubble Constant. The last estimate of this constant was measured by Planck with $H = 67.8\ \mathrm{km\,s^{-1}\ Mpc^{-1}}$ (Aghanim et al. 2018). For the following parts of the thesis, we introduce the notion of "redshift", which happens when the light emitted by a moving object increases in wavelength and is thus shifted to the red part of the electromagnetic spectrum. The redshift, z, is linked to the observed wavelength of the source λ_{obs} and its vacuum wavelength λ_0 by the equation:

$$\lambda_{obs} = \lambda_0(1 + z) \tag{3.2}$$

In astronomy, this shift in wavelength is linked to the distance of the object in the universe. Because of the expansion of the Universe, a galaxy that is farther

away will have a larger receding velocity, and thus a larger redshift. This means that if we look at galaxies at higher redshift we look further back in time. We can thus study galaxy evolution by observing the galaxies at different redshifts. Modern telescopes are now powerful enough to observe galaxies at redshift beyond 6, probing galaxy populations in the early universe.

3.1.2 Evolution of the star formation rate

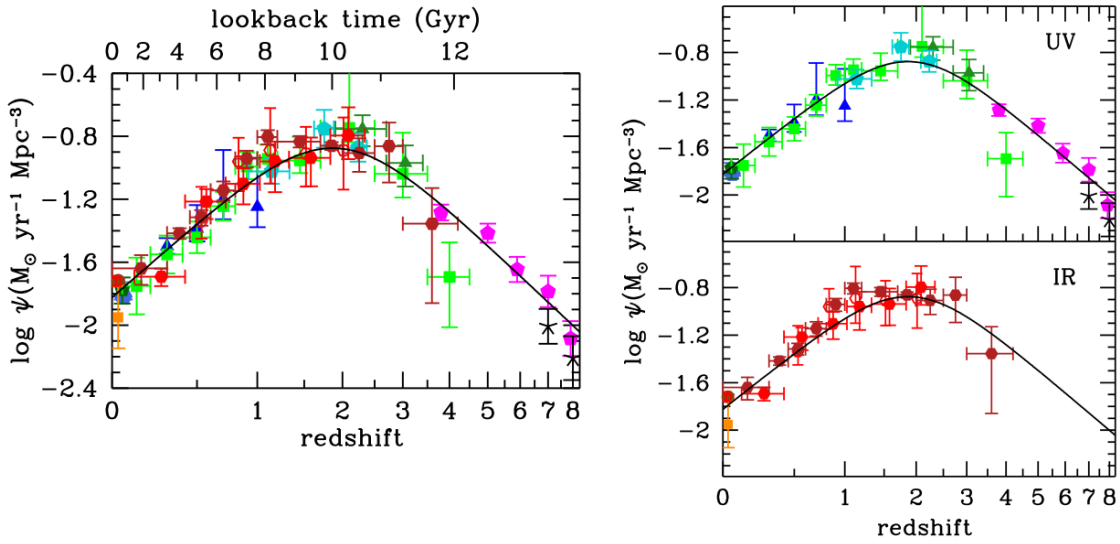

Figure 3.2: The history of cosmic star formation derived from far-infrared and far ultra-violet rest-frame measurements on the right panel and on the whole range on the left panel. The different symbols correspond to the different survey data sets. Blue-gray hexagons: Wyder et al. (2005); blue triangles: Schiminovich et al. (2005); green pentagons and squares: Robotham & Driver (2011) and Cucciati et al. (2012); turquoise pentagons: Dahlen et al. (2007); dark green triangles: Reddy & Steidel (2009), magenta pentagons: Bouwens et al. (2012a,b); black crosses: Schenker et al. (2013); brown circles: Sanders et al. (2003); orange squares: Takeuchi et al. (2003); red open hexagons: Magnelli et al. (2011); red filled hexagons: Magnelli et al. (2013); dark red filled hexagons; Gruppioni et al. (2013). *Credit: Madau & Dickinson, 2014*

Some fundamental galaxy properties are used by astronomers to trace their evolution. Such is the case for the star formation rate (SFR) which gives the mass of stars (in solar units) formed by a galaxy per year. To quantify the star formation rate, studies generally rely on the observed luminosities and luminosity functions (eg. Madau & Dickinson 2014).

Various methods and indicators are used to estimate the SFR. The typical star formation rate indicators are often the ultra-violet (UV) luminosity which gives a direct estimate of the young stellar population, $H\alpha$ luminosity and nebular emission lines, or the infra-red (IR) luminosity. Assuming a linear scaling between the SFR and the continuum luminosity integrated over a fixed band, evolutionary synthesis models infer the relation between the SFR per unit mass and the luminosity.

From the evolutionary synthesis model of Kennicutt (1998a, 1998b) the SFRs inferred from the three luminosities are described as:

$$SFR_{UV}(M_\odot\, yr^{-1}) = K_{UV} \times L_{UV}\,(erg\, s^{-1}\, Hz^{-1}) \tag{3.3}$$

$$SFR_{H\alpha}(M_\odot\, yr^{-1}) = K_{H\alpha} \times L_{H\alpha}\,(erg\, s^{-1}) \tag{3.4}$$

$$SFR_{IR}(M_\odot\, yr^{-1}) = K_{IR} \times L_{IR}\,(L_\odot) \tag{3.5}$$

The value of the conversion parameter K depends of the star formation history, the metal-enrichment history and the IMF chosen for the evolutionary synthesis model (Kennicutt 1998a, 1998b; Madau & Dickinson, 2014; Smit et al., 2012; Katsianis et al., 2017).

In their work, Madau & Dickinson (2014) take into account several data sets acquired from different surveys performed with instruments such as *Spitzer* or *GALEX*. In the estimation of the galaxy luminosity the dust attenuation along the line of sight must be taken into account. A corrective term must then be applied. From the computed integrated luminosity density, the cosmic star formation density is estimated using the appropriate equation 3.3, 3.4 or 3.5.

Figure 3.2 shows the results of this study. A clear picture is emerging, it seems that the cosmic star formation reaches a maximum around $z \approx 2.5$ and then decreases for lower redshifts. The Universe was much more active in the past with a star formation rate higher than what is seen for $z < 1$. Katsianis et al. (2017) investigate the evolution of the cosmic star formation rate density for $z = 0 - 7$ from different cosmological hydrodynamic simulations and observations and found the same evolutionary trend as Madau et & Dickinson (2014). Despite differences in the measurements the different SFR indicators produce consistent results. They

suggest that the evolution of the cosmic star formation is mostly determined by a balance between gas accretion and feedback processes.

3.1.3 Evolution of the stellar mass density of galaxies

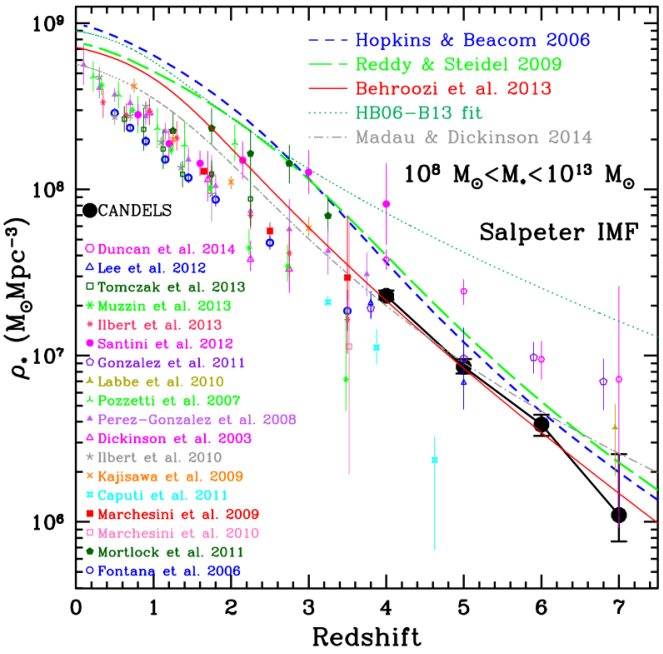

Figure 3.3: The integrated stellar mass density estimated from various studies over a large redshift range. *Credit: Grazian et al. (2015)*

Another powerful proxy to characterize galactic evolution is to investigate the stellar mass density of galaxies across cosmic time.

Several studies (Bundy et al., 2005; Mortlock et al., 2011; Madau & Dickinson, 2014; Duncan et al., 2014; Grazian et al., 2015; Davidzon et al., 2017) are in good agreements over the trend of the stellar mass density evolution. One of the methods usually used to derive the stellar mass density is to first estimate the stellar mass of large samples of galaxies, often by fitting the spectral energy distribution (SED) of galaxies. This method consists in using model predictions and minimization procedures to best fit the observed SED using a set of template spectra. The best fit obtained gives the information on the physical properties of the observed galaxy, like the redshift, stellar mass, star formation rate, dust mass, or metallicity. Then construct the stellar mass function for different redshifts by calculating the

number of galaxies per co-moving volume and mass range for each redshift interval. The last step is to integrate over the Schechter function (Schechter 1976) between two mass limits to derive the total stellar mass contained into galaxies for each redshift interval per co-moving volume.

Figure 3.3 shows the redshift evolution of the stellar mass density from several analyses (Grazian et al., 2015). It seems that the stellar mass density evolves greatly with redshift with a swift increase of the mass between $1 < z < 4$. About half of all stellar mass is assembled in galaxies by $z = 1.5$. Many authors conclude that the majority of the stellar mass of a galaxy is already in place before the star formation seems to stop and suggest that star formation alone is not enough to explain these massive galaxies and other building processes must be at works, for example galaxy mergers.

3.2 Galaxy mergers versus cold gas accretion

As discussed above, strong evidence that galaxies have undergone a significant evolution over cosmic time were found over the past decades. However, what are the main driving mechanisms behind the growth of these galaxies remains a fundamental question. We now believe that galaxy mergers and cold gas accretion are the main processes contributing to the build-up of galaxies since the early universe.

3.2.1 The role of cold gas flows in feeding galaxies

Galaxies are not closed-box systems, they interact with their environment. In the cold gas accretion scenario, fresh cool gas falls onto the galaxy from cold gas streams following the cosmic web of large-scale structures (see Fig. 3.4).

Several observational studies and hydrodynamic simulations show that this process is needed by galactic evolution models as a way to supply star formation on long timescales, as well as to explain chemical evolution models (Chiappini et al. 2001; Semelin & Combes 2002; Bournaud et al. 2011; Anglés-Alcázar et al. 2017; Qu et al. 2017; Rodriguez-Gomez et al. 2016). This process is well studied trough

Figure 3.4: This is an artist's view of a galaxy in the process of pulling in cool gas from its environments. The bright object to the left of the galaxy is a background quasar which shine through the accreted gas flows. It illustrates how we find indirect evidence of the cold gas accretion theory through ingenious methods such as, in this case, the use of the background quasar to probe absorption features due to the gas inflows and outflows. *Credit: ESO/L. Calçada/ESA*

numerical simulations (see Fig 3.5), where the accretion of gas along filaments comes from the growth of dark matter halos which pulls the cold baryons along.

While it is established that gas accretion plays an important role in galaxy growth, the details of how this mechanism takes place is still unknown. Indeed, direct observational evidence of this phenomenon have been difficult to obtain. Only indirect proofs have been available up to now, as for example the so-called "G-dwarf problem". Indeed, the metallicity distribution of G-stars in the Milky Way does not seems to be consistent with predictions from chemical evolution models unless some fresh gas infall is added (Schmidt 1963; Pagel & Patchett 1975).

Another indirect argument for gas accretion comes from the presence of expected absorption features along background quasar sight-lines (see Fig. 3.4; Caimmi 2008; Sancisi et al. 2008; Bournaud et al. 2011; Stewart et al. 2011a; Bouché et al., 2013, 2016). Since the infalling gas is not rotationally supported (Stewart et al. 2011a),

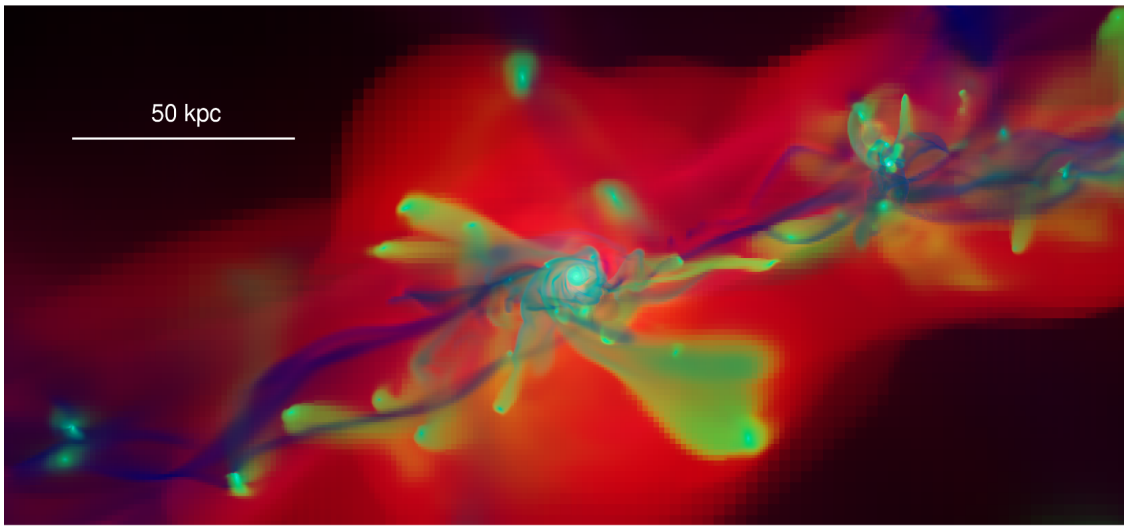

Figure 3.5: From numerical simulations, this picture shows a disk galaxy accreting gas along cosmic web filaments at $z \approx 3$. The shock heated gas around the galaxy is colored in red, in blue we can see the cold gas stream connecting to the edge of the disc and in green the metal rich gas stripped from smaller satellites galaxies around. In their related paper, the authors conclude that with its interactions with hot halo gas, the accreted cold gas seems to settles into large disc-like objects and thus explain that clump-cluster or chain-galaxies could come from enhanced gas accretion from cold dense filaments and interactions with smaller galaxy companions. *Credit: Agertz et al, 2009.*

if we observe the absorption along bright background sources, like quasars, its kinematics is expected to be offset from the galaxy own systemic velocity. Bouché et al. (2013) present an analysis of the absorbing gas properties such as kinematics, metallicity and dust properties for a star forming galaxy at $z \approx 2.3$, using a background quasar at a distance of 26 kpc from the galaxy. In a more recent article (Bouché et al. 2016), a similar analysis was performed on a $z = 0.91$ low-mass star-forming galaxy with data from the new Multi Unit Spectroscopic Explorer (MUSE). Distinct signatures, extended up to 12 kpc, like the ones expected for a cold gas flow were found. The associated infalling gas accretion rate is estimated to be at least two times larger than the SFR.

Conselice et al. (2013) also argue that accretion from the intergalactic medium is necessary to sustain star formation in galaxies and could be the dominant mechanism for new stellar mass assembly for the most massive galaxies at $1.5 < z < 3$, with 66% of all star formation at this epoch resulting from gas accretion. This result is corroborated by some cosmological simulations which estimate that the mean

fraction of mass assembled by accretion is about 77%, compared to 23% for galaxy mergers (L'Huillier et al., 2012).

Recently, from narrow-band imaging, a large and luminous filament, was discovered near the quasi-stellar object QSO UM287 at $z \approx 2.28$. In their paper, Martin et al. (2015) proposed a spectroscopic investigation of the emitting structure. They find that the region may be a giant proto-galactic disk connected to a quiescent filament which extend behind the virial radius of the halo. Moreover its geometry supports a cold accretion flow approach (Martin et al., 2015).

3.2.2 The role of galaxy mergers in galaxy evolution

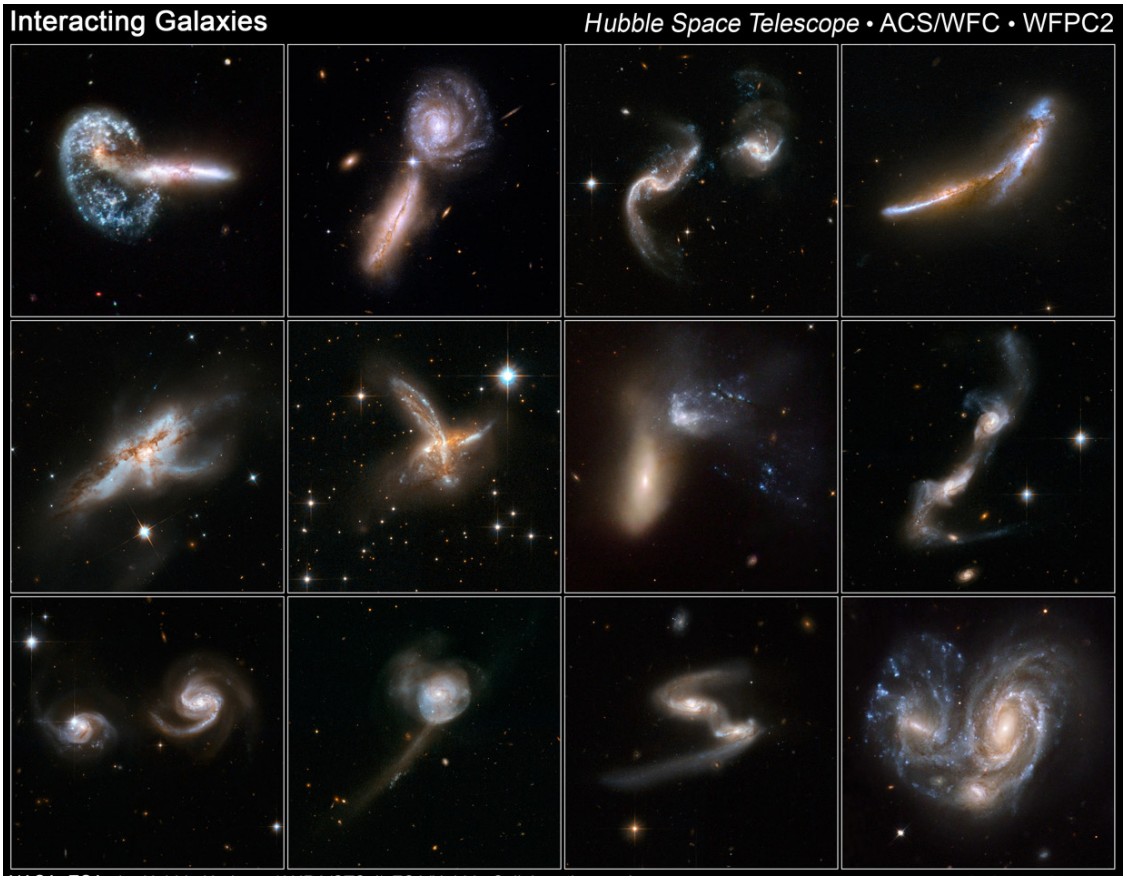

Figure 3.6: Hubble images of galaxies in the merging process. *Credit: NASA/ESA, Hubble collaboration and A. Evans.*

Galaxy mergers are among the most spectacular events observed in the universe (Fig 3.6). Two galaxies colliding can lead to a galaxy merger if they do not have

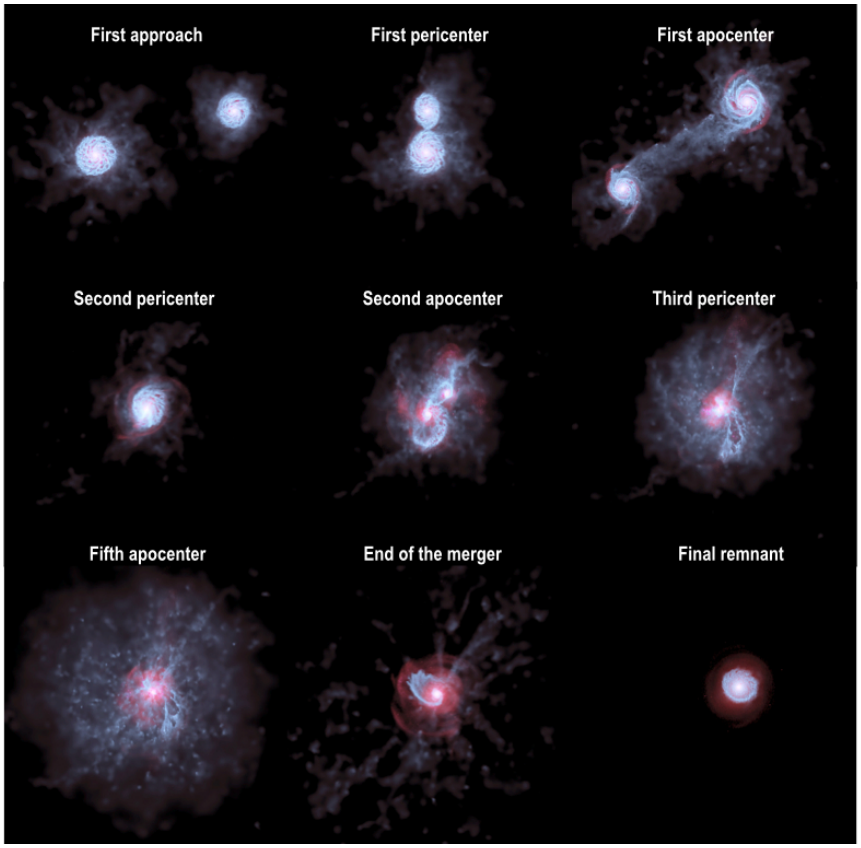

Figure 3.7: From hydrodynamical simulations, the time sequence of a galaxy merger event. The two galaxies have a mass ratio of 1:2. The initial separation between the galaxies is set near the sum of the two virial radii. *Credit: IAP, M. Volonteri*

enough momentum to resist the gravitational pull between them. This results in the two galaxies orbiting each other in a sort of dance before succumbing to one another and merging into a single galaxy. Various parameters such as relative velocity, angle of the collision, size, composition or mass of galaxies can affect the result of two colliding galaxies.

These events have been well studied in the nearby universe through both observational and simulation analyses. Figure 3.7 shows a simulation of two galaxies in the process of merging. As the time passes the two parent galaxies get closer until they interact for the first time, which is call the first pass or first pericenter passage. Then the two galaxies will start to move away from each other before being pulled again toward each other. Depending on many factors such as the mass ratio between the two galaxies, orbital configurations, gas fractions and others, the galaxies can

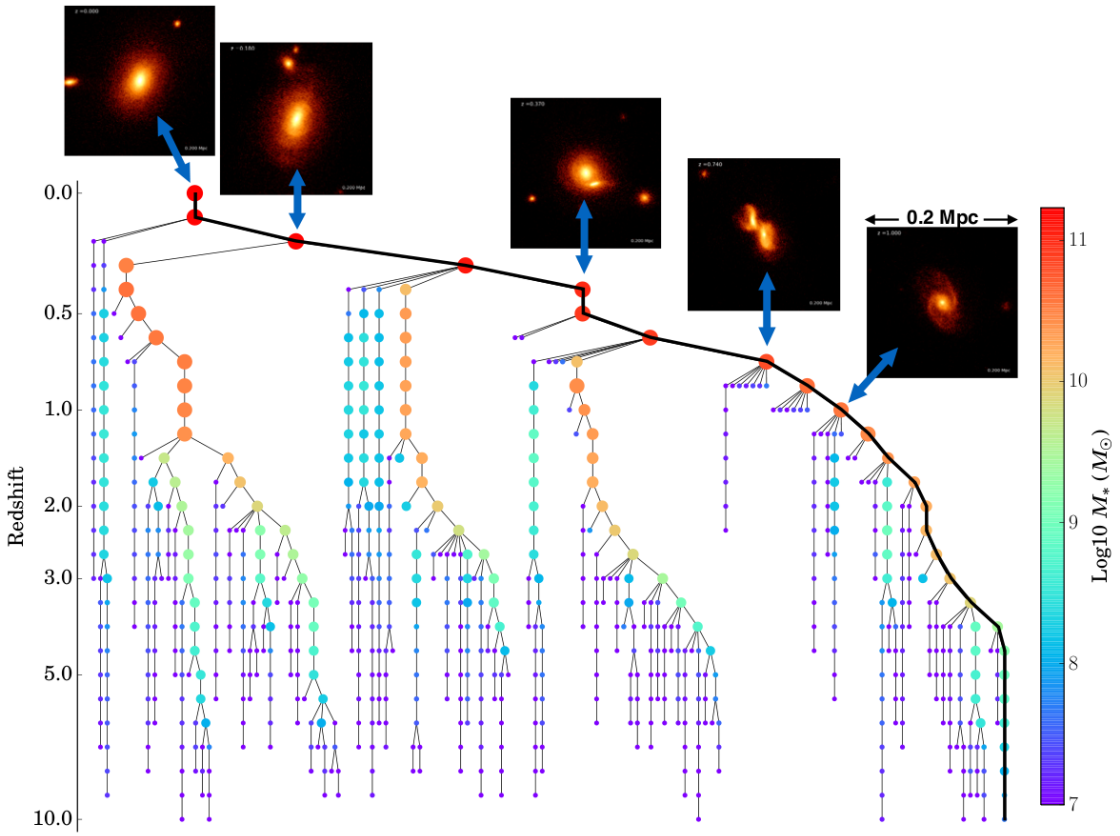

Figure 3.8: An example from Qu et al. (2017) of a galaxy merger history from numerical simulation. We follow a galaxy through the main branch (black line) that experience several merging and interactions events, for redshift between $0 < z < 1$, additional images of the galaxy's stellar mass distribution is displayed at the top. The size and color of the symbols are logarithmically scaled with stellar mass. *Credit: Qu et al., 2017.*

suffer several passes before merging. At each close pass, the galaxies can strip material from each other, creating tidal tails and other morphological disturbances. It can also trigger an enhancement of the star formation activiy within the galaxies and fuel starbursts (Joseph & Wright 1985; Di Matteo et al. 2007; Kaviraj 2014). This phenomenon is a relatively slow one, indeed the typical timescale for a merger between two massive galaxies of approximately the same mass is around 1 Gyr (Kitzbichler & White 2008; Jian et al. 2012; Moreno et al. 2013).

It is acknowledged that galaxy merger play a key role in the formation and evolution of galaxies. They are in part responsible for shaping galaxy morphologies, internal structures and dynamics (e.g. Mihos & Hernquist 1994; López-Sanjuan et al., 2012; Perret et al. 2014; Lagos et al. 2017). For example equal mass spiral

galaxy mergers are known to form elliptical galaxies. It is believed that even mergers with small companion galaxies can affect the disk of spiral galaxies and multiple mergers of different mass ratios can transform spiral galaxies into lenticular or elliptical systems (Bournaud et al., 2007).

Galaxy merger have also an important role in the mass assembly of galaxies (De Lucia & Blaizot 2007; Guo & White 2008). N-body/Hydrodynamical simulations are powerful tool to study the relative contributions of mergers to the stellar mass assembly of galaxies (Genel et al. 2009; Rodriguez-Gomez et al. 2016; Qu et al. 2017). The history of galaxies can be inferred from merger trees (see Fig 3.8). Thanks to these simulations, a given galaxy can be followed as it evolved through severals merging events along cosmic time. From Illustris simulations, Rodriguez-Gomez et al. (2016) estimated that about 50% of the ex-situ stellar mass of galaxies come from merger of equal mass galaxies and 20% from mergers with a small companion.

To conclude, understanding how galaxy mergers influence galactic evolution is a key aspect for every galaxy formation models.

Galaxy mergers classification

Different properties can be used to classify galaxy mergers. For example, using the gas richness of the galaxies allows the distinction between wet, dry and mixed merger (Lin et al. 2010). A merger between gas-rich or blue galaxies is called a wet merger. These interactions generally can trigger a larger amount of star formation, and even produce quasar activity. A dry merger involves two gas-poor or red galaxies, although they do not have a strong impact on the star formation they still contribute to the mass growth of the galaxies. Lin et al. (2010) suggest that dry mergers are important in the mass assembly of massive red galaxies in dense environments, like galaxy groups or clusters, contributing to 38% of their mass accretion in the last 8 billion year. Lastly, a mixed merger, as indicate by his name, is a merger between a gas-rich and gas-poor galaxy.

The most common way used by astronomers to distinguish between galaxy mergers is to use the mass ratio between the two galaxies as a proxy. Thus major

mergers occur when two galaxies of approximately the same size or mass collide. This is a violent event which often trigger star formation and strongly impact the morphology of the galaxies. For example, major merger are well known for forming elliptical galaxies from spiral parent galaxies. In comparison, minor mergers involve a companion galaxy significantly smaller and less massive than the primary galaxy (the most massive of the two). The satellite galaxy will be completely stripped from its gas and stars by the other galaxy who will suffer little effect. It is some sort of cosmological cannibalism. These events are more frequent in the nearby universe than major mergers. As a simple example of minor merger, our own galaxy, the Milky Way, seems to currently absorb smaller satellite galaxies like the Canis Major dwarf galaxy, and possibly the Magellanic Clouds. Minor mergers also play a role in galactic evolution for example they contribute significantly to the size growth of quiescent galaxies (Newman et al., 2012; Bédorf et al., 2013) and to the cosmic star formation budget (Kaviraj, 2014).

The relative contribution of major and minor mergers to the build-up of galaxies is still unclear. Although major mergers play a key role at low redshift (López-Sanjuan et al., 2012), is it the same in the early universe ? Some recent studies imply that major mergers are not the primary drivers behind galaxy growth at high redshift (Williams et al., 2011; Kaviraj et al., 2014) and other mechanisms like minor merger or cold gas accretion are at play.

3.3 How can we detect galaxy mergers ?

Galaxy mergers and cold gas accretion are mechanisms that play a key role in galaxy evolution. However, the relative importance of both phenomena remains uncertain, since the total amount of mass accretion onto galaxies by merging is still poorly constrained, especially in the early epoch of galaxy evolution due to the difficulty to observe these events at high redshift.

Several methods have been used to investigate merging activity across cosmic time, for instance by identifying mergers through perturbations in galaxy

morphologies or by close pair counts of galaxies. We detail these two methods in the following sub-sections.

3.3.1 Morphological studies

The study of the structure of galaxies is a very powerful method for determining galaxies that are in the process of merging. During these interactions, galaxy mergers deform the morphologies of the galaxies involved, some of them even become peculiar. This is particularly true for major mergers.

The main methods to detect galaxy mergers trough morphological clues use the CAS (concentration, C; asymmetry, A; clumpiness, S), Gini/M_{20} parameters or visual identification (Le Févre et al. 2000; Conselice et al. 2003, 2008; Lotz et al. 2006; Kampczyk et al. 2007; Bluck et al. 2012; Casteels et al. 2014).

The CAS quantitative morphological system (Conselice et al., 2003, 2006; 2014) uses the concentration, asymmetry, and clumpiness of a galaxy's light profile to distinguish galaxies in different phases of evolution in a three dimensional CAS space. Merging galaxies are identified mostly through the asymmetry index A, which accounts for the asymmetric appearance of a galaxy after a rotation of 180 degrees along the galaxy's line of sight center axis. Galaxy mergers generally present an important asymmetry value higher than the clumpiness parameter. This selective condition translating as $A > 0.35$ and $A > S$ allows the potential identification of about 50% of real mergers (Conselice, 2014). This method is more sensitive to major mergers (Conselice et al., 2003; Bluck et al. 2012).

Another approach uses the Gini or G and M_{20} indicators which is another non-parametric measure of galaxy morphology. In Lotz et al. (2004; 2006) they are described as: the relative distribution of the galaxy pixel flux values, G, and the second-order moment of the brightest 20% of the flux of the galaxy. Galaxy mergers can thus be identified using the following relation between G and M_20: $G > -0.115 \times M_{20} + 0.84$ (Lotz et al., 2006). This relationship is not sensitive to a particular type of merger but adapted to all types of mergers, minors and majors.

All these morphological methods trace post-mergers or galaxy mergers when the interactions between galaxies have already begun, contrary to the study of the close pairs which favors the detection of possible future mergers, only identifying close pair of galaxies. These methods are applicable to low redshift. However, instruments spatial resolution is often too poor to be able to calculate these morphological parameters at high redshifts ($z > 3$). Moreover morphological disturbances are not always related to merger events, as suggested by galaxy kinematics (e.g. Förster Schreiber et al. 2009, 2011), this is even more the case for high redshift. Therefore most studies at high redshift $z > 2$ have favored the close pair counts method to probe merger abundance.

3.3.2 Close pair counts of galaxies

A more statistical approach to trace merger abundance is through galaxy close pair counts analysis. Before they merge all these systems appeared as gravitationally bound pairs of two galaxies. Thus the idea is to detect close pairs of galaxies as a proxy for potential future mergers since these close pairs are expected to merge within an estimated timescale.

Ideally, close pairs of galaxies would be identified based on their true physical separation distance (i.e. in real space), however it is not directly applicable to observational survey.

While the first analyses on galaxy close pairs used the apparent angular separation and angular diameter of the galaxies as selection criteria (Turner 1976a; Peterson 1979), in more recent works a close pair is defined as two galaxies within a limited projected angular separation, $r_p < r_p^{max}$ (kpc), and line-of-sight relative velocity, $\Delta v < \Delta v_{max}$, based on the redshift of the two galaxies (Patton et al. 2000; de Ravel et al. 2009; Lopez-Sanjuan et al. 2013; Tasca et al. 2014; Man et al. 2016). The value range of the selection criteria used for the detection of close pairs of galaxies can vary according to the study.

Close pairs counts analysis have been conducted on both photometric and spectroscopic surveys. While photometric surveys have the advantages of providing

large samples of galaxies, which bring strong statistic for the estimation of the close pair fraction and rate, photometric redshifts are less reliable than spectroscopic ones, which usually translate in a velocity limit criterion higher than the one for spectroscopic survey. Thus the probability that the close galaxy pair will finally merge is lower, contaminating the sample by possible chance pairing (i.e. pairs which will satisfy the selection criteria but are not gravitationally bound). Using spectroscopic redshift is a more robust way to confirm the physical closeness of the two galaxies. For spectroscopic surveys a selection criterion of $\Delta v > 300 - 500$ $\mathrm{km\,s^{-1}}$ is often used, which offers a good compromise between contamination and pair statistics (Patton et al. 2000; Lin et al. 2008). The value range for the projected separation criterion varies a lot in the literature, $0 - 10 < r_p < 25 - 50 - 100 - 200$ $\mathrm{h^{-1}kpc}$. The difference in the selection criteria adopted can make direct comparisons difficult.

During this thesis, I use the close pairs count method in my analysis to infer the merger fraction and rate evolution in the MUSE data sets.

3.4 The galaxy merger fraction and rate up to $z \approx 3$

The merger fraction is usually defined as the number of galaxies involved in a merger divided by the number of individual galaxies in the sample for a given redshift interval. Various corrective terms must be applied to take into account potential selection effects and completeness, since observations are limited in volume and luminosity. The galaxy merger rate, which is the number of mergers suffered by a galaxy per Gyr, can then be derived from the fraction using merger time scales.

Until this PhD thesis, the galaxy major merger fraction and rate was rather well constrained from morphological and close pairs counts analyses up to $z \sim 1$. Overall, the major merger fraction is only about 2% in the nearby universe, then increases with redshift up to $z \sim 1$ (Lin et al. 2008; Bundy et al. 2009; de Ravel et al. 2009; Lopez-Sanjuan et al. 2012). The evolution of the major merger fraction can be parametrized as a function of redshift as a power law of the form $(1 + z)^m$ with

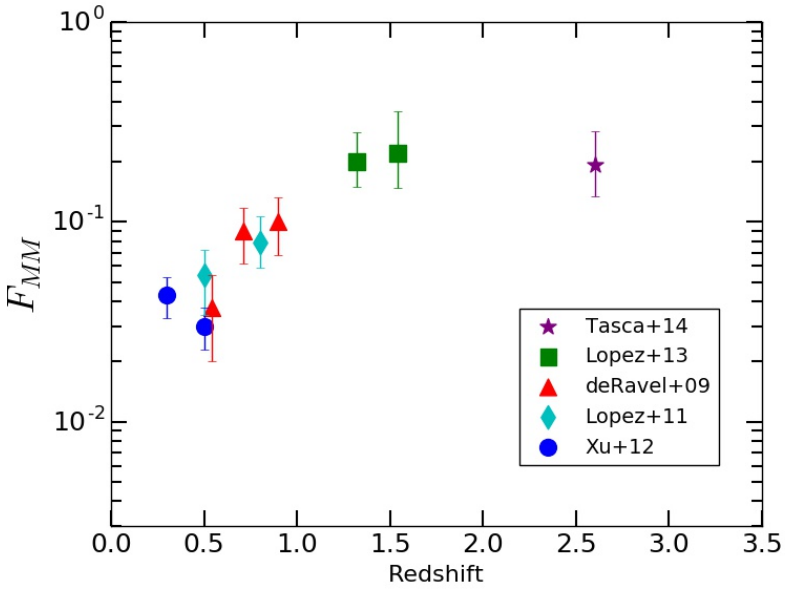

Figure 3.9: Evolution of the major merger fraction from spectroscopic close pair counts studies. Each symbol refers to a different survey: Tasca et al. (2014; purple star), Lopez-Sanjuan et al. (2011, cyan diamonds; 2013; green squares), de Ravel et al. (2009; red triangles), and Xu et al. (2012; blue points).

several values for the coefficient m reported in the literature, ranging from 0 to 5 (e.g. Le Fèvre et al. 2000; Kampczyk et al. 2007; Kartaltepe et al. 2007; de Ravel et al. 2009; Lotz et al. 2011, Keenan et al. 2014). This discrepancy between measurements usually comes from the various methods and selection criteria adopted.

Beyond $z \sim 1.5$, photometric and spectroscopic close pairs count studies report that the major merger fraction/rate seems either to increase up to $z \sim 2-3$ (Bluck et al. 2009; Man et al. 2012, 2016) for flux-ratio selected samples, or reach a maximum at $z \approx 2$ and then remains constant or turn down at higher redshift for mass-ratio selected samples (Lopez-Sanjuan et al. 2013; Tasca et al. 2014).

The large scatter between these results can be attributed to the selection criteria used for identifying major mergers either through the stellar mass ratio of the two galaxies, or their luminosity ratio. Indeed Man et al. (2016) reveal that by using a flux-selected ratio as proxy for major merger, the sample is in fact contaminated by a large number of minor mergers, with a mass ratio lower than 1:4. Thus flux-ratio-based galaxy merger fractions and rates must be treated carefully.

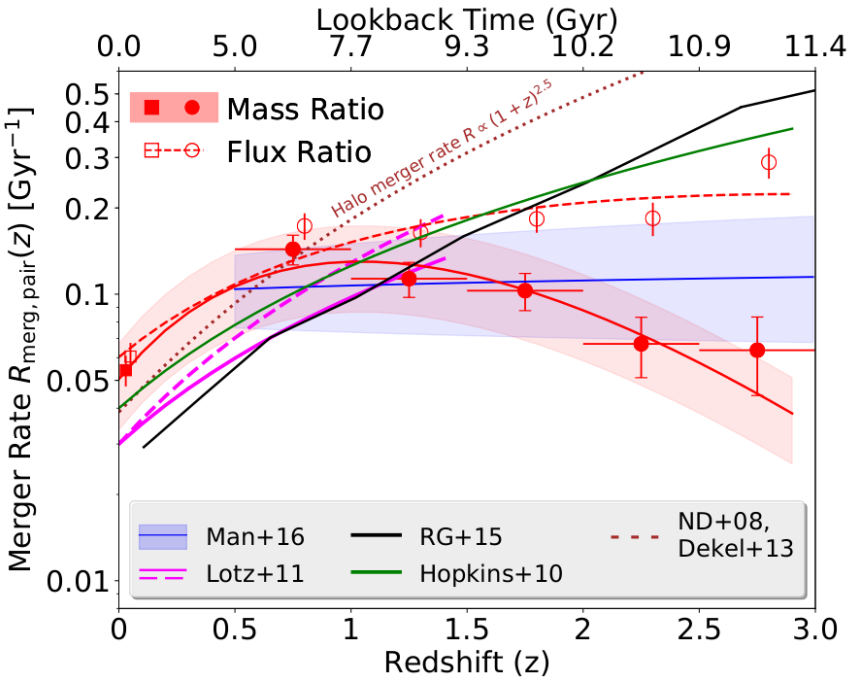

Figure 3.10: Comparison of the major merger rate derived from CANDELS and SDSS surveys for mass-ratio (filled red points) and flux-ratio (open red points) selected samples and for massive galaxies ($M^\star > 2 \times 10^{10}\ M_\odot$). The major merger rate from Mantha et al. (2018) photometric close pair counts analysis is also compared to previous works such as Lotz et al. (2011; dashed and solid magenta line), Man et al. (2016; blue line and associated uncertainties), as well as simulation predictions from Rodriguez-Gomez et al. (2015; black line) and Hopkins et al. (2010; green line). Lastly, the analytical predictions of major merger rate for $M_{halo} \approx 10^{12}\ M_\odot$ dark matter haloes $R \approx (1+z)^{2.5}$ is represented by the brown dashed line (Neistein & Dekel, 2008; Dekel et al., 2013). *Credit: Mantha et al., 2018*

Figure 3.10 illustrates the different evolutionary trends of the major merger rate obtained with either mass ratios or flux ratios (Mantha et al. 2018). Figure 3.9 shows the evolutionary trend of the major merger fraction along cosmic time obtained from a compilation of different spectroscopic close pairs counts studies with a mass-ratio selection criteria. As discussed previously, the major merger fraction seems to converge toward a value around 20% at $z = 2 - 3$ (Lopez-Sanjuan et al., 2013; Tasca et al., 2014). This evolutionary trend seems to be in agreement with recent predictions of cosmological simulations, like Horizon-AGN (Kaviraj et al. 2015) or EAGLE (Qu et al. 2017).

At the beginning of my PhD thesis, no measurement beyond $z \sim 3$ were reported due mainly to the difficulty of detecting spectroscopic close pairs of

galaxies at these redshifts.

As for the evolution of the minor merger fraction and rate of galaxies, these quantities were almost unconstrained, with very few attempts so far (eg. Lopez-Sanjuan et al. 2011, 2012, Lotz et al., 2011, Bluck et al., 2012).

In this context, the exquisite new data provided by second generation instruments such as the Multi Unit Spectroscopic Explorer (MUSE) are ideal to study pair counts and derive merger fractions and rates at high redshift.

3.5 Organization of the thesis

In this manuscript, I present my work on the investigation of cosmological evolution of the galaxy merger fraction and rate from MUSE deep fields. The following chapter describes the MUSE instrument and project as well as the data sets used in this study. I detail MUSE deep observations over four different regions of the universe, the Hubble Deep Field South and the Hubble Ultra Deep Field, the galaxy cluster Abell 2744 and a small region in the COSMOS field centered around the galaxy group GR30. The methods used to derived redshift measurements and other properties are also summarized in this section.

In chapter 5, I present my first analysis of the major merger fraction evolution from the first two deep MUSE fields, the Hubble Ultra Deep Field and the Hubble Deep Field South, which has been published in the *Astronomy & Astrophysics* journal (Ventou et al. 2017). I explain the method used to highlight the presence of companion galaxies orbiting around another and give estimates of the major merger fraction up to $z \approx 6$ for different stellar mass ranges of galaxies. Results are compared to previous close pair count studies and recent simulation predictions.

The second part of my thesis focused on the improvement of the galaxy close pairs criteria using Illustris cosmological simulations to investigate the relation between close pair selection criteria (separation distance and relative velocity) and whether the two galaxies will finally merge. I extend my close pair study to the whole data set (four deep MUSE fields in total) and derived robust estimates of the major and

minor merger fractions along cosmic time. This work is presented in chapter 6 in a paper format that will be submitted soon to the *Astronomy & Astrophysics* journal.

Finally, in the last chapter, I convert my results of the merger fraction in major and minor merger rates. In this section, I also discuss the uncertainties of the merger time scale and its influence on the merger rate.

4
MUSE observations

Contents

4.1 The project 47
4.2 The instrument 49
4.3 MUSE deep fields 52
4.3.1 Hubble Deep Field South 52
4.3.2 Hubble Ultra Deep Field 55
4.3.3 Abell 2744 60
4.3.4 COSMOS-Gr30 63

4.1 The project

The Multi Unit Spectroscopic Explorer, known as MUSE, is the culmination of a decade of research and development. Commissioned in 2014, Muse is installed on the Nasmyth focus of Yepun, the fourth Very Large Telescope at the Paranal Observatory in the middle of the Chilean Atacama desert. The project was born as an answer to the European Southern Observatory (ESO) call for proposals for second generation VLT instruments in early 2000s. The MUSE instrument is based on an innovative concept: coupling the capabilities of an imager and spectrograph in one device. The outcome is a unique and powerful instrument able to cover a large field of view with high resolution and acquire spectra for each pixel at the same time.

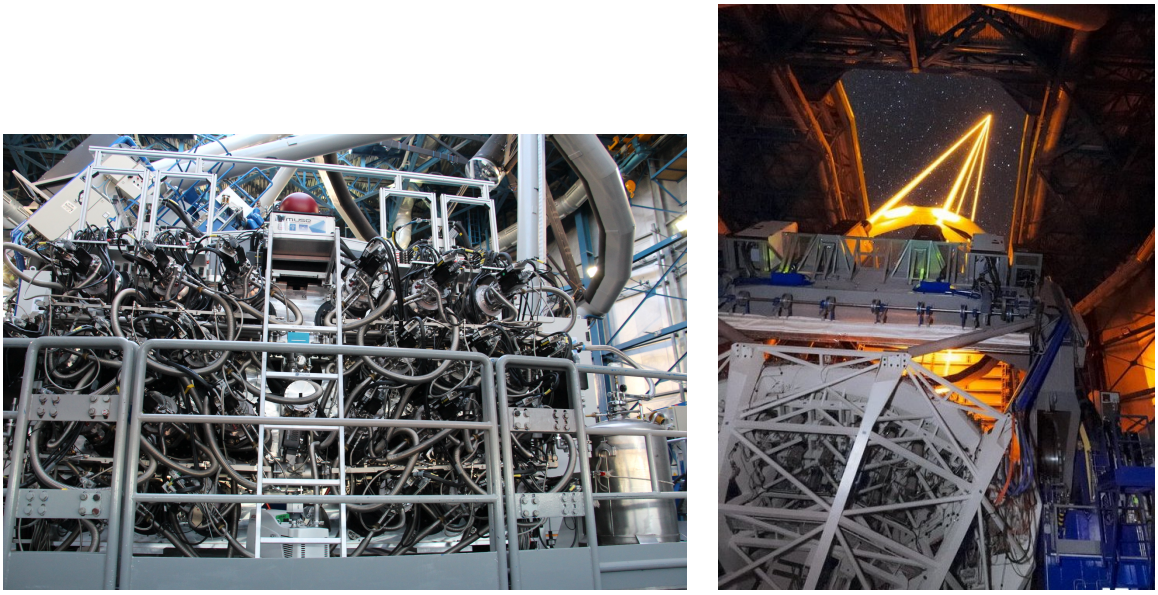

Figure 4.1: Photographs of MUSE on the Nasmyth focus of Yepun (UT4), one of the Very Large Telescope at the Cerro Paranal Observatory in Chile. This was taken in September 2016 during my stay at the VLT Observatory for a GTO run on behalf of the MUSE consortium (*left image*). The *right image* shows the recent coupling of the MUSE instrument with the Adaptive Optics Facility called "GALACSI". The four Laser Guide Stars Facility point to the sky creating artificial stars used to determine the atmospheric conditions.
Credit: Emmy Ventou, Roland Bacon.

The project is supported by seven European research institutes:

- The Centre de Recherche Astrophysique (CRAL) at Lyon, France
- The Potsdam Astrophysikalisches Institut (AIP), Germany
- The Institut de Recherche en Astrophysique et Planétologie (IRAP) at Toulouse, France
- The Leiden Observatory, Netherlands
- The Göttingen Astrophysics Institute (AIG), Germany
- The Astrophysics department of the Zurich Polytechnic Institute of Technology (ETH), Switzerland
- The European Southern Observatory (ESO)

After being assembled and tested at CRAL in Lyon, the instrument finally arrived at Paranal 10 years after the beginning of the project where it successfully saw its first light on January 31, 2014. Promising exquisite data sets and new discoveries for modern astrophysics in the years to come. The MUSE consortium, lead by Roland Bacon (CRAL) the project PI, gather more than 80 researchers, including post-docs and PhD students. All interested in various science goals such as formation and evolution of galaxies, stellar population in nearby galaxies, quasars, super massive black holes, early stage of stellar evolution and small bodies in the Solar system.

Members of the consortium get together for one week every six month during the famous “MUSE Busy Week”, where everyone present and discuss their science projects and work together to exploit MUSE wealth of data. Overall, the collaboration obtained 255 observation nights as Guaranteed Time Observation. This observation time is shared between 14 science programs with ambitious goals such as: the MUSE deep investigation of the Hubble Ultra Deep Field ("MUSE-Deep" program, PI: Roland Bacon, CRAL), probing highly magnified regions of massive lensing clusters (PI: Johan Richard, CRAL), or studying how the environment affect galaxy evolution over the past 8 Gyr (PI: Thierry Contini, IRAP). During my thesis, I personally contributed to this last project.

4.2 The instrument

MUSE is a second generation integral field spectrograph, an innovative and powerful instrument merging imaging and spectroscopy capabilities in order to probe the universe in 3 dimensions (Fig 4.3). Compared to other Multi-IFU (Integral-Field Unit), MUSE does not require to pre-select the sources beforehand, leading to the potential discovery of objects not detected in the pre-imaging observations.

This is made possible by an assembly of 24 integral field spectrographs with a complex optical schematic system (see Fig 4.2). The light coming from the observed region in the southern sky enters the instrument and first encounters the derotator which compensate for the earth rotation. After being magnified by mirrors, the field-of-view is then splitted a first time into 24 optical beams by the field splitter

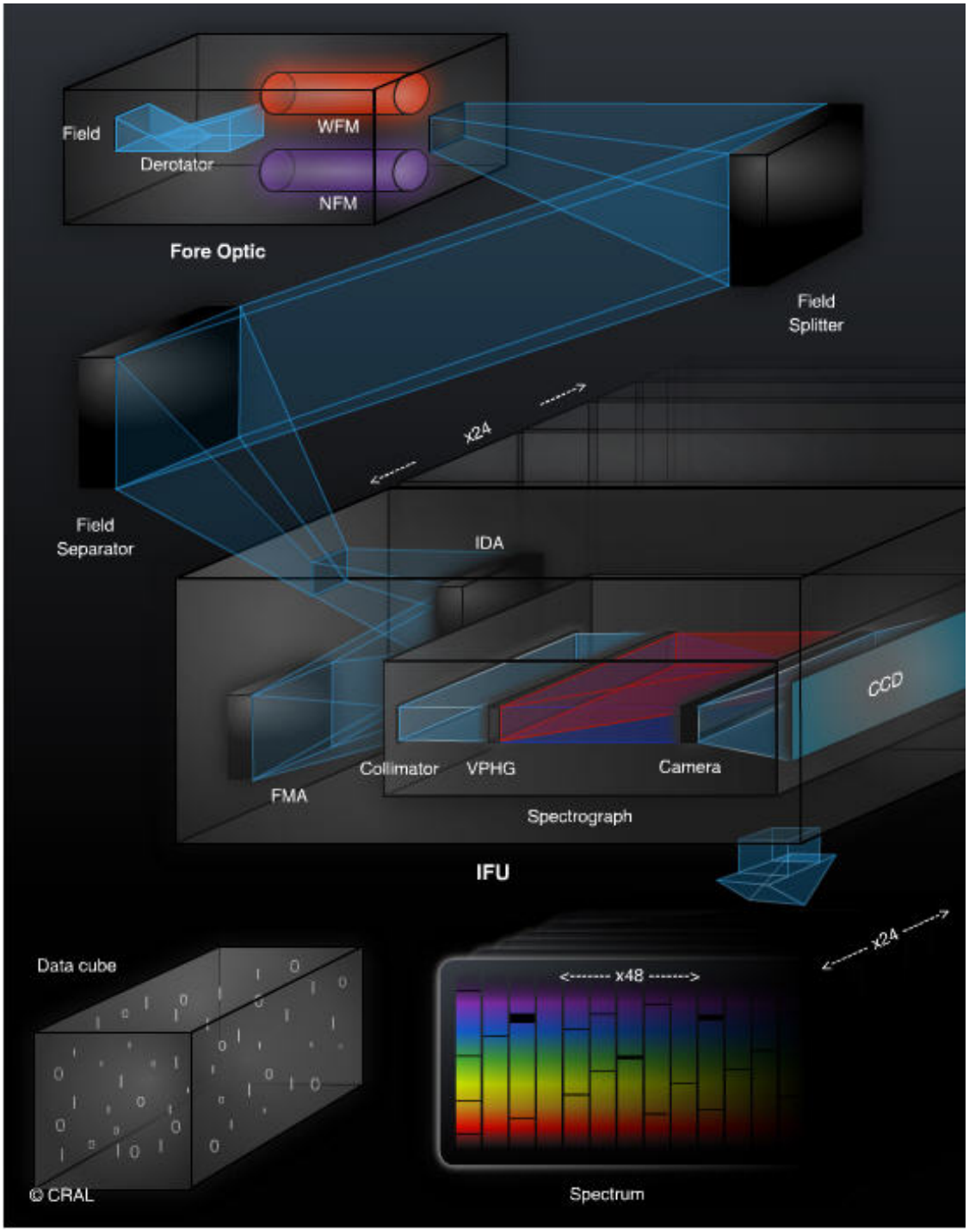

Figure 4.2: Illustration of MUSE optical schematic system and data acquisition as described in section 4.2. *Credit: CRAL*

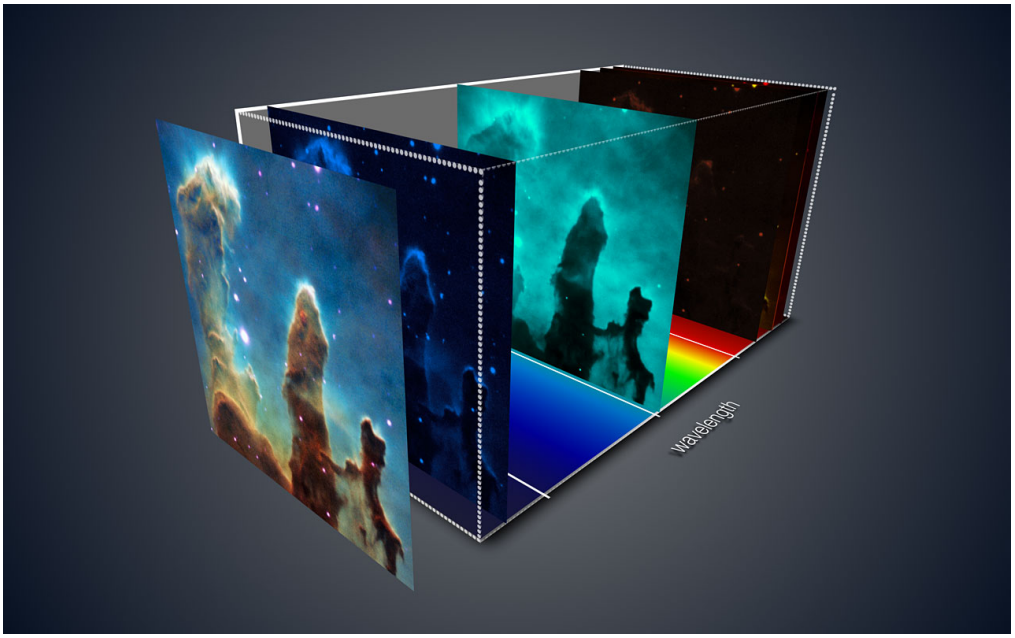

Figure 4.3: Illustration of a MUSE data cube, showing the three-dimensional view of the Pillars of Creation nebula in the Messier 16 region. The slices correspond to different views of the nebula at different wavelengths revealing motion and chemical gas components. *Credit: ESO*

and field separators. Each of these beams are distributed to the 24 spectrographs. The light is splitted again in 48 slices by a slicer, a revolutionary piece of technology composed of two set of 48 spherical mirrors (corresponding to the Image Dissector Array, IDA, and Focusing Mirrors Array, FMA, see Fig 4.2). Each slices follow their courses and enter the spectrograph where the light is dispersed according to its wavelength and finally arrive on a CCD detector of 16.8 million pixels.

The result is a 360 million pixels image containing 90 000 spectra covering a $4750 - 9300$Å wavelength range (Fig 4.3). Overall, MUSE covers a 1×1 arcmin^2 field-of-view in Wide Field Mode with a relatively good spectral resolution of $R = 2000$ in the blue to 4000 in the red, for each 0.2" $\times$ 0.2" spatial pixels. MUSE has also a second mode of observation, the Narrow Field Mode, which achieves a much better spatial resolution of $0.03" - 0.05"$ with a 0.025" spactial sampling, but covering a much smaller area 7.5" $\times$ 7.5".

For this thesis only observations made with the Wide Field Mode were used, the corresponding MUSE fields are introduced in the next section.

In June 2017, another adventure started with the coupling of the Adaptive Optics Facility (AOF) called "GALACSI" with the instrument, thereby improving the quality of the produced data set by correcting in real time the atmospheric distortion thanks to deformable mirrors. The Four Laser Guide Star Facility (4LGSF) consist in four laser beams pointed to the sky to mimic stars (see Fig 4.1, right image). These artificial guide stars are then used to compute atmospheric conditions and estimate the corrections to be applied to the deformable secondary mirror of the telescope. This ingenious system can thus compensate for the atmospheric disturbances up to one km above the telescope, where most of the atmospheric turbulences occurs. The resulting images are sharper, boosting further the capacity of the instrument to detect faint galaxies.

4.3 MUSE deep fields

Throughout these 3 years, my work was based on MUSE observations over 4 well known regions of the universe, the Hubble Deep Field South (4.3.1), the Hubble Ultra Deep Field (4.3.2), the Abell 2744 lensing cluster (4.3.3), and a galaxy group in the COSMOS field (4.3.4), obtained during a commissioning run in August 2014 (for the Hubble Deep Field South) and two years of the MUSE Guaranteed Time Observations (GTO), from September 2014 to February 2016 (for the others).

4.3.1 Hubble Deep Field South

The Hubble Deep Field South (HDF-S) is part of Hubble legacy. After the success of the Hubble Deep Field North in 1995, it was decided to acquire another deep optical image of the distant universe but this time in the southern hemisphere. Thereby 3 years later, the first HST images of this part of the sky were assembled over 10 days between September and October 1998 (Williams et al., 2000), leading to fruitful studies and breakthrough scientific results in modern astronomy especially in the domain of the formation and evolution of galaxies over cosmic time. Since then many other ground- or space-based instruments have observed this region providing large amount of data that are complementary to each other. Hence it

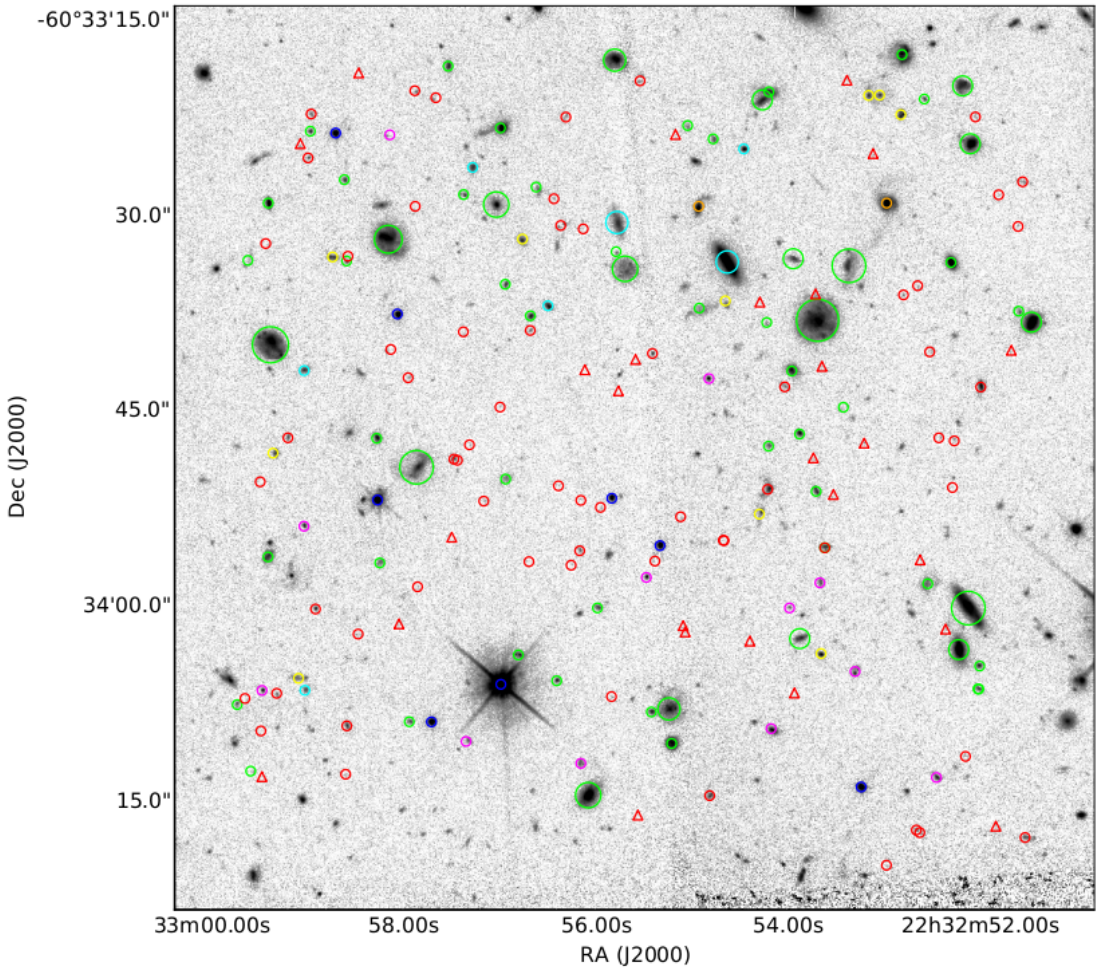

Figure 4.4: View of the HDF-S in the WFPC2 F814W image. Different symbols and colors served to classify objects as: stars (blue), AGN (orange), nearby objects with $z < 0.3$ (cyan), objects identified solely with absorption lines (yellow), [O II] λ3726,3729 (green) and C III] λ1907,1909 (magenta) emitters, and lastly Lyα emitters with or without HST counterpart (red circles and red triangles respectfully) *Image from Bacon et al. (2015).*

was an appropriate target for the last commissioning run of MUSE, in order to test and optimize the performance of the instrument and data reduction pipeline in the first deep field targeted with MUSE.

In August 2014, a 1×1 arcmin^2 area in the HDF-S centered around $\alpha = 22h32'55.64$" and $\delta = -60^o33'47$", chosen to include a bright-enough star for PSF monitoring, was observed during 6 nights, resulting in a single field of 27 hours of total exposure time. The data cube reaches a 1σ emission line surface brightness limit of 1×10^{-19} erg s^{-1} cm^2 arcsec^{-2}, with a spectral resolution of ~ 2.3 Å and a

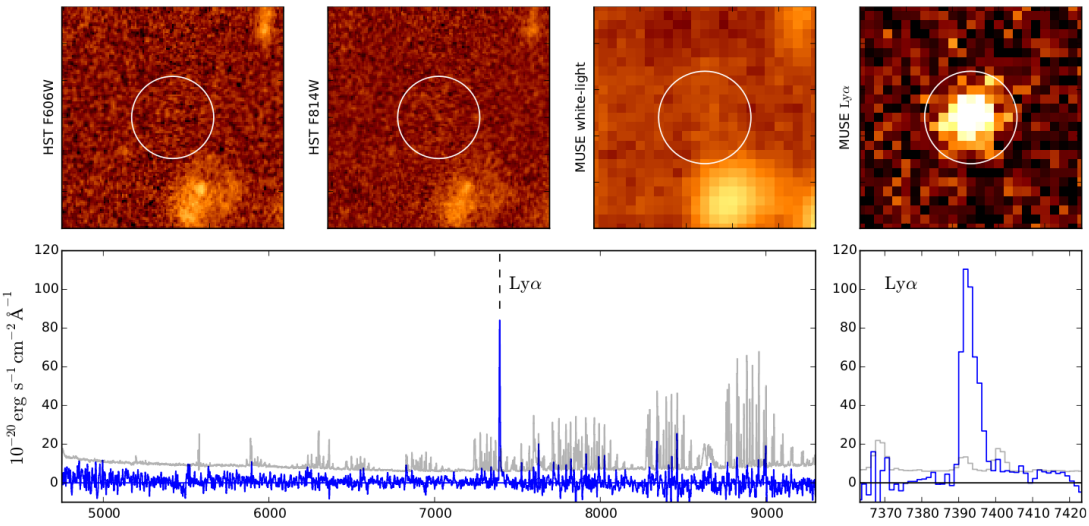

Figure 4.5: One of the Lyα emitters (MUSE ID 553) identified by MUSE without any HST counterpart at $z \approx 5.08$. *Top:* HST images in 2 filters (F606W and F814W) as well as MUSE reconstructed white light and Lyα narrow band images centered around the emission line location delimited by a white circle. *Bottom:* The full spectrum smoothed with a 4 Å boxcar (in blue) and its 3σ error (in grey), followed by a zoom of the unsmoothed spectrum centered around the Lyα emission line. *Image from Bacon et al. (2015).*

spatial resolution ranging between 0.6" for the red end of the spectral range and 0.7" in the blue. 1D and 2D spectra were extracted for all continuum detected objects in the master catalog of Casertano et al. (2000) within MUSE field of view. A complementary approach allowed the identification of emission line sources through visual inspection or automatic detection tools. One of the strategy uses SExtractor (Bertin & Arnouts 1996) on a set of numerous narrow-band images created over the full wavelength range of the cube to enhance the detection of emission lines. Another strategy uses the LSDCat software (Herenz et al., 2016, 2017) to probe the cube for line emitters not associated with any continuum sources (see Bacon et al., 2015 for more details on data reduction and spectral extractions). Each spectra were inspected manually to identify emission or absorption features. A confidence level was assigned to the redshift measurement, 0 for undetermined redshift, 1 for redshift likely correct based on one feature, 2 secure redshift based on one feature and 3 for secure redshift based on several features. Overall the spectroscopic redshift of 189 sources were accurately measured up to a magnitude of $I_{814} = 29.5$, about ten times more than what was previously known and spanning a

broad range $0 < z < 7$. Location of these objects and their classification in different categories (stars, AGN, early-type galaxies, [O II] λ3726,3729, C III] λ1907,1909 and Lyα emitters, ...) is shown in Fig. 4.4. The biggest surprise was the discovery of 26 Lyα emitting galaxies not detected in previous HST deep broad-band images. An example of such object with no HST counterpart is given in Fig. 4.5. More details on data reduction and redshift determination as well as the source catalog can be found in Bacon et al. (2015).

This first data set offers a spectroscopic sample of galaxies spread over a large redshift range and extending to objects with very low luminosities. I started my thesis trying to identify close pairs of galaxies by probing the environment of the galaxies in this field and highlighting the possible presence of a companion galaxy. This leaded to the first discovery of close pairs of galaxy at very high redshift ($z > 3$) with robust spectroscopic measurements. Once my method was tested and optimized, I extended my analysis to other fields, starting with data obtained with MUSE over another Hubble Deep Field, the Hubble Ultra Deep Field.

4.3.2 Hubble Ultra Deep Field

Observed for the first time in 2003, the Hubble Ultra Deep Field known as HUDF is still up to this day the deepest image ever taken of the visible universe. Located in the Fornax constellation, the field cover a total area of about 11 arcmin^2 with a total exposure time around 270 hours taken over the course of 400 HST orbits around Earth. The first images published in 2004, reveal a zoo of $\sim$10 000 galaxies of various sizes, shapes, colors and redshifts. Some of them may be among the most distant astronomical objects known, dating back to 800 million years after the Big Bang, allowing scientists to delve deeper into their research on the formation and evolution of galaxies since early epoch of the universe (Beckwith et al., 2006).

Since then the HUDF was observed many times by all kind of instruments, notably in 2009 with the installation on the HST of a new camera, the Wide Field Camera 3 (WFC3/IR), capable of making exquisite infrared observations with an improved resolution over a wilder field of view. Relaunching the hunt for the most

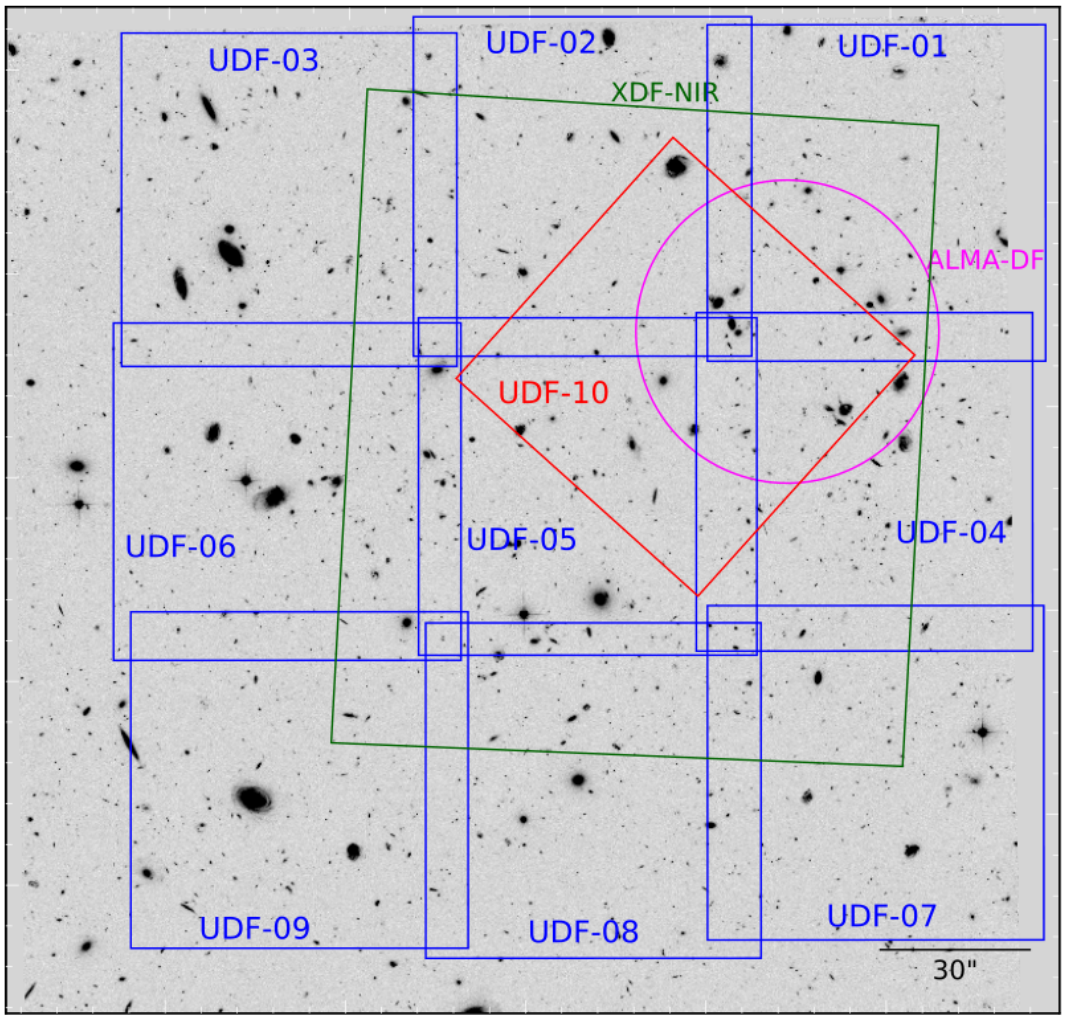

Figure 4.6: Orientation and position of the UDF-Mosaic (From UDF-01 to UDF-09, in blue) and UDF10 (in red) MUSE fields in the HST F775W image of the HUDF region. Regions observed with other instruments: the ALMA deep field (magenta circle) and the XDF region (green rectangle) are also shown. *Image from Bacon et al. (2017).*

distant galaxies ever observed, up to $z \approx 10$ (Bouwens et al. 2010, 2011, 2013). Released in 2012, the Hubble eXtreme Deep Field (XDF) is the combination of all the HST images that have been obtained over the HUDF in 10 years, from optical to near-infrared surveys (Illingworth et al. 2013). It covers approximately 80% of the HUDF area. Reaching a combined magnitude limit of 30.7 AB mag, its sensitivity is unparalleled. The HUDF was also observed in the X-ray, UV and radio wavelengths with surveys using telescopes such as Chandra, HST WFC3/UVIS camera, XMM-Newton or ALMA (Xue et al. 2011; Teplitz et al. 2013; Antonucci

et al. 2015; Luo et al. 2017; Dunlop et al. 2017).

It was thus natural to choose this region of the sky for the MUSE Deep Fields program to complement this wealth of data with deep spectroscopic observations. Between September 2014 and February 2016, MUSE observed the HUDF for a total of 137h of telescope time, resulting into two data cubes: the UDF-Mosaic, a medium-deep mosaic of 9 MUSE pointings covering 90% of the HUDF area, and a deeper single MUSE pointing, called udf-10, diving into the HUDF area covered by the deepest HST near-infrared WFC3 and ALMA images.

Figure 4.6 shows the positions and orientations of the UDF-Mosaic (consisting of 9 MUSE fields from UDF-01 to UDF-09) and the overlapping single field udf-10 in the HST image. In total the UDF-Mosaic covers a 3.15×3.15 arcmin^2 area with an average of 10 hours exposure time and an achieved spatial resolution of 0.65" at 7000 Å. The spectral resolution ranges from 3.0 Å at the blue end, to 2.4 Å at 7500 Å (for more details see Bacon et al. 2017). Centered around $\alpha = 03h32'38.7$" and $\delta = -27^o46'44$" in the XDF area, the udf-10 is an 1.15 arcmin^2 region overlapping the UDF-Mosaic and ALMA deep field. Combining 21 hours of udf-10 pointing and 10 hours of the UDF-Mosaic, it reaches a total deepness of 31 hours of exposure time. This is the deepest field observed with MUSE up to now, with spatial and spectral resolutions similar to the UDF-mosaic.

The data reduction follows approximately the same strategy used for the HDFS (Bacon et al. 2015). Using first MUSE standard pipeline[1] (Weilbacher et al. 2012), each exposures are first corrected from instrumental effects (using dark, flat and bias calibration files) and calibrated in wavelength. These informations are stored in a pixtable (pixel table) created for every exposures, which is in turn astrometric and flux calibrated and produce a data cube. Additional calibrations such as artifacts masking or sky background subtraction were performed (Bacon et al. 2017; Conseil et al. 2016), before combining the 227 individual data cubes into a final one. The reconstructed MUSE white-light images of both final data cubes for the UDF-Mosaic and udf-10 are displayed in Fig. 4.7.

[1]MUSE standard pipeline is available from ESO: http://www.eso.org/sci/software/pipelines/muse/muse-pipe-recipes.html

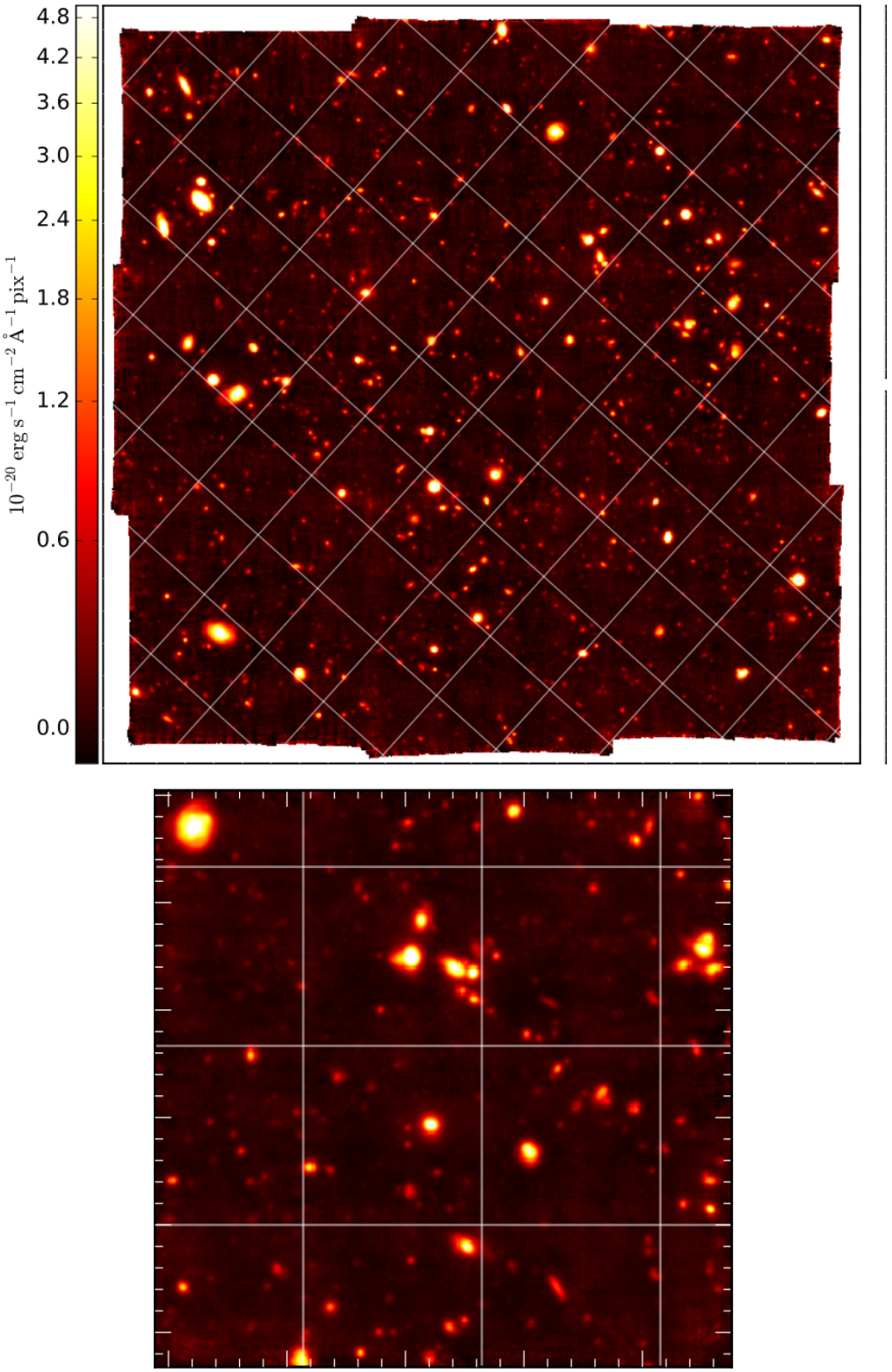

Figure 4.7: Reconstructed white-light images for the UDF-Mosaic (*Top*) and UDF10 (*Bottom*). *Image from Bacon et al. (2017).*

Two complementary methods were used for the redshift measurement (Inami et al. 2017). A first approach consists in using HST detected sources from the UVUDF catalog (Rafelski et al. 2015) as the priors to extract continuum selected objects. The second method involves a blind detection of emission-line objects in the data cube. Due to the spatial resolution limit of MUSE, sources located within 0.6" are detected as one blended object. The blind detection was performed using the new automated software ORIGIN (detectiOn and extRactIon of Galaxy emIssion liNes; Bacon et al. 2017). It uses a matched filter in 3D data correlated to spectral templates to detect spectral signatures in the data cube. Several tests such as narrow-band images are then performed to determine if its a real detected line or not (see Bacon et al. 2017 for more details). Following the combination of the two methods over the udf-10, it was decided to use a magnitude cut of 27 mag in the F775W band, only inspecting with the first method objects below this magnitude threshold, in order to maximize the efficiency of the redshift measurement in the UDF-Mosaic (Inami et al. 2017). Thanks to the blind emission-line detection approach, 72 new objects were identified in the MUSE data that were not detected previously in the HST images.

Redshift measurement was done through an automated method using a customized version of the redshift finding code MARZ (Hinton et al. 2016), followed by a visual inspection. MARZ find the best fitting spectral template to the input spectrum of the source and thereby estimates its redshift. HST, MUSE white-light and narrow-band images are also available for each source (Inami et al. 2017). At least two investigators measured independently each redshifts, a final careful check allowed to consolidated the redshifts for the catalog. A confidence level in the measurement was attributed following these conditions: CONFID= 3 for secure redshift based on several spectral features, CONFID= 2 for redshift based on one well-identified feature, such as a Lyα emission line for example, and CONFID= 1 for a likely redshift determined by a single feature with uncertainties on the nature of this feature. The redshift distribution of all objects as a function of their confidence level as well as their classification type (nearby emission line object, absorption line galaxy, as well as [O II] λ3726,3729, [O III] λ4959,5007, C III] λ1907,1909 and Lyα

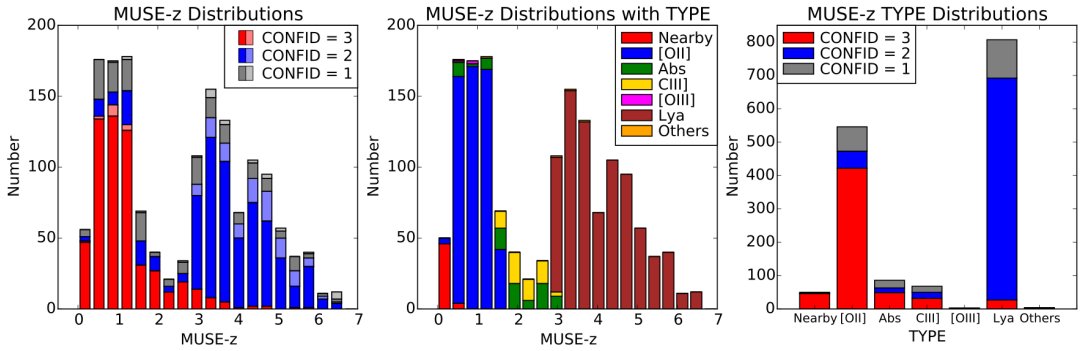

Figure 4.8: Redshift distribution of all objects detected in the combined UDF-Mosaic and UDF10 surveys. From *left to right*: redshift histogram over the whole redshift range by step of 0.35 showing the contribution of the different redshift confidence levels 3, 2 and 1 (red, blue and gray), lighter colors indicate objects detected only with the ORIGIN method; followed by the redshift histogram color-coded according to the different object types; and the last histogram shows the same classified objects but color-coded by their redshift confidence levels. *Image from Inami et al. (2017).*

emitters) are shown in Fig. 4.8. Overall the spectroscopic redshift of 1439 sources was measured in the final combined catalog of the mosaic and udf-10 surveys, increasing by a factor of eight the number of spectroscopically-known objects in the UDF, with a depth ranging up to the 30th magnitude (F775W, see Fig. 4.9) (Inami et al. 2017).

This is the largest data set used for my PhD work on galaxy mergers (Ventou et al. 2017) as well as for several other studies from the properties of C III] λ1907,1909 emitters (Maseda et al. 2017), the stellar kinematics of spatially-resolved galaxies at $0.2 \leq z \leq 0.8$ (Guérou et al. 2017), the faint end of the Lyα luminosity function at $2.91 < z < 6.64$ and its implications for reionisation (Drake et al. 2017b), the properties of FeII* emission in star-forming galaxies (Finley et al. 2017b), the extended Lyα haloes around high-z star-forming galaxies (Leclercq et al. 2017), and the study of Lyα equivalent widths at $2.9 < z < 6.6$ (Hashimoto et al. 2017).

4.3.3 Abell 2744

A galaxy cluster is a collection of hundreds to thousands of galaxies bound together by gravity. Abell 2744 is part of a large catalog of such galaxy clusters which was first compiled in 1958 by George O. Abell from his "Northern survey". It was updated later in 1989 with the participation of Harold G. Corwin and Ronald

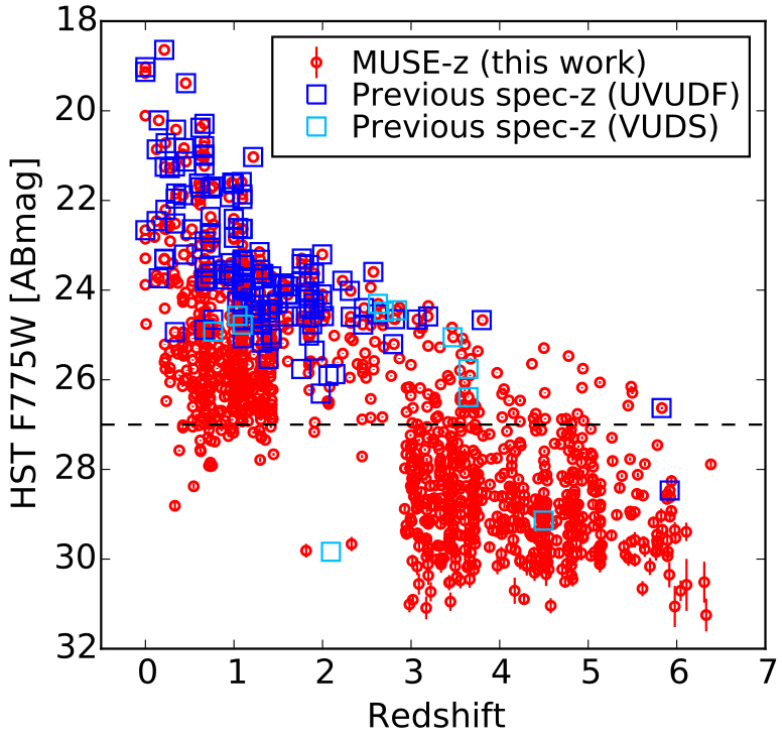

Figure 4.9: Magnitude vs redshift diagram for all objects with secure redshifts (confidence level ≥ 2) of the combined MUSE data set over UDF-Mosaic and UDF10 (red circle). The squares indicate reliable spectroscopic redshifts collected in the UVUDF (blue) and VUDS (cyan) surveys. The dashed line corresponds to the 27mag cut performed for the redshift determination of the mosaic with MUSE. *Image from Inami et al. (2017).*

P. Olowin (Abell et al., 1989), adding clusters from parts of the south celestial hemisphere not covered in the original survey. The resulting catalog contains more than 4 000 galaxy clusters with at least 30 bright galaxy members. Abell 2744 also called Pandora's cluster is located in the Sculptor constellation at a redshift around $z \approx 0.308$. This rich galaxy cluster has been well-studied since its discovery. Chosen as one of the targets for the Hubble Frontier Field initiative (Lotz et al., 2017), the field was observed by Hubble, Spitzer and Chandra. Combining these deep observations allowed astronomers to study galaxy structure, history and mass of giant galaxy cluster, as well as discover very distant galaxies via gravitational lensing. This technique consists in using the gravity of the cluster as a lens to brighten and magnify background galaxies. The mass of a cluster, typically ranging from $10^{14} - 10^{15}$ $M_{\odot}$, warps space around it. The light is then bent and redirected, like it would have been if it was passing through a glass lens. Background galaxies

are brightened and magnified and thus, very faint and distant galaxies that could not be seen before may now be observable, gravitational lensing naturally improve the optical performance of a telescope. Because of this phenomenon, the lensed galaxy image appears stretched, distorted and in some cases can be duplicated. Thus, multiple images of the same galaxy can be detected across the field. Figure 4.11 shows an example of such multiple-images system. Several remote galaxies were discovered in A2744 with an estimated redshift between $7 \leq z \leq 10$ (Laporte et al., 2014; Zitrin et al., 2014; Lam et al., 2014; Oesch et al., 2015). A2744 seems to be a giant cluster resulting from the complex merging of at least 4 sparser smaller galaxy clusters (Owers et al., 2011; Merten et al., 2011). The mass distribution and magnification maps of the cluster were derived from both strong- and weak-lensing analysis and parametric mass modeling (Richard et al., 2014; Jauzac et al., 2015).

A2744 was observed with MUSE as part of a GTO program leaded by J. Richard focusing on probing the highly magnified regions of massive lensing clusters. This ambitious program combines MUSE spectroscopy and the lensing properties of clusters to address numerous science goals such as characterizing lensing clusters (Richard et al., 2015; Lagattuta et al., 2017), and studying faint and distant populations of galaxies (Patrićio et al., 2016; Bina et al., 2016). A2744 was observed by MUSE between September 2014 and October 2015, achieving a total exposure time of 18.5h. The observations cover a $2'' \times 2''$ mosaic centered around $\alpha = 00h14'20.95$" and $\delta = -30°23'53.88$" (see Fig. 4.10). As for the UDF-Mosaic, sources were extracted using a combination of different detection methods (Mahler et al., 2018), accounting for the sensitivity of the instrument to emission-line objects. First, spectral extractions were carried out at the location of known faint sources in the deep Hubble Frontier Field (HFF) images. The apertures for this spectral extraction were defined using a photometric catalog build from HFF images. Effects of the diffuse intra-cluster light of the cluster core on the detection of faint sources were taken into account, by using a median subtraction process described in Mahler et al. (2018) to remove this light in each filters. Later, a photometric analysis using SExtractor (Bertin & Arnouts 1996) was performed

on objects detected in the combined images. In parallel, automatic line detection tools based on narrow-band filtering were used to search for sources detected only by their line emission. The software MUSELET[2] produced narrow-band images over the whole wavelength of the MUSE data cube, SExtractor was then applied to these narrow-band images to detect the flux excess due to emission lines. Lastly, manual extractions were performed on sources identified by visual inspection but not detected by the two previous methods. The redshift measurement for the detected objects was done independently by a team of six investigators, the confidence level associated to each estimation is based on the same system as the one used for the UDF-Mosaic (CONFID 3 and 2 correspond to secure redshift whereas a CONFID 1 was attributed to unsecure redshift). The final catalog counts 514 sources with 414 new identifications (Mahler et al., 2018). Figure 4.10 shows the spatial and redshift distributions of all objects. Thanks to this incredible data set, several multiple-images systems were either confirmed or rejected (Mahler et al., 2018). For this work, I used a derived catalog from this master catalog, where the multiple-images systems were removed and with sources positions computed in the source plane (ie. corrected for lensing effects).

4.3.4 COSMOS-Gr30

The Cosmic Evolution Survey (COSMOS) field covers a wide 2 square degree region in the constellation of Sextans (Scoville et al., 2007). The field was observed over a broad wavelength range (from X-ray to radio) by numerous space- and ground-based telescopes, such as Hubble, Spitzer, GALEX, XMM-Newton, Chandra, Herschel, Keck, Subaru, VLA, ALMA, ESO-VLT and others. Knobel et al. (2012) present a catalog of galaxy groups selected in the optical and based on spectroscopic redshifts between $0.1 \leq z \leq 1$ from the zCOSMOS survey (Lilly et al. 2007, 2009). The properties of the 1498 groups, as well as the identification of the galaxy group members, are listed in Knobel et al. (2012).

[2]MUSELET is an analysis software released by the consortium as part of the MPDAF suite http://mpdaf.readthedocs.io/en/latest/muselet.html

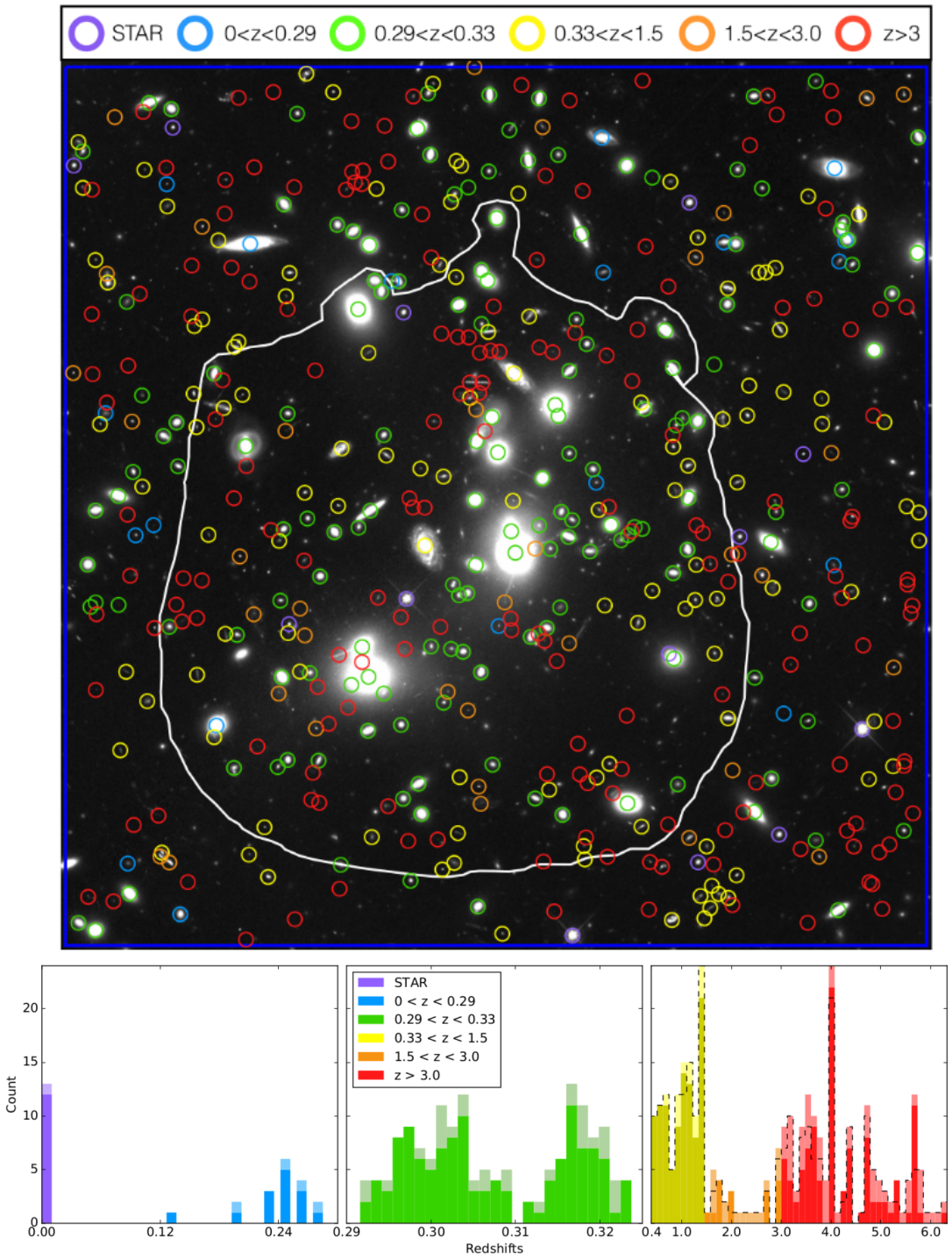

Figure 4.10: *Top:* View of A2744 in the RGB HST image, delimited by the MUSE mosaic field of view (blue box). The white line defines the multiple image area for $z \leq 10$ objects. The colored circles show the different sources located in this field, color-coded with respect to their redshifts: purple for stars, green for cluster members, blue for foreground objects with respect to the cluster, while yellow, orange and red are background sources. *Bottom:* Redshift histogram of the same sources. The darker and lighter colors represent confidence 3 and 2 objects respectively. In the right panel, the black dashed line correspond to the number of independent background objects, corrected from multiplicity due to lensing. *Image from Mahler et al. (2018).*

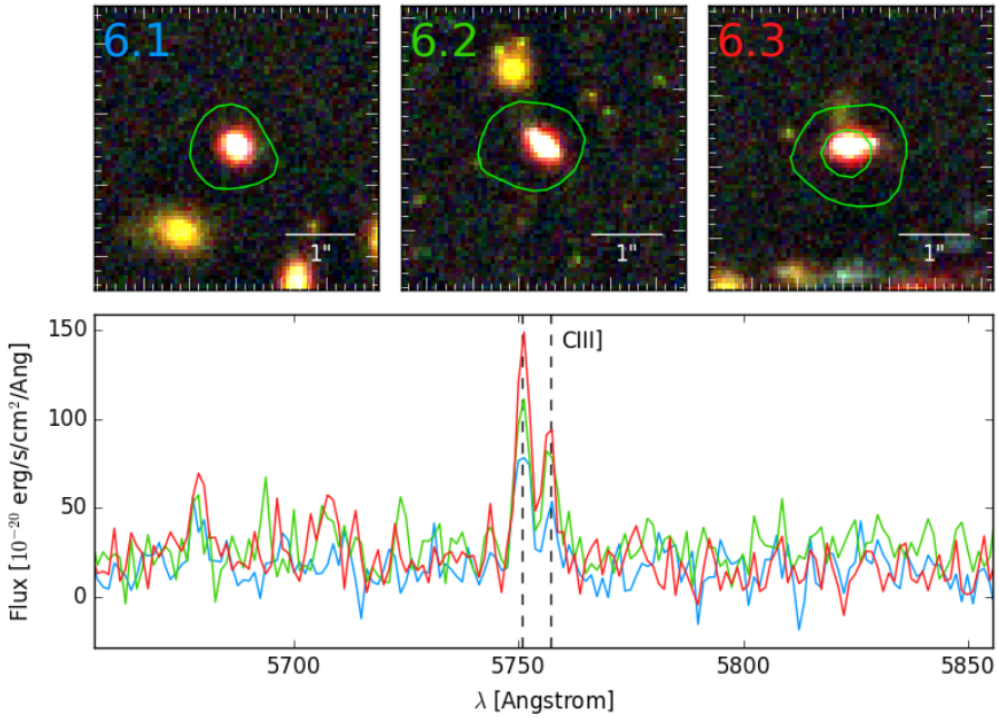

Figure 4.11: An example of a multiple image system identified in A2744. The *top panel* shows the HST RGB images created from the median-subtracted images used for the photometry-based spectral extraction. While the *bottom panel* displays the different spectra around the main spectral feature used to determine the redshift of the system. *Image from Mahler et al. (2018).*

One of these galaxy groups, Gr30 at $z \sim 0.7$, was targeted for MUSE deep observation as part of the GTO program that aims to study how the environment affect galaxy evolution over the past 8 Gyr (PI: T. Contini, IRAP). Between December 2014 and May 2015, a total of 10h of exposure time was obtained on a single field of 1×1 arcmin^2. The data reduction was performed using the same MUSE standard pipeline as the UDF-Mosaic or A2744 (see details in Epinat et al., 2018). The resulting data cube presents the same spatial and spectral sampling characteristics as for the previous fields introduced in this section. The final spatial resolution is estimated to be around $0.68''$ at 7000Å (Epinat et al., 2018). As for the previous fields, the spectral extraction of continuum detected objects was performed on sources selected from COSMOS2015 photometric catalog (Laigle et al., 2016), which contains most of the ancillary data available for this field. The resulting MUSE catalog was further completed by the addition of emission line

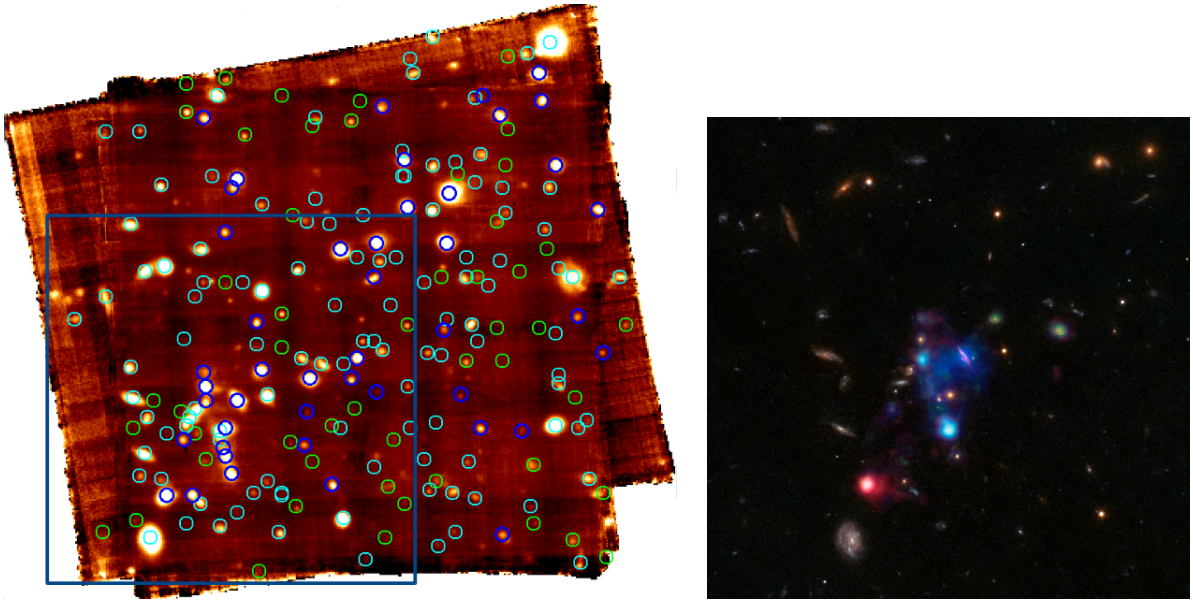

Figure 4.12: View of the galaxy group COSMOS-Gr30 in the MUSE reconstructed white light (left) and HST RGB (right) images. The *left panel* shows the spatial distribution of all sources superimposed on MUSE white-light image of COSMOS-Gr30. Blue circles represent the 45 group members identified in the data cube. Cyan and green circles indicate the secure (confidence 3 or 2) and unsecure (confidence 1) spectroscopic redshift. An HST RGB image of an over-dense region in the field (corresponding to the blue box in the MUSE image) is displayed in the *right panel*. In this region a bubble of ionized gas has been discovered thanks to the sensitivity of the MUSE. The bubble contains 10 individual galaxies in total (Einat et al., 2018). *Credit: Right image; ESO, T. Contini (IRAP, Toulouse), B. Epinat (LAM, Marseille).*

sources detected by the ORIGIN software (describe in sect 4.3.2). A PSF-weighted spectrum was extracted for each objects using a similar method as Inami et al. (2017) without imposing any magnitude limit. Then a customized version of the redshift finding code MARZ (Hinton et al., 2016; Inami et al., 2017) was applied to asses the redshift. The process is briefly described in the UDF-Mosaic section (above) as well as the corresponding confidence level system.

The final catalog contains 208 objects with 157 secure spectroscopic redshifts (CONFID 3 or 2) as well as 45 secure galaxy group members of COSMOS-Gr30. This is the last data set used for my thesis. The spatial distribution of the group members as well as the localization of the secure and unsecure redshift sources are given in Fig 4.12, left panel. In an over-dense region of this field, a ionized gas structure of 100 kpc was detected in [O II] λ3726,3729at $z \approx 0.7$ (see Fig 4.12,

right panel) . This is the largest gaseous structure discovered up to this day at any redshift (Epinat et al., 2018). An investigation of its physical properties such as its kinematics revealed that the "bubble" is composed of two sub-structures that seem to be linked to the two most massive galaxies enclosed in the ionized gas.

5

Evolution of the major merger fraction since $z \approx 6$

Contents

5.1 The MUSE Hubble Ultra Deep Field Survey IX: Evolution of galaxy major merger fraction since $z \approx 6$ . . . 69

5.1 The MUSE Hubble Ultra Deep Field Survey IX: Evolution of galaxy major merger fraction since $z \approx 6$

In this section, I present my first analysis on the major merger fraction evolution in the deep MUSE observations over the Hubble Ultra Deep Field and the Hubble Deep Field South. This analysis has been published in September 2017 along with 11 other papers as part of the MUSE Hubble Ultra Deep Field Survey series.

In this publication, I show the potential of instruments such as MUSE, which enable to perform deep spectroscopic surveys blindly without any pre-selection of galaxies, for the study of galaxy mergers at different redshifts. Indeed in this first analysis, I was able to identify close pairs of galaxies at very high redshift ($z > 3$) and probe a much larger range of stellar masses than before. The organization of

the paper is quite simple with an introduction of the MUSE data sets in the first section, followed by a description of the selection method used to identify galaxy close pairs in the sample. I discuss the main limitations of this method and how some selection biases were taken into account and corrected like the recovery of the systemic redshift of Lyα emitters. In the final part of the article, I detail how the major merger fraction is computed and give an estimate of the major merger fraction evolution up to $z \sim 6$ for several stellar mass ranges. In a final discussion, I compare the results obtained both to previous spectroscopic close pair count studies as well as predictions from recent numerical simulations.

My contribution to this work is major since most of the analysis was performed by myself. The MUSE data-cubes and redshift catalogs used in this study are the products of a team effort led by Roland Bacon (CRAL) and involving most co-authors. The stellar mass for galaxies at $z > 3$ was estimated by Daniel Lam (Leiden). I also collaborated with Anne Verhamme (Geneva Observatory) to the building of an empirical relation between the observed Lyα FWHM and the shift of the peak to correct my Lyα-based redshifts for this velocity offset.

A&A 608, A9 (2017)
DOI: 10.1051/0004-6361/201731586

Astronomy & Astrophysics
Special issue

The MUSE Hubble Ultra Deep Field Survey

The MUSE *Hubble* Ultra Deep Field Survey

IX. Evolution of galaxy merger fraction since $z \approx 6$*

E. Ventou[1], T. Contini[1], N. Bouché[1], B. Epinat[1,2], J. Brinchmann[3,4], R. Bacon[5], H. Inami[5], D. Lam[3], A. Drake[5], T. Garel[5], L. Michel-Dansac[5], R. Pello[1], M. Steinmetz[6], P. M. Weilbacher[6], L. Wisotzki[6], and M. Carollo[7]

[1] Institut de Recherche en Astrophysique et Planétologie (IRAP), Université de Toulouse, CNRS, UPS, 31400 Toulouse, France
e-mail: emmy.ventou@irap.omp.eu
[2] Aix-Marseille Université, CNRS, LAM, Laboratoire d'Astrophysique de Marseille, UMR 7326, 13388 Marseille, France
[3] Leiden Observatory, Leiden University, PO Box 9513, 2300 RA Leiden, The Netherlands
[4] Instituto de Astrofísica e Ciências do Espaço, Universidade do Porto, CAUP, Rua das Estrelas, 4150-762 Porto, Portugal
[5] Univ. Lyon, Univ. Lyon1, ENS de Lyon, CNRS, Centre de Recherche Astrophysique de Lyon, UMR 5574, 69230 Saint-Genis-Laval, France
[6] Leibniz-Institut für Astrophysik Potsdam (AIP), An der Sternwarte 16, 14482 Potsdam, Germany
[7] Institute for Astronomy, Department of Physics, ETH Zurich, 8093 Zurich, Switzerland

Received 17 July 2017 / Accepted 4 September 2017

ABSTRACT

We provide, for the first time, robust observational constraints on the galaxy major merger fraction up to $z \approx 6$ using spectroscopic close pair counts. Deep Multi Unit Spectroscopic Explorer (MUSE) observations in the *Hubble* Ultra Deep Field (HUDF) and *Hubble* Deep Field South (HDF-S) are used to identify 113 secure close pairs of galaxies among a parent sample of 1801 galaxies spread over a large redshift range ($0.2 < z < 6$) and stellar masses (10^7–10^{11} $M_\odot$), thus probing about 12 Gyr of galaxy evolution. Stellar masses are estimated from spectral energy distribution (SED) fitting over the extensive UV-to-NIR HST photometry available in these deep *Hubble* fields, adding *Spitzer* IRAC bands to better constrain masses for high-redshift ($z \geqslant 3$) galaxies. These stellar masses are used to isolate a sample of 54 major close pairs with a galaxy mass ratio limit of 1:6. Among this sample, 23 pairs are identified at high redshift ($z \geqslant 3$) through their Lyα emission. The sample of major close pairs is divided into five redshift intervals in order to probe the evolution of the merger fraction with cosmic time. Our estimates are in very good agreement with previous close pair counts with a constant increase of the merger fraction up to $z \approx 3$ where it reaches a maximum of 20%. At higher redshift, we show that the fraction slowly decreases down to about 10% at $z \approx 6$. The sample is further divided into two ranges of stellar masses using either a constant separation limit of $10^{9.5}$ $M_\odot$ or the median value of stellar mass computed in each redshift bin. Overall, the major close pair fraction for low-mass and massive galaxies follows the same trend. These new, homogeneous, and robust estimates of the major merger fraction since $z \approx 6$ are in good agreement with recent predictions of cosmological numerical simulations.

Key words. Galaxy: evolution – galaxies: interactions – galaxies: high-redshift

1. Introduction

Galaxy mergers play a key role in the formation and evolution of galaxies (e.g. Baugh 2006; Conselice 2014), especially in a Λ cold dark matter (ΛCDM) cosmology where structures of dark matter halos (DMH) grow hierarchically (e.g. White & Rees 1978). These events have an important impact on the evolution of galaxies, such as their mass assembly (De Lucia & Blaizot 2007; Guo & White 2008; Genel et al. 2009; Rodriguez-Gomez et al. 2016; Qu et al. 2017), and their star formation history (Mihos & Hernquist 1996; Somerville et al. 2001). Mergers are also responsible for drastic changes in galaxy morphologies, internal structures, and dynamics (e.g. Mihos & Hernquist 1994; Naab & Burkert 2003; Bell et al. 2008; Perret et al. 2014; Lagos et al. 2017). Understanding the role of mergers in the evolution of galaxies and their importance relative to other processes, such as cold gas accretion (e.g. Keres et al. 2005; Ocvirk et al. 2008; Genel et al. 2008), is thus a key aspect of galaxy formation models.

The most simple and direct way to investigate the role of mergers in galaxy evolution is to count the number of observed events. There are several approaches for the identification of mergers in the universe. The occurrence of morphologically disturbed systems, through visual inspection (e.g. Brinchmann et al. 1998; Bundy et al. 2005; Kampczyk et al. 2007) or quantitative measurements (e.g. Abraham et al. 1996; Conselice et al. 2000, 2003, 2009; Lotz et al. 2008; Lopez-Sanjuan 2009a,b; Casteels et al. 2014), has been widely used thanks to deep and high-resolution images such as those from HST. A second approach is to count close pairs of galaxies, i.e. two galaxies with low values of projected angular separations ($\leqslant$25 h^{-1} kpc) and line-of-sight relative radial velocities ($\leqslant$500 km s^{-1}). Simulations have shown that the vast majority of pairs meeting these criteria indeed merge on reasonable timescales, typically shorter than 1 Gyr (Boylan-Kolchin et al. 2008; Kitzbichler & White 2008; Jian et al. 2012; Moreno et al. 2013). However, these different methods of selecting merger candidates might be sensitive to different

* Based on observations made with ESO telescopes at the La Silla-Paranal Observatory under programmes 094.A-0289(B), 095.A-0010(A), 096.A-0045(A) and 096.A-0045(B).

stages in the merging process, for example pre-merging or early merging for close pair counts and ongoing merging or post-merging from morphological identification. Observational constraints on the merger fractions can then differ by up to an order of magnitude and yield very different redshift evolution depending on the method adopted (see next paragraphs).

Major close pairs, usually defined to be those involving galaxies with a mass ratio greater than 1:4, are now well studied up to $z \sim 1$. The early measurements using photometric redshifts (Patton et al. 1997; Le Fèvre et al. 2000) have been superseded by spectroscopic surveys, confirming physical pairs from the redshift measurement of both components (e.g. Lin et al. 2008; de Ravel et al. 2009; Lopez-Sanjuan et al. 2012, 2013; Tasca et al. 2014), even if some recent photometric surveys, such as ALHAMBRA or SHARDS, allow the computation of accurate close pair fractions (Ferreras et al. 2014; Lopez-Sanjuan et al. 2015).

In the nearby universe, the major merger fraction is only about 2% (e.g. Patton & Atfield 2008; Casteels et al. 2014). But this fraction increases significantly up to $z \sim 1$ indicating that major mergers could be responsible for 20% of the growth of stellar mass density of galaxies from $z \sim 1$ (e.g. Bundy et al. 2009; de Ravel et al. 2009; Lopez-Sanjuan et al. 2012). The evolution of the major merger fraction as a function of redshift is commonly parameterized as a power law of the form $(1 + z)^m$. Even if the pair fraction is thought to be an increasing function of redshift, the range of reported values is almost unconstrained with $m = 0-5$ (e.g. Le Fevre et al. 2000; Lin et al. 2004, 2008; Kampczyk et al. 2007; Kartaltepe et al. 2007; de Ravel et al. 2009; Lotz et al. 2011; Keenan et al. 2014). However, these discrepancies could be decreased when introducing an observability timescale for identifying galaxy mergers (Lotz et al. 2011).

Beyond $z \sim 1$, direct measurements of the major merger fraction are still limited. Previous attempts to measure the major merger rate at $z > 1$ have focussed on the identification of merger remnants from morphological studies (e.g. Conselice et al. 2008, 2011; Bluck et al. 2012) or photometric close pairs (e.g. Ryan et al. 2008; Bluck et al. 2009; Man et al. 2012, 2016). These studies find an increase of the merger rate up to $z \sim 2-3$ but with a large scatter between different measurements. Estimates of major merger rates from spectroscopic close pairs, which is a much more robust way to confirm the physical closeness of the two galaxies, are still sparse with a handful of merger systems identified in Lyman-break galaxy samples (Cooke et al. 2010), MASSIV (Lopez-Sanjuan et al. 2013) and VVDS/VUDS surveys (Tasca et al. 2014). These studies converge towards a fraction around 20% at these redshifts. Because of the difficulty of detecting close spectroscopic pairs of galaxies, no measurements beyond $z \sim 3$ have been reported so far.

The fact that the fraction of major mergers remains constant or turns over beyond $z \sim 1$ is in agreement with the prediction of recent cosmological simulations, such as Horizon-AGN (Kaviraj et al. 2015), EAGLE (Qu et al. 2017) and Illustris (Snyder et al. 2017). It remains also an intriguing question, down to which galaxy masses mergers will play an important role. There are indications in the nearby universe that low-mass dwarf galaxies experienced strong gravitational interactions and/or merging events in the past (e.g. Harris & Zaritsky 2009; Besla et al. 2012; Koch et al. 2015). But estimates on the major merger rate in the distant universe have been restricted so far to massive galaxies alone ($\geqslant 10^{10}\ M_{\odot}$).

This paper aims to provide new constraints on the evolution of the galaxy major merger fraction over the last 12 billion years, i.e. extending up to redshift $z \sim 6$, and over a large range of galaxy masses. This analysis is based on deep MUSE observations in two fields: one in the *Hubble* Deep Field South (HDF-S) and one in the *Hubble* Ultra Deep Field (HUDF). Thanks to its wide field of view and unprecedented sensitivity, MUSE enables us to perform deep spectroscopic surveys without any pre-selection of galaxies, which was the main drawback of previous spectroscopic surveys. This new and powerful instrument is thus perfectly suited to identify close pairs of galaxies at very high redshift ($z > 3$) with spectroscopic redshifts, and to probe a much larger range of stellar masses than before. As we are exploring new territories with MUSE, the conversion of the merger fractions into merger rates is postponed to a second paper. Indeed, the merger (or pair observability) timescale, usually derived from the prescription of Kitzbichler & White (2008), is a model-dependent parameter. which is so far unconstrained for very high-redshift and/or low-mass galaxies (see e.g. Snyder et al. 2017).

This paper is organized as follows. In Sect. 2, we introduce the MUSE data sets used to detect galaxy close pairs. We describe the method to identify close pairs in the spectroscopic redshift catalogues, how we can recover the systemic redshift of Lyα emitters, and the main limitations of the method in Sect. 3. We make the distinction between minor and major close pairs according to the stellar mass ratio between the two galaxies in Sect. 4. We give an estimate of the major merger fraction evolution up to $z \sim 6$ and compare our results with recent numerical simulations in Sect. 5. A summary and conclusion are given in Sect. 6.

Throughout our analysis, we use a standard ΛCDM cosmology with $H_0 = 100\ h\ \mathrm{km\,s^{-1}\,Mpc^{-1}}$, $h = 0.7$, $\Omega_\mathrm{m} = 0.3$, $\Omega_\Lambda = 0.7$.

2. MUSE data set

This analysis is based on MUSE observations in the *Hubble* Deep Field South (HDF-S; Williams et al. 2000) and the *Hubble* Ultra Deep Field (HUDF; Beckwith et al. 2006). MUSE field of view covers a 1×1 arcmin^2 area over a wavelength range of 4750−9300 Å.

2.1. Hubble Deep Field South

The HDF-S was observed during a MUSE commissioning run in August 2014, resulting in a single field of 27 h of total exposure time centred around α = 22h32′55.64″ and δ = −60°33′47″. The data cube contains spectra with a spectral resolution of ∼2.3 Å and a spatial resolution ranging between 0.6″ for the red end of the spectral range and 0.7″ in the blue. The spectroscopic redshift of 189 sources were accurately measured up to a magnitude of $I_{814} = 29.5$. Details on the data reduction, source identification, redshift determination, and source catalogue can be found in Bacon et al. (2015).

2.2. Ultra Deep Field-Mosaic

The HUDF region was observed with MUSE during Guaranteed Time Observations from September 2014 to February 2016, resulting in one medium-deep mosaic of nine MUSE pointings covering the entire HUDF and one single MUSE deep (∼31 h) pointing, udf-10 (see below). The UDF-Mosaic consists of nine MUSE fields of 1×1 arcmin^2, which resulted in a field of 3.15×3.15 arcmin^2 with an average of 10 h exposure time. The achieved spatial resolution is 0.71″ (at 4750 Å) and 0.57″

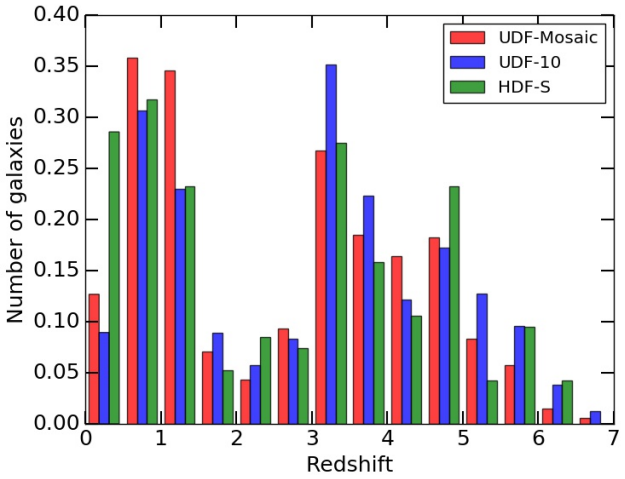

Fig. 1. Spectroscopic redshift distribution of galaxies in the three MUSE data cubes used in this analysis.

(at 9350 Å), and the spectral resolution ranges from 3.0 Å at the blue end to 2.4 Å at 7500 Å (see Bacon et al. 2017 for more details). Overall the spectroscopic redshifts of 1439 sources were measured (Inami et al. 2017).

2.3. Ultra Deep Field-10

With 31 h of exposure time, which consist of 21 h of udf-10 pointing and 10 h of Mosaic pointing, udf-10 is the deepest field observed with MUSE up to now (Bacon et al. 2017). This 1.15 arcmin^2 field is located in the XDF area, centred around $\alpha = 03h32'38.7''$ and $\delta = -27°46'44''$ and overlapping with the UDF-Mosaic. The spectral and spatial resolution are similar to those for the UDF-Mosaic. In this region, 313 spectroscopic redshifts were measured (Inami et al. 2017). To avoid confusion, from now on, the UDF-Mosaic that we used for this analysis corresponds to the whole Mosaic field without its udf-10 region. For this overlapping region we used the 31 h udf-10 data.

3. Detection of galaxy close pairs

3.1. Parent galaxy sample

The parent sample used for this analysis includes all galaxies with measured spectroscopic redshift from the catalogues associated with each of the three fields: HDF-S, udf-10 and UDF-Mosaic (for more details see Inami et al. 2017 and Bacon et al. 2015). As explained in Sect. 2.3, we removed all sources present in the udf-10 region from the UDF-Mosaic catalogue.

The combined fields result in a parent sample of 1801 galaxies with spectroscopic redshift assigned with a confidence level from 3 to 1. A confidence flag of 3 or 2 means that the redshift is secure, with a measurement based on multiple features or a clearly identified single feature ([O II] $\lambda\lambda$3726, 3729 or C III] $\lambda\lambda$1907, 1909 doublet, asymmetric Lyα line). For the lowest confidence level of 1, the redshift was determined by a single feature but with uncertainties on the nature of this feature (no clear doublet or asymmetry). The global estimate of the redshift uncertainty corresponds to $\sigma_z = 0.00012(1 + z)$ (Inami et al. 2017). Figure 1 shows that our parent sample extends over a broad range of spectroscopic redshifts, extending up to $z \approx 7$. Compared to HDF-S and udf-10 redshift distributions, the histogram in UDF-Mosaic peaks at $z \approx 1$ because of an over-dense structure detected around this redshift. Between $1.5 \leqslant z \leqslant 2.8$, the interval described as the redshift desert for optical surveys, there is a dearth of spectroscopic measurements because the instruments we used are sensitive to strong emission-line galaxies up to $z = 1.5$ with [O II] $\lambda\lambda$3726, 3729 and above $z \geqslant 2.8$ with Lyα, but MUSE spectral range is missing such bright emission lines in between. Thereby the sources detected in this range tend to be continuum-bright galaxies corresponding to a more massive galaxy population (see Sect. 5.1). Their redshifts are based on absorption features or CIII] emission.

3.2. Selection criteria for close pair

We identified a close pair as a system of two galaxies within a limited projected separation distance in the sky plane, $r_p^{min} \leqslant r_p \leqslant r_p^{max}$, and a rest-frame relative velocity, $\Delta v \leqslant \Delta v_{max}$. These parameters are computed as follows:

$$r_p = \theta \times d_A(z_m) \quad (1)$$

where θ is the angular distance (in arcsec) between the two galaxies, $d_A(z_m)$ is the angular scale (in kpc arcsec^{-1}), and z_m is the mean redshift of the two galaxies. The rest-frame velocity is written as

$$\Delta v = \frac{c \times |z_1 - z_2|}{(1 + z_m)}, \quad (2)$$

where z_1 and z_2 are the redshifts of each galaxy in the pair.

Previous observational and theoretical studies revealed 25 h^{-1} kpc to be the approximate scale on which the majority of the pairs start to exhibit interacting features such as tidal tails, bridges, distortions, or enhancement of the star formation rate in the galaxies (Patton et al. 2000; Alonso et al. 2004; Nikolic et al. 2004). We thus selected a limit of $r_p^{max} = 25$ h^{-1} kpc to select close pairs with a high probability of merging. For the maximum rest-frame velocity difference of a galaxy pair, $\Delta v_{max} = 500$ km s^{-1} offers a good compromise between contamination and statistics. A smaller velocity separation would reduce the sample size, which limits the robustness of the pair statistics. These effects have also been discussed in Patton et al. (2000).

3.3. Selection method

From the spectroscopic parent sample of 1801 galaxies (see Sect. 3.1), we searched for close kinematic galaxy pairs following the projected separation distance and the rest-frame relative velocity criteria defined above. In order to assess the reliability of these pairs, we then extracted a sub-cube of approximately 60 h^{-1} kpc around the position of the galaxy and created narrow-band images for each emission lines identified in the spectrum of the primary galaxy, which corresponds to the most massive galaxy in the pair. This procedure was found to be very helpful in constructing the final version of the spectroscopic catalogues (Bacon et al. 2015; Inami et al. 2017) by identifying and rejecting some spurious pairs (see Sect. 3.3.2). Finally, all the close pairs selected from the redshift catalogues and used in this analysis were checked and validated.

3.3.1. Recovering the systemic redshift of Lyα emitters

For redshifts below $z \approx 2.8$, emission lines such as [O II] $\lambda\lambda$3726, 3729 and C III] $\lambda\lambda$1907, 1909 accurately trace the systemic redshift of the observed galaxy. However most spectroscopic redshifts for galaxies above $z \approx 2.8$ are derived from the peak

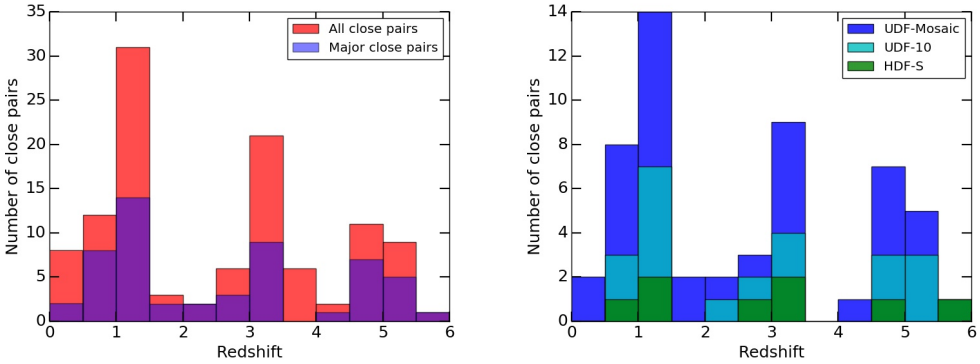

Fig. 2. *Left*: redshift distribution of all the galaxy close pairs (red) and the contribution of major close pairs (purple). *Right*: redshift histogram of the major close pairs showing the contribution of the different MUSE fields: UDF-Mosaic (dark blue), udf-10 (light blue), and HDF-S (green).

of Lyα emission line, which introduces uncertainties in redshift estimates since Lyα is usually red-shifted by several hundreds of km s^{-1} from systemic redshift (e.g. McLinden et al. 2011; Hashimoto et al. 2013; Erb et al. 2014; Shibuya et al. 2014). This could have a major impact on our pair selection at high redshift as this velocity shift is of the same order as the velocity criteria used to define a close pair. We must then find a way to correct the spectroscopic redshift of our Lyα emitters before performing the selection of close pairs above $z \approx 2.8$.

Idealized models of radiative transfer (e.g. Verhamme et al. 2015) have predicted that the full width at half maximum (FWHM) of Lyα is correlated with the column density of the scattering medium, as is the velocity shift of the emission peak relative to the systemic velocity. This trend has been investigated recently to build an empirical relation between these two parameters (Verhamme et al. 2017). This study includes a sample of Lyα emitters from the UDF-Mosaic and udf-10 in their data sets to investigate this relation. The observed Lyα FWHM is thus used as a proxy to correct our Lyα-based redshifts for this velocity offset.

We applied this correction to our parent sample using Eq. (2) of Verhamme et al. (2017), and then performed our selection of close pairs with the corrected spectroscopic redshifts. Although this correction impacts the "true" velocity difference between the galaxies in the pairs, it has a small impact on the final number of close pairs, with a variation of only three pairs, corresponding to ≈3% of the total number of pairs.

3.3.2. Some limitations of the method

Because of the limited spatial resolution of MUSE data, it is nearly impossible to distinguish two galaxies within an angular separation of $\theta \leqslant 0.7''$, which corresponds to an inner projected separation radius of $r_{\rm p}^{\rm min} \sim 3$–$5$ h^{-1} kpc depending on the redshift. For most of these cases, galaxies are undergoing a merging process. These missing pairs are taken into account later (see Sect. 5) in the expression of the merger fraction.

In some cases, primary galaxies have a strong extended emission line that contaminates the spectrum of close companions, and as such, were detected as a close pair. Only a careful check in the data cube, for example by producing narrowband images around the line of interest, allowed us to separate these candidates from real spectroscopic pairs. This careful cleaning was applied iteratively on the incremented versions of the catalogue to reach a maximum of purity.

Since most of the spectroscopic redshifts are based on emission lines, we introduced a bias towards star-forming or active galaxies in the sample; thus, we are missing a significant percentage of continuum-faint quiescent galaxies.

Finally, for close pairs with at least one galaxy with a low-confidence redshift (see Sect. 3.1), leading to "unsecure" pairs, we applied a lower weight than for secure pairs in the expression of the merger fraction (see Sect. 5).

3.4. Results

Based on the method described above, we identified a total of 113 close pairs: 65 in the UDF-Mosaic, 31 in the udf-10, and 17 in the HDF-S, distributed over a broad range of redshifts, from $z \sim 0.2$ to 6 (see Fig. 2, left panel).

We detected, for the first time, more than 10 spectroscopic (and thus secure) close pairs of galaxies at high redshift ($z > 4$). The peak around $z = 1$ for the UDF-Mosaic is partially due to the presence of an over-dense structure at this redshift in the HUDF (Popesso et al. 2009; Table 2). The gap around $z = 2$ is due to the well-known redshift desert of spectroscopic surveys in the optical (see also Inami et al. 2017). Examples of close pairs of galaxies in each redshift bins chosen for the fraction computation (see Sect. 5.1) are shown in Figs. 3–5.

4. Stellar mass estimates and close pair classification

The stellar mass ratio between galaxies in a close pair is a good proxy to distinguish between major and minor mergers, and hence to determine the associated fractions and rates. We thus used this proxy to isolate close pairs of galaxies with similar stellar masses and then focused the subsequent analysis on this sample. We chose a mass ratio limit of 1:6 (defined as the ratio between the secondary and the primary galaxies) to really differentiate between the major and minor close pairs. This choice is justified by the fact that, with MUSE deep observations, we are probing a much broader range of galaxy masses than previous studies, allowing us to detect galaxy pairs with a mass ratio much lower than 1:4 at any redshift (see Fig. 6), which is the limit usually adopted in previous studies (see e.g. Lopez-Sanjuan et al. 2013; Tasca et al. 2014).

We estimated the stellar masses of all the galaxies in the parent sample using the stellar population synthesis code FAST (Fitting and Assessment of Synthetic Templates; Kriek et al. 2009); which fits model templates to the spectral energy distribution

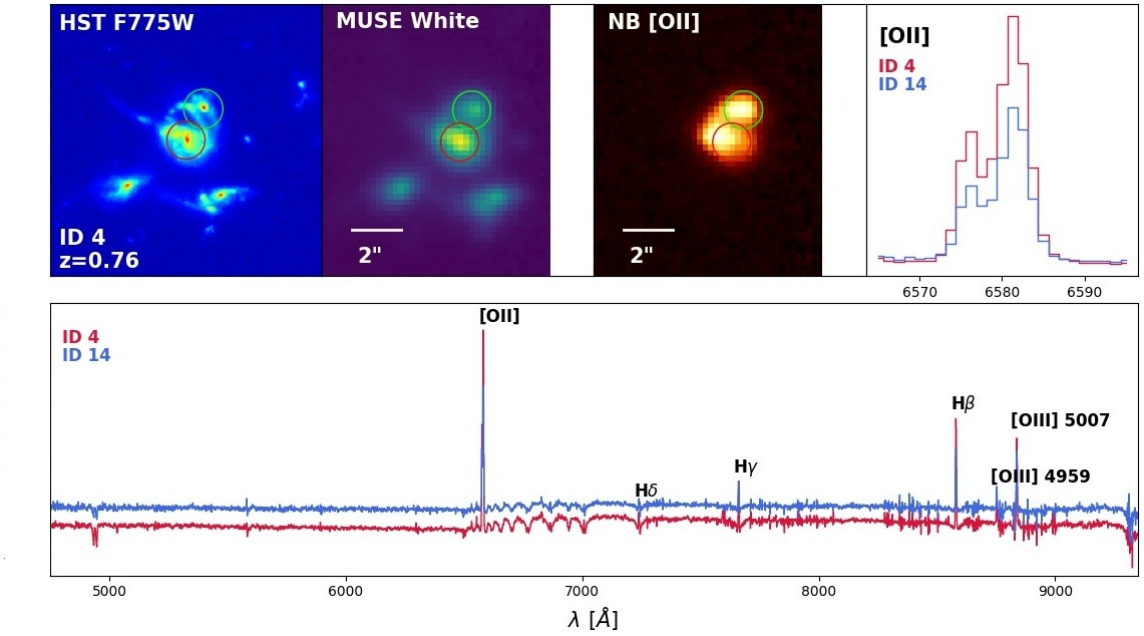

(a)

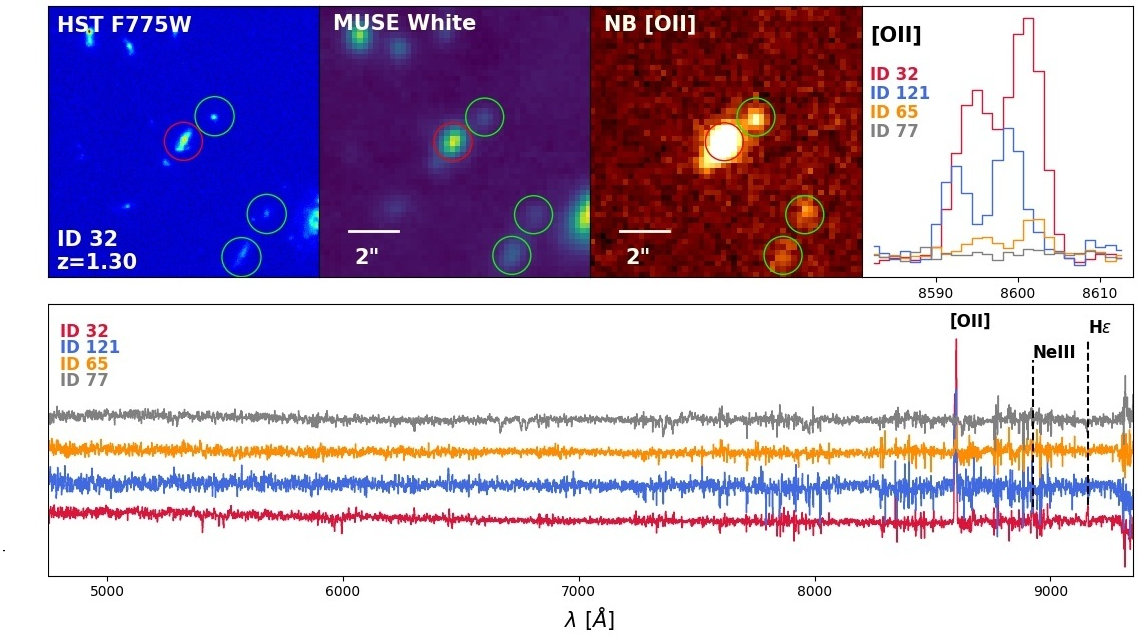

(b)

Fig. 3. Examples of galaxy close pairs. *Top line, from left to right*: HST image in the *F*775*W* filter with the labelled MUSE ID and redshift of the primary galaxy, MUSE reconstructed white light image, narrowband image of one of the brightest emission lines of the pair, and the zoomed spectra around this line. Images are 10″ in linear size and centred around the primary galaxy, i.e. the most massive one, circled in red. The green circle(s) denote its companion(s). *Bottom line*: spectrum (red for the primary and blue or other colours for its companion) over the whole wavelength range observed with MUSE, differentiated by an arbitrary offset. Fluxes are in arbitrary units. The main emission(absorption) lines are labelled in black(grey). *Panel a*: A low redshift close pair of galaxies in udf-10 at $z = 0.76$ with $r_p \sim 6$ kpc and $\Delta v \sim 7$ km s^{-1}. This pair has a strong [O II] $\lambda\lambda$3726, 3729 emission line slightly of-centred, and shows signs of interactions such as tidal tails. *Panel b*: A quadruplet of galaxies in udf-10 at $z = 1.30$ within a projected separation distance of $r_p \sim 41$ kpc between the primary galaxy, MUSE ID 32, in the centre, and the most distant satellite galaxy at the bottom right of the image and within a maximum rest-frame velocity of $\Delta v \sim 220$ km s^{-1}. The MUSE ID of the companion galaxies are, *from top to bottom*, 121, 77, and 65. Objects 32, 121, and 65 all have a secure spectroscopic redshift with a confidence flag in the measurement of 3, whereas object 77 has a confidence level of 1, which is taken into account in the computation of the fraction (see Sect. 5.2). The 1D spectrum of this galaxy shows a much fainter [O II] $\lambda\lambda$3726, 3729 emission than the other galaxies, but the galaxy is clearly identified in the narrowband image. The strong absorption lines in its spectrum belong to another source, ID 18. In such a case of multiple close pairs, where some of the paired galaxies have another partner, the number of close pairs corresponds to the number of satellite galaxies, i.e. we account for 3 close pairs in this system.

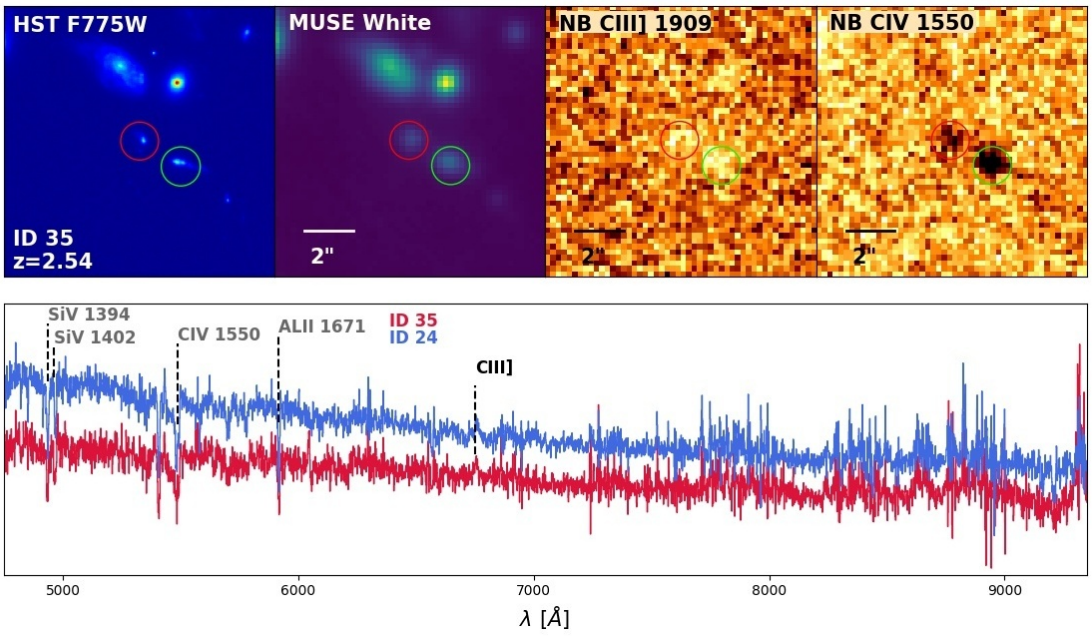

(a)

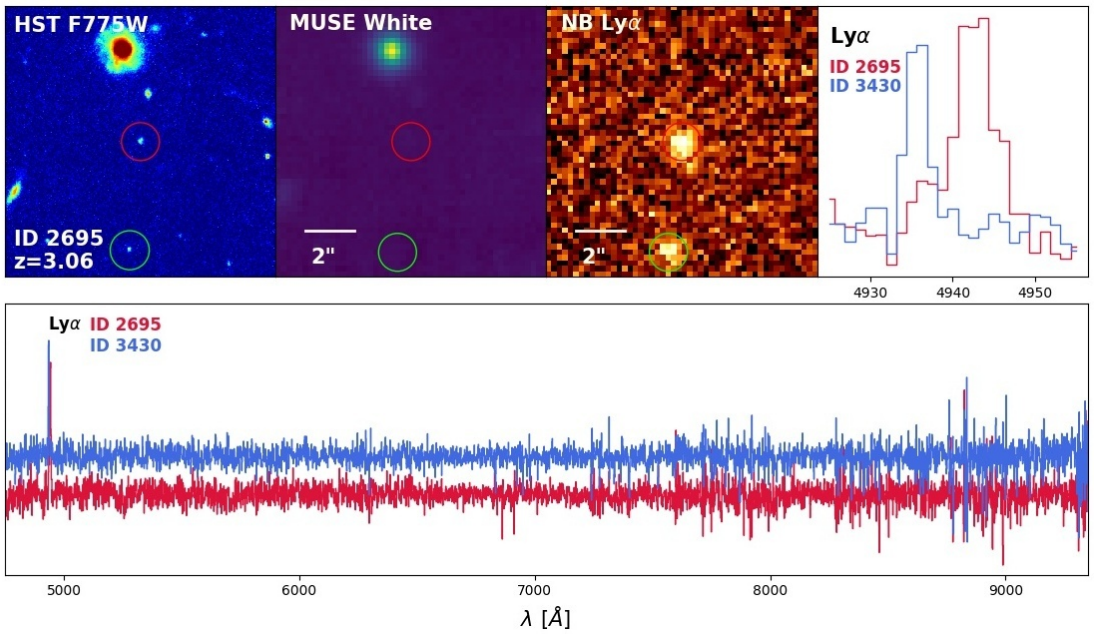

(b)

Fig. 4. Same as Fig. 3. *Panel a*: A close pair in udf-10 at a redshift of $z = 2.54$ with $r_p \sim 15$ kpc and $\Delta v \sim 6$ km s^{-1}. This is a good example of the galaxy pair population detected in the redshift desert bin. The two continuum-bright galaxies reveal a faint C III] $\lambda\lambda$1907, 1909 emission line, as is shown in the first narrowband image, but are clearly identified thanks to their strong absorption lines. *Panel b*: A close pair of Lyα emitters (LAE) in the UDF-Mosaic at $z = 3.06$, one of the three close pairs with a rest-frame relative velocity higher than 300 km s^{-1} with $\Delta v \sim 317$ km s^{-1} and $r_p \sim 31$ kpc.

(SED) of galaxies based on the HST photometry, as described in Contini et al. (2016) for the HDF-S galaxies. For UDF-Mosaic and udf-10, we used the extended UV-to-NIR ACS and WFC3 photometry of Rafelski et al. (2015). We chose Bruzual & Charlot (2003) for the stellar library, Calzetti et al. (2000) for the dust attenuation law, and a Chabrier (2003) initial mass function.

Stellar masses of galaxies below $z \approx 3$ are well constrained with the UV-to-NIR photometry. However, stellar masses of higher redshift galaxies, derived with observed-frame UV-to-NIR photometry only, are known to be more uncertain. In order to increase the robustness of stellar mass estimates for high-redshift galaxies ($z \geqslant 3$) we used additional mid-infrared IRAC photometry from the GOODS Re-ionization Era wide-Area Treasury from *Spitzer* programme (GREATS; PI: Ivo Labbe), which provides the deepest data available over the MUSE-HUDF region. Photometry is measured using the software mophongo (Labbe et al. 2015), which subtracts any neighbouring objects by a segmented, PSF-matched, HST image. This process is critical for accurate photometry because of the broader *Spitzer* IRAC PSF (see details in Lam et al, in prep.). We further checked

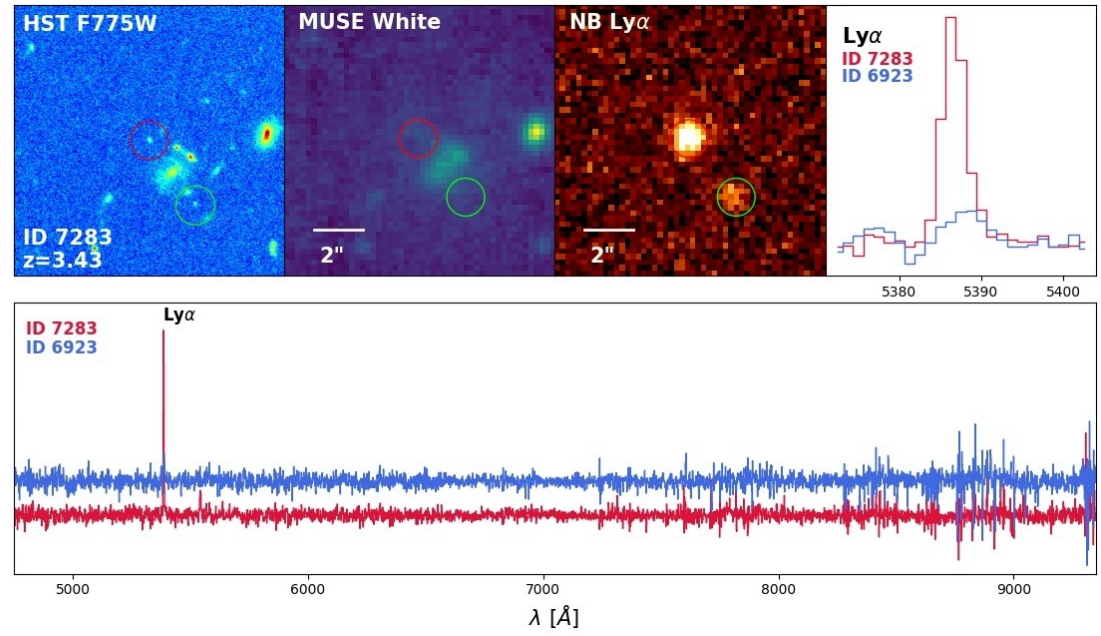

(a)

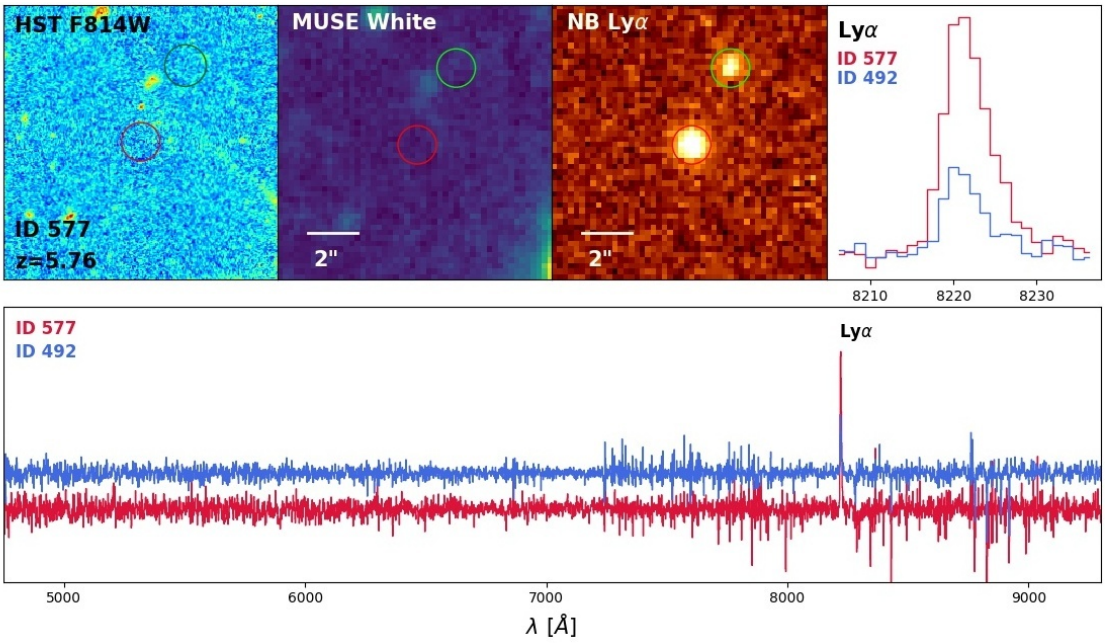

(b)

Fig. 5. Same as Fig. 3. *Panel a*: A close pair at $z = 3.43$ in the UDF-Mosaic with the primary galaxy showing a strong Lyα emission, compared to its companion, which has a much fainter Lyα emission. The two galaxies are separated with a projected distance of $r_p \sim 22$ kpc and a difference in velocity of $\Delta v \sim 49$ km s^{-1}. *Panel b*: At $z = 5.76$, this close pair of LAE is the highest redshift pair of our sample, located in the HDF-S with $r_p \sim 19$ kpc and $\Delta v \sim 16$ km s^{-1}.

that the SED–derived mass ratios are consistent with the difference in near-infrared HST magnitudes of the two galaxies, as magnitudes in these bands can be considered as a rough proxy for stellar mass.

With this sample of close pairs, as for the parent sample of galaxies, we probed a large domain of galaxy stellar masses in the range $\sim 10^7 - 10^{11}$ $M_\odot$ (see Fig. 7), in which there is a high percentage of low-mass galaxies ($<10^{9.5}$ $M_\odot$), especially at very high redshift ($z > 3$). From our sample of 113 close pairs (see Fig. 6), we identified a total of 54 major close pairs with a stellar mass ratio higher than 1:6. If we apply a mass ratio limit of 1:4, as in previous studies, we only lose eight pairs. But if we push this limit up to 1:10 we gain twenty-two pairs, as we are clearly entering into the minor merger regime. We checked that the relative number of identified close pairs scales roughly with the mass ratio, as expected from theory. To do so, we compared our measurements for two mass ratios regimes (major: $\leqslant 1/4$ and major+minor: $\leqslant 1/10$) to the most recent predictions from numerical simulations: Illustris (Rodriguez-Gomez et al. 2015) and EAGLE (Qu et al. 2017). The results are very consistent

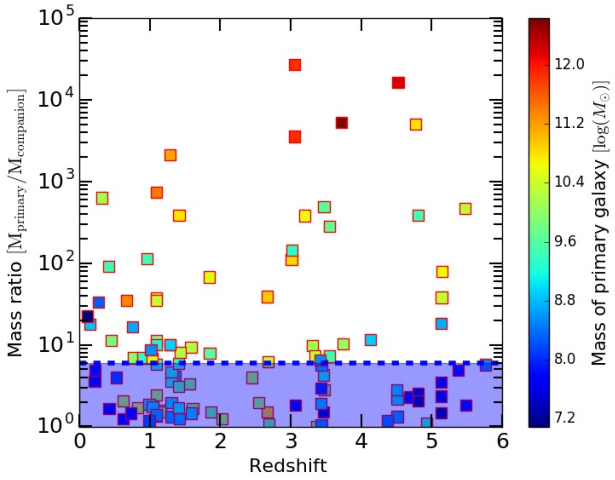

Fig. 6. Stellar mass ratio of 113 close pairs identified in the MUSE deep fields as a function of redshift, colour coded with respect to the stellar mass of the primary galaxy. The blue dashed line indicates a mass ratio (primary over companion galaxy) limit of 6 chosen to distinguish major close pairs (blue coloured area) from minor close pairs.

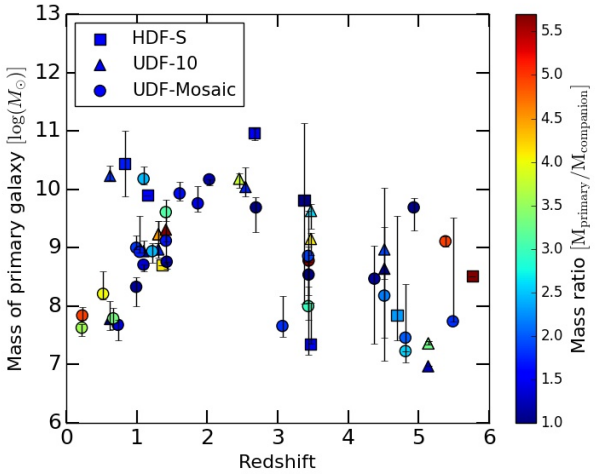

Fig. 7. Stellar mass of the primary galaxy as a function of redshift for our major close pairs sample, colour coded with respect to the galaxy mass ratio in the pair. The primary galaxy is the more massive galaxy of the pair. The circles are pairs in the UDF-Mosaic, triangles in udf-10, and squares in HDF-S. Except in the redshift "desert" ($z \sim 1.5$–2.8), the mass range probed with MUSE observations does not change significantly with redshift, with a fairly good completeness level between $\approx 10^7$–$10^{10}\ M_\odot$.

taking into account measurement uncertainties such as cosmic variance. We measured an increase of the fraction of close pairs by a factor 1.65 between the major (mass ratio $\leqslant 1/4$) and the major+minor ($\leqslant 1/10$) regime, which is in very good agreement with Illustris (factor of 1.5 to 2, see their Fig. 7, top/middle panel) and EAGLE (factor of 1.5 to 1.8) predictions. The fact that the measured value from MUSE data is close to the lower limit predicted by the simulations may reflects an edge effect due to the sharp cut-off in the mass ratio threshold. But this effect is marginal and does significantly not affect the measured pair fractions.

The basic properties (such as redshift, stellar mass, projected separation, and velocity difference) for the sample of major galaxy close pairs identified in the three MUSE deep fields are given in Table A.1.

5. Redshift evolution of the galaxy major merger fraction

5.1. Redshift bins

In order to estimate the evolution of the merger fraction and rate, we divided our redshift domain into five bins containing enough close pairs for statistical significance.

The first redshift bin $0.2 \leqslant z_r < 1$, corresponding to our lowest redshift range, contains 10 pairs of galaxies. The second bin, $1 \leqslant z_r < 1.5$, extends up to the loss of the [O II] $\lambda\lambda$3726, 3729 emission-line doublet in the MUSE spectral range and contains 14 pairs. The third redshift bin $1.5 \leqslant z_r < 2.8$ is associated with the well-known redshift desert, where we do not have bright emission line falling in the MUSE spectral range, except a few C III] $\lambda\lambda$1907, 1909 emitters (Maseda et al. 2017). This bin includes 9 pairs. Above $z = 2.8$, the vast majority of the galaxies are identified through their Lyα emission. We divided this very high-redshift domain into two bins according to the distribution of close pairs, $2.8 \leqslant z_r < 4$ and $4 \leqslant z_r \leqslant 6$. These two last bins contain 10 and 13 pairs, respectively.

5.2. Major merger fraction up to $z \approx 6$

The merger fraction from a spectroscopic pair count is simply the number of pairs divided by the number of primary individual galaxies in the sample. However, as our observations are limited in volume and luminosity, we must correct the merger fraction from these selection effects and incompleteness (e.g. de Ravel et al. 2009).

Similarly to the relation used, for example, in Lopez-Sanjuan et al. (2013), the major merger fraction for a chosen redshift bin z_r is defined as

$$f_{\rm MM}(z_r) = \frac{N_{\rm p}^{\rm corr}}{N_{\rm g}^{\rm corr}} = C_1 \frac{\sum_{K=1}^{N_{\rm p}} \frac{\omega_z^{K_1}}{C_2(z_r)} \frac{\omega_z^{K_2}}{C_2(z_r)} \omega_{\rm A}^K}{\sum_{i=1}^{N_{\rm g}} \frac{\omega_z^i}{C_2(z_r)}}, \quad (3)$$

where $N_{\rm g}$ is the number of primary galaxies in the parent sample; $N_{\rm p}$ is the number of major close pairs; C_1 accounts for the missing companions due to our limit in spatial resolution (see Sect. 3.3.2); ω_z is the redshift confidence weight, which takes into account the confidence in the z measurement (e.g. Inami et al. 2017); $\omega_{\rm A}$ is the area weight, which takes into account that some galaxies are located on the border of the MUSE field of view; and finally $C_2(z_r)$ is a correction term for the redshift incompleteness.

All these terms are defined as

- $C_1 = \frac{(r_{\rm p}^{\rm max})^2}{(r_{\rm p}^{\rm max})^2 - (r_{\rm p}^{\rm min})^2}$
- ω_z, the redshift confidence weight,

$$\omega_z = \begin{cases} 1 & \text{if } z_{\rm conf} = 3 \text{ or } 2 \\ 0.6 & \text{if } z_{\rm conf} = 1. \end{cases}$$

  A maximum value of 1 is chosen for the weight of secure redshifts (with confidence of 3 or 2). To reduce the influence of unsecure pairs, i.e. with one of the galaxy flagged with a redshift confidence of 1, a weight of 0.6 is applied (i.e. we are 60% sure of the redshift estimate). Varying this value in the range 0.5–0.7 has almost no impact on the final fractions.
- $\omega_{\rm A}$, the area weight

$$\omega_{\rm A} = \frac{A_{\rm rp}}{A_{\rm MUSE}},$$

Table 1. Major merger fractions up to $z \approx 6$ from the HDF-S, udf-10 and UDF-Mosaic combined analysis.

z_r	$\overline{z_r}$	$C_1(z_r)$	$C_2(z_r)$	σ_v	$\overline{M_g^\star}$	$\overline{M_p^\star}$	N_g	N_p	f_{MM}
–	–	–	–	–	[log($M_\odot$)]	[log($M_\odot$)]	–	–	–
(1)	(2)	(3)	(4)	(5)	(6)	(7)	(8)	(9)	(10)
$0.2 \leqslant z < 1$	0.68	0.48	0.45	0.15	8.21	8.03	404	10	$0.054^{+0.042}_{-0.021}$
$1 \leqslant z < 1.5$	1.25	0.45	0.44	0.18	8.96	9.17	297	14	$0.107^{+0.076}_{-0.044}$
$1.5 \leqslant z < 2.8$	2.35	0.43	0.30	0.15	9.58	9.93	152	9	$0.188^{+0.110}_{-0.051}$
$2.8 \leqslant z < 4$	3.39	0.42	0.20	0.36	8.58	8.82	399	10	$0.087^{+0.054}_{-0.033}$
$4 \leqslant z \leqslant 6$	4.99	0.55	0.35	0.52	8.36	7.91	382	13	$0.072^{+0.068}_{-0.043}$

Notes. Columns (1) and (2): range of the redshift bin and its associated mean redshift for the close pairs sample. Columns (3) and (4): weight corresponding to spectroscopic redshift completeness for the two deep fields, based on the udf-10, $C_1(z_r)$, and the UDF-Mosaic, $C_2(z_r)$. Column (5): total cosmic variance for the combined field study, depending on the redshift bin and the median of stellar masses for the close pairs. Columns (6) and (7): median values of stellar masses for the parent and pairs samples respectively. Columns (8) and (9): number of galaxies, N_g, and pairs, N_p, for the redshift bin. Column (10): major merger fraction.

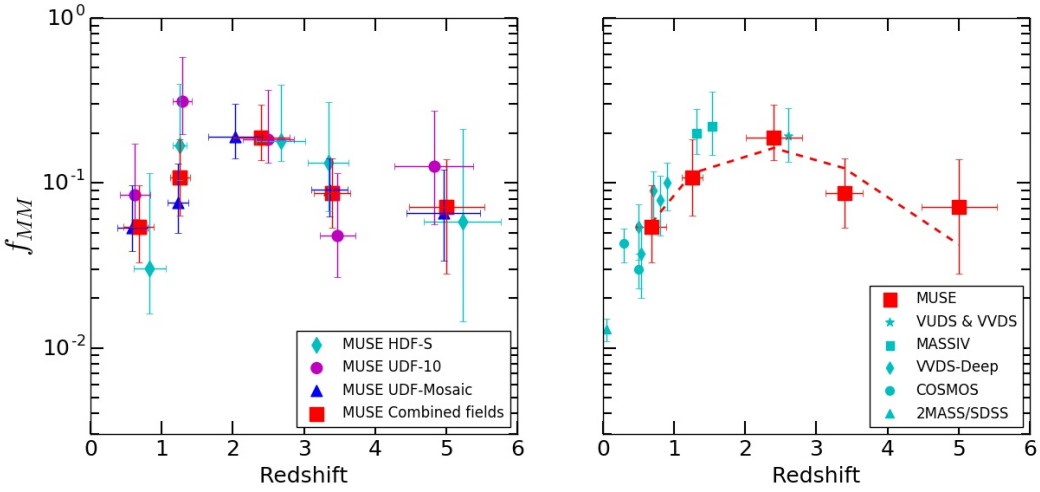

Fig. 8. Evolution of the galaxy major merger fraction up to $z \sim 6$. *Left*: red squares correspond to the fraction for the combined analysis of the three MUSE fields. The other symbols indicate the estimates of the fraction from HDF-S, udf-10 and UDF-Mosaic individually. *Right*: combined major merger fractions from MUSE data (red squares) are compared to previous estimates (light blue symbols; de Ravel et al. 2009; Lopez-Sanjuan et al. 2011, 2013; Xu et al. 2012; Tasca et al. 2014). The dashed line is the least-squares fit of a combined power-law and exponential function, $f_{MM} \sim 0.056(1+z)^{5.910}e^{-1.814(1+z)}$, to the data.

where A_{rp} is the area of a circle of radius r_p^{max} and A_{MUSE} is the corresponding area in the MUSE data cubes. This term has a very low impact on the fraction.

– $C_2(z_r)$ corrects for the spectroscopic redshift incompleteness and is defined, in each field and redshift bin, as the number of spectroscopic redshifts divided by the number of photometric redshifts, estimated in Brinchmann et al. (2017). We assumed that the photometric redshift measurements are uniformly representative of the true redshift distribution. For galaxies at $z \leqslant 1.5$, and $1.5 < z < 2.8$, we applied a magnitude cut of $F775W \leqslant 29$ and 27 mag on the parent sample, corresponding to the magnitude limit for the spectroscopic redshift identification of galaxies in these redshift intervals (see Inami et al. 2017). This concerns galaxies at $z \leqslant 2.8$ only, since the emission-line source detection method using ORIGIN (see details in Bacon et al. 2017) identifies fainter objects for $z \geqslant 2.8$. Moreover, since the photometry in the udf-10 has a much larger multi-wavelength coverage compared with the HDF-S, and these two fields have approximately the same sensitivity with MUSE (factor of 1.6 better for udf-10; Bacon et al. 2017), we used the udf-10 completeness corrections for the HDF-S. Values for these completeness corrections are listed in Table 1. As expected, at high redshift, the completeness is higher in the udf-10 than in the UDF-Mosaic, which is consistent with the difference in depth between these two fields. Up to $z \sim 1.5$, we are almost 50% complete both for the deep fields and the medium-deep UDF-mosaic. The completeness decreases between $z \approx 1.5$ and $z \approx 2.8$, corresponding to the redshift "desert" and stays almost constant over the two last redshift bins at approximately 40–50% and 20–30%, respectively, for the udf-10 and UDF-Mosaic.

The error budget on the merger fraction was obtained by combining a purely statistical error on the estimated fractions and an error due to the cosmic variance. We derived the statistical error as a confidence interval from a Bayesian approach (see e.g. Cameron 2011). The cosmic variance is a term inherent to observational studies and translates the impact of cosmic large-scale structures in measurements. We applied the recipes of Moster et al. (2011) to compute the total cosmic variance (see Table 1) for the two uncorrelated fields: the HDF-S and UDF-Mosaic. This depends strongly on the geometry and volume of each field and on the redshift and mass bins assumed. For $z \leqslant 2$, it does not

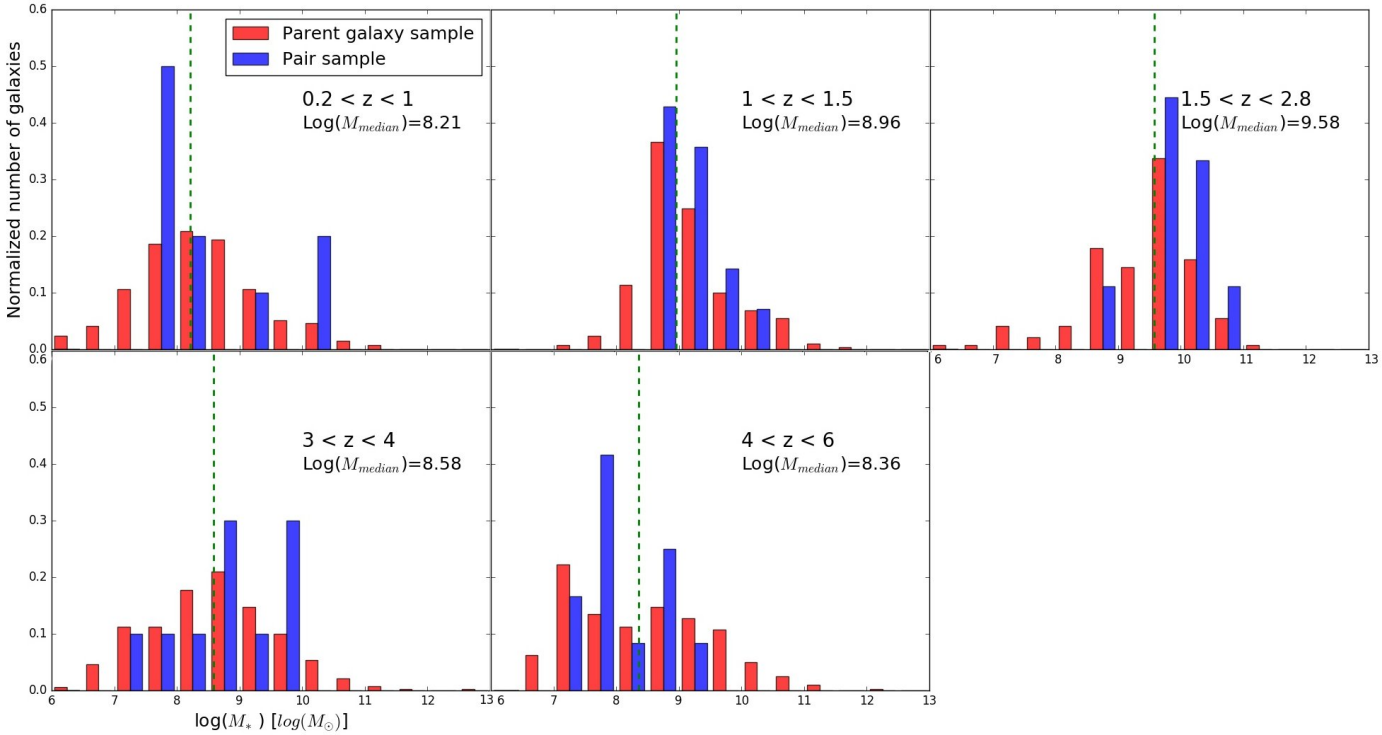

Fig. 9. Stellar mass distribution of the parent (red) and close pair (blue) samples in each redshift bins. The reported median value of the parent sample is represented by the dashed green line. The distributions are normalized to the sum of stellar mass bins.

have a great influence since the uncertainties due to the cosmic variance are below 20%. For this redshift range the error budget is dominated by the low statistics. Whereas for $z \geqslant 3$, the cosmic variance predominates with uncertainties up to ≈50%.

We estimated the fraction of major close pairs for each field individually and for the combined study of the three MUSE fields put together (see Fig. 8, left and right panels, respectively). The comparison of the fractions for the individual fields clearly shows the effect of the cosmic variance. However, taking into account error bars, the measurements in the individual fields are in good agreement over the five redshift bins. As more than half of the pairs are detected in the UDF-Mosaic, this field has a higher weight on the combined fraction than the other two deeper but smaller fields. Table 1 summarizes, for each redshift bins, the completeness correction factors, error due to cosmic variance, median values of stellar masses, and number and fraction of major close pairs.

In Fig. 8 (right panel), we compared our estimates with previous results from the literature, restricting the comparison to other samples of close pairs robustly identified with spectroscopic studies. Similar values for separation limits, i.e. $r_{\rm p}^{\rm max} = 20{-}30$ h^{-1} kpc and $\Delta v_{\rm max} \sim 500$ km s^{-1}, were used in the MASSIV (Lopez-Sanjuan et al. 2013), VVDS/VUDS (Tasca et al. 2014), and VVDS-deep (de Ravel et al. 2009; Lopez-Sanjuan et al. 2011) analyses to select close pairs. A typical mass ratio limit of 1:4 for major-merger pairs is usually adopted, except in de Ravel et al. (2009) who choose a magnitude difference limit of 1.5 mag between pair members. The major close pairs selection in the 2MASS/SDSS and COSMOS samples (Xu et al. 2012) follow approximately the same criteria with $5 \leqslant r_{\rm p} \leqslant 20$ h^{-1} kpc but with a lower mass ratio limit of 1:2.5. We must however keep in mind that the comparison is not so straightforward as the close pairs detected in the MUSE fields involve galaxies spread over a large range of stellar masses ($\sim 10^7{-}10^{11}$ $M_\odot$; see Sect. 4), whereas the close pairs analysed so far in the literature involve massive galaxies only ($\geqslant 10^{10}$ $M_\odot$).

However, the major merger fractions estimated in the MUSE fields are in good agreement with those derived from previous analyses in similar redshifts, with a constant increase of the merger fraction with look-back time up to $z \approx 3$. At higher redshift, the fraction seems to decrease slowly or flatten down.

Since we chose a mass ratio limit of 1:6 to define our major close pair sample, some pairs could be missed at $z \geq 3$ owing to the non-detection of the companion of a primary galaxy with a very low stellar mass, i.e. with $M_* \approx 10^7{-}10^8$ $M_\odot$. Consequently, we might probe a different mass regime at low and high redshifts. However, as shown in Fig. 6, we detect close pairs at $z \geq 3$ with a mass ratio ≤1:4 and a primary galaxy stellar mass around $M_* \approx 10^7{-}10^8$ $M_\odot$, as in the lower redshift range ($z \leq 1.5$). It is also clear from Fig. 6 that for a mass ratio lower than 1:6; i.e. in the minor close pair regime, the primary galaxy stellar mass range for $z \leqslant 3$ galaxies is comparable to that for $z \geqslant 3$. We further checked that the evolutionary trend seen in Fig. 8 does not change if the mass ratio threshold used to define our major close pair sample is set to a value of 1:3 or 1:4. Such a trend has a low impact on the estimate of the fraction, with a decrease of the fraction of ≈3% on average between a mass ratio limit of 1:6 and 1:3, but the evolution remains consistent. The conclusions are the same if we increase the lower limit of the primary galaxy stellar mass to 10^8 $M_\odot$.

5.3. Separation by stellar mass

Figure 9 shows the normalized stellar mass distributions of the parent and close pair samples in each redshift bins. At all redshifts and stellar masses of the parent sample extend over four

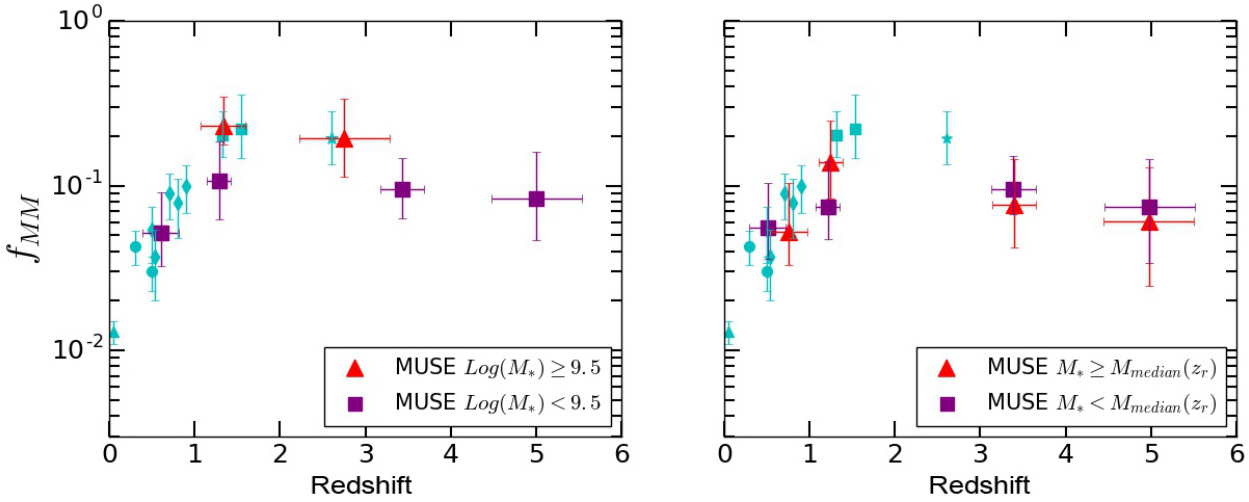

Fig. 10. Evolution of the major merger fraction for two ranges of stellar mass, assuming a constant separation limit of $M^\star = 10^{9.5}$ $M_\odot$ (*left panel*) or adopting the median value of stellar mass in each redshift bin as the separation limit (*right panel*). The purple squares and red triangles show the MUSE estimates for low-mass and massive galaxies, respectively. Previous estimates from the literature are shown with light blue symbols (see Fig. 8 for references).

orders of magnitude from $\sim 10^7$ $M_\odot$ to $\sim 10^{11}$ $M_\odot$. With median values between 10^8 $M_\odot$ to 10^9 $M_\odot$ (see Table 1), it is clear that with MUSE we are probing a lower mass domain than previous spectroscopic surveys, which pre-selected the targets according to their apparent magnitude. The only exception is the bin corresponding to the redshift desert, with a median mass above 10^9 $M_\odot$, in agreement with the fact that most of the galaxies identified in this redshift range have a bright continuum. The stellar mass distributions of galaxies in close pairs broadly follow the distributions of the parent sample. However, we have not found major close pairs made of very low-mass galaxies (i.e. $\leqslant 10^{7.5}$ $M_\odot$) below $z \sim 3$, nor pairs of massive galaxies (i.e. $\geqslant 10^{10}$ $M_\odot$) above this redshift.

An attempt to separate our sample of close pairs in stellar masses is shown in Fig. 10. We use the stellar mass of the primary galaxy to discriminate the pairs and test two different stellar mass limit criteria.

First, a constant stellar mass limit of $10^{9.5}$ $M_\odot$ is chosen to distinguish low mass from massive galaxies over the entire redshift range (Fig. 10, left panel). For this analysis, the redshift bins defined previously (see Sect. 5.1) are modified to keep a significant statistic. We thus remove the bin corresponding to the redshift desert for the low-mass sample, and we define three new redshift bins $0.2 \leqslant z_{r1} < 1$, $1 \leqslant z_{r2} < 2$ and $2 \leqslant z_{r3} \leqslant 4$ for the sample of "massive" galaxies (see Table 2). As we have two pairs only in the first redshift bin, this data point is not shown in Fig. 10 (left panel) but is still reported in Table 1.

The major merger fractions estimated for the high-mass samples are, within uncertainties, fairly consistent with previous works, with an increase of the fraction up to 23% and 19% at $z \approx 1.3$ and 2.7. The major merger fraction evolution of the low-mass sample seems to follow the same trend with a monotonically increases up to $z \sim 1.3$–3, where it reaches a maximum of 11% and then flattens or slightly decreases to 8–9% between $3 \leqslant z \leqslant 6$ (see Table 2).

Since we probe a particularly low-mass regime in stellar masses with MUSE, a second approach is to define the mass limit as the median value of the mass distribution for the parent galaxy sample. This limit varies with redshift, as described in Sect. 5.1. With this separation, the two close pairs samples are more evenly distributed. Figure 10 (right panel) shows a trend similar to the left panel with small differences between the two estimates of the major merger fraction according to these median mass limits. Overall, the major close pair fraction for low-mass and massive galaxies follow the same trend. However, there is a potential reverse trend between the two mass bins in this figure, even if the uncertainties on the fraction do not allow any firm conclusion. Indeed, around $z \approx 1.5$, the merger fraction is higher for massive galaxies than for low-mass galaxies, but at higher redshift ($z \geqslant 3$) this trend is reversed, as seen in some simulations (e.g. Qu et al. 2017).

5.4. Comparison with recent simulations

We can compare our merger fractions to predictions from hydrodynamic simulations that model the dark matter and baryonic components of a cosmological volume consistently. Until recently, there have been very few attempts (e.g. Maller et al. 2006) to determine the evolution of galaxy merger fractions using such simulations because it was not possible to produce large enough samples of realistic galaxies. This situation greatly improved over the last years with simulations such as HORIZON-AGN (Dubois et al. 2014), Illustris (Vogelsberger et al. 2014), and EAGLE (Crain et al. 2015; Schaye et al. 2015).

A straightforward comparison with observations is to measure the close pair fraction directly from the simulations, to be compared to observations without having to make any assumption about the merger timescales (see Sect. 1). Estimates of the major merger fraction evolution with redshift are available from the HORIZON-AGN (Kaviraj et al. 2015), EAGLE (Qu et al. 2017), and Illustris (Snyder et al. 2017) simulations.

Using the EAGLE simulations, Qu et al. (2017) have built merger trees to connect galaxies to their progenitors. From snapshots at different redshifts, they searched for pairs of galaxies following selection criteria similar to those used in observational close-pair analysis, such as the separation distance and mass ratio of the galaxies. Estimates of the major close pairs fraction are given in three stellar mass ranges up to redshift ≈4. This fraction increases monotonically before leveling off at $z = 1.5$–3 and

Table 2. Major merger fraction up to $z \approx 6$ from MUSE observations for different redshift and stellar mass intervals.

z_r	$\overline{z_r}$	$\overline{M_p^\star}$	N_p	N_g	f_{MM}
–	–	[log($M_\odot$)]	–	–	–
(1)	(2)	(3)	(4)	(5)	(6)
			$M^\star < M_{median}(z_r)$		
$0.2 \leqslant z < 1$	0.51	7.68	5	207	$0.055^{+0.048}_{-0.019}$
$1 \leqslant z \leqslant 1.5$	1.21	8.76	5	153	$0.074^{+0.066}_{-0.027}$
$3 \leqslant z < 4$	3.39	7.86	4	211	$0.096^{+0.054}_{-0.029}$
$4 \leqslant z \leqslant 6$	4.98	7.52	7	223	$0.074^{+0.071}_{-0.040}$
			$M^\star \geqslant M_{median}(z_r)$		
$0.2 \leqslant z < 1$	0.76	9.00	4	197	$0.053^{+0.050}_{-0.020}$
$1 \leqslant z \leqslant 1.5$	1.24	9.28	9	146	$0.139^{+0.0107}_{-0.055}$
$3 \leqslant z < 4$	3.39	9.45	6	188	$0.077^{+0.067}_{-0.034}$
$4 \leqslant z \leqslant 6$	4.86	8.83	6	197	$0.060^{+0.068}_{-0.035}$
			$\log(M^\star) < 9.5$		
$0.2 \leqslant z < 1$	0.60	7.81	8	357	$0.052^{+0.040}_{-0.019}$
$1 \leqslant z \leqslant 1.5$	1.28	8.97	11	230	$0.106^{+0.081}_{-0.044}$
$3 \leqslant z < 4$	3.43	8.54	7	329	$0.095^{+0.052}_{-0.031}$
$4 \leqslant z \leqslant 6$	4.99	7.91	13	344	$0.083^{+0.076}_{-0.037}$
			$\log(M^\star) \geqslant 9.5$		
$0.2 \leqslant z < 1$	0.73	10.34	2	47	$0.071^{+0.105}_{-0.018}$
$1 \leqslant z < 2$	1.33	9.88	6	112	$0.232^{+0.112}_{-0.056}$
$2 \leqslant z \leqslant 4$	2.75	9.94	8	118	$0.195^{+0.142}_{-0.081}$

Notes. Columns (1) and (2): range of the redshift bin and its associated mean redshift for the close pairs sample. Columns (3): median value of stellar mass of the pairs sample. Columns (4) and (5): number of pairs, N_p, and galaxies, N_g. Columns (6): major merger fraction.

even declines for the most massive galaxies. This trend is best fitted with a combined power-law and exponential function.

Based on the HORIZON-AGN simulation, Kaviraj et al. (2015) have probed the merger histories of massive galaxies and predicted the fractions of galaxy pairs in the redshift range $1 < z < 4$ and various mass ratios. The trend is roughly similar to predictions by EAGLE in the same redshift range with a flat increase of the merger fraction up to $z \approx 3$ and then a decrease towards higher redshift.

From the Illustris simulation, Snyder et al. (2017) have created three synthetic light cone catalogues and measured pair fractions using a velocity criterion inspired by photometric redshift precision in deep surveys, i.e. $\Delta v_{max} = 18\,000$ km s^{-1} at $z = 2$. The fraction seems to be roughly flat between $z \approx 0.5$–3 and then decreases up to $z \approx 4$. However this trend requires a decreasing observability timescale with redshift, which corresponds to the timescale at which a close pair can be identified in a snapshot catalogue.

Figure 11 compares the predictions from these simulations to our major merger fraction estimates. Even though the simulated samples are biased towards more massive galaxies than studied in this work, the trend of the fraction evolution in these simulations is consistent with our study, especially when pairs of both low- and high-mass galaxies, which have stellar mass ratios down to ~1:10, are taken into account in the simulations.

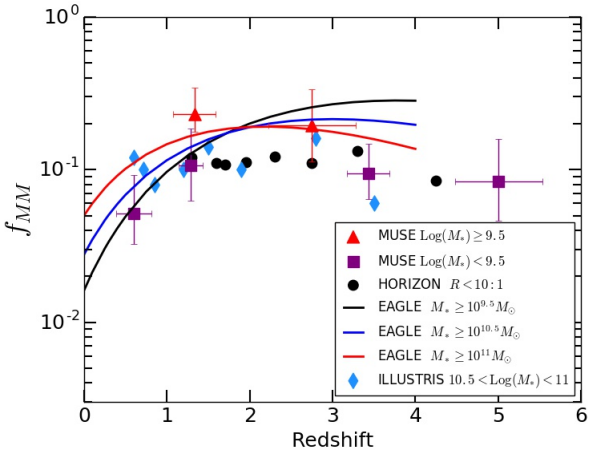

Fig. 11. Major merger fraction compared to recent numerical simulations. Symbols with error bars are estimates from our MUSE sample divided into low-mass ($\leqslant 10^{9.5}$ $M_\odot$; purple squares) and massive ($>10^{9.5}$ $M_\odot$; red triangles) galaxies. The black points indicate the predictions from the HORIZON-AGN simulation (Kaviraj et al. 2015) and correspond to the pair fraction for massive galaxies ($\geqslant 10^{10}$ $M_\odot$) with a mass ratio between the primary and companion galaxy that is lower than 10:1. The solid lines indicate estimates from the EAGLE simulations for three galaxy stellar mass ranges. For these predictions a combined power-law and exponential fitting function, $f_{MM} \sim a(1+z)^b e^{-c(1+z)}$, was used (see Qu et al. 2017 for details). Finally, the blue diamonds correspond to the major pair fraction for massive galaxies in the ILLUSTRIS simulation (Snyder et al. 2017).

6. Summary and conclusions

We used deep MUSE observations in the HUDF and HDF-S to identify 113 secure close pairs of galaxies among a parent sample of 1801 galaxies spread over a large redshift range ($0.2 < z < 6$) and stellar masses (10^7–10^{11} $M_\odot$), thus probing about 12 Gyr of galaxy evolution. We used stellar masses derived from SED fitting to isolate a sample of 54 major close pairs with a galaxy mass ratio limit of 1:6. Thanks to this exquisite data set, we provided, for the first time, robust observational constraints on the galaxy major merger fraction up to $z \approx 6$ using spectroscopic close pair counts.

Among this sample of major close pairs, we identified 20 systems at high redshift ($z \geqslant 3$) through their Lyα emission. For these galaxies, we used the FWHM of the Lyα emission line as a proxy to retrieve their systemic redshift, following theoretical and observational arguments recently developed in Verhamme et al. (2017). The sample of major close pairs was divided into five redshift intervals to probe the evolution of the merger fraction with cosmic time. Our estimates are in very good agreement with previous close pair counts with a constant increase of the merger fraction up to $z \approx 3$, where it reaches a maximum of 20%. At higher redshift, we show that the fraction slowly decreases down to about 10% at $z \approx 6$.

We further divided the sample into two ranges of stellar masses using either a constant separation limit of $10^{9.5}$ $M_\odot$ or the median value of stellar mass computed in each redshift bin. We show that there is a potential reversed trend between the cosmic evolution of the merger fraction in these two mass regimes. Indeed, around $z \approx 1.5$, the merger fraction is higher for massive galaxies, but at higher redshift ($z \geqslant 3$) this trend is reversed. The cosmic evolution of these new estimates of the major merger fraction up to $z \approx 6$ is in agreement with recent predictions of cosmological numerical simulations, such as HORIZON-AGN (Kaviraj et al. 2015), EAGLE (Qu et al. 2017), and Illustris (Snyder et al. 2017).

The shape of the cosmic evolution of the galaxy major merger fraction up to $z \approx 6$ derived from our MUSE data set, which shows an increase up to $z \approx 3$ and then a decrease at higher redshifts, is reminiscent of the well-known cosmic star formation rate evolution (e.g. Madau & Dickinson 2014). This similarity will be further investigated in subsequent papers, making use of larger MUSE data sets acquired over the course the Guaranteed Time Observations to better assess the role of mergers in the growth of galaxies over more than 12 Gyr.

Acknowledgements. This work has been carried out thanks to the support of the ANR FOGHAR (ANR-13-BS05-0010-02), the OCEVU Labex (ANR-11-LABX-0060), and the A*MIDEX project (ANR-11-IDEX-0001-02) funded by the "Investissements d'avenir" French government programme. B.E. acknowledges financial support from "Programme National de Cosmologie et Galaxies" (PNCG) of CNRS/INSU, France. L.W. acknowledges funding by the Competitive Fund of the Leibniz Association through grant SAW-2015-AIP-2. P.M.W. received support through BMBF Verbundforschung (project MUSE-AO, grant 05A14BAC). J.B. acknowledges support by Fundação para a Ciência e a Tecnologia (FCT) through national funds (UID/FIS/04434/2013) and Investigador FCT contract IF/01654/2014/CP1215/CT0003, and by FEDER through COMPETE2020 (POCI-01-0145-FEDER-007672). T.G. is grateful to the LABEX Lyon Institute of Origins (ANR-10-LABX-0066) of the Université de Lyon for its financial support within the programme "Investissements d'Avenir" (ANR-11-IDEX-0007) of the French government operated by the National Research Agency (ANR).

References

Abraham, R. G., van den Bergh, S., Glazebrook, K., et al. 1996, ApJS, 107, 1
Alonso, M. S., Tissera, P. B., Coldwell, G., & Lambas, D. G. 2004, MNRAS, 352, 1081
Bacon, R., Brinchmann, J., Richard, J., et al. 2015, A&A, 575, A75
Bacon, R., Conseil, S., Mary, D., et al. 2017, A&A, 608, A1 (MUSE UDF SI, Paper I)
Baugh, C. M. 2006, Rep. Progr. Phys., 69, 3101
Beckwith, S. V. W., Stiavelli, M., Koekemoer, A. M., et al. 2006, AJ, 132, 1729
Bell, E. F., Zucker, D. B., Belokurov, V., et al. 2008, ApJ, 680, 295
Besla, G., Kallivayalil, N., Hernquist, L., et al. 2012, MNRAS, 421, 2109
Bluck, A. F. L., Conselice, C. J., Bouwens, R. J., et al. 2009, MNRAS, 394, L51
Bluck, A. F. L., Conselice, C. J., Buitrago, F., et al. 2012, ApJ, 747, 34
Brinchmann, J., Abraham, R., Schade, D., et al. 1998, ApJ, 499, 112
Brinchmann, J., Inami, H., Bacon, R., et al. 2017, A&A, 608, A3 (MUSE UDF SI, Paper III)
Bruzual, G., & Charlot, S. 2003, MNRAS, 344, 1000
Bundy, K., Ellis, R. S., & Conselice, C. J. 2005, ApJ, 625, 621
Bundy, K., Fukugita, M., Ellis, R. S., et al. 2009, ApJ, 697, 1369
Calzetti, D., Armus, L., Bohlin, R. C., et al. 2000, ApJ, 533, 682
Cameron, E. 2011, PASA, 28, 128
Casteels, K. R. V., Conselice, C. J., Bamford, S. P., et al. 2014, MNRAS, 445, 1157
Chabrier, G. 2003, PASP, 115, 763
Conselice, C. J. 2014, ARA&A, 52, 291
Conselice, C. J., Bershady, M. A., & Jangren, A. 2000, ApJ, 529, 886
Conselice, C. J., Bershady, M. A., Dickinson, M., & Papovich, C. 2003, AJ, 126, 1183
Conselice, C. J., Rajgor, S., & Myers, R. 2008, MNRAS, 386, 909
Conselice, C. J., Yang, C., & Bluck, A. F. L. 2009, MNRAS, 394, 1956
Conselice, C. J., Bluck, A. F. L., Ravindranath, S., et al. 2011, MNRAS, 417, 2770
Contini, T., Epinat, B., Bouché, N., et al. 2016, A&A, 591, A49
Cooke, J., Berrier, J. C., Barton, E. J., Bullock, J. S., & Wolfe, A. M. 2010, MNRAS, 403, 1020
Crain, R. A., Schaye, J., Bower, R. G., et al. 2015, MNRAS, 450, 1937
De Lucia, G., & Blaizot, J. 2007, MNRAS, 375, 2
de Ravel, L., Le Fèvre, O., Tresse, L., et al. 2009, A&A, 498, 379
Dubois, Y., Pichon, C., Welker, C., et al. 2014, MNRAS, 444, 1453
Erb, D. K., Steidel, C. C., Trainor, R. F., et al. 2014, ApJ, 795, 33
Ferreras, I., Trujillo, I., Mármol-Queraltó, E., et al. 2014, MNRAS, 444, 906
Genel, S., Genzel, R., Bouché, N., et al. 2008, ApJ, 688, 789
Genel, S., Genzel, R., Bouché, N., Naab, T., & Sternberg, A. 2009, ApJ, 701, 2002
Guo, Q., & White, S. D. M. 2008, MNRAS, 384, 2
Harris, J., & Zaritsky, D. 2009, AJ, 138, 1243
Hashimoto, T., Ouchi, M., Shimasaku, K., et al. 2013, ApJ, 765, 70
Inami, H., Bacon, R., Brinchmann, et al. 2017, A&A, 608, A2 (MUSE UDF SI, Paper II)
Jian, H.-Y., Lin, L., & Chiueh, T. 2012, ApJ, 754, 26
Kampczyk, P., Lilly, S. J., Carollo, C. M., et al. 2007, ApJS, 172, 329
Kartaltepe, J. S., Sanders, D. B., Scoville, N. Z., et al. 2007, ApJS, 172, 320
Kaviraj, S., Devriendt, J., Dubois, Y., et al. 2015, MNRAS, 452, 2845
Keenan, R. C., Foucaud, S., De Propris, R., et al. 2014, ApJ, 795, 157
Kereš, D., Katz, N., Weinberg, D. H., & Davé, R. 2005, MNRAS, 363, 2
Kitzbichler, M. G., & White, S. D. M. 2008, MNRAS, 391, 1489
Koch, A., Frank, M. J., Pasquali, A., Rich, R. M., & Rabitz, A. 2015, ApJ, 815, 105
Kriek, M., van Dokkum, P. G., Labbé, I., et al. 2009, ApJ, 700, 221
Labbé, I., Oesch, P. A., Illingworth, G. D., et al. 2015, ApJS, 221, 23
Lagos, C. d. P., Stevens, A. R. H., Bower, R. G., et al. 2017, MNRAS, submitted [arXiv:1701.04407]
Le Fèvre, O., Abraham, R., Lilly, S. J., et al. 2000, MNRAS, 311, 565
Lin, L., Koo, D. C., Willmer, C. N. A., et al. 2004, ApJ, 617, L9
Lin, L., Patton, D. R., Koo, D. C., et al. 2008, ApJ, 681, 232
López-Sanjuan, C., Balcells, M., García-Dabó, C. E., et al. 2009a, ApJ, 694, L643
López-Sanjuan, C., Balcells, M., Pérez-González, P. G., et al. 2009b, A&A, 501, L505
López-Sanjuan, C., Le Fèvre, O., de Ravel, L., et al. 2011, A&A, 530, A20
López-Sanjuan, C., Le Fèvre, O., Ilbert, O., et al. 2012, A&A, 548, A7
López-Sanjuan, C., Le Fèvre, O., Tasca, L. A. M., et al. 2013, A&A, 553, A78
López-Sanjuan, C., Cenarro, A. J., Varela, J., et al. 2015, A&A, 576, A53
Lotz, J. M., Davis, M., Faber, S. M., et al. 2008, ApJ, 672, 177
Lotz, J. M., Jonsson, P., Cox, T. J., et al. 2011, ApJ, 742, 103
Madau, P., & Dickinson, M. 2014, ARA&A, 52, 415

Maller, A. H., Katz, N., Kereš, D., Davé, R., & Weinberg, D. H. 2006, ApJ, 647, 763
Man, A. W. S., Toft, S., Zirm, A. W., Wuyts, S., & van der Wel, A. 2012, ApJ, 744, 85
Man, A. W. S., Zirm, A. W., & Toft, S. 2016, ApJ, 830, 89
Maseda, M., Brinchmann, J., Franx, M., et al. 2017, A&A, 608, A4 (MUSE UDF SI, Paper IV)
McLinden, E. M., Finkelstein, S. L., Rhoads, J. E., et al. 2011, ApJ, 730, 136
Mihos, J. C., & Hernquist, L. 1994, ApJ, 437, L47
Mihos, J. C., & Hernquist, L. 1996, ApJ, 464, 641
Moreno, J., Bluck, A. F. L., Ellison, S. L., et al. 2013, MNRAS, 436, 1765
Moster, B. P., Somerville, R. S., Newman, J. A., & Rix, H.-W. 2011, ApJ, 731, 113
Naab, T., & Burkert, A. 2003, ApJ, 597, 893
Nikolic, B., Cullen, H., & Alexander, P. 2004, MNRAS, 355, 874
Ocvirk, P., Pichon, C., & Teyssier, R. 2008, MNRAS, 390, 1326
Patton, D. R., & Atfield, J. E. 2008, ApJ, 685, 235
Patton, D. R., Pritchet, C. J., Yee, H. K. C., Ellingson, E., & Carlberg, R. G. 1997, ApJ, 475, 29
Patton, D. R., Carlberg, R. G., Marzke, R. O., et al. 2000, ApJ, 536, 153
Perret, V., Renaud, F., Epinat, B., et al. 2014, A&A, 562, A1
Popesso, P., Dickinson, M., Nonino, M., et al. 2009, A&A, 494, 443
Qu, Y., Helly, J. C., Bower, R. G., et al. 2017, MNRAS, 464, 1659
Rafelski, M., Teplitz, H. I., Gardner, J. P., et al. 2015, AJ, 150, 31
Rodriguez-Gomez, V., Genel, S., Vogelsberger, M., et al. 2015, MNRAS, 449, 49
Rodriguez-Gomez, V., Pillepich, A., Sales, L. V., et al. 2016, MNRAS, 458, 2371
Ryan, Jr., R. E., Cohen, S. H., Windhorst, R. A., & Silk, J. 2008, ApJ, 678, 751
Schaye, J., Crain, R. A., Bower, R. G., et al. 2015, MNRAS, 446, 521
Shibuya, T., Ouchi, M., Nakajima, K., et al. 2014, ApJ, 788, 74
Snyder, G. F., Lotz, J. M., Rodriguez-Gomez, V., et al. 2017, MNRAS, 468, 207
Somerville, R. S., Primack, J. R., & Faber, S. M. 2001, MNRAS, 320, 504
Tasca, L. A. M., Le Fèvre, O., López-Sanjuan, C., et al. 2014, A&A, 565, A10
Verhamme, A., et al. 2017, MNRAS, submitted
Verhamme, A., Orlitová, I., Schaerer, D., & Hayes, M. 2015, A&A, 578, A7
Vogelsberger, M., Genel, S., Springel, V., et al. 2014, MNRAS, 444, 1518
White, S. D. M., & Rees, M. J. 1978, MNRAS, 183, 341
Williams, R. E., Baum, S., Bergeron, L. E., et al. 2000, AJ, 120, 2735
Xu, C. K., Zhao, Y., Scoville, N., et al. 2012, ApJ, 747, 85

Appendix A: Additional table.

Table A.1. Basic properties for the sample of major galaxy close pairs in the HDF-S, udf-10, and UDF-Mosaic.

MUSE ID$_1$	z_1	$zconf_1$	$M_1^\star$	MUSE ID$_2$	z_2	$zconf_2$	$M_2^\star$	r_p	Δ_v	MUSE field
–	–	–	[log($M_\odot$)]	–	–	–	[log($M_\odot$)]	[kpc]	[km s^{-1}]	–
(1)	(2)	(3)	(4)	(5)	(6)	(7)	(8)	(9)	(10)	(11)
29	0.831	3	10.44	58	0.832	1	10.21	25.3	138	HDF-S
45	1.155	3	9.90	134	1.155	2	9.78	20.0	56	HDF-S
50	2.672	3	10.96	55	2.674	3	10.78	6.6	119	HDF-S
88	1.360	2	8.70	589	1.359	2	8.08	5.0	15	HDF-S
183	3.374	2	9.81	261	3.375	1	9.81	2.4	78	HDF-S
433	3.470	2	7.35	478	3.469	1	7.17	20.9	145	HDF-S
441	4.695	2	7.85	453	4.701	1	7.49	24.6	438	HDF-S
492	5.760	2	8.22	577	5.764	1	8.51	18.6	16	HDF-S
551	3.180	2	9.81	578	3.180	1	9.81	3.8	59	HDF-S
3	0.622	3	9.92	9	0.619	3	10.23	14.6	411	udf-10
24	2.544	3	9.75	35	2.543	3	10.04	14.5	62	udf-10
30	1.096	3	8.94	84	1.096	3	8.81	35.7	54	udf-10
32	1.307	3	9.23	77	1.310	1	8.68	33.8	413	udf-10
32	1.307	3	9.23	121	1.306	3	8.56	11.7	72	udf-10
46	1.413	3	9.31	92	1.414	3	8.54	8.2	21	udf-10
61	2.454	3	9.58	67	2.449	3	10.18	12.2	399	udf-10
65	1.307	3	8.97	77	1.310	1	8.68	13.6	378	udf-10
96	0.622	3	7.69	108	0.622	3	7.78	20.7	63	udf-10
344	3.471	2	8.52	6871	3.474	1	9.15	19.7	195	udf-10
399	5.137	2	7.52	627	5.135	2	7.15	26.2	99	udf-10
399	5.137	2	7.52	6339	5.131	2	6.98	27.8	305	udf-10
430	4.514	2	8.64	6340	4.510	2	8.97	30.5	223	udf-10
430	4.514	2	8.64	6342	4.514	2	8.52	4.0	3	udf-10
627	5.135	2	7.15	6339	5.131	2	6.98	22.8	206	udf-10
6302	3.473	2	9.18	6925	3.474	2	9.63	32.7	68	udf-10
430	4.513	2	7.84	7197	4.513	2	8.18	30.8	2	UDF-Mosaic
891	0.227	3	7.84	6891	0.227	3	7.15	21.2	35	UDF-Mosaic
899	1.097	3	10.18	934	1.096	3	9.79	30.5	94	UDF-Mosaic
950	0.993	3	9.00	1107	0.993	3	8.73	8.3	3	UDF-Mosaic
997	1.041	3	8.93	1454	1.041	3	8.69	32.6	24	UDF-Mosaic
999	1.608	3	9.93	1268	1.609	2	9.71	7.4	46	UDF-Mosaic
1027	0.219	3	7.63	1167	0.219	3	7.08	16.5	43	UDF-Mosaic
1044	2.028	3	10.17	1048	2.028	2	10.08	31.8	81	UDF-Mosaic
1065	0.522	3	8.21	1444	0.523	3	7.61	28.1	290	UDF-Mosaic
1178	2.691	3	9.69	1279	2.691	1	9.66	32.5	65	UDF-Mosaic
1188	1.412	2	9.61	1219	1.413	2	9.12	28.0	118	UDF-Mosaic
1267	1.866	3	9.58	6947	1.866	2	9.76	32.5	10	UDF-Mosaic
1341	1.413	3	9.12	1373	1.413	3	8.89	9.3	36	UDF-Mosaic
1345	1.095	3	8.57	1605	1.095	3	8.71	26.9	37	UDF-Mosaic
1545	0.992	3	8.33	6991	0.991	3	8.26	19.0	156	UDF-Mosaic
1561	0.733	3	7.68	1644	0.732	3	7.52	7.0	67	UDF-Mosaic
1611	0.666	3	7.79	1688	0.665	1	7.27	22.9	150	UDF-Mosaic
1678	1.425	2	8.76	7101	1.427	2	8.67	32.2	262	UDF-Mosaic
1990	1.219	3	8.55	6885	1.216	2	8.94	20.4	496	UDF-Mosaic
2071	4.930	2	9.33	6412	4.928	2	9.37	14.0	98	UDF-Mosaic

Notes. Labels 1 and 2 denote the primary and secondary galaxy, respectively. Columns (1) and (5): identification number in the MUSE-based catalogues of Bacon et al. (2015) for HDF-S galaxies, and Inami et al. (2017) for HUDF galaxies. Columns (2) and (6): MUSE spectroscopic redshift with associated confidence level (2 and 3 = secure redshift, 1 = possible redshift, see Inami et al. 2017 for details) in Cols. (3) and (7). Columns (4) and (8): stellar masses in logarithmic units. Columns (9) and (10): projected separation (in kpc) and velocity difference (in km s^{-1}) between the two galaxies in the pair, respectively.

Table A.1. continued.

MUSE ID$_1$	z_1	$zconf_1$	$M_1^\star$	MUSE ID$_2$	z_2	$zconf_2$	$M_2^\star$	r_p	Δ_v	MUSE field
–	–	–	[log($M_\odot$)]	–	–	–	[log($M_\odot$)]	[kpc]	[km s^{-1}]	–
(1)	(2)	(3)	(4)	(5)	(6)	(7)	(8)	(9)	(10)	(11)
2672	3.439	2	8.78	7351	3.433	2	8.03	33.2	400	UDF-Mosaic
2695	3.067	2	7.66	3430	3.061	2	7.40	30.5	436	UDF-Mosaic
2757	5.380	2	7.91	5398	5.382	1	7.22	33.4	86	UDF-Mosaic
3840	4.813	2	7.30	5508	4.807	2	6.89	27.2	318	UDF-Mosaic
4532	3.438	2	8.52	7221	3.435	2	8.54	34.1	215	UDF-Mosaic
4542	4.811	2	7.16	5882	4.811	2	6.85	26.2	2	UDF-Mosaic
6402	4.372	2	8.40	7311	4.372	2	8.47	20.7	6	UDF-Mosaic
6517	3.432	2	8.86	6531	3.432	1	8.58	28.6	3	UDF-Mosaic
6923	3.433	2	7.53	7283	3.432	2	8.00	21.2	62	UDF-Mosaic
7285	5.486	2	7.74	7353	5.485	2	7.48	33.8	46	UDF-Mosaic

6

Using new selection criteria from Illustris simulations to investigate the evolution of the major and minor merger fraction

Contents

6.1 New criteria for the selection of galaxy close pairs from cosmological simulations: evolution of the major and minor merger fraction in MUSE deep fields 87

6.1 New criteria for the selection of galaxy close pairs from cosmological simulations: evolution of the major and minor merger fraction in MUSE deep fields

After my first analysis performed on the MUSE Hubble Ultra Deep Field and Hubble Deep Field South surveys, I tried to investigate and better refine companion selection criteria for close pair count studies in order to trace more accurately the galaxy merger fraction.

The aim of the following paper is thus to provide new selection criteria for close pair count analysis. To achieve this goal, I used Illustris cosmological simulations

to investigate the relation between close pair selection criteria (separation distance and relative velocity) and whether the two galaxies will finally merge by $z = 0$. These numerical data were kindly provided by S. Genel (CCA, New-York).

The first part of this article (first three sections) is thus dedicated to the establishment of a new set of selection criteria. In the second part of this work, I applied these new criteria to MUSE deep observations performed over four regions: the Hubble Deep Field South, the Hubble Ultra Deep Field, the galaxy cluster Abell 2744, and the COSMOS-Gr30 galaxy group. From this large parent sample, I found a total of 183 major, 142 minor and 47 very minor close pairs corresponding to a mass ratio range of 1:1-1:6, 1:6-1:100 and lower than 1:100, respectively. The last part of the article presents the major and minor merger fraction evolution along cosmic time.

Astronomy & Astrophysics manuscript no. output
April 10, 2019

New criteria for the selection of galaxy close pairs from cosmological simulations: evolution of the major and minor merger fraction in MUSE deep fields⋆

E.Ventou[1], T. Contini[1], N. Bouché[1,2], B. Epinat[1,3], J. Brinchmann[4,5], H. Inami[6,2], J. Richard[2], I. Schroetter[1,7], G. Soucail[1], M. Steinmetz[8], and P.M. Weilbacher[8]

[1] Institut de Recherche en Astrophysique et Planétologie (IRAP), Université de Toulouse, CNRS, UPS, F-31400 Toulouse, France
[2] Univ Lyon, Univ Lyon1, Ens de Lyon, CNRS, Centre de Recherche Astrophysique de Lyon UMR5574, F-69230, Saint-Genis-Laval, France
[3] Aix Marseille Univ, CNRS, CNES, LAM, Marseille, France
[4] Instituto de Astrofísica e Ciências do Espaço, Universidade do Porto, CAUP, Rua das Estrelas, PT4150-762 Porto, Portugal
[5] Leiden Observatory, Leiden University, P.O. Box 9513, 2300 RA, Leiden, The Netherlands
[6] Hiroshima Astrophysical Science Center, Hiroshima University, 1-3-1 Kagamiyama, Higashi-Hiroshima, Hiroshima 739-8526, Japan
[7] GEPI, Observatoire de Paris, PSL Université, CNRS, 5 Place Jules Janssen, 92190 Meudon, France
[8] Leibniz-Institut für Astrophysik Potsdam (AIP), An der Sternwarte 16, 14482 Potsdam, Germany

Received date

ABSTRACT

It is still a challenge to assess the merger fraction of galaxies at different cosmic epochs in order to probe the evolution of their mass assembly. Using the Illustris cosmological simulation project, we investigate the relation between the separation of galaxies in a pair, both in velocity and projected spatial separation space, and the probability that these interacting galaxies will merge in the future. From this analysis, we propose a new set of criteria to select close pairs of galaxies along with a new corrective term to be applied to the computation of the galaxy merger fraction. We then probe the evolution of the major and minor merger fraction using the latest MUSE deep observations over the Hubble Ultra Deep Field, Hubble Deep Field South, COSMOS-Gr30 and Abell 2744 regions. From a parent sample of 2483 galaxies with spectroscopic redshifts, we identify 372 close pairs spread over a large range of redshifts ($0.2 < z < 6$) and stellar masses ($10^7 - 10^{11} M_\odot$). Using the stellar mass ratio between the secondary and primary galaxy as a proxy to split the sample into major, minor and very minor mergers, we found a total of 183 major, 142 minor and 47 very minor close pairs corresponding to a mass ratio range of 1:1-1:6, 1:6-1:100 and lower than 1:100, respectively. Due to completeness issues, we do not consider the very minor pairs in the analysis. Overall, the major merger fraction increases up to $z \approx 2-3$ reaching 25% for pairs with the most massive galaxy with a stellar mass $M^\star \geq 10^{9.5} M_\odot$. Beyond this redshift, the fraction decreases down to $\sim 5\%$ at $z \approx 6$. The major merger fraction for lower mass primary galaxies $M^\star \leq 10^{9.5} M_\odot$, seems to follow a more constant evolutionary trend with redshift. Thanks to the addition of new MUSE fields and new selection criteria, the increased statistics of the pair samples allow to narrow significantly the error bars compared to our previous analysis (Ventou et al. 2017). The evolution of the minor merger fraction is roughly constant with cosmic time, with a fraction of 20% at $z < 3$ and a slow decrease between $3 \leq z \leq 6$ to $8-13\%$.

Key words. Galaxies: evolution - Galaxies: high-redshift - Galaxies: interactions

1. Introduction

Understanding the processes behind the mass assembly of galaxies in dark matter halos remains one of the most outstanding issues of modern astrophysics. Thanks to the development of more and more sophisticated cosmological models and simulations as well as new data coming from deep and wide photometric and spectroscopic surveys, much progress has been made both on the theoretical and observational side of galaxy evolution. Several mechanisms, such as cold gas accretion and galaxy mergers, contribute to the build-up of galaxies along cosmic time (eg. Anglés-Alcázar et al. 2017). In the first scenario, fresh gas is supplied to the galaxy from cold filaments following the cosmic web of large-scale structure. While direct observational evidence of this phenomenon has been difficult to obtain, indirect arguments, such as evidences from internal kinematic, expected absorption features along background quasar sight-lines or chemical evolution models with the well known G-dwarf problem, has been accumulating over the past decade (Chiappini 2001; Caimmi 2008; Sancisi et al. 2008; Bournaud et al. 2011; Stewart et al. 2011; Bouché et al. 2016; Zabl et al. 2019). In comparison many examples of colliding and merging galaxies have been observed and studied in the local universe. Galaxy mergers are known to not only enhance star formation and fuel starbursts (Joseph & Wright 1985; Di Matteo et al. 2007; Kaviraj 2014), but also to strongly affect galaxy morphologies and dynamics (Bell et al. 2008; Perret et al. 2014; Borlaff et al. 2014; Lagos et al. 2018).

The relative contribution of these processes to the mass growth of galaxies is still unclear. Cosmological simulations suggest that a large fraction of cold gas can be accreted by galax-

⋆ Based on observations made with ESO telescopes at the Paranal Observatory under programmes 094.A-0289, 094.A-0115, 094.A-0247, 095.A-0118, 095.A-0010, and 096.A-0045

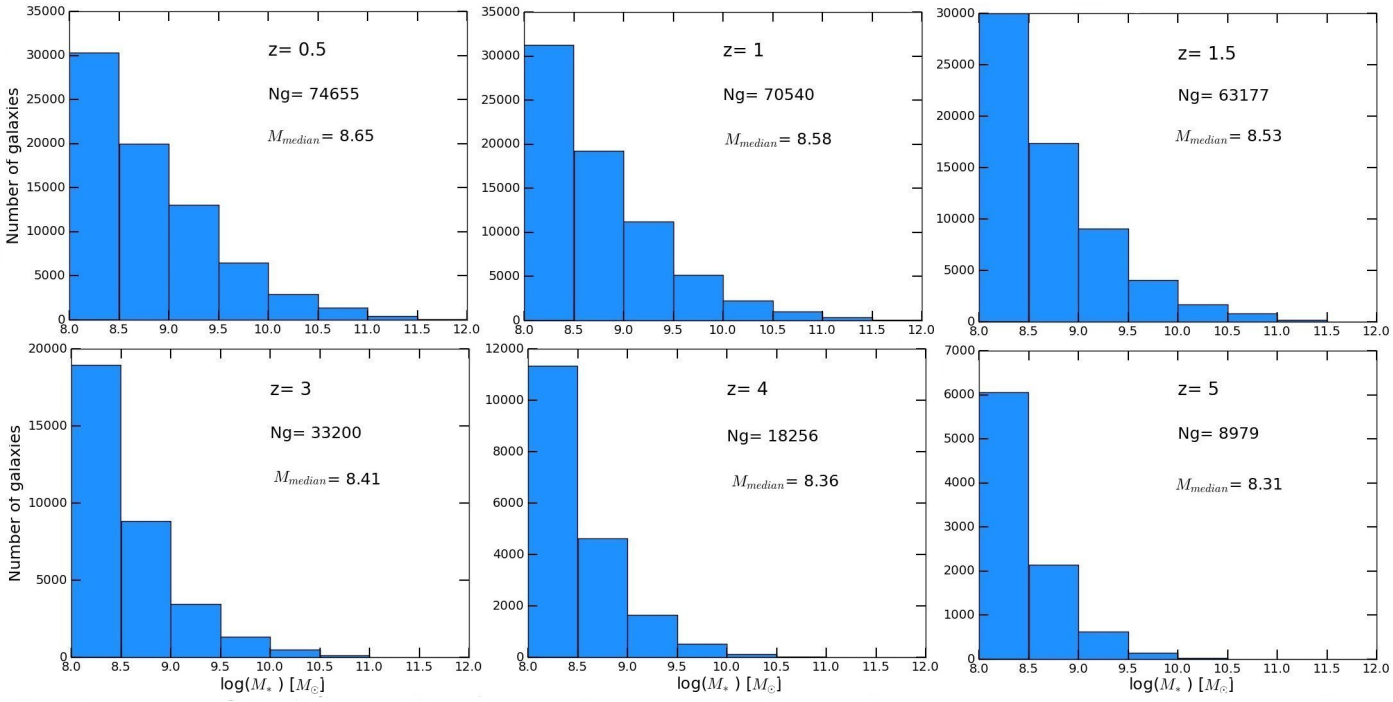

Fig. 1: Stellar mass distribution of galaxies in the Illustris simulation for six snapshots corresponding to redshifts z = 0.5, 1, 1.5, 3, 4 and 5. The total number of galaxies and the median stellar mass are indicated in each panel.

ies and smooth gas accretion may dominate galaxy assembly at least for massive galaxy (Murali et al. 2002; Keres et al. 2005; Williams et al. 2011; L'Huillier et al. 2012; van de Voort et al. 2012; Conselice et al. 2013). However, the relative importance of both phenomena remains uncertain, since the total amount of mass accretion onto galaxies by merging is still poorly constrained, especially in the early epoch of galaxy evolution due to the difficulties to observe these events at high redshift.

Several methods have been used to investigate merging activity across cosmic time, for instance by identifying mergers through perturbations in galaxy morphologies (Le Févre et al. 2000; Conselice et al. 2003; Conselice 2006; Kampczyk et al. 2007; Conselice et al. 2008; Heiderman et al. 2009; Bluck et al. 2012; Casteels et al. 2014). However these approaches are limited by the poor spatial resolution of high redshift objects, even with HST images, and to the fact that morphological disturbances are not always related to merger events, as suggested by galaxy kinematics (e.g. Förster Schreiber et al. 2009, 2011). At high redshift ($z \geq 2$), studies have thus focused on the close pair counts method to probe merger abundance. These close pairs are gravitationally bound systems of two galaxies and are expected to merge within an estimated timescale of about 1 Gyr (Kitzbichler & White 2008; Jian et al. 2012; Moreno et al 2013) for nearly equal-mass galaxies (major merger with a mass ratio between the two galaxies greater than 1:4).

Several photometric and spectroscopic surveys have found that the major merger fraction and rate increase with redshift up to $z \sim 1$ (Lin et al. 2008; Bundy et al. 2009; de Ravel et al. 2009; Lopez-Sanjuan et al. 2012). Only a few estimates of this fraction and rate have been attempted for $z \geq 1.5$ and the conclusions reached on their evolution across cosmic time depend strongly on the adopted selection method. Photometric and flux-ratio-selected major pairs studies reveal that the major merger rate increases steadily up to $z \sim 2-3$ (Bluck et al. 2009; Man et al. 2012, 2016), but see Mantha et al. (2018) for a contradictory result, whereas spectroscopic and mass-ratio-selected pairs from recent surveys found that beyond $z \geq 2$, the incidence of major mergers remains constant or decreases at early times (Lopez-Sanjuan et al. 2013; Tasca et al. 2014; Ventou et al. 2017). This discrepancy could be explained by the contamination of photometric samples by a large number of minor mergers, with a mass ratio lower than 1:4, (Lotz et al. 2011; Mantha et al. 2018). The large scatter between measurements using the same selection method can also be attributed to the wide range of companion selection criteria used in previous surveys. While it would be more accurate to identify close pairs of galaxies based on their true (i.e. in real space) physical separation, it is not applicable directly to the observed datasets. Thereby various criteria have been considered.

The first analyses of galaxy pairs formulated a criterion mostly relying on apparent angular separation and angular diameter of the galaxies (Turner 1976a; Peterson 1979). In more recent sudies (Patton et al. 2000; de Ravel et al. 2009; Tasca et al. 2014; Man et al. 2016; Ventou et al. 2017) close pairs of galaxies are frequently defined as two galaxies within a limited projected angular separation and line-of-sight relative velocity. For spectroscopic surveys a relative velocity difference of $\Delta_V \leqslant 300-500$ km s^{-1} is often applied, which offers a good compromise between contamination by chance pairing, i.e. pairs which will satisfy the selection criteria but are not gravitationally bound, and pair statistics (Patton et al. 2000; Lin et al. 2008). The projected separation criterion however varies a lot in the literature, $0-10 \leqslant r_p \leqslant 25-50$ h^{-1}kpc, which makes direct comparisons difficult (Patton et al. 2000; de Ravel et al. 2009; Lopez-Sanjuan et al. 2013; Tasca et al. 2014; Ventou et al. 2017; Mantha et al. 2018). Furthermore, recent studies based on the Sloan Digital Sky Survey have shown that effect of galaxy interactions can be detected in galaxy pairs with separation greater than 50 h^{-1}kpc. Star formation rate (SFR) enhancements, for example, are present out to projected separations of 150 h^{-1}kpc (Scudder

et al. 2012; Patton et al. 2013). This shows the need to investigate and better refine companion selection criteria for close pair count study.

While major mergers are relatively easy to identify, minor mergers are more frequent in the nearby universe and may also be an important driver of galaxy evolution (Naab et al. 2009; McLure et al. 2013; Kaviraj 2014). However the cosmic evolution of the minor merger fraction and rate of galaxies is almost unconstrained, with very few attempts so far (eg. Lopez-Sanjuan et al. 2011, 2012).

In the present paper, we aim to provide new selection criteria for close pair count analysis. We make use of the Illustris cosmological simulation project to investigate the relation between close pair selection criteria, i.e. separation distance and relative velocity, and whether the two galaxies will finally merge by $z = 0$. Following the analysis of Ventou et al. (2017), we apply these new criteria to MUSE (Multi-Unit Spectroscopic Explorer) deep observations performed over four regions: the Hubble Deep Field South, the Hubble Ultra Deep Field, the galaxy cluster Abell 2744, and the COSMOS-Gr30 galaxy group, in order to better constrain the cosmic evolution of the merger fraction. Thanks to its large field-of-view, MUSE allows to explore the close environment of galaxies and thus to probe the evolution of the major and minor merger fraction over a wide range of stellar masses and redshift domain.

This paper is organized as follows: In section 2, we introduce the Illustris simulation and we detail in section 3 the analysis performed on the companion selection criteria and its results. The MUSE data sets used to detect galaxy close pairs as well as the final close pairs sample, are described in section 4.1. Finally we give an estimate of the major and minor merger fraction evolution up to $z \sim 6$ in section 5. A summary and conclusion are given in section 6.

Throughout this work, we use a standard ΛCDM cosmology with $H_0 = 100h$ kms^{-1} Mpc^{-1}, $h = 0.7$, $\Omega_m = 0.3$, $\Omega_\Lambda = 0.7$. Magnitudes are in given in the AB system.

2. Illustris simulation

The Illustris cosmological simulation project (Vogelsberger et al. 2014; Genel et al. 2014; Nelson et al. 2015), is a series of N-body/hydrodynamical simulations reproducing the formation and evolution of galaxies across cosmic time over a large volume of 106.5 Mpc^3. The simulations uses the moving-mesh code AREPO (Springel 2010) and includes many ingredients for galaxy evolution such as primordial and metal-line cooling with self-shielding corrections, stellar evolution, stellar feedback, galactic-scale outflows with an energy-driven kinetic wind scheme, chemical enrichment, super-massive black hole growth, and feedback from active galactic nuclei (Vogelsberger et al. 2013).

Merger trees were constructed from the main Illustris-1 simulation using the SUBLINK algorithm, which identifies a unique sub-halo descendant from the next snapshot using a merit function that takes into account the binding energy rank of each particle to discriminate between the potential sub-halo candidates (see Rodriguez-Gomez et al. 2015 for more details on the creation of merger tree of sub-halos and galaxies). The Illustris-1 simulation has already been used in previous works related to galaxy mergers. These analyses suggest that major pair fractions change little or decrease with increasing redshift for $z > 1$ (Snyder et al. 2017), which is in agreement with recent surveys, and that 50(20)% of the ex-situ stellar mass in nearby of elliptical galaxies comes from major(minor) mergers (Rodriguez-Gomez et al. 2016).

For this analysis, mock catalogs were created from six snapshots of the Illustris-1 simulation, corresponding to six different redshifts: $z = 0.5$, 1, 1.5, 3, 4 and 5. For each of them, merger tree information was generated. The simulation produces galaxies spread over a large range of stellar masses, $10^8 \leq M^\star \leq 10^{11.5} M_\odot$ (see Fig. 1). The lower mass cut of $10^8 M_\odot$ is about two order of magnitude higher than the nominal baryonic mass resolution of the Illustris-1 simulation. The number of galaxies in these mocks decreases with redshift, from $\sim$ 75 000 at $z = 0.5$ to $\sim$ 9 000 at $z = 5$. This variation in the number of galaxies is reflected in Figs. 2 and 3, where the statistics decreases at high redshift. Since mock data are versions of the real simulation in which the geometry and selection effects of observational surveys are reproduced, it can be analyzed using similar methods, which is a powerful advantage for comparisons between theory and observations.

3. New criteria for the selection of galaxy close pairs

A close pair of galaxies is defined as two galaxies with a small rest-frame relative velocity and projected separation distance in the sky plane. These selection parameters are respectively computed as follows in most observational surveys:

$$r_p^{min} \leqslant r_p = \theta \times d_A(z_m) \leqslant r_p^{max}, \quad (1)$$

where θ is the angular distance between the two galaxies, $d_A(z_m)$ is the angular scale (in kpc arcsec^{-1}) and z_m is the mean redshift of the two galaxies, and:

$$\Delta v = \frac{c \times |z_1 - z_2|}{(1 + z_m)} \leqslant \Delta v_{max}, \quad (2)$$

where z_1 and z_2 are the redshifts of each galaxy in the pair and c is the speed of light.

For each of these two criteria, a wide range of values can be found in the literature (see sect.1). In the following subsections, we try to improve these parameters by analyzing the relation between the velocity-distance relative separation of a close pair of galaxies and the probability that this pair will merge in the future.

3.1. Galaxy pairs identification

For each of the six mock catalogs created from Illustris-1 simulation (see section 2), we applied selection techniques that are commonly used in observational surveys. Knowing the position and velocity of each galaxy in real space, we detect pairs of galaxies with a difference in relative velocity amplitude $\Delta v \leqslant 500$ km s^{-1}, since most studies have shown that pairs with $\Delta v > 500$ km s^{-1} are not likely to be gravitationally bound (Patton et al. 2000; De Propris et al. 2007), and a separation distance, $\Delta r \leqslant 500$ kpc, which allows us to explore a large range of values for the separation distance criterion. From the merger trees, we can then follow the descendant branch informations for each sub-halo in the subsequent snapshot, and so on, until $z = 0$ and thus identify which ones of the galaxy pairs become a true merger in the future.

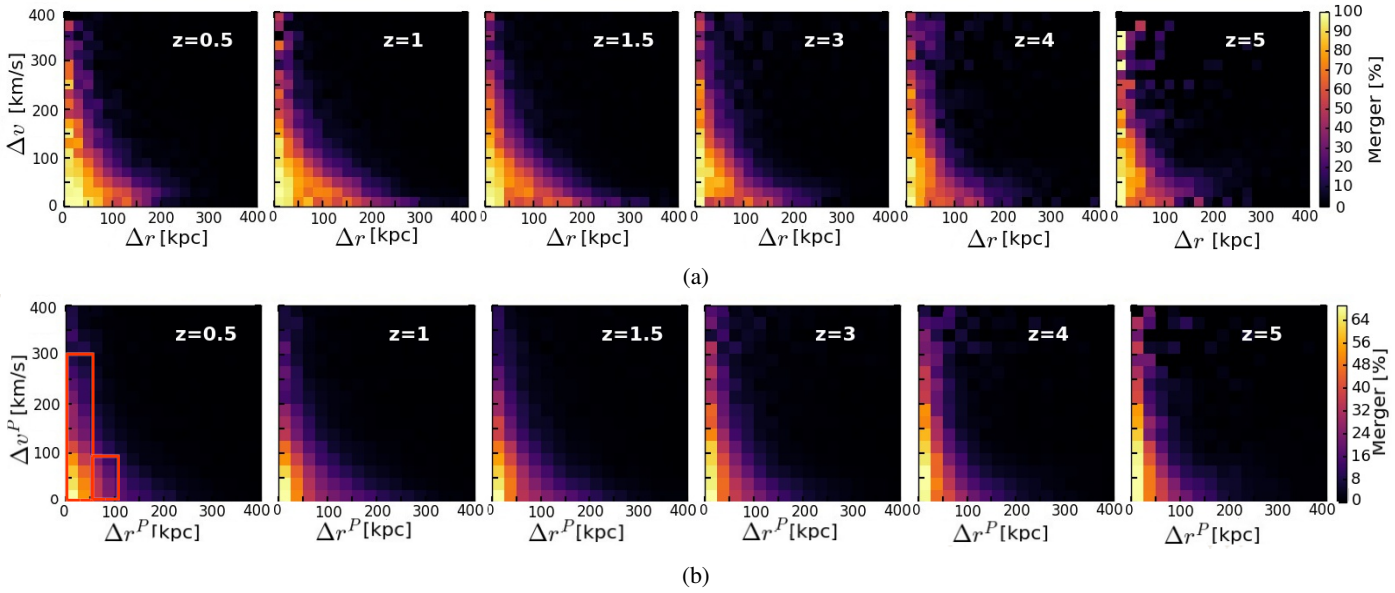

Fig. 2: (a) The galaxy pair velocity-separation distance diagram from Illustris-1 simulation for six snapshots at different redshifts, color-coded with respect to the fraction of future mergers within the pair sample. (b) Same diagram as (a) but with *projected* velocity-separation distances. The two red boxes correspond to the new criteria introduced in sect 3.2.3.

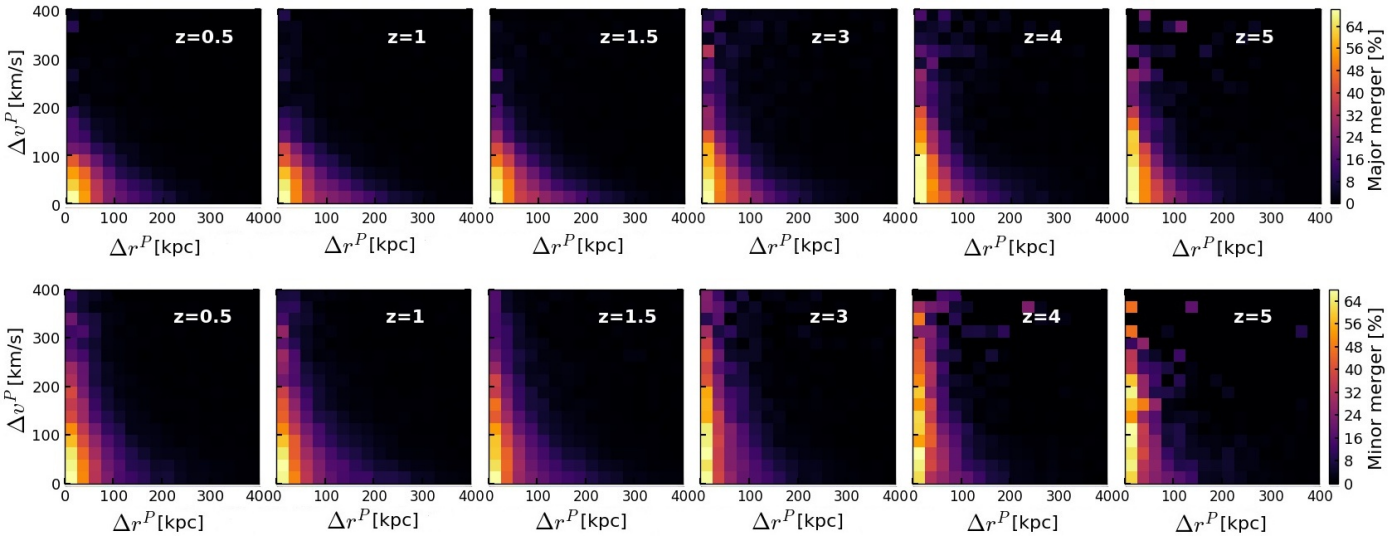

Fig. 3: Influence of the galaxy mass ratio in the pair on the velocity-separation distance diagram and the probability of the pair to merge for different redshifts. *Top*: Major merger distribution, with a mass ratio between the primary galaxy and its companion within 1:1 and 1:6. *Bottom*: Minor merger distribution with a mass ratio in the pair lower than 1:6.

3.2. Results

3.2.1. Projection effect

Figure 2(a) shows the relation between the true velocity-distance separation of the galaxy pairs in real space and their probability to merge for the different redshifts. As expected the probability of a pair to merge decreases both with the separation distance, Δr, and with the velocity difference, Δv, of the galaxy pair. The decrease is slower for Δv than for Δr. Thus, a galaxy pair within a separation distance of $\Delta r \leqslant 50$ kpc and velocity difference of $\Delta v \leqslant 200$ km s^{-1} has between 100 and 80% of chance to merge by $z = 0$. For the highest redshift snapshots, $z = 4$ and 5, statistical effects, due to much lower numbers of pairs, begin to appear for $\Delta v \geqslant 400$ km s^{-1}.

However true, unprojected, velocity differences and physical separation distances are not available in observations. Thereby we use projected values of the relative velocity and distance which reflect the projected separation distance in the sky plane and the rest-frame velocity difference in redshift space from observations. The probability for a galaxy pair to merge as a function of its position in the projected velocity-distance diagram (Δv^P vs. Δr^P) is shown in Figure 2(b). Using projected values clearly affects the probability of a pair to merge because of contamination effects, dropping the probability to 70% for a pair with $\Delta r^P \leqslant 25$ kpc and $\Delta v^P \leqslant 100$ km s^{-1}. In the projected space, pairs with $\Delta v^P \geqslant 300$ km s^{-1} have less than 10% chance to end up as a merging system.

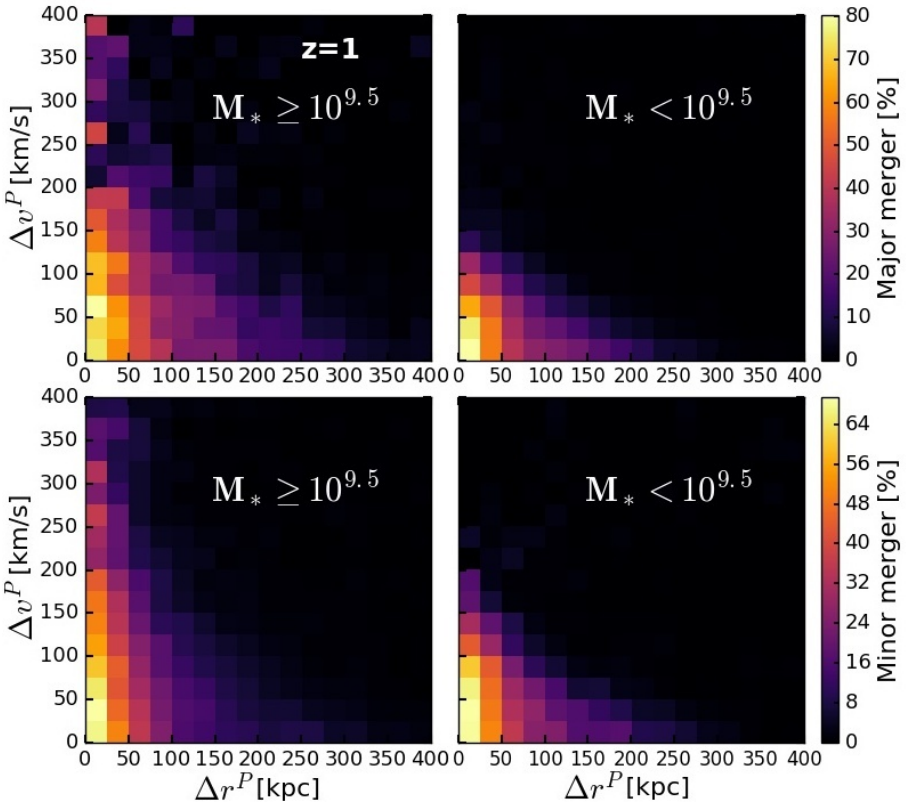

Fig. 4: Influence of the primary galaxy's stellar mass on the merger velocity-separation distance diagram. A constant stellar mass limit of $10^{9.5}M_\odot$ is chosen to distinguish low-mass from massive primary galaxies within the major (*top*) and the minor (*bottom*) pair samples at $z = 1$.

3.2.2. Dependence on stellar mass

Interacting galaxies can end up in a merging system if the two colliding galaxies do not have enough momentum to overcome the gravitational hold they have on one another and continue their courses after the collision. Velocities, angles of the collision, sizes, relative composition or masses are all parameters that can affect the result of two colliding galaxies. The more massive the primary galaxy is, the more gravitational pull it will have, the harder it will be for its companion to liberate itself from its hold.

An attempt to study the influence of the mass ratio on the relation between the velocity-separation distance diagram of the galaxy pairs and their probability to merge is shown in Fig. 3. The influence of the primary galaxy stellar mass on this relation is shown in Fig. 4.

First, we use the mass ratio between the two galaxies to discriminate the pairs. Figure 3 shows the relation between the projected velocity-distance separation of the pair and their probability to merge for major close pairs, with a stellar mass ratio higher than 1:6 (as adopted in Ventou et al. 2017), and minor close pairs, i.e. with stellar mass ratio lower than 1:6. The main difference seen in Fig. 3 between the two samples comes from the rest-frame relative velocity condition. For a fixed projected separation distance $\Delta r^P \leqslant 25$ kpc, ~70% of the major close pairs will merge if their rest-frame relative velocity Δv^P is lower than ~ 50 km s^{-1}(see Fig.3, top panels), whereas the same fraction of mergers will be reached by minor close pairs with Δv^P up to 100 km s^{-1}(see Fig.3, bottom panels).

We further separate our sample into two regimes using the stellar mass of the primary galaxy, i.e. the most massive one of the pair, as a limit. In Fig. 4 we distinguish, for the $z = 1$ snapshot, between low-mass and massive galaxies within the major and minor close pair samples by applying a separation limit of $10^{9.5}M_\odot$, similar to the limit adopted in Ventou et al. (2017).

As for the major-minor discrimination, the stellar mass separation affects mainly the condition on the rest-frame velocity. For a primary galaxy with a stellar mass, $M^\star > 10^{9.5}M_\odot$, a pair within $\Delta r^P \leqslant 25$ kpc and $\Delta v^P \leqslant 150$ km s^{-1} has between 75 and 60% chance to merge, for a major and minor close pair respectively. However, for pairs with a lower-mass primary galaxy, $M^\star \leqslant 10^{9.5}M_\odot$, and for the same probability to merge, the threshold in relative velocity is smaller: $\Delta r^P \leqslant 25$ kpc and $\Delta v^P \leqslant 75$ km s^{-1}. Similar results are obtained for the other redshift snapshots, showing that these conditions have almost no dependance with redshift.

To summarize, the stellar mass of the galaxies involved in the pair will mostly have an impact on the rest-frame relative velocity selection criterion. Massive primary galaxies with their strong gravitational pull can retain satellite galaxies with larger relative velocity difference than lower-mass galaxies.

3.2.3. New criteria for pair selection and weighting scheme

From this analysis we propose new criteria for the selection of galaxy close pairs. We define a close pair as two galaxies within a limited projected separation distance in the sky plane and a rest-frame relative velocity of:

$$\begin{cases} 5 \leqslant \Delta r^P \leqslant 50 \text{ kpc} \text{ and } \Delta v^P \leqslant 300 \text{ km s}^{-1} \\ \text{or } 50 \leqslant \Delta r^P \leqslant 100 \text{ kpc} \text{ and } \Delta v^P \leqslant 100 \text{ km s}^{-1} \end{cases}$$

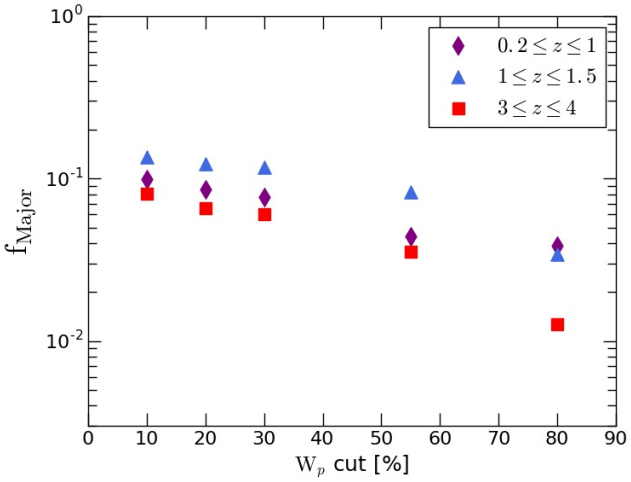

Fig. 5: Major merger fraction of close pairs selected in MUSE deep observations over the Hubble Ultra Deep Field (so-called UDF-mosaic) for three redshift bins and five values of merging probability threshold (10, 20, 30, 55, and 80%). The choice of a 30% threshold is motivated by the convergence of the merger fraction below this value.

With these parameters, all close pairs with at least 30% of chance of merging are considered, regardless of the mass ratio or stellar mass of the primary galaxy (see red boxes in lower left panel of Fig. 2) . We choose this threshold of 30% as the fraction of mergers converge below this value. This is illustrated in Fig. 5 where we show the major merger fraction computed in the Hubble Ultra Deep Field for three redshift intervals as a function of five different values of merging probability threshold (10, 20, 30, 55, and 80%). Adding pairs with a probability to merge below the 30% threshold would increase the major merger fraction by a few percent only.

The limit $\Delta r^P_{min} \sim 5$ kpc comes from the limitation in spatial resolution of the MUSE data (see Ventou et al. 2017). Indeed, two galaxies within an angular separation of $\theta \leqslant 0.7''$ which corresponds approximately to $\Delta r^P_{min} \sim 5$ h^{-1}kpc at $z \sim 1$, are nearly impossible to distinguish and would appear as a blended object. Further in the analysis, a corrective term is applied to the expression of the merger fraction to account for the missing pairs. We note that these values are similar to those applied by Scudder et al. (2012) and Patton et al. (2013) in their SDSS-based study of the SFR enhancement in pairs of interacting galaxies.

Based on a least-squares fit to the simulated datasets shown in Fig. 2(b) with a non-linear regression, a new weighting scheme can be applied to the merger fraction which takes into account the probability of the galaxy pair to merge as a function of their relative velocity (in kpc) and projected separation (in km s^{-1}) distances (see Appendix A for more details):

$$W(\Delta r^P, \Delta v^P) = 1.407 \pm 0.035 \; e^{-0.017 \pm 0.0004 \; \Delta r^P \; - 0.005 \pm 0.0001 \; \Delta v^P} \quad (3)$$

If we further divide the sample by the stellar mass of the primary galaxy (see Fig. 4), we propose the following two equations for galaxies with a stellar mass above or below $M^\star = 10^{9.5} M_\odot$ respectively:

$$W(\Delta r^P, \Delta v^P) = \begin{cases} 1.617 \pm 0.064 \; e^{-0.016 \pm 0.0006 \; \Delta r^P \; - 0.008 \pm 0.0003 \; \Delta v^P} \\ 1.375 \pm 0.052 \; e^{-0.018 \pm 0.0005 \; \Delta r^P \; - 0.004 \pm 0.0002 \; \Delta v^P} \end{cases} \quad (4)$$

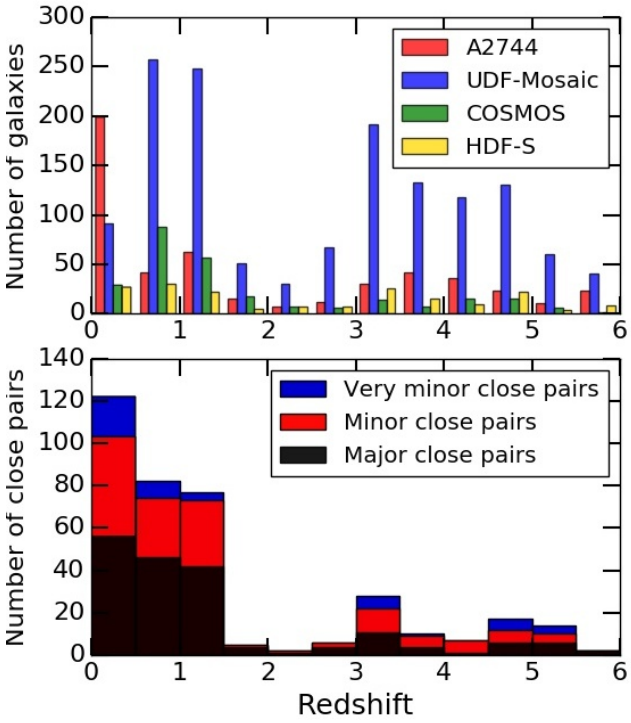

Fig. 6: *Top*: The spectroscopic redshift distribution of the parent galaxies in the four MUSE data cubes used in this analysis. *Bottom*: Redshift histogram of the close pairs sample showing the contribution of major (black), minor (red), and very minor close pairs (blue).

This new corrective term allows us to give an estimate of the close pair fraction that reflects more accurately the true merger fraction. The following sections present the application of these new selection criteria and weighting scheme on MUSE deep fields in order to derive the evolution of the major and minor galaxy pair fractions over the last 13 Gyr.

4. Data description

The analysis presented in this paper is based on MUSE (Multi Unit Spectroscopic Explorer, Bacon et al. 2010) observations obtained during the last commissioning run of the instrument in August 2014 and 1.5 years of MUSE Guaranteed Time Observations (GTO), from September 2014 to February 2016.

4.1. Parent sample

For this analysis, a large spectroscopic sample of 2483 galaxies is constructed from MUSE deep observations over four different regions of the southern sky, the Hubble Deep Field South (HDF-S; Bacon et al., 2015), the Hubble Ultra Deep Field (HUDF; Bacon et al., 2017), the lensing cluster Abell 2744 (Mahler et al., 2018), and the galaxy group COSMOS-Gr30 at $z \sim 0.7$ (Epinat et al., 2018). The two first MUSE datasets in HDFS and HUDF are already described in Ventou et al. (2017). In the following subsections, we describe the additional MUSE datasets in Abell 2744 and COSMOS-Gr30.

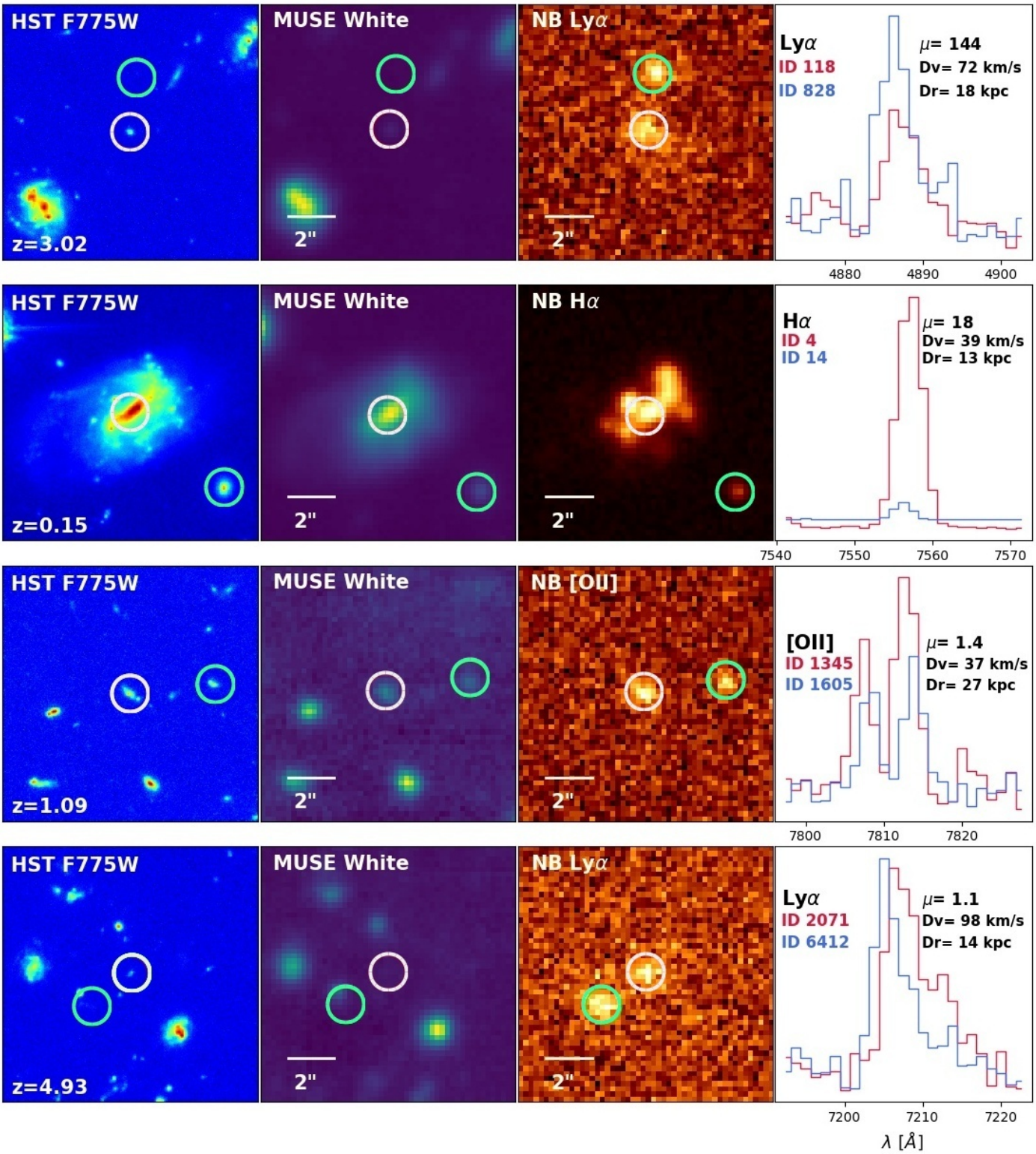

Fig. 7: Examples of close pairs of galaxies, at different redshifts and with various mass ratios in the UDF-Mosaic field. *From left to right*: HST image in the F775W filter with the redshift of the primary galaxy, MUSE reconstructed white light image, narrow-band image of one of the brightest emission lines of the pair, and the zoomed spectra of the two galaxies around this line (red for the primary galaxy and blue for its companion) with the labeled MUSE ID, mass ratio, relative velocity difference and projected separation distance. Images are 10″ in linear size and centered around the primary galaxy, i.e. the most massive one, circled in white. The green circle indicates the location of its companion. The first two close pairs correspond to the very minor and minor regimes, the last two are major close pairs at low and high redshift.

4.1.1. Abell 2744

Abell 2744 was observed as part of a GTO program aimed at probing the highly magnified regions of massive lensing clusters (PI: J. Richard). The resulting data cube is a 2′ × 2′ mo-

saic centered around $\alpha = 00h14'20.95$" and $\delta = -30°23'53.88$" with about 10h exposure time. Instrumental setup was similar to HUDF observations. Sources were extracted using three complementary detection methods described in Mahler et al. (2018): spectral extraction at the location of known faint sources in the deep Hubble Frontier Field images, emission line detection based on narrow-band filtering in the MUSE data cube using the software MUSELET[1], and finally manual extraction for sources found by visual inspection and not detected with the previous methods. Overall the spectroscopic redshift of 514 sources was measured, with 414 new identifications (Mahler et al., 2018). For this study, we kept one galaxy only for all the confirmed multiple-images systems. The source positions were corrected for lensing effects and estimated in the source plane (Mahler et al., 2018). Howerver, lensing does not affect the redshift and velocity differences measured in the MUSE data.

4.1.2. COSMOS-Gr30

The deep observations of the galaxy group COSMOS-Gr30 at $z \sim 0.7$ are part of a large GTO program that aims to study how the environment affect galaxy evolution over the past 8 Gyr (PI: T. Contini). A single field of 1×1 arcmin^2 and 10h exposure time was obtained, comprising 40 exposures of 900 seconds. The data cube presents the same spatial and spectral sampling characteristics as for the HUDF and Abell 2744. The seeing was estimated to be around 0.68″ at 7000 Å (Epinat et al., 2018). As for the UDF-Mosaic, sources were selected from the COSMOS2015 photometric catalogue (Laigle et al., 2016), complemented by emission-line detection using ORIGIN software (Bacon et al. 2017). A customized version of the redshift finding code MARZ (Hinton et al., 2016) was used to assess the spectroscopic redshift of the sources. The final catalog consists of 208 spectroscopic redshifts.

4.1.3. Redshift and stellar masses

By combining the catalogs associated with each of the four surveys, we build a parent sample of 2483 galaxies with spectroscopic redshift up to $z \sim 6$. Each redshift measurement is assigned a confidence level based mostly on the detected spectral features (see details in Inami et al. 2017). Confidence 3 and 2 are secure redshifts based on several spectral features, such as strong emission lines, or a clearly identified single one (mainly [O II] $\lambda\lambda$3726,3729 and Lyα), or strong absorption features. Confidence 1 is a tentative redshift with uncertainties on the nature of the feature from the line profile, most of the time Lyα versus [O II] $\lambda\lambda$3726,3729. This redshift confidence is later taken into account in the merger fraction estimate, a weight is thus applied to distinguish between secure galaxy pairs involving two galaxies with a confidence level of 3 or 2, and unsecure ones involving at least one galaxy with confidence 1. As in previous paper (Ventou et al. 2017), we used the empirical relation between the velocity shift of the Lyα emission peak relative to the systemic velocity and the FWHM of the line (Verhamme et al. 2018) to compute the systemic redshift of all the Lyα emitters.

Stellar masses were derived using FAST (Fitting and Assessment of Synthetic Templates), a code that fits stellar population synthesis templates to broad-band photometry and spectra (Kriek et al. 2009). We assume for all four fields a Chabrier (2003) initial mass function, an exponentially declining star formation history and the dust attenuation law from Calzetti et al. (2000). As described in Ventou et al. (2017), extended UV-to-NIR ACS and WFC3 photometric measurements (Rafelski et al. 2015) were used for the UDF-Mosaic, with the addition of mid-infrared IRAC photometry from the *GOODS Re-ionization Era wide-Area Treasury from Spitzer* program to better constrain the stellar mass of high-redshift galaxies ($z \geqslant 3$). The optical-NIR photometric bands used for the HDF-S are also listed in Ventou et al. (2017). As described in Epinat et al. (2018), the photometric measurements for COSMOS-Gr30 come from the extensive dataset available in the COSMOS field (Scoville et al. 2007) and summarized in the COSMOS2015 catalog (Laigle et al., 2016). It includes infrared and far-infrared photometry from Spitzer and Herschel, radio data from the VLA, UV-to-infrared from HST-ACS, SDSS, VIRCAM/VISTA camera, WIRCam/CFHT and MegaCam/CFHT camera as well as HSC/Subaru *Y* band and SuprimeCam/Subaru, near and far ultraviolet measurements from the Galaxy Evolution Explorer, Chandra and XMM observations for X-ray data (see Epinat et al., 2018 for details). For the lensing cluster A2744, seven HST bands (ACS; F435W, F606W, F814W and WFC3; F105W, F125W, F140W, F160W) were used. A median boxcar subtraction was applied to these images in order to better estimate the stellar masses of faint background galaxies, which can be contaminated by the light of the cluster galaxies. Results are all corrected for lensing magnification effects.

The final parent galaxy sample assembled from the four MUSE deep surveys probes a large domain in stellar mass, from $\sim 10^7 - 10^{12}$ M$_\odot$, distributed over a large redshift range $0.2 \leqslant z \leqslant 6.8$. Note that no stellar mass has been derived for the few Lyα emitters in the UDF-Mosaic which are not detected in deep HST images (see Inami et al. 2017). These galaxies are not considered further in the analysis.

Figure 6 (*top*) shows the spectroscopic redshift distribution of the parent galaxy sample for all individual fields. Peaks in the histograms account for particular structures detected in each data cube. In the UDF-Mosaic an over-dense structure is detected around $z \approx 1$ (see Inami et al. 2017), the peak at $z \approx 0.3$ in A2744 corresponds to the galaxy cluster, overall the redshifts of 156 cluster members were measured from MUSE observations over this region (Mahler et al., 2018). The green peak around $z \approx 0.7$ represents the galaxy group Gr30 in COSMOS. The dearth of spectroscopic redshifts between $1.5 \leqslant z \leqslant 2.8$ is expected, as it covers the well known "redshift desert" interval for optical instrument such as MUSE. Due to the absence of bright emission lines in this range (in between Lyα and [O II] $\lambda\lambda$3726,3729), the redshifts are measured mainly on absorption features or C III] $\lambda\lambda$1907,1909 emission-line doublet.

4.2. Close pair sample

Applying the criteria defined in section 3.2.3 to the MUSE data set, a total of 372 close pairs of galaxies were identified. About 44% of them were detected in the UDF-Mosaic, 40% in A2744, 9% in COSMOS-Gr30, and 7% in HDF-S. As mentioned in sect. 4.1.3, we do not include in this sample the few $z > 3$ pairs detected in the UDF-Mosaic ($\sim$ 1.8% of the total pair sample) of one or two Lyα emitters without a HST counterpart, and thus without any stellar mass estimate.

The mass ratio, defined as the ratio between the stellar mass of the companion and that of the primary galaxies, is used as a proxy to divide this sample into major mergers, with a mass ratio of 1:1−1:6 as chosen in Ventou et al. (2017), minor mergers (1:6−1:100), and very minor mergers with a mass ratio lower

[1] MUSELET is an analysis software released by the consortium as part of the MPDAF suite http://mpdaf.readthedocs.io/en/latest/muselet.html

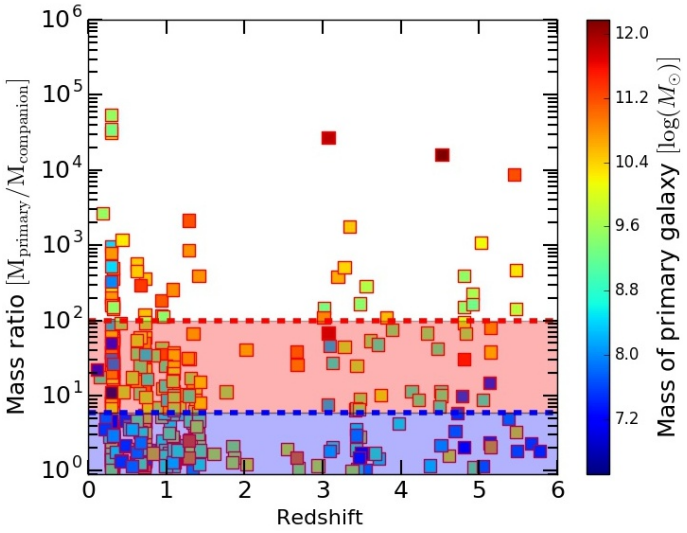

Fig. 8: Stellar mass ratio and redshift distribution of the whole close pairs sample from the combined analysis of the four MUSE deep fields. Symbols are color-coded with respect to the primary galaxy's stellar mass, ie. the most massive one in the pair. The dashed lines indicate the mass ratio (primary over companion galaxy) limits chosen to distinguish major close pairs (limit of 6, blue dashed line and colored area) from minor (between a mass ratio limit of 6 and 100, red dashed line and colored area) and very minor ones (mass ratio greater than 100).

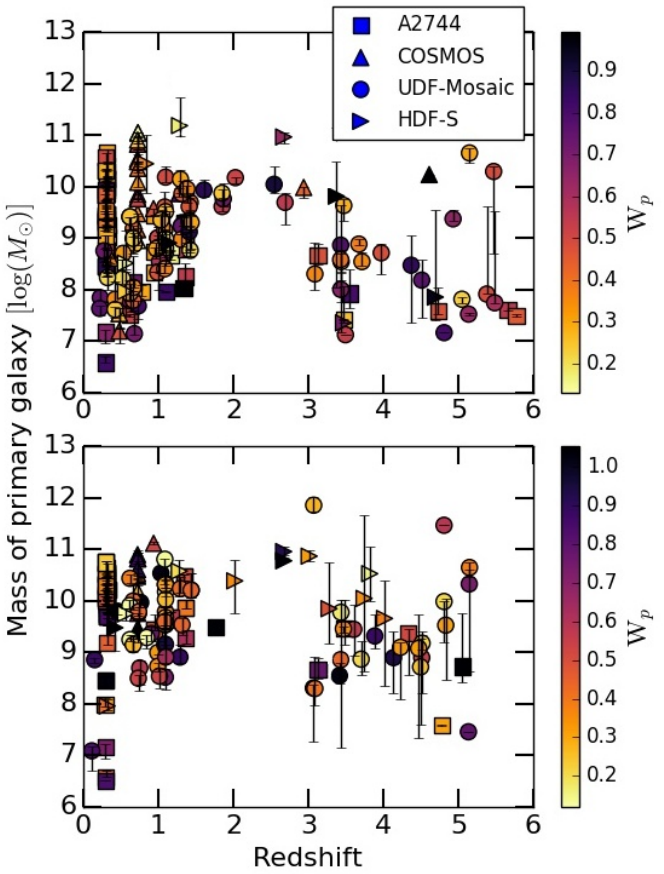

Fig. 9: Stellar mass of the primary galaxy as a function of redshift for our major (*top*) and minor (*bottom*) close pair samples. Right pointing triangles correspond to close pairs in the HDF-S, other triangles to close pairs in the COSMOS-Gr30 field, squares are pairs from A2744, and circles from the UDF-Mosaic. Symbols are color-coded with respect to the weight, W_p described in section 3.2.3, used for the computation of merger fractions. Darker pairs have a higher probability to merger by $z = 0$ and will thus have a higher contribution on the estimated merger fraction. Except in the redshift "desert" ($z \sim 1.5 - 2.8$), we have a fairly good stellar mass completeness level for major close pairs down to a primary galaxy stellar mass of $\approx 10^7 M_\odot$. However, for the minor close pairs sample, a lower mass limit of $10^9 M_\odot$ must be applied to keep a reasonable level of completeness for the merger fraction estimates.

than 1:100. In this last regime the primary galaxy is so much more massive than its companion that it is getting closer to the regime of smooth gas accretion than to a galaxy merger. The secondary galaxy is completely stripped and absorbed by the massive one.

Within our sample, we thus identify a total of 183 major close pairs, 142 minor and 47 very minor close pairs, distributed over a broad range of redshift $0.2 \leqslant z \leqslant 6$ (see Fig. 6, bottom). As stated before, the peaks around $z \approx 0.3$ and $z \approx 0.7$ in the redshift distributions are due to the lensing cluster and galaxy group respectively. More than 30(32) major(minor) close pairs are detected at high redshift $z \geqslant 3$. Examples of close pairs in each mass ratio regimes are displayed in Fig. 7. The first two raws correspond to a very minor and minor pair at $z \sim 3$ and $z \sim 0.15$ respectively. The last two rows are both major close pairs at $z \sim 1$ and $z \sim 5$.

Figures 8 and 9 reveal the mass ratio and stellar mass domain of our samples. With deep enough MUSE observations, we manage to probe galaxy pairs with very low mass ratios (down to $1{:}10^4$, see Fig. 8) at any redshift, except for the "redshift desert" interval. Pairs with a mass ratio lower than 1:100 are considered as very minor, close to the smooth accretion regime. Likewise the stellar masses range of the primary galaxies extend over 4 dex, from $\sim 10^7$ to $10^{11} M_\odot$ (see Fig. 9). Within this mass range, the major close pair sample has a good level of stellar mass completeness, as already discussed in Ventou et al. (2017). However, due to the extended mass ratio range down to 1:100 considered for the minor close pairs, the low-mass threshold must be reduced to keep a fairly good mass completeness for this regime. Thereby, for the minor close pair sample, we adopt a low-mass cut of $10^9 M_\odot$. This effect is even more dramatic for very minor pairs. In this regime, the mass completeness is too poor for the sample to be useful. We thus focus the rest of the analysis on the major and minor samples, within their corresponding mass ranges, and estimate the associated fractions.

In Fig. 9, the weighting scheme described in equation 3 is also shown, differentiating between pairs with a high probability to merge (darkest symbols) and the others, which will have a lower contribution to the merger fractions estimated in the next section.

5. Evolution of the galaxy major and minor merger fraction up to $z \approx 6$ in MUSE deep fields

In order to probe the evolution of the galaxy merger fraction along cosmic time, the redshift range is divided into different bins containing enough pairs to be statistically significant. We thus follow the division adopted in Ventou et al. (2017), with the lowest redshift bin corresponding to the interval $0.2 \leqslant$

$z_r < 1$, then $1 \leqslant z_r < 1.5$ which end up with the loss of the [O II] $\lambda\lambda$3726,3729 emission-line in the MUSE spectral range, following the "redshift desert" domain $1.5 \leqslant z_r < 2.8$ and two more bins $2.8 \leqslant z_r < 4$ and $4 \leqslant z_r \leqslant 6$ for the highest redshift close pairs.

5.1. Major merger fraction

To obtain a merger fraction from a close pair count study, for each redshift bin z_r, the number of galaxy pairs, N_p, must be divided by the number of primary galaxies in the parent sample, N_g, and corrected from all selection effects. Indeed, observations are limited in volume and luminosity and it must be taken into account and corrected in the fraction estimates (e.g. de Ravel et al. 2009).

The expression from Ventou et al. (2017) is used to define the major merger fraction with the addition of the new weighting scheme described in sect. 3.2.3:

$$f_{\rm M}(z_r) = C_1 \frac{\sum_{K=1}^{N_p} \frac{\omega_z^{K_1}}{C_2(z_r)} \frac{\omega_z^{K_2}}{C_2(z_r)} W(\Delta r^P, \Delta v^P)\, \omega_A^K}{\sum_{i=1}^{N_g} \frac{\omega_z^i}{C_2(z_r)}} \quad (5)$$

where C_1 accounts for the missing companions due to our limit in spatial resolution at small radii (sect. 3.2.3), and is defined as $C_1 = \frac{(r_{max}^P)^2}{(r_{max}^P)^2 - (r_{min}^P)^2}$. The redshift confidence weight, ω_z, represents the confidence level associated to the spectroscopic redshift measurement:

$$\omega_z = \begin{cases} 1 & \text{if } z_{conf} = 3 \text{ or } 2, \text{ for secure redshifts} \\ 0.6 & \text{if } z_{conf} = 1, \text{ for unsecure redshifts} \end{cases}$$

The area weight takes into account the missing companion galaxy for primary galaxies on the border of the MUSE field:

$$\omega_A = \frac{r_{max}^P}{(r_{max}^P - r_{\rm MUSE})}$$

where r_{max}^P is the radius corresponding to the projected distance limit, and $r_{\rm MUSE}$ the radius available in MUSE observations. $W(\Delta r^P, \Delta v^P)$, defined in equation 4, is the new weight corresponding to the probability of the close pair to merge by $z = 0$ based on their relative velocity and projected separation distance. The parameter $C_2(z_r)$ corrects for redshift incompleteness. To compute this value we use the same method as described in Ventou et al. (2017) for the UDF-Mosaic and HDF-S and applied to the two other fields. Assuming that photometric redshift measurements are uniformly representative of the real redshift distribution, the number of spectroscopic redshifts is divided by the number of photometric redshifts for each bin. Photometric redshift measurements for the UDF-Mosaic field are estimated in Brinchmann et al. (2017) and reported in the COSMOS2015 catalog (Laigle et al., 2016) for COSMOS-Gr30 field. Photometric redshifts for A2744 were estimated using the spectral energy distribution (SED) fitting code HyperZ (Bolzonella at al. 2000), based on photometry from the publicly available Hubble Frontier Field images of A2744 in 7 filters (ACS; F435W, F606W, F814W and WFC3; F105W, F125W, F140W, F160W; Lotz et al. 2017). A constant star formation history, a Chabrier (2003) initial mass function, a Calzetti et al. (2000) extinction law and templates from Bruzual & Charlot (2003) stellar library were used as input parameters.

Finally, uncertainties due to the cosmic variance and statistical errors on the estimated fractions are taken into account in the error budget on the merger fractions. The computed total cosmic variance for the four fields follows the recipes of Moster et al. (2011). A purely statistical error was derived as a confidence interval from a Bayesian approach (see e.g. Cameron 2011).

Compared to Ventou et al. (2017), we improve our results with smaller error bars due to the increased number of galaxies in the parent and close pair samples thanks to the addition of two new observed fields A2744 and COSMOS-Gr30, as well as the new selection criteria. At first glance, it could be surprising to find similar pair fractions compared with our previous study. Indeed, in Ventou et al. (2017) we made the (strong) assumption that all the selected close pairs will merge by $z = 0$ and thus we did not apply any weight for those pairs in the fraction estimates. With our new selection criteria, we indeed found a lower probability (between $\sim 30\%$ and 80%) for the pairs to merge and applied a corresponding weight in the fraction estimate. However, the expected decrease of the pair fractions due to the lower probability of merging is compensated by the higher number of selected close pairs, even with a probability to merge as low as 30%.

Figure 10 shows the cosmic evolution of the major merger fraction up to $z \approx 6$, for a variety of primary galaxy stellar mass ranges. Results are summarized in Table 1 for each redshift bin and mass range.

We first estimate the fractions for each field individually as well as for the combined data set for major close pairs with a stellar mass primary galaxy in the range $10^7 - 10^{11} {\rm M}_\odot$ (Fig. 10, left panel). Although the measurements are in good agreement within the error bars for the majority of the redshift bins, the impact of the environment on these estimates is clearly seen for the lowest redshift bin, $0.2 \leqslant z_r < 1$. Due to the presence of the galaxy cluster Abell 2744 at $z \approx 0.3$ and the galaxy group in COSMOS area at $z \approx 0.7$, we observe an enhancement of the close pair counts and hence the merger fraction for these two fields compared to the UDF-Mosaic estimate. Whereas we measure a major merger fraction of 21% in A2744 and 25% in COSMOS Gr30, which is about twice the value estimated in the UDF-Mosaic for this redshift bin, these fractions drop to 5% and 9% respectively if we remove the members belonging to the galaxy cluster and to the galaxy group.

In the subsequent analysis and discussion of the merger fraction, we will restrict the samples of close pairs in the low-redshift bins by excluding those belonging to these massive structures. Indeed galaxy clusters and groups provide high-density environments where near neighbors are common. However, the high velocity dispersion of low-z virialized clusters and groups ($\sim 500 - 1000$ km s^{-1}) are not conducive to active merging among galaxies (see Mihos 2004 for a review). Indeed, measurements of the merger rate in low-redshift galaxy clusters do not generally exceed $2 - 3\%$ (Adams et al. 2012; Cordero et al. 2016). Nonetheless, recent studies of high-redshift proto-clusters have shown evidence of enhanced merger rates, suggesting that merging in dense environments may play an important role in galaxy mass assembly in the early universe (Lotz et al. 2013; Hine et al. 2016).

Assuming a constant stellar mass separation of $10^{9.5} {\rm M}_\odot$ for the primary galaxy, we push this analysis further and split the sample into two mass bins. Figure 10 (right panel) shows the resulting evolution of the major merger fraction for massive and low-mass galaxies separately, using different merging probabilities $W(\Delta r^P, \Delta v^P)$ computed from equations 4.

We observe an increase of the fraction for the high-mass sample up to 25% at $z \approx 2$ where it reaches its maximum, followed by a decrease of the fraction down to 4-5% between

Table 1: Major merger fractions up to $z \approx 6$ from MUSE deep observations for different redshift and stellar mass intervals. Cols. (1) and (2): Range of the redshift bin and its associated mean redshift for the close pairs sample. Col. (3): Median value of stellar mass for the pair sample. Cols. (4) and (5): Number of pairs, N_p, and galaxies, N_g. Col (6): Major merger fraction estimates from the combined analysis of the MUSE data, corresponding to the stellar mass range indicated for the primary galaxy. The results given in this table correspond to the fractions estimated without taking into account the members of the cluster and galaxy group for the lowest redshift bin.

z_r	$\overline{z_r}$	$\overline{M^\star}$	N_p	N_g	f_{MM}
-	-	[log($M_\odot$)]	-	-	-
(1)	(2)	(3)	(4)	(5)	(6)
		$f_{\rm Major} : 7 \leqslant \log(M_{primary}) \leqslant 11$			
$0.2 \leqslant z < 1$	0.56	9.63	98	626	$0.078^{+0.039}_{-0.020}$
$1 \leqslant z < 1.5$	1.26	9.41	43	352	$0.127^{+0.079}_{-0.047}$
$1.5 \leqslant z < 2.8$	2.07	9.90	7	141	$0.172^{+0.111}_{-0.051}$
$2.8 \leqslant z < 4$	3.46	8.57	13	332	$0.081^{+0.053}_{-0.032}$
$4 \leqslant z \leqslant 6$	5.01	7.72	14	365	$0.075^{+0.068}_{-0.044}$
		$f_{\rm Major} : 7 \leqslant \log(M_{primary}) < 9.5$			
$0.2 \leqslant z < 1$	0.53	8.55	63	459	$0.102^{+0.038}_{-0.026}$
$1 \leqslant z \leqslant 1.5$	1.25	8.83	30	246	$0.131^{+0.079}_{-0.047}$
$3 \leqslant z < 4$	3.47	8.23	11	265	$0.090^{+0.054}_{-0.034}$
$4 \leqslant z \leqslant 6$	5.03	7.54	10	272	$0.084^{+0.071}_{-0.046}$
		$f_{\rm Major} : 9.5 \leqslant \log(M_{primary}) \leqslant 11$			
$0.2 \leqslant z < 1$	0.55	10.20	35	152	$0.023^{+0.027}_{-0.016}$
$1 \leqslant z < 1.5$	1.27	9.73	13	98	$0.172^{+0.083}_{-0.051}$
$1.5 \leqslant z < 2.8$	2.12	9.90	7	72	$0.255^{+0.118}_{-0.050}$
$2.8 \leqslant z < 4$	3.49	9.63	2	70	$0.039^{+0.045}_{-0.024}$
$4 \leqslant z \leqslant 6$	4.93	10.01	4	81	$0.052^{+0.062}_{-0.038}$
		$f_{\rm Major} : 7 \leqslant \log(M_{primary}) < M_{median}(z_r) \leqslant 11$			
$0.2 \leqslant z < 1$	0.48	7.92	31	284	$0.088^{+0.039}_{-0.020}$
$1 \leqslant z \leqslant 1.5$	1.20	8.47	15	150	$0.064^{+0.073}_{-0.041}$
$3 \leqslant z < 4$	3.45	7.85	5	140	$0.076^{+0.052}_{-0.031}$
$4 \leqslant z \leqslant 6$	5.10	7.48	8	141	$0.106^{+0.077}_{-0.052}$
		$f_{\rm Major} : 7 \leqslant M_{median}(z_r) \leqslant \log(M_{primary}) \leqslant 11$			
$0.2 \leqslant z < 1$	0.60	9.60	67	313	$0.076^{+0.040}_{-0.018}$
$1 \leqslant z < 1.5$	1.29	9.43	28	171	$0.193^{+0.085}_{-0.053}$
$1.5 \leqslant z < 2.8$	2.01	9.87	7	72	$0.260^{+0.119}_{-0.059}$
$2.8 \leqslant z < 4$	3.40	8.68	8	175	$0.081^{+0.053}_{-0.032}$
$4 \leqslant z \leqslant 6$	4.80	9.37	6	197	$0.051^{+0.062}_{-0.038}$

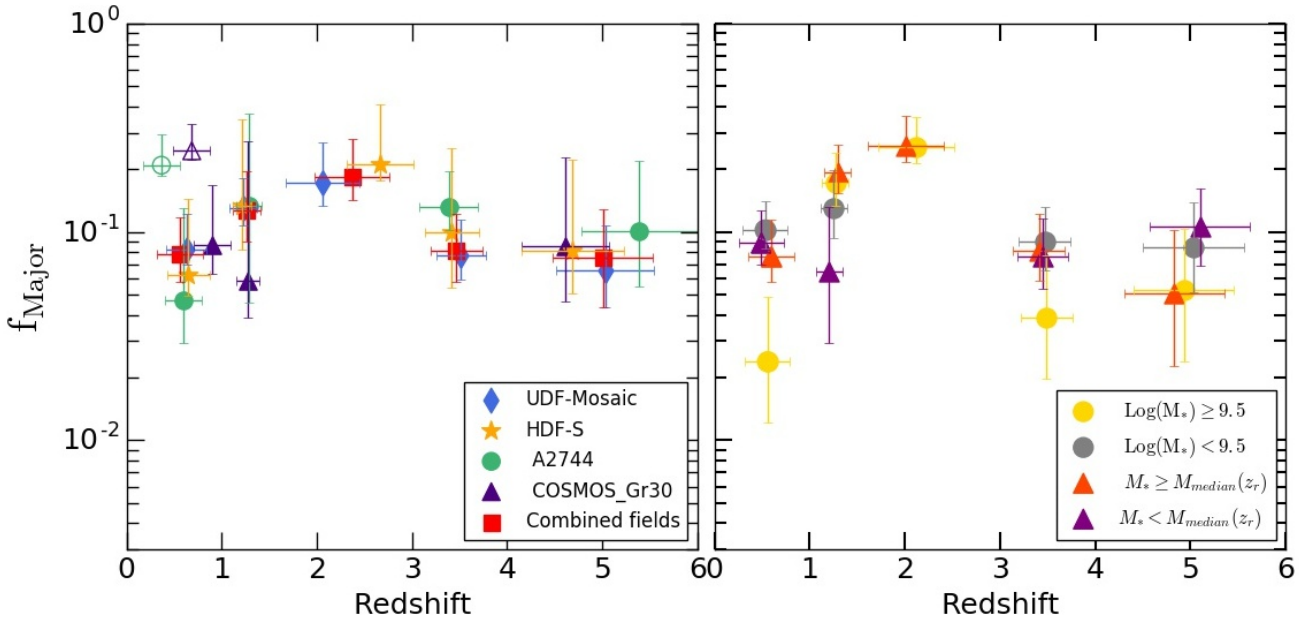

Fig. 10: Evolution of the galaxy major merger fraction up to $z \sim 6$ from MUSE deep fields. *Left*: Blue diamonds, green circles, yellow stars and purple triangles are estimates of the fraction from the UDF-mosaic, Abell 2744, HDF-S and COSMOS-Gr30 regions respectively, whereas red squares correspond to the fraction for the combined analysis of the MUSE data. For the lowest redshift bin, fractions were computed without (filled symbols) and with (open symbols) members of the galaxy cluster A2744 and galaxy group COSMOS-Gr30. *Right*: Evolution of the major merger fraction for two ranges of stellar mass, assuming first a constant separation limit of $M^\star = 10^{9.5} M_\odot$ (grey and yellow circles show the MUSE estimates for low-mass and massive galaxies respectively), then taking the median mass of the parent sample in each redshift bin as the limit (orange and purple triangles). As for the combined fraction of the left panel, the fractions were computed without taking into account the clusters and group members. The median stellar mass estimated in the range $10^7 - 10^{11} M_\odot$ for each redshift intervals are listed in Table 1.

$3 \leqslant z \leqslant 6$. The major merger fraction evolution of the low-mass sample is less pronounced with a nearly flat trend, with an almost constant fraction of 8-13% over the whole redshift range probed by our MUSE sample. Similar results are found if we consider the median mass of the parent sample in each redshift bin as the separation limit, as was done in Ventou et al. (2017) (see Figure 10, right panel).

These evolutionary trends of the major merger fractions are in fairly good agreement with those derived from previous spectroscopic analyses (see Fig. 11), where they claim that beyond $z \geq 2$, the incidence of major mergers remains constant or turn over at early times (Lopez-Sanjuan et al. 2013; Tasca et al. 2014; Ventou et al. 2017). As discussed in Ventou et al. (2017), recent predictions from cosmological simulations, such as HORIZON-AGN (Kaviraj et al. 2015), EAGLE (Qu et al. 2017) and Illustris (Snyder et al. 2017), are also in good agreement with this cosmic evolution of the major merger fraction (see Fig. 11).

5.2. Minor merger fraction

We derive the minor merger fraction, from the number count of galaxy close pairs with stellar mass ratio between 1:6 and 1:100, using the same expression (equation 5) as for the major merger fraction. In order to keep a fairly good mass completeness in our sample, the fractions are estimated for a stellar mass range of $10^9 - 10^{11} M_\odot$ for the primary galaxy.

Figure 12 shows the individual fractions for each field (left panel) and the combined data set (right panel). For A2744 and COSMOS-Gr30 only the estimates for the lowest redshift bins are shown as we are not statistically robust enough for these two fields in higher redshift intervals. For the merger fraction estimated from the combined MUSE fields, we excluded in the computations minor pairs belonging to the cluster A2744 and to the group COSMOS-Gr30.

The minor merger fraction shows little evolution between $0.2 \leqslant z \leqslant 1.5$ with a roughly constant fraction of 20%. Beyond $z \approx 3$, we observe a slight decrease of the fraction down to $8 - 13\%$ in this high redshift range. Fraction estimates for the combined MUSE data set are listed in Table 2.

An attempt is made to separate the minor merger sample into two stellar mass ranges, as was done for the major close pair in section 5.1. We take the median stellar mass in the range $10^9 - 10^{11} M_\odot$ of the parent sample reported in Table 2 as the separation limit. For statistical reasons it is only computed for the two first redshift bins. Thus for massive primary galaxy in the range $10 \leq \log(M^\star) \leq 11$, the minor merger fraction is roughly constant around 18% at $z \sim 0.2 - 1.5$ and around $6 - 9\%$ for the low-mass sample, i.e. with $9 \leq \log(M^\star) < 10$.

Comparison to the few previous estimates of the minor merger fraction from spectroscopic pair counts are made in Fig. 12 (right panel). Lopez-Sanjuan et al. (2012) computed the minor fraction for a mass ratio range of 1:4-1:10 and a projected separation of $10 \leq r^P \leq 30 h^{-1}$ kpc. They found a fraction around $4.5 - 6\%$ for $z \sim 0.29 - 0.86$. Since their selection criteria on the minor merger sample, i.e. the projected distance and the mass ratio range, are narrower compared to ours, it is not surprising that our estimates of $\sim 20\%$ are higher for the same redshift interval. In Lopez-Sanjuan et al. (2011), a minor merger fraction for bright galaxies within $r^P_{max} \sim 100 h^{-1}$ kpc and a luminosity ratio in the $B-$band of 1:4−1:10 is reported. Their projected separation distance is more similar to this work, and their estimated

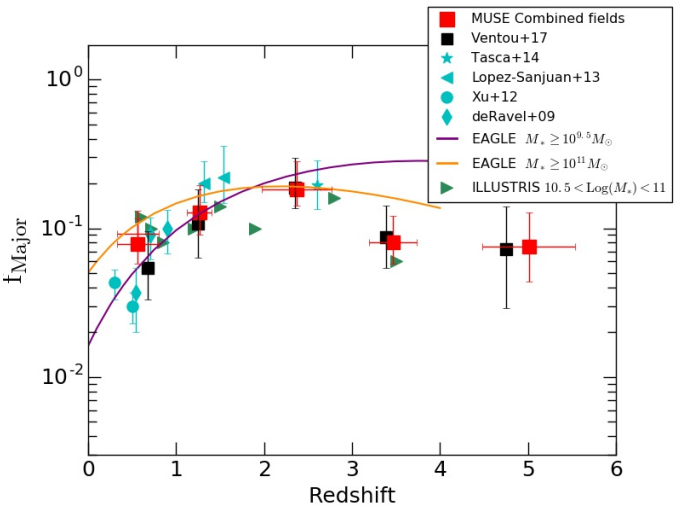

Fig. 11: The major merger fraction compared to previous close pairs count studies and recent simulations. Combined major merger fractions from this work (red squares) are compared to previous estimates from MUSE observations (black squares: Ventou et al. 2017) and other surveys (light blue symbols: de Ravel et al. 2009; Xu et al. 2012; Lopez-Sanjuan et al. 2013; Tasca et al. 2014). The purple and orange solid lines show the predictions from the EAGLE simulations for two different mass ranges (see Qu et al. 2017 for details) whereas the green triangles correspond to the major pair fractions estimated in the Illustris simulation (Snyder et al. 2017)

fraction of 25% and 21% at $z = 0.5$ and $z = 0.8$ respectively are in good agreement with our results.

A comparison of our minor merger fraction with recent cosmological simulations is not straightforward as the latter usually focus on the major merger fraction only and/or use different mass ratio limits to discriminate between major and minor mergers. However, we found that on average the minor merger fraction is higher than the major one by a factor of ~ 4, in relative good agreement with the HORIZON-AGN simulations (Kaviraj et al 2015) which predict a factor of $2.5 - 3$ between minor and major merger fractions. The difference between these two values can be explained by the different mass ratio limits to separate minor mergers from major ones.

6. Summary and conclusion

Using the Illustris cosmological simulation project, we investigated the relation between the velocity-distance relative separation of galaxies in a close pair and the probability that these galaxies will merge by $z = 0$. We propose a new set of selection criteria for galaxy close pair counts, along with a new weighing scheme to be applied to the merger fraction. This takes into account the probability of merging for the pair derived from their relative velocity and projected separation distance.

We found that combining constraints on the projected separation distance in the sky plane and the rest-frame relative velocity of $\Delta r^P \leqslant 50$ kpc with $\Delta v^P \leqslant 300$ km s^{-1} and $50 \leqslant \Delta r^P \leqslant 100$ kpc with $\Delta v^P \leqslant 100$ km s^{-1} allows the selection of all close pairs with at least 30% of probability to merge.

Deep MUSE observations in the HUDF, HDF-S, A2744 and COSMOS-Gr30 fields are used to construct a large spectroscopic sample of 2483 galaxies. Applying the new selection criteria, 372 secure close pairs of galaxies spread over a large redshift range ($0.2 < z < 6$) and stellar masses ($10^7 - 10^{11} M_\odot$) were identified. We use stellar masses derived from SED fitting to distinguish between major, minor and very minor close pairs using their mass ratio as proxy. We end up with a sample of 183 major, 142 minor and 47 very minor close pairs with a respective galaxy mass ratio limit of 1:6, 1:100, and lower than 1:100.

Splitting the redshift domain into five intervals, we probe the evolution of the major and minor merger fractions up to $z \approx 6$. We leave aside the very minor close pairs which are close to the regime of smooth gaz accretion. We observe an increase of the major pair fraction in A2744 and COSMOS-Gr30 with respect to lower-density fields (HUDF and HDF-S) at $z < 1$ due to the presence of the cluster ($z \sim 0.3$) and galaxy group ($z \sim 0.7$) at these redshifts. The pairs found in these two dense structures are then removed for the analysis of the merger fractions.

The sample is further divided into two ranges of stellar masses using a constant separation limit of $10^{9.5} M_\odot$. Estimates for the high-mass galaxy sample show an increase of the major merger fraction up to $z \approx 2 - 3$ reaching a fraction of 21% and a decrease at high redshift dropping to $\sim 5\%$ at $z \approx 6$. The fraction for lower mass primary galaxies ($M_* \leq 10^{9.5} M_\odot$) seems to follow a more constant evolutionary trend along cosmic time. Similar trends are found for a median stellar mass separation.

Although we trace more accurately the merger fraction with the new criteria, the results are similar to our previous analysis over the HUDF and HDF-S fields (Ventou et al. 2017), especially taking into account the error bars. However, error bars are narrower due to the increased number of galaxies in the parent and close pair samples.

The evolution of the minor merger fraction is roughly constant around 20% for $z < 1.5$ and slightly decreases for $z \geq 3$ with a fraction of $8 - 13\%$. The ratio between minor and major merger fractions is in good agreement with the predictions of HORIZON-AGN simulations (Kaviraj et al. 2015), taking into account the different mass ratio limits used to discriminate minor pairs from major ones.

Acknowledgements. This work has been carried out thanks to the support of the ANR FOGHAR (ANR-13-BS05-0010-02), the OCEVU Labex (ANR-11-LABX-0060), and the A*MIDEX project (ANR-11-IDEX-0001-02) funded by the "Investissements d'avenir" French government programme. BE acknowledges financial support from "Programme National de Cosmologie et Galaxies" (PNCG) of CNRS/INSU, France. JB acknowledges support by FCT/MCTES through national funds by this grant UID/FIS/04434/2019 and through the Investigador FCT Contract No. IF/01654/2014/CP1215/CT0003.

References

Adams, S. M., Zaritsky, D., Sand, D. J., et al. 2012, AJ, 144, 128
Anglés-Alcázar, D., Faucher-Giguère, C.-A., Kereš, D., et al. 2017, MNRAS, 470, 4698
Bacon, R., Accardo, M., Adjali, L., et al. 2010, in Proc. SPIE, Vol. 7735, Ground-based and Airborne Instrumentation for Astronomy III, 773508
Bacon, R., Brinchmann, J., Richard, J., et al. 2015, A&A, 575, A75
Bacon, R., Conseil, S., Mary, D., et al. 2017, A&A, 608, A1
Bell, E. F., Zucker, D. B., Belokurov, V., et al. 2008, ApJ, 680, 295
Bluck, A. F. L., Conselice, C. J., Bouwens, R. J., et al. 2009, MNRAS, 394, L51
Bolzonella, M., Miralles, J.-M., & Pelló, R. 2000, A&A, 363, 476
Borlaff, A., Eliche-Moral, M. C., Rodríguez-Pérez, C., et al. 2014, A&A, 570, A103
Bouché, N., Finley, H., Schroetter, I., et al. 2016, ApJ, 820, 121
Bournaud, F., Dekel, A., Teyssier, R., et al. 2011, ApJ, 741, L33
Brinchmann, J., Inami, H., Bacon, R., et al. 2017, A&A, 608, A3
Bruzual, G. & Charlot, S. 2003, MNRAS, 344, 1000
Bundy, K., Fukugita, M., Ellis, R. S., et al. 2009, ApJ, 697, 1369
Caimmi, R. 2008, New A, 13, 314
Calzetti, D., Armus, L., Bohlin, R. C., et al. 2000, ApJ, 533, 682
Cameron, E. 2011a, PASA, 28, 128
Cameron, E. 2011b, PASA, 28, 128

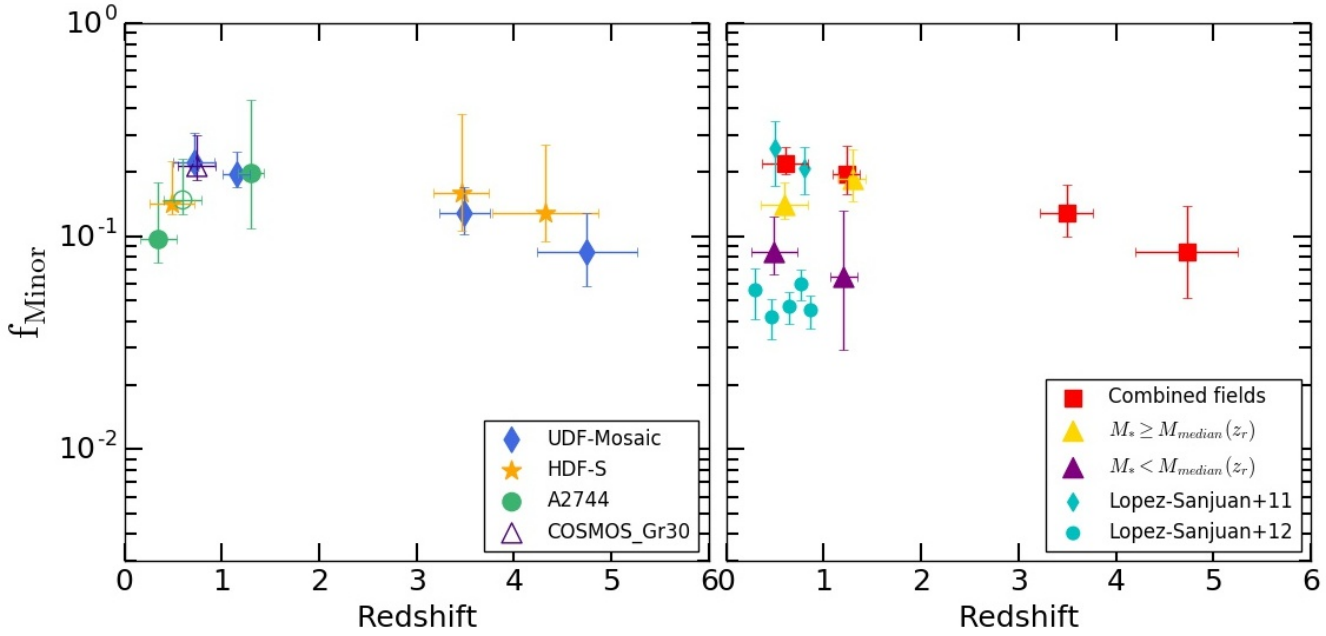

Fig. 12: Evolution of the galaxy minor merger fraction up to $z \sim 6$ from MUSE deep fields, for primary galaxies with a stellar mass range between $\sim 10^9 - 10^{11}$M$_\odot$. *Left*: As in Fig. 10 different symbols show the results from the four regions individually. *Right*: red squares are estimates of the combined minor merger fraction from the whole MUSE data and over the whole stellar mass range $\sim 10^9 - 10^{11}$M$_\odot$. Using the median value of stellar mass in each redshift bin as a separation limit ($\sim 10^{10}$M$_\odot$, see Table 2), the purple and golden triangles correspond to the minor merger fraction for low-mass and massive galaxies respectively. Similar as in Fig. 10 filled and open symbols correspond to the fractions computed without or with galaxy members of the cluster and group for $0.2 \leq z \leq 1$. Cyan points are estimates from previous spectroscopic minor pair counts (Lopez-Sanjuan et al. 2011, 2012).

Casteels, K. R. V., Conselice, C. J., Bamford, S. P., et al. 2014, MNRAS, 445, 1157
Chabrier, G. 2003, PASP, 115, 763
Chiappini, C. 2001, in Revista Mexicana de Astronomia y Astrofisica Conference Series, Vol. 11, Revista Mexicana de Astronomia y Astrofisica Conference Series, 171
Conselice, C. J. 2006, ApJ, 638, 686
Conselice, C. J., Bershady, M. A., Dickinson, M., & Papovich, C. 2003, AJ, 126, 1183
Conselice, C. J., Mortlock, A., Bluck, A. F. L., Grützbauch, R., & Duncan, K. 2013, MNRAS, 430, 1051
Conselice, C. J., Rajgor, S., & Myers, R. 2008, MNRAS, 386, 909
Cordero, J. P., Campusano, L. E., De Propris, R., et al. 2016, ApJ, 817, L6
De Propris, R., Conselice, C. J., Liske, J., et al. 2007, ApJ, 666, 212
de Ravel, L., Le Fèvre, O., Tresse, L., et al. 2009, A&A, 498, 379
Di Matteo, P., Combes, F., Melchior, A.-L., & Semelin, B. 2007, A&A, 468, 61
Epinat, B., Contini, T., Finley, H., et al. 2018, A&A, 609, A40
Förster Schreiber, N. M., Genzel, R., Bouché, N., et al. 2009, ApJ, 706, 1364
Förster Schreiber, N. M., Shapley, A. E., Erb, D. K., et al. 2011, ApJ, 731, 65
Genel, S., Vogelsberger, M., Springel, V., et al. 2014, MNRAS, 445, 175
Heiderman, A., Jogee, S., Marinova, I., et al. 2009, in Astronomical Society of the Pacific Conference Series, Vol. 419, Galaxy Evolution: Emerging Insights and Future Challenges, ed. S. Jogee, I. Marinova, L. Hao, & G. A. Blanc, 257
Hine, N. K., Geach, J. E., Alexander, D. M., et al. 2016, MNRAS, 455, 2363
Hinton, S. R., Davis, T. M., Lidman, C., Glazebrook, K., & Lewis, G. F. 2016, Astronomy and Computing, 15, 61
Inami, H., Bacon, R., Brinchmann, J., et al. 2017, A&A, 608, A2
Jian, H.-Y., Lin, L., & Chiueh, T. 2012, ApJ, 754, 26
Joseph, R. D. & Wright, G. S. 1985, MNRAS, 214, 87
Kampczyk, P., Lilly, S. J., Carollo, C. M., et al. 2007, ApJS, 172, 329
Kaviraj, S. 2014, MNRAS, 437, L41
Kaviraj, S., Devriendt, J., Dubois, Y., et al. 2015, MNRAS, 452, 2845
Kereš, D., Katz, N., Weinberg, D. H., & Davé, R. 2005, MNRAS, 363, 2
Kitzbichler, M. G. & White, S. D. M. 2008, MNRAS, 391, 1489
Kriek, M., van Dokkum, P. G., Labbé, I., et al. 2009, ApJ, 700, 221
Lagos, C. d. P., Stevens, A. R. H., Bower, R. G., et al. 2018, MNRAS, 473, 4956
Laigle, C., McCracken, H. J., Ilbert, O., et al. 2016, ApJS, 224, 24
Le Fèvre, O., Abraham, R., Lilly, S. J., et al. 2000, MNRAS, 311, 565
L'Huillier, B., Combes, F., & Semelin, B. 2012, A&A, 544, A68
Lin, L., Patton, D. R., Koo, D. C., et al. 2008, ApJ, 681, 232
López-Sanjuan, C., Le Fèvre, O., de Ravel, L., et al. 2011, A&A, 530, A20
López-Sanjuan, C., Le Fèvre, O., Ilbert, O., et al. 2012, A&A, 548, A7
López-Sanjuan, C., Le Fèvre, O., Tasca, L. A. M., et al. 2013, A&A, 553, A78
Lotz, J. M., Jonsson, P., Cox, T. J., et al. 2011, ApJ, 742, 103
Lotz, J. M., Koekemoer, A., Coe, D., et al. 2017, ApJ, 837, 97
Lotz, J. M., Papovich, C., Faber, S. M., et al. 2013, ApJ, 773, 154
Mahler, G., Richard, J., Clément, B., et al. 2018, MNRAS, 473, 663
Man, A. W. S., Toft, S., Zirm, A. W., Wuyts, S., & van der Wel, A. 2012, ApJ, 744, 85
Man, A. W. S., Zirm, A. W., & Toft, S. 2016, ApJ, 830, 89
Mantha, K. B., McIntosh, D. H., Brennan, R., et al. 2018, MNRAS, 475, 1549
McLure, R. J., Pearce, H. J., Dunlop, J. S., et al. 2013, MNRAS, 428, 1088
Mihos, J. C. 2004, Clusters of Galaxies: Probes of Cosmological Structure and Galaxy Evolution, 277
Moreno, J., Bluck, A. F. L., Ellison, S. L., et al. 2013, MNRAS, 436, 1765
Moster, B. P., Somerville, R. S., Newman, J. A., & Rix, H.-W. 2011, ApJ, 731, 113
Murali, C., Katz, N., Hernquist, L., Weinberg, D. H., & Davé, R. 2002, ApJ, 571, 1
Naab, T., Johansson, P. H., & Ostriker, J. P. 2009, ApJ, 699, L178
Nelson, D., Pillepich, A., Genel, S., et al. 2015, Astronomy and Computing, 13, 12
Patton, D. R. & Atfield, J. E. 2008, ApJ, 685, 235
Patton, D. R., Carlberg, R. G., Marzke, R. O., et al. 2000, ApJ, 536, 153
Patton, D. R., Torrey, P., Ellison, S. L., Mendel, J. T., & Scudder, J. M. 2013, MNRAS, 433, L59
Perret, V., Renaud, F., Epinat, B., et al. 2014, A&A, 562, A1
Peterson, S. D. 1979, ApJS, 40, 527
Qu, Y., Helly, J. C., Bower, R. G., et al. 2017, MNRAS, 464, 1659
Rafelski, M., Teplitz, H. I., Gardner, J. P., et al. 2015, AJ, 150, 31
Rodriguez-Gomez, V., Genel, S., Vogelsberger, M., et al. 2015, MNRAS, 449, 49
Rodriguez-Gomez, V., Pillepich, A., Sales, L. V., et al. 2016, MNRAS, 458, 2371
Sancisi, R., Fraternali, F., Oosterloo, T., & van der Hulst, T. 2008, A&A Rev., 15, 189
Scoville, N., Aussel, H., Brusa, M., et al. 2007, ApJS, 172, 1
Scudder, J. M., Ellison, S. L., Torrey, P., Patton, D. R., & Mendel, J. T. 2012, MNRAS, 426, 549
Snyder, G. F., Lotz, J. M., Rodriguez-Gomez, V., et al. 2017a, MNRAS, 468, 207

Table 2: Minor merger fractions up to $z \approx 6$ from MUSE deep observations for different redshift and stellar mass intervals. Same columns as in Table1 with Col (6) corresponding to the minor merger fraction estimates from the combined analysis of the MUSE data, associated to the stellar mass range indicated for the primary galaxy. These fractions are estimated without taking into account the members of the galaxy group and cluster.

z_r	$\overline{z_r}$	$\overline{M^\star}$	N_p	N_g	f_{mm}
-	-	[log($M_\odot$)]	-	-	-
(1)	(2)	(3)	(4)	(5)	(6)
		$f_{\rm Minor} : 9 \leqslant \log(M_{primary}) \leqslant 11$			
$0.2 \leqslant z < 1$	0.60	10.00	50	260	$0.199^{+0.053}_{-0.032}$
$1 \leqslant z \leqslant 1.5$	1.23	9.85	23	159	$0.196^{+0.086}_{-0.054}$
$2.8 \leqslant z < 4$	3.49	9.36	7	100	$0.129^{+0.061}_{-0.041}$
$4 \leqslant z \leqslant 6$	4.73	9.48	10	114	$0.084^{+0.071}_{-0.046}$
		$f_{\rm Minor} : 11 \geqslant \log(M_{primary}) \geqslant M_{median}(z_r) \geqslant 9$			
$0.2 \leqslant z < 1$	0.59	10.55	22	68	$0.141^{+0.039}_{-0.019}$
$1 \leqslant z \leqslant 1.5$	1.29	10.37	10	33	$0.184^{+0.084}_{-0.052}$
		$f_{\rm Minor} : 9 \leqslant \log(M_{primary}) < M_{median}(z_r) \leqslant 11$			
$0.2 \leqslant z < 1$	0.49	9.64	28	153	$0.085^{+0.040}_{-0.018}$
$1 \leqslant z \leqslant 1.5$	1.20	9.61	13	96	$0.064^{+0.073}_{-0.041}$

Snyder, G. F., Lotz, J. M., Rodriguez-Gomez, V., et al. 2017b, MNRAS, 468, 207
Springel, V. 2010, MNRAS, 401, 791
Stewart, K. R., Kaufmann, T., Bullock, J. S., et al. 2011, ApJ, 735, L1
Tasca, L. A. M., Le Fèvre, O., López-Sanjuan, C., et al. 2014, A&A, 565, A10
Turner, E. L. 1976, ApJ, 208, 20
van de Voort, F., Schaye, J., Altay, G., & Theuns, T. 2012, MNRAS, 421, 2809
Ventou, E., Contini, T., Bouché, N., et al. 2017, A&A, 608, A9
Verhamme, A., Garel, T., Ventou, E., et al. 2018, MNRAS, 478, L60
Vogelsberger, M., Genel, S., Sijacki, D., et al. 2013, MNRAS, 436, 3031
Vogelsberger, M., Genel, S., Springel, V., et al. 2014, MNRAS, 444, 1518
Williams, R. J., Quadri, R. F., & Franx, M. 2011, ApJ, 738, L25
Xu, C. K., Shupe, D. L., Béthermin, M., et al. 2012, ApJ, 760, 72
Zabl, J., Bouché, N. F., Schroetter, I., et al. 2019, MNRAS, 485, 1961

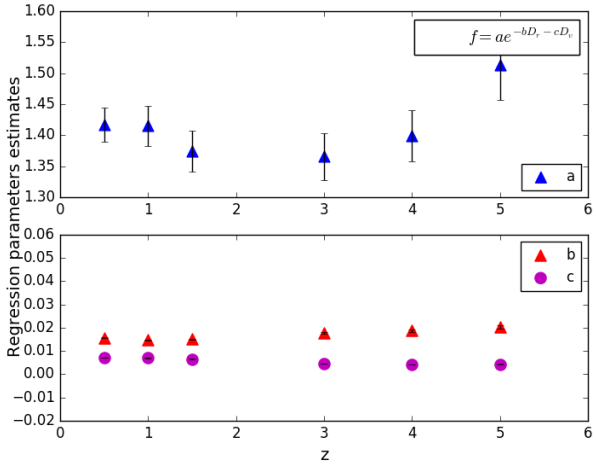

Fig. A.1: Redshift evolution of the regression parameters estimates with the reported approximate function. The error bars represent the computed 1σ errors on the parameters.

Appendix A: A new weighting scheme for the merger fraction

In Fig A.2 we compare, for the six redshift snapshots, the projected velocity-separation distance diagrams obtained in section 3 to the least-squares fits of an exponential function using a non-linear regression to the simulated datasets. The redshift evolution of the parameter estimates is shown in Fig A.1. We decide to use the median of the parameter estimates in the final expression of the probability weight, $W(\Delta r^P, \Delta v^P)$, effective for all redshift (see equation 3), since there is little evolution of the different parameters with redshift.

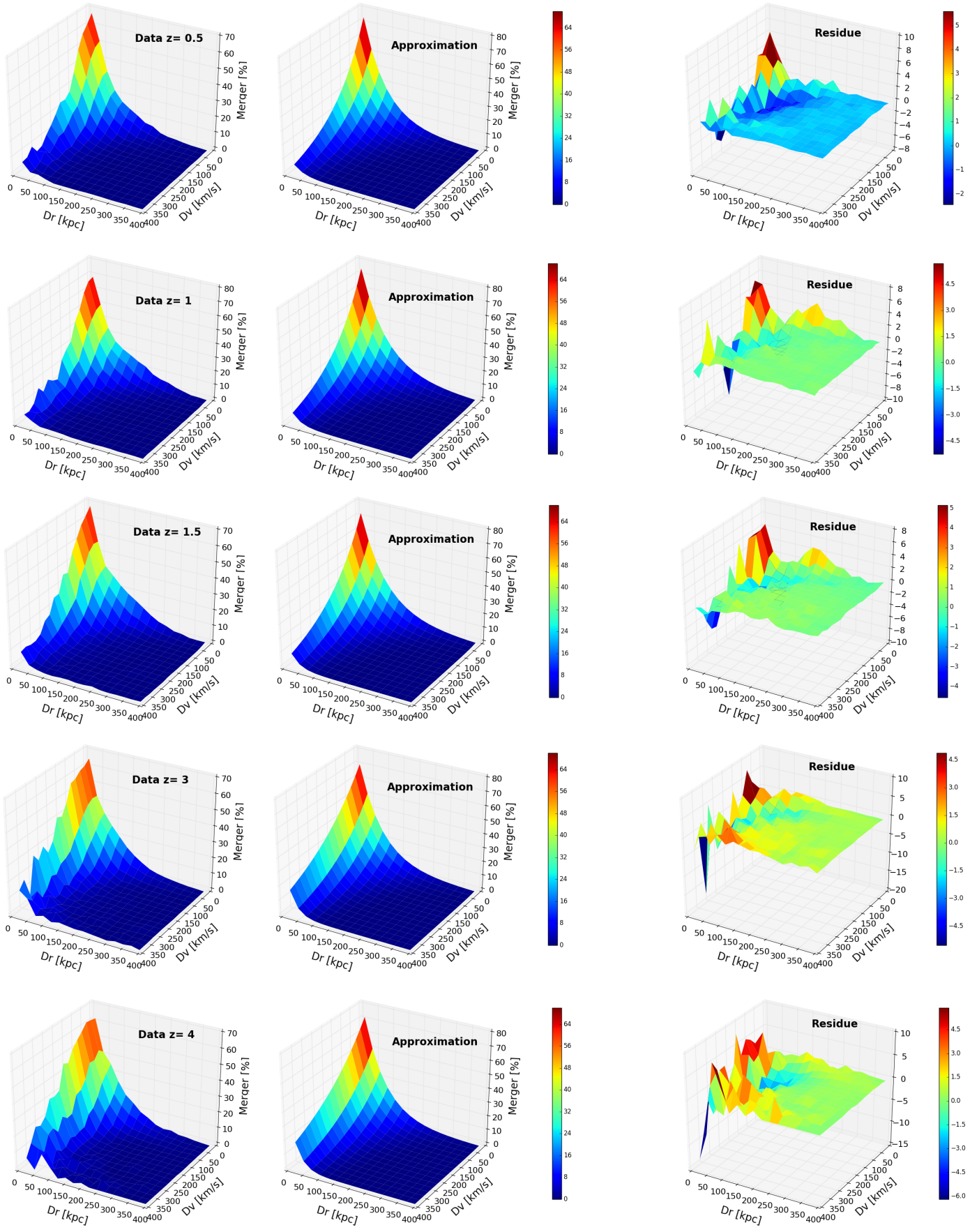
Data z= 0.5
Approximation
Residue
Data z= 1
Approximation
Residue
Data z= 1.5
Approximation
Residue
Data z= 3
Approximation
Residue
Data z= 4
Approximation
Residue
Dr [kpc]
Dv [km/s]
Merger [%]

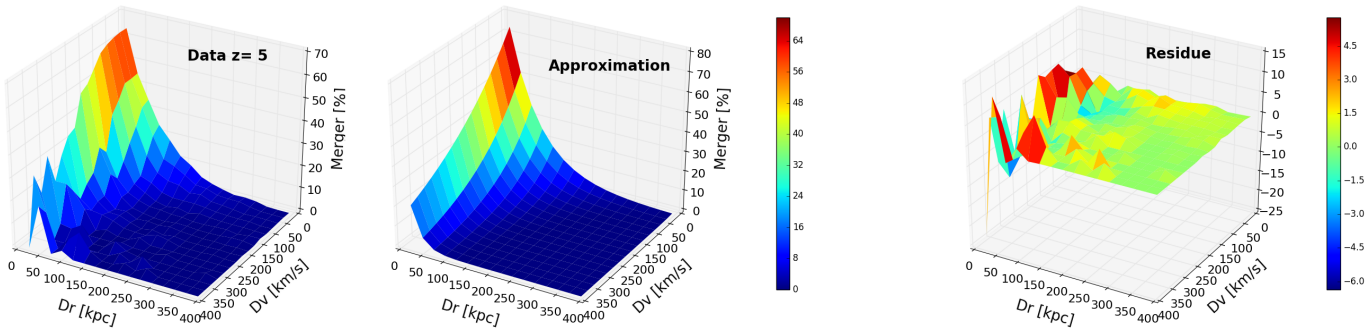

Fig. A.2: *From left to right* : For each redshift, the projected velocity-separation distance diagram, the approximate function from the nonlinear regression and the residual of their subtraction.

7

Evolution of the major and minor merger rates since $z \approx 6$

Contents

7.1 The galaxy merger timescale 107
7.2 Results 110

The galaxy major merger rate describes the number of major mergers suffered by a galaxy per Gyr (de Ravel et al., 2009) and is defined as:

$$R_{MM} = f_{MM}\ T_{MM}^{-1}, \tag{7.1}$$

with f_{MM}, the major merger fraction computed in the previous section, and T_{MM} the typical merger time scale in Gyr.

7.1 The galaxy merger timescale

Most of the uncertainties on the merger rate come from the difficulty to estimate accurately the galaxy merger timescale. Indeed this value depend on various parameters such as orbital parameters, internal spins and morphology of the galaxies involved. Most of the formula found in the literature, from theory or simulations studies, use mild variations of the same relation linking the merger time scale to the

dynamical friction time estimated from the relative orbit of the two objects at the moment of sub-halo disruption (Binney & Tremaine, 1987). It is modeled as (Boylan-Kolchin et al., 2008; Jiang et al. 2008; McCavana et al., 2012; Solanes et al., 2018):

$$\frac{T_{merg}}{T_{dyn}} = A\frac{\eta^B}{\ln(1+\eta)} \times f(\epsilon; C) \times (\frac{r_{cir}}{R_p})^D \tag{7.2}$$

Where η is the mass ratio of the galaxies, r_{cir} the reduced orbital energy, $\ln(1+\eta)$ is the approximation of the Coulomb logarithm (Lacey & Cole, 1993; Jiang et al., 2008), and $f(\epsilon; C)$ is a function that characterizes the dependence on the orbital circularity ϵ. Several models give different best-fit parameters and functions for $f(\epsilon; C)$ as well as the coefficients A, B and D (Boylan-Kolchin et al., 2008; Jiang et al., 2008; McCavana et al. 2012). In the most recent paper of Solanes et al. (2018), the authors compare in details the different major merger time scales issued from the different numerical studies cited above. They reveal important discordances between the different predictions that are not entirely explained by the difference in metric or the context of the simulations. It illustrates the need to have a better understanding of the physical mechanisms governing the merging process in order to reach a clear definition of the parameters involved, and thus give an accurate formula of the merger time scale for different range of mass ratios and orbital parameters.

However, due to the lack of information on orbital parameters, these time scales cannot be directly applied to observational surveys such as our close pair counts analysis.

Since we use close pairs of galaxies as a proxy for galaxy mergers, the time scale used in such cases is slightly different and is defined as the time duration after which a close pair of galaxies at a given separation distance is expected to merge together. The relevant time scale must then depend on pair properties and redshift. Some studies have tried to estimate this merger time scale for major merger events and mostly massive primary galaxies, $M_* \approx 10^{10}\ M_\odot$, (Kitzbichler & White, 2008; Lotz et al., 2008, 2010, 2011; Jiang et al., 2014). From their Millenium cosmological and N-body simulations, Kitzbichler & White (2008) conclude that the merger timescale depends strongly on the stellar mass of the primary galaxy

in the pair and its separation distance, but poorly on the redshift. It can be approximated by the relation:

$$T1_{MM}^{-1/2} = T0^{-1/2} + f1 \times z + f2 \times (log(M_*) - 10) \tag{7.3}$$

where T0, f1 and f2 are parameters depending on pair selection criteria such as projected physical separation distance and radial velocity difference.

Lotz et al. (2008, 2010) found that the timescale depends mainly on the mass ratio of the merging galaxies, on their gas fraction before the merger event and on the method used to identify the merger. In a subsequent study, Lotz et al. (2011) give an estimate of the cosmologically averaged observability time scale for both close pair selected samples and morphologically selected ones, based either on $G - M_{20}$ parameter or the asymmetry of galaxies. They found that whereas the timescales for close pair counts and $G - M_{20}$ studies are relatively insensitive to the assumptions about the distribution of galaxy merger properties, this is not the case for sample selected through the asymmetry indicator. In this case, the timescale can vary by a factor of 2 to 3 for different distributions of baryonic gas fractions. This work highlights the importance of the selection method used in the measurement of the merger rate and the estimation of the merger time scale.

Another merger timescale is computed in Xu et al. (2012) (also used by Keenan et al. 2014) which combines the merger timescale of Kitzbichler & White (2008) and the prescription of Lotz et al. (2010). Their merger timescale is defined as:

$$T2_{MM} = 0.3 \times (\frac{M_*}{10^{10.7} M_\odot})^{-0.3} \times (1 + \frac{z}{8}) \tag{7.4}$$

Using this equation, we find typical merging timescales of 0.5 Gyr for galaxies with $M^\star = 10^{10} M_\odot$ and 4 Gyr for $M^\star = 10^7 M_\odot$ around $z \sim 1$.

So far, no clear picture of the merger timescale has emerged and any formula used for the merger timescale has a lot of uncertainties. Moreover all of the timescales describe in this section are for major mergers and for relatively massive primary galaxies ($M_* \approx 10^{10}\ M_\odot$) and are mostly valid for low redshift. Since we probe a

large redshift domain and stellar mass range with MUSE, the error on the merger timescale for our low-mass galaxy samples are even more important.

Jiang et al. (2014) give a relation for the merger timescale for massive galaxies ($M_* \approx 10^{10}\ M_\odot$) but which extend to a larger range of mass ratio (up to 1:30). However, in their expression they use virial masses instead of the stellar mass.

For the following part of this thesis, I express the major merger rate computed with the two different timescales in equation 7.3 and 7.4. For the minor merger rate, I follow the expression used in Lopez-Sanjuan et al. (2011) which give a minor merger time scale derived from the major merger one:

$$T_{mm} = \gamma \times T_{MM} \tag{7.5}$$

Where γ accounts for the difference in the minor merger timescale with respect to the major merger one in close pairs (Jiang et al., 2008; Lotz et al., 2010). Similarly to Lopez-Sanjuan et al. (2011), we take $\gamma = 1.5$.

Lastly, in an effort to explain the discrepancy between the merger rate derived from observational surveys, like close pair counts, and predictions from simulations, Snyder et al. (2016) introduced an observability time scale which takes into account the time when a close pair can be identified in a simulation. It is expressed as $T \approx (1+z)^{-2}$. In the next section, we take into account this observability time scale for the comparison with simulation predictions.

7.2 Results

Using equation 7.1, we derive the major merger rate for our different redshift and stellar mass bins introduced in sect. 6.1. As the merger timescale depends strongly on the mass of the (primary) galaxy in the pair, it is important to consider low-mass and massive galaxies separately.

Figure 7.1 (right panel) shows the evolution of the major merger rate along cosmic time, when we assume a constant stellar mass separation of $10^{9.5} M_\odot$ (see previous subsection). The timescale is derived using equation 7.3 (Kitzbichler & White 2008) since it is the timescale used by most of the previous studies

Table 7.1: Major merger rates from MUSE observations over the HUDF, HDF-S, A2744 and COSMOS-GR30 regions. In this sample the primary galaxies have a stellar mass of $10^7 < M^\star < 10^{11}\ M_\odot$. Cols. (1) and (2): Range of the redshift bin and its associated mean redshift for the close pairs sample. Cols (3): Median value of stellar mass of the pairs sample. Cols (4): Major merger fraction. Col. (5): Merger timescale from Kitzbichler & White (2008). Col. (6): Major merger rates derived with Kitzbichler & White (2008) timescale. Col. (7): Merger timescale from Xu et al. (2012). Col. (8): Major merger rates derived with Xu et al.(2012) timescale.

z_r	$\overline{z_r}$	$\overline{M_p^\star}$	f_{MM}	$T1_{MM}$	$R1_{MM}$	$T2_{MM}$	$R2_{MM}$
-	-	$[\log(M_\odot)]$	–	[Gyr]	[Gyr^{-1}	[Gyr]	[Gyr^{-1}]
(1)	(2)	(3)	(4)	(5)	(6)	(7)	(8)
$0.2 < z < 1$	0.56	9.63	$0.126^{+0.047}_{-0.027}$	1.5	$0.042^{+0.022}_{-0.011}$	0.7	$0.106^{+0.057}_{-0.030}$
$1 < z < 1.5$	1.26	9.41	$0.127^{+0.079}_{-0.047}$	2	$0.063^{+0.034}_{-0.018}$	0.8	$0.150^{+0.080}_{-0.044}$
$1.5 < z < 2.8$	2.07	9.90	$0.172^{+0.111}_{-0.051}$	1.8	$0.099^{+0.052}_{-0.021}$	0.7	$0.270^{+0.144}_{-0.059}$
$2.8 < z < 4$	3.46	8.57	$0.081^{+0.053}_{-0.032}$	3.4	$0.022^{+0.015}_{-0.018}$	1.6	$0.049^{+0.025}_{-0.014}$
$4 < z < 6$	5.01	7.72	$0.075^{+0.068}_{-0.044}$	5.5	$0.015^{+0.029}_{-0.015}$	2.2	$0.034^{+0.024}_{-0.015}$

Table 7.2: Minor merger rates from MUSE observations over the same fields as in Table 7.1. The mass range for the primary galaxies in our pairs sample is between $10^9 < M^\star < 10^{11}\ M_\odot$. Same columns as in Table 7.1 with Col (4) corresponding to the minor merger fraction estimates from the combined analysis of the MUSE data. Col. (5) and (6) give the minor merger timescales as described in the previous section and their associated minor merger rate.

z_r	$\overline{z_r}$	$\overline{M_p^\star}$	f_{mm}	T_{mm}	R_{mm}
-	-	$[\log(M_\odot)]$	–	[Gyr]	[Gyr^{-1}]
(1)	(2)	(3)	(4)	(5)	(6)
$0.2 < z < 1$	0.60	10.00	$0.199^{+0.053}_{-0.032}$	2.3	$0.088^{+0.027}_{-0.019}$
$1 < z < 1.5$	1.23	9.85	$0.196^{+0.086}_{-0.054}$	2.5	$0.078^{+0.029}_{-0.016}$
$2.8 < z < 4$	3.49	9.3	$0.129^{+0.061}_{-0.041}$	3.4	$0.039^{+0.013}_{-0.012}$
$4 < tz < 6$	4.73	9.48	$0.084^{+0.071}_{-0.046}$	3.7	$0.023^{+0.014}_{-0.011}$

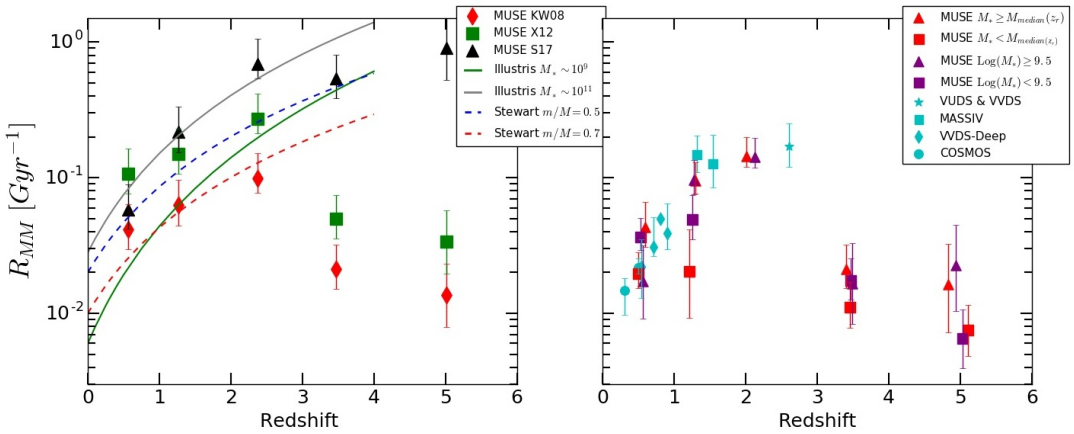

Figure 7.1: The major merger rate from MUSE data compared to previous spectroscopic studies and numerical simulations. *Left panel:* The data points are estimates from our MUSE sample over the complete mass range 10^7-$10^{11} M_\odot$. The red diamonds and green squares correspond to the major merger rates derived with the timescale from Kitzbichler & White (2008, KW08) and Xu et al. (2012, X12), respectively. The black triangles are major merger rates computed with the observability timescale defined in Snyder et al. (2017, S17). The two full lines are predictions of the merger rate from the Illustris simulation (Rodriguez-Gomez et al. 2015) for galaxies with M$^\star \approx 10^9 M_\odot$ (green line; $R_{MM} \approx (1+z)^{2.87}$), and M$^\star \approx 10^{11} M_\odot$ (blue line; $R_{MM} \approx (1+z)^{2.43}$).The dashed lines are from a LCDM N-body simulation (Stewart et al. 2009), for L $>0.1 L_*$ galaxies with dark matter halo mass ratio cut $m/M > 0.5$ (blue line) and 0.7 (red line). *Right panel:* Evolution of the major merger rate for two ranges of stellar mass, assuming a constant separation limit of M$^\star = 10^{9.5} M_\odot$ (purple colored symbol) or adopting the median value of stellar mass in each redshift bins as the separation limit (red colored symbol). Red squares and triangles show the MUSE estimates for low-mass and massive galaxies respectively. Previous estimates from the literature are shown with light blue symbols (de Ravel et al. 2009; Lopez-Sanjuan et al. 2011; Xu et al. 2012; Lopez-Sanjuan et al. 2013; Tasca et al. 2014).

introduced here. For the massive galaxies sample at $z > 1.5$, our results are in good agreement with those derived for MASSIV (Lopez-Sanjuan et al. 2013) or VUDS (Tasca et al. 2014) surveys.

The evolution of the major merger rate follows the trend of the fraction, i.e. an increase up to $R_{MM} \approx 0.15$ Gyr^{-1} at $z \sim 2$ for the high-mass sample and $R_{MM} \approx 0.03$ Gyr^{-1} at $z \sim 3$ for the low-mass one. Between $z \approx 4-6$, the rates decrease to $R_{MM} \approx 0.025$ Gyr^{-1}. The same trend is seen when using the median values as mass separation (see Fig. 7.1, right panel).

In Fig. 7.1, left panel, we display major merger rates from the combined fields study of MUSE observations computed with two different time scales from

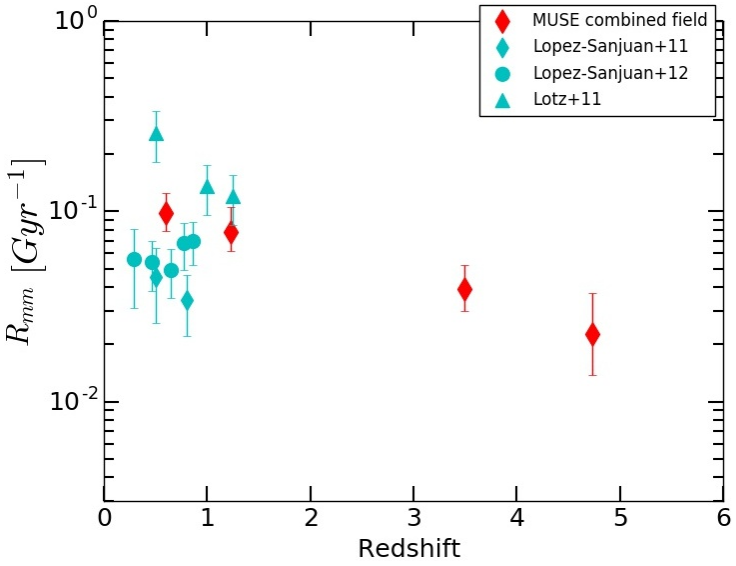

Figure 7.2: Evolution of the minor merger rate from MUSE combined samples (red diamonds) analyzed in this thesis. Cyan points are estimates from previous works: squares and points from Lopez-Sanjuan et al. (2011, 2012) and triangles from Lotz et al. (2011).

Kitzbichler & White (2008) and Xu et al. (2012). The difference between the two rates comes from the timescale. Indeed the one from Xu et al. (2012) gives generally a shorter merger timescale than the one from Kitzbichler & White (2008). These results are summarized in Table 7.1.

We also compare our merger rates to predictions from both the Illustris hydrodynamic simulations (Vogelsberger et al. 2014), and pure dark matter N-body simulations (e.g. Genel et al. 2009; Stewart et al. 2009).

Using Illustris, Rodriguez-Gomez et al. (2015) find that the major (taking 1:4 as the limit in mass ratio) merger rate of low-mass $10^9 M_\odot$ galaxies evolves with redshift up to $z \sim 7$ as $(1+z)^{2.87}$, while for massive galaxies of $10^{11} M_\odot$ it evolves as $(1+z)^{2.43}$ up to $z \sim 3.5$. This strong and positive correlation with redshift is in agreement with our (and previous) merger rate measurements up to $z \sim 2$, but it fully disagrees for higher redshift where we observe a flattening at $z \sim 3$ and a decrease at higher redshifts (see Fig. 7.1, left panel). However if we take into account the observability time scale of Snyder et al. (2017), $T \approx (1+z)^{-2}$, we found that in fact our estimates are in pretty good agreement with these predictions. This illustrates well the importance of the timescale in the estimations of the merger rate.

We derive the minor merger rate using the timescale described in equation 7.5 and the minor merger fractions estimated from our count of galaxy close pairs with stellar mass ratio between 1:6 and 1:100 (see Table 7.2).

In Figure 7.2, the minor merger rate is roughly constant ($R_{mm} \approx 0.019 - 0.016$ Gyr^{-1}) between $0.2 \leqslant z \leqslant 1.5$, and then slowly decreases down to $R_{mm} \approx 0.012$ Gyr^{-1} for $z > 3$. An attempt to compare our results to some of the few previous estimates of the minor merger rate is displayed in Figure 7.2. Lopez-Sanjuan et al. (2012) give an estimate of the minor merger rate from a close pair selected sample with a mass ratio range of 1:4-1:10 and a projected separation of $10 \leq r_p \leq 30\mathrm{h}^{-1}$ kpc. Their estimates are slightly below ours which is expected since their mass ratio range is narrower than ours. Lotz et al. (2011) report a inferred minor merger rate per galaxy, from $G - M_{20}$ selected mergers and mass-selected ratio range of 1:4-1:10, $R_{mm} = 0.27(1 + z)^{-0.1}$. The discrepancy of the results can be explained by the different selection method used in each cases.

Finally, our results must also be taken carefully since, as explained before, the stellar mass and mass ratio range of the galaxies probed with MUSE are larger than what was achieved in previous studies. Often the expressions used for the merger timescale are outside their validity domain and thus the estimates are highly uncertain.

The concluding remark would be that there is still considerable work to be done on theoretical models and simulations to give an accurate galaxy merger rate.

8

Conclusion and perspective

The processes that govern the evolution of baryons, and thus the mass assembly of galaxies in dark matter halos, are still unclear. Two mechanisms are competing for the key role in how galaxies accumulated mass over cosmic time: violent merging events, when two or more galaxies collide, or the smooth and continuous flow of gas onto galaxies. Understanding their importance relative to each other is thus a crucial aspect for galaxy evolution. A simple and direct way to quantify and investigate if galaxy mergers played a key role at significant look-back time is to count close pair of galaxies, i.e. two galaxies within a limited projected angular separation and line-of-sight relative radial velocity. However due to the difficulty to detect close spectroscopic pairs of galaxies, the major merger fraction and rate, involving two galaxies of similar masses, was constrained so far up to redshift $z \approx 3$ from spectroscopic pair counts. Moreover, the minor merger rate of galaxies was almost unconstrained so far, with a few attempts only.

Using deep (about 10 to 30 hours) MUSE observations of the Hubble Ultra Deep Field and Hubble Deep Field South, I was able to identify, for the first time, close spectroscopic pairs of galaxies at $z \geq 4$. Indeed, thanks to its wide field-of-view and sensitivity, MUSE allows to perform spectroscopic deep fields blindly without any pre-selection of galaxies, and is thus perfectly suited to identify close pairs

of galaxies with secure spectroscopic redshift, especially at high redshift ($z > 3$) through the detection of Lyαemission. I developed a selection method in order to highlight the presence of satellite galaxies orbiting around another.

However as the Lyα emission-line is usually red-shifted by several hundreds of $\mathrm{km\,s^{-1}}$ from the systemic redshif of the galaxy, which is of the same order as the velocity criteria used to define a close pair, I thus needed to correct the spectroscopic redshift derived from the peak of the Lyα line before performing the selection. I collaborated with Anne Verhamme (Geneva Observatory) to the building of an empirical relation between the observed Lyα FWHM and the shift of the peak to correct my Lyα-based redshifts for this velocity offset (Verhamme et al. 2018).

From a parent sample of 1801 galaxies, I identified 113 secure galaxy close pairs, spread over a large redshift range ($0.2 < z < 6$) and stellar masses ($10^7 - 10^{11}\ M_\odot$). Defining major mergers as having a mass ratio of 1:1-1:6, I found 56 major close pairs, among this sample, 23 pairs are identified at high redshift (z>3). From this initial analysis, I estimated the major merger fraction evolution up to z≈6 in a first paper part of the UDF public release (Ventou et al. 2017). My results are in good agreement with previous close pair counts estimates, with a constant increase of the major merger fraction up to z≈ 2-3 where it reaches a maximum of 20%. At higher redshift, I show for the first time that the fraction slowly decreases or flattens down to about 10% at z ≈ 6.

In the last year of my PhD, I tried to refine the criteria for the selection of galaxy close pairs using Illustris simulations. $\Delta_r \leq 30$ kpc and $\Delta_V \leq 500$ km $\mathrm{s^{-1}}$, the previous limits, were a compromise between statistics and contamination, assuring that the majority of close pairs meeting these criteria will merger. Mock catalogs from Illustris simulation were created from 6 snapshots corresponding to different redshifts from z=0.5 to z=5. For each snapshot, merger tree informations were generated, allowing me to investigate the relation between the relative velocity and projected separation distance of two galaxies and whether or not they will

indeed merge. In a second paper, I propose new selection criteria for close galaxy pairs, as well as a new corrective term to better estimate the major and minor merger fractions. Using the latest MUSE deep observations over the Hubble Ultra Deep Field, Hubble Deep Field South, COSMOS-Gr30 and Abell 2744 regions to expand my study, I gathered a large spectroscopic parent sample of 2483 galaxies, in which 372 close pairs were identified. The results of this work concerning the major merger evolution is in good agreement with our previous analysis. The same evolutionary trend was found. Our investigations on the evolution of the minor merger fraction indicates a roughly flat evolution with cosmic time, with a fraction of 20% at $z < 3$ and a slow decrease to 8-13% for higher redshift.

The last part of my PhD consisted in deriving galaxy merger rates from these estimated merger fractions. This last step is not so easy considering the difficulty to give an accurate estimate of the galaxy merger timescale.

With this study, I show the potential for using blind spectroscopy from IFU surveys to study pair counts at high redshift. Expanding this analysis to include more galaxies will significantly improve any estimates on the merger fraction or rate. Indeed the uncertainties are dominated at high redshift by the cosmic variance. Using new large spectroscopic surveys such as the VIMOS-based VUDS (Le Fèvre et al. 2015) or VANDELS (Pentericci et al. 2018; McLure et al. 2018), the new MUSE deep observations that will be acquired during the upcoming GTO observations, and the future MOONS/VLT surveys (Cirasuolo et al. 2011, 2016) could improve the statistics, especially at $z > 3$. Furthermore with the adaptive optics facility GALACSI now available to the community, MUSE will deliver incredibly rich data with impressive spatial resolution for assessing the role of mergers in the growth of galaxies or probing the environments of high-redshift galaxies. Such data could be used for example to investigate the potential selection effects of using Lyα emission-line to trace galaxies at high redshift, since at $z > 3$ not all galaxies are LAEs how do the close pairs detected relate to the underlying population ? Furthermore Lyα tend to trace star-forming galaxies, preferentially low-mass, so we may miss dry mergers of massive galaxies or quenched galaxies. Such studies

will be step stones for the next generation instruments like the giant ELT telescope or the James Webb Space Telescope.

9
Conclusion et perspective (French)

Les processus qui régissent l'évolution des baryons, et donc l'assemblage en masse des galaxies dans les halos de matière noire, sont encore largement inconnus. Deux mécanismes jouent un rôle clé dans la croissance en masse des galaxies au cours du temps cosmique: les fusions de galaxies, lorsque deux ou plusieurs galaxies se rencontrent, ou l'accrétion continue de gaz. Estimer leur importance relative est primordiale pour comprendre l'évolution des galaxies sur des echelles de temps cosmologiques. Une manière simple et directe de quantifier et d'étudier si les fusions de galaxies ont joué un rôle prépondérant à des époques reculées de l'histoire de l'univers, et de compter les paires proches de galaxies, c'est-à-dire deux galaxies physiquement proches avec une faible séparation angulaire projetée et une faible différence de vitesses radiales. En raison de la difficulté à détecter ces évènements violents, la fraction de fusions majeures et l'évolution de son taux, impliquant deux galaxies de masses similaires, n'était contrainte jusqu'alors que jusqu'à $z \sim 3$. De plus, le taux de fusions mineures des galaxies n'est pratiquement pas contraint, avec très peu de tentatives jusqu'à présent.

En utilisant des observations profondes (environ 10 à 30 heures de temps depose) réalisées avec MUSE sur le Hubble Ultra Deep Field et le Hubble Deep Field South, j'ai pu identifier des galaxies spectroscopiquement proches à $z \geq 4$. En effet, MUSE permet de réaliser des champs profonds spectroscopiques de façon

aveugle, c'est-à-dire sans aucune pré-sélection des galaxies. MUSE est donc un instrument idéal pour détecter des paires proche de galaxies, en particulier à haut redshift ($z > 3$) grâce à la détection de raies d'émission.

Dans mon analyse j'ai développé une méthode pour mettre en évidence la présence de galaxies satellites en orbite autour d'une galaxie centrale. Pour les objets à grand redshift, celui-ci est mesuré à partir du pic de la raie Lyα, ce qui peut introduire des incertitudes importantes. J'ai collaboré avec Anne Verhamme (Observatoire de Genève) à la définition d'une relation empirique entre la largeur à mi-hauteur (FWHM) de la raie Lyα et le décalage spectral de son pic pour corriger mes mesures de redshift basées sur cette raie (Verhamme et al. 2018). A partir d'un premier échantillon parent de 1801 galaxies, j'ai pu identifier 113 paires proches de galaxies, réparties sur un domaine étendu de redshifts ($0.2 < z < 6$) et de masses stellaires (10^7 à 10^{11} $M_\odot$). Définissant les fusions majeures avec un rapport de masse compris entre 1:1 et 1:6, j'ai finalement détecté 56 paires proches majeures parmi cet échantillon, 23 étant identifiées à un redshift élevé ($z > 3$). À partir de cette première analyse, j'ai estimé la fraction de fusions majeures. Mes résultats sont en bon accord avec les études précédentes, montrant une augmentation de la fraction de fusions jusqu'à $z \approx 2 - 3$ où elle atteint un maximum de 20%. Pour un redshift plus élevé, je montre pour la première fois que la fraction décroît ou s'aplatit lentement jusqu'à $z = 6$ (Ventou et al. 2017).

Au cours de la dernière année de ma thèse, j'ai essayé d'affiner les critères de sélection des paires proches de galaxies à l'aide des simulations Illustris. $\Delta_r \leq$ 30 kpc et $\Delta_v \leq 500$ km s^{-1}, les limites précédentes, constituaient un compromis entre statistique et contamination, garantissant que la majorité des paires finiraient par fusionner. Des catalogues ont été créés à partir des simulations cosmologiques Illustris pour 6 snapshots pris à différents redshifts allant de $z = 0.5$ à $z = 5$. Des informations sur l'arbre de fusion des galaxies ont été générées pour chaque snapshot, ce qui m'a permis d'étudier la relation entre la vitesse relative et la distance de séparation de deux galaxies et leur probabilité de fusionner. Dans un deuxième

article, je propose donc de nouveaux critères de sélection pour améliorer l'estimation de la fraction de fusion. Pour élargir mon étude, j'ai utilisé les dernières données profondes récoltées par MUSE sur deux autres régions: COSMOS-Gr30 et Abell 2744, obtenant ainsi un échantillon parent plus important de 2483 galaxies avec des redshift spectroscopiques, En tout, 372 paires proches ont pu être identifiées. Les résultats de ce travail concernant la fusion majeure sont en bon accord avec notre analyse précédente. La même tendance évolutive a été trouvée. Mon analyse sur l'évolution des fusions mineures, quant à elle, montre une évolution à peu près constante au cours du temps, avec une fraction de 20% à $z < 3$ et une légère diminution jusqu'à 8 à 13% pour des redshifts plus élevés.

La dernière partie de ma thèse consiste à transformer les fractions de fusions obtenues précédemment en taux de fusion des galaxies. Cette dernière étape n'est pas si facile compte tenu de la difficulté de donner une estimation précise du temps de fusion des galaxies.

Avec cette étude, je montre le potentiel d'utilisation de la spectroscopie "en aveugle" dans le domaine de l'études des paires proches de galaxies pour retracer l'évolutin du taux de fusions des galaies au cours du temps. Élargir cette analyse à un échantillon plus grand améliorera considérablement les estimations de la fraction ou du taux de fusion. En effet, les incertitudes sont dominées à grand redshift par la variance cosmique. L'utilisation de nouveaux grands relevés spectroscopiques comme VUDS (Le Fèvre et al. 2015) et VANDELS (Pentericci et al. 2018; McLure et al. 2018) basés sur VIMOS, les nouveaux champs profonds MUSE qui seront observés dans la dernière partie du GTO, et les futurs grands relevés avec MOONS au VLT (Cirasuolo et al. 2011, 2016) permettront d'améliorer la statistique et de diminuer les problèmes de variance cosmique, particulièrement à grand redshift $z > 3$.

De plus, avec le système d'optique adaptative GALACSI maintenant disponible pour la communauté, MUSE fournira des données incroyablement riches avec une résolution spatiale impressionnante, idéale pour évaluer le rôle des fusions dans la croissance des galaxies ou pour sonder l'environnement des galaxies à grand redshift.

De telles études constitueront un pas en avant pour les instruments de la prochaine génération, tels que le télescope géant ELT ou le télescope spatial James Webb.

Bibliography

[1] G. O. Abell, H. G. Corwin, Jr., and R. P. Olowin. A catalog of rich clusters of galaxies. ApJS, 70:1–138, May 1989.

[2] O. Agertz, R. Teyssier, and B. Moore. Disc formation and the origin of clumpy galaxies at high redshift. MNRAS, 397:L64–L68, July 2009.

[3] D. Anglés-Alcázar, C.-A. Faucher-Giguère, D. Kereš, P. F. Hopkins, E. Quataert, and N. Murray. The cosmic baryon cycle and galaxy mass assembly in the FIRE simulations. MNRAS, 470:4698–4719, Oct. 2017.

[4] M. Antonucci, A. Talavera, F. Vagnetti, D. Trevese, A. Comastri, M. Paolillo, P. Ranalli, and C. Vignali. The XMM Deep Survey in the CDF-S. VII. UV catalogue of the Optical Monitor observations. A&A, 574:A49, Feb. 2015.

[5] R. Bacon, J. Brinchmann, J. Richard, T. Contini, A. Drake, M. Franx, S. Tacchella, J. Vernet, L. Wisotzki, J. Blaizot, N. Bouché, R. Bouwens, S. Cantalupo, C. M. Carollo, D. Carton, J. Caruana, B. Clément, S. Dreizler, B. Epinat, B. Guiderdoni, C. Herenz, T.-O. Husser, S. Kamann, J. Kerutt, W. Kollatschny, D. Krajnovic, S. Lilly, T. Martinsson, L. Michel-Dansac, V. Patricio, J. Schaye, M. Shirazi, K. Soto, G. Soucail, M. Steinmetz, T. Urrutia, P. Weilbacher, and T. de Zeeuw. The MUSE 3D view of the Hubble Deep Field South. A&A, 575:A75, Mar. 2015.

[6] R. Bacon, S. Conseil, D. Mary, J. Brinchmann, M. Shepherd, M. Akhlaghi, P. M. Weilbacher, L. Piqueras, L. Wisotzki, D. Lagattuta, B. Epinat, A. Guerou, H. Inami, S. Cantalupo, J. B. Courbot, T. Contini, J. Richard, M. Maseda, R. Bouwens, N. Bouché, W. Kollatschny, J. Schaye, R. A. Marino, R. Pello, C. Herenz, B. Guiderdoni, and M. Carollo. The MUSE Hubble Ultra Deep Field Survey. I. Survey description, data reduction, and source detection. A&A, 608:A1, Nov. 2017.

[7] S. V. W. Beckwith, M. Stiavelli, A. M. Koekemoer, J. A. R. Caldwell, H. C. Ferguson, R. Hook, R. A. Lucas, L. E. Bergeron, M. Corbin, S. Jogee, N. Panagia, M. Robberto, P. Royle, R. S. Somerville, and M. Sosey. The Hubble Ultra Deep Field. AJ, 132:1729–1755, Nov. 2006.

[8] J. Bédorf and S. Portegies Zwart. The effect of many minor mergers on the size growth of compact quiescent galaxies. MNRAS, 431:767–780, May 2013.

[9] E. Bertin and S. Arnouts. SExtractor: Software for source extraction. A&AS, 117:393–404, June 1996.

[10] D. Bina, R. Pelló, J. Richard, J. Lewis, V. Patrício, S. Cantalupo, E. C. Herenz, K. Soto, P. M. Weilbacher, R. Bacon, J. D. R. Vernet, L. Wisotzki, B. Clément, J. G. Cuby, D. J. Lagattuta, G. Soucail, and A. Verhamme. MUSE observations of the lensing cluster Abell 1689. A&A, 590:A14, May 2016.

[11] J. Binney and S. Tremaine. *Galactic dynamics*. 1987.

[12] A. F. L. Bluck, C. J. Conselice, R. J. Bouwens, E. Daddi, M. Dickinson, C. Papovich, and H. Yan. A surprisingly high pair fraction for extremely massive galaxies at z ˜ 3 in the GOODS NICMOS survey. MNRAS, 394:L51–L55, Mar. 2009.

[13] A. F. L. Bluck, C. J. Conselice, F. Buitrago, R. Grützbauch, C. Hoyos, A. Mortlock, and A. E. Bauer. The Structures and Total (Minor + Major) Merger Histories of Massive Galaxies up to z = 3 in the HST GOODS NICMOS Survey: A Possible Solution to the Size Evolution Problem. ApJ, 747:34, Mar. 2012.

[14] N. Bouché, H. Finley, I. Schroetter, M. T. Murphy, P. Richter, R. Bacon, T. Contini, J. Richard, M. Wendt, S. Kamann, B. Epinat, S. Cantalupo, L. A. Straka, J. Schaye, C. L. Martin, C. Péroux, L. Wisotzki, K. Soto, S. Lilly, C. M. Carollo, J. Brinchmann, and W. Kollatschny. Possible Signatures of a Cold-flow Disk from MUSE Using a z = 1 Galaxy-Quasar Pair toward SDSS J1422-0001. ApJ, 820:121, Apr. 2016.

[15] N. Bouché, M. T. Murphy, G. G. Kacprzak, C. Péroux, T. Contini, C. L. Martin, and M. Dessauges-Zavadsky. Signatures of Cool Gas Fueling a Star-Forming Galaxy at Redshift 2.3. *Science*, 341:50–53, July 2013.

[16] F. Bournaud. Galaxy formation hydrodynamics: From cosmic flows to star-forming clouds. In J. Alves, B. G. Elmegreen, J. M. Girart, and V. Trimble, editors, *Computational Star Formation*, volume 270 of *IAU Symposium*, pages 491–498, Apr. 2011.

[17] F. Bournaud, C. J. Jog, and F. Combes. Multiple minor mergers: formation of elliptical galaxies and constraints for the growth of spiral disks. A&A, 476:1179–1190, Dec. 2007.

[18] R. J. Bouwens, G. D. Illingworth, I. Labbe, P. A. Oesch, M. Trenti, C. M. Carollo, P. G. van Dokkum, M. Franx, M. Stiavelli, V. González, D. Magee, and L. Bradley. A candidate redshift z˜10 galaxy and rapid changes in that population at an age of 500Myr. Nature, 469:504–507, Jan. 2011.

[19] R. J. Bouwens, G. D. Illingworth, P. A. Oesch, M. Franx, I. Labbé, M. Trenti, P. van Dokkum, C. M. Carollo, V. González, R. Smit, and D. Magee. UV-continuum Slopes at z =4-7 from the HUDF09+ERS+CANDELS Observations: Discovery of a Well-defined UV Color-Magnitude Relationship for z >= 4 Star-forming Galaxies. ApJ, 754:83, Aug. 2012.

[20] R. J. Bouwens, G. D. Illingworth, P. A. Oesch, M. Stiavelli, P. van Dokkum, M. Trenti, D. Magee, I. Labbé, M. Franx, C. M. Carollo, and V. Gonzalez. Discovery of z ˜ 8 Galaxies in the Hubble Ultra Deep Field from Ultra-Deep WFC3/IR Observations. ApJ, 709:L133–L137, Feb. 2010.

[21] R. J. Bouwens, G. D. Illingworth, P. A. Oesch, M. Trenti, I. Labbé, M. Franx, M. Stiavelli, C. M. Carollo, P. van Dokkum, and D. Magee. Lower-luminosity Galaxies Could Reionize the Universe: Very Steep Faint-end Slopes to the UV Luminosity Functions at z = 5-8 from the HUDF09 WFC3/IR Observations. ApJ, 752:L5, June 2012.

[22] R. J. Bouwens, P. A. Oesch, G. D. Illingworth, I. Labbé, P. G. van Dokkum, G. Brammer, D. Magee, L. R. Spitler, M. Franx, R. Smit, M. Trenti, V. Gonzalez, and C. M. Carollo. Photometric Constraints on the Redshift of z ˜ 10 Candidate UDFj-39546284 from Deeper WFC3/IR+ACS+IRAC Observations over the HUDF. ApJ, 765:L16, Mar. 2013.

[23] M. Boylan-Kolchin, C.-P. Ma, and E. Quataert. Dynamical friction and galaxy merging time-scales. MNRAS, 383:93–101, Jan. 2008.

[24] J. Brinchmann, H. Inami, R. Bacon, T. Contini, M. Maseda, J. Chevallard, N. Bouché, L. Boogaard, M. Carollo, S. Charlot, W. Kollatschny, R. A. Marino, R. Pello, J. Richard, J. Schaye, A. Verhamme, and L. Wisotzki. The MUSE Hubble Ultra Deep Field Survey. III. Testing photometric redshifts to 30th magnitude. A&A, 608:A3, Nov. 2017.

[25] K. Bundy, R. S. Ellis, and C. J. Conselice. The Mass Assembly Histories of Galaxies of Various Morphologies in the GOODS Fields. ApJ, 625:621–632, June 2005.

[26] K. Bundy, M. Fukugita, R. S. Ellis, T. A. Targett, S. Belli, and T. Kodama. The Greater Impact of Mergers on the Growth of Massive Galaxies: Implications for Mass Assembly and Evolution since z sime 1. ApJ, 697:1369–1383, June 2009.

[27] R. Caimmi. The G-dwarf problem in the Galaxy. New A, 13:314–339, July 2008.

[28] S. Casertano, D. de Mello, M. Dickinson, H. C. Ferguson, A. S. Fruchter, R. A. Gonzalez-Lopezlira, I. Heyer, R. N. Hook, Z. Levay, R. A. Lucas, J. Mack, R. B. Makidon, M. Mutchler, T. E. Smith, M. Stiavelli, M. S. Wiggs, and R. E. Williams. WFPC2 Observations of the Hubble Deep Field South. AJ, 120:2747–2824, Dec. 2000.

[29] K. R. V. Casteels, C. J. Conselice, S. P. Bamford, E. Salvador-Solé, P. R. Norberg, N. K. Agius, I. Baldry, S. Brough, M. J. I. Brown, M. J. Drinkwater, S. P. Driver, A. W. Graham, J. Bland-Hawthorn, A. M. Hopkins, L. S. Kelvin, A. R. López-Sánchez, J. Loveday, A. S. G. Robotham, and J. A. Vázquez-Mata. Galaxy And Mass Assembly (GAMA): refining the local galaxy merger rate using morphological information. MNRAS, 445:1157–1169, Dec. 2014.

[30] C. Chiappini. A New Picture for the Chemical Evolution of the Galaxy: the Two Infall Model. In *Revista Mexicana de Astronomia y Astrofisica Conference Series*, volume 11 of *Revista Mexicana de Astronomia y Astrofisica Conference Series*, page 171, July 2001.

[31] M. Cirasuolo, J. Afonso, R. Bender, P. Bonifacio, C. Evans, L. Kaper, E. Oliva, and L. Vanzi. MOONS: The Multi-Object Optical and Near-infrared Spectrograph. *The Messenger*, 145:11–13, Sept. 2011.

[32] M. Cirasuolo and MOONS Consortium. MOONS: A New Powerful Multi-Object Spectrograph for the VLT. In I. Skillen, M. Balcells, and S. Trager, editors, *Multi-Object Spectroscopy in the Next Decade: Big Questions, Large Surveys, and Wide Fields*, volume 507 of *Astronomical Society of the Pacific Conference Series*, page 109, Oct. 2016.

[33] S. Conseil, R. Bacon, L. Piqueras, and M. Shepherd. Advanced Data Reduction for the MUSE Deep Fields. *ArXiv e-prints*, Dec. 2016.

[34] C. J. Conselice. The fundamental properties of galaxies and a new galaxy classification system. MNRAS, 373:1389–1408, Dec. 2006.

[35] C. J. Conselice. The Evolution of Galaxy Structure Over Cosmic Time. ARA&A, 52:291–337, Aug. 2014.

[36] C. J. Conselice, M. A. Bershady, M. Dickinson, and C. Papovich. A Direct Measurement of Major Galaxy Mergers at z<=3. AJ, 126:1183–1207, Sept. 2003.

[37] C. J. Conselice, A. Mortlock, A. F. L. Bluck, R. Grützbauch, and K. Duncan. Gas accretion as a dominant formation mode in massive galaxies from the GOODS NICMOS Survey. MNRAS, 430:1051–1060, Apr. 2013.

[38] C. J. Conselice, S. Rajgor, and R. Myers. The structures of distant galaxies - I. Galaxy structures and the merger rate to z=3 in the Hubble Ultra-Deep Field. MNRAS, 386:909–927, May 2008.

[39] O. Cucciati, L. Tresse, O. Ilbert, O. Le Fèvre, B. Garilli, V. Le Brun, P. Cassata, P. Franzetti, D. Maccagni, M. Scodeggio, E. Zucca, G. Zamorani, S. Bardelli, M. Bolzonella, R. M. Bielby, H. J. McCracken, A. Zanichelli, and D. Vergani. The star formation rate density and dust attenuation evolution over 12 Gyr with the VVDS surveys. A&A, 539:A31, Mar. 2012.

[40] T. Dahlen, B. Mobasher, M. Dickinson, H. C. Ferguson, M. Giavalisco, C. Kretchmer, and S. Ravindranath. Evolution of the Luminosity Function, Star Formation Rate, Morphology, and Size of Star-forming Galaxies Selected at Rest-Frame 1500 and 2800 Å. ApJ, 654:172–185, Jan. 2007.

[41] I. Davidzon, O. Ilbert, C. Laigle, J. Coupon, H. J. McCracken, I. Delvecchio, D. Masters, P. Capak, B. C. Hsieh, O. Le Fèvre, L. Tresse, M. Bethermin, Y.-Y. Chang, A. L. Faisst, E. Le Floc'h, C. Steinhardt, S. Toft, H. Aussel, C. Dubois, G. Hasinger, M. Salvato, D. B. Sanders, N. Scoville, and J. D. Silverman. The COSMOS2015 galaxy stellar mass function . Thirteen billion years of stellar mass assembly in ten snapshots. A&A, 605:A70, Sept. 2017.

[42] G. De Lucia and J. Blaizot. The hierarchical formation of the brightest cluster galaxies. MNRAS, 375:2–14, Feb. 2007.

[43] L. de Ravel, O. Le Fèvre, L. Tresse, D. Bottini, B. Garilli, V. Le Brun, D. Maccagni, R. Scaramella, M. Scodeggio, G. Vettolani, A. Zanichelli, C. Adami, S. Arnouts, S. Bardelli, M. Bolzonella, A. Cappi, S. Charlot, P. Ciliegi, T. Contini, S. Foucaud, P. Franzetti, I. Gavignaud, L. Guzzo, O. Ilbert, A. Iovino, F. Lamareille, H. J. McCracken, B. Marano, C. Marinoni, A. Mazure, B. Meneux, R. Merighi, S. Paltani, R. Pellò, A. Pollo, L. Pozzetti, M. Radovich, D. Vergani, G. Zamorani, E. Zucca, M. Bondi, A. Bongiorno, J. Brinchmann, O. Cucciati, S. de La Torre, L. Gregorini, P. Memeo, E. Perez-Montero, Y. Mellier, P. Merluzzi, and S. Temporin. The VIMOS VLT Deep Survey. Evolution of the major merger rate since z ˜ 1 from spectroscopically confirmed galaxy pairs. A&A, 498:379–397, May 2009.

[44] A. Dekel, A. Zolotov, D. Tweed, M. Cacciato, D. Ceverino, and J. R. Primack. Toy models for galaxy formation versus simulations. MNRAS, 435:999–1019, Oct. 2013.

[45] P. Di Matteo, F. Combes, A.-L. Melchior, and B. Semelin. Star formation efficiency in galaxy interactions and mergers: a statistical study. A&A, 468:61–81, June 2007.

[46] A. B. Drake, T. Garel, L. Wisotzki, F. Leclercq, T. Hashimoto, J. Richard, R. Bacon, J. Blaizot, J. Caruana, S. Conseil, T. Contini, B. Guiderdoni, E. C. Herenz, H. Inami, J. Lewis, G. Mahler, R. A. Marino, R. Pello, J. Schaye, A. Verhamme, E. Ventou, and P. M. Weilbacher. The MUSE Hubble Ultra Deep Field Survey. VI. The faint-end of the Lyα luminosity function at 2.91 <z <6.64 and implications for reionisation. A&A, 608:A6, Nov. 2017.

[47] K. Duncan, C. J. Conselice, A. Mortlock, W. G. Hartley, Y. Guo, H. C. Ferguson, R. Davé, Y. Lu, J. Ownsworth, M. L. N. Ashby, A. Dekel, M. Dickinson, S. Faber, M. Giavalisco, N. Grogin, D. Kocevski, A. Koekemoer, R. S. Somerville, and C. E. White. The mass evolution of the first galaxies: stellar mass functions and star formation rates at 4 <z < 7 in the CANDELS GOODS-South field. MNRAS, 444:2960–2984, Nov. 2014.

[48] J. S. Dunlop, R. J. McLure, A. D. Biggs, J. E. Geach, M. J. Michałowski, R. J. Ivison, W. Rujopakarn, E. van Kampen, A. Kirkpatrick, A. Pope, D. Scott, A. M. Swinbank, T. A. Targett, I. Aretxaga, J. E. Austermann, P. N. Best, V. A. Bruce, E. L. Chapin, S. Charlot, M. Cirasuolo, K. Coppin, R. S. Ellis, S. L. Finkelstein, C. C. Hayward, D. H. Hughes, E. Ibar, P. Jagannathan, S. Khochfar, M. P. Koprowski, D. Narayanan, K. Nyland, C. Papovich, J. A. Peacock, G. H. Rieke, B. Robertson, T. Vernstrom, P. P. v. d. Werf, G. W. Wilson, and M. Yun. A deep ALMA image of the Hubble Ultra Deep Field. MNRAS, 466:861–883, Apr. 2017.

[49] D. M. Elmegreen and B. G. Elmegreen. Flocculent and Grand Design Spiral Arm Structure in Field, Binary, and Group Galaxies. In *Bulletin of the American Astronomical Society*, volume 14 of BAAS, page 643, Mar. 1982.

[50] D. M. Elmegreen and B. G. Elmegreen. Arm classifications for spiral galaxies. ApJ, 314:3–9, Mar. 1987.

[51] B. Epinat, T. Contini, H. Finley, L. A. Boogaard, A. Guérou, J. Brinchmann, D. Carton, L. Michel-Dansac, R. Bacon, S. Cantalupo, M. Carollo, S. Hamer, W. Kollatschny, D. Krajnović, R. A. Marino, J. Richard, G. Soucail, P. M. Weilbacher, and L. Wisotzki. Ionised gas structure of 100 kpc in an over-dense region of the galaxy group COSMOS-Gr30 at z 0.7. A&A, 609:A40, Jan. 2018.

[52] H. Finley, N. Bouché, T. Contini, M. Paalvast, L. Boogaard, M. Maseda, R. Bacon, J. Blaizot, J. Brinchmann, B. Epinat, A. Feltre, R. A. Marino, S. Muzahid, J. Richard, J. Schaye, A. Verhamme, P. M. Weilbacher, and L. Wisotzki. The MUSE Hubble Ultra Deep Field Survey. VII. Fe II* emission in star-forming galaxies. A&A, 608:A7, Nov. 2017.

[53] N. M. Förster Schreiber, R. Genzel, N. Bouché, G. Cresci, R. Davies, P. Buschkamp, K. Shapiro, L. J. Tacconi, E. K. S. Hicks, S. Genel, A. E. Shapley, D. K. Erb, C. C. Steidel, D. Lutz, F. Eisenhauer, S. Gillessen, A. Sternberg, A. Renzini, A. Cimatti, E. Daddi, J. Kurk, S. Lilly, X. Kong, M. D. Lehnert, N. Nesvadba, A. Verma, H. McCracken, N. Arimoto, M. Mignoli, and M. Onodera. The SINS Survey: SINFONI Integral Field Spectroscopy of z ˜ 2 Star-forming Galaxies. ApJ, 706:1364–1428, Dec. 2009.

[54] N. M. Förster Schreiber, A. E. Shapley, D. K. Erb, R. Genzel, C. C. Steidel, N. Bouché, G. Cresci, and R. Davies. Constraints on the Assembly and Dynamics of Galaxies. I. Detailed Rest-frame Optical Morphologies on Kiloparsec Scale of z ˜ 2 Star-forming Galaxies. ApJ, 731:65, Apr. 2011.

[55] S. Genel, R. Genzel, N. Bouché, T. Naab, and A. Sternberg. The Halo Merger Rate in the Millennium Simulation and Implications for Observed Galaxy Merger Fractions. ApJ, 701:2002–2018, Aug. 2009.

[56] A. Grazian, A. Fontana, P. Santini, J. S. Dunlop, H. C. Ferguson, M. Castellano, R. Amorin, M. L. N. Ashby, G. Barro, P. Behroozi, K. Boutsia, K. I. Caputi, R. R. Chary, A. Dekel, M. E. Dickinson, S. M. Faber, G. G. Fazio, S. L. Finkelstein, A. Galametz, E. Giallongo, M. Giavalisco, N. A. Grogin, Y. Guo, D. Kocevski, A. M. Koekemoer, D. C. Koo, K.-S. Lee, Y. Lu, E. Merlin, B. Mobasher, M. Nonino, C. Papovich, D. Paris, L. Pentericci, N. Reddy, A. Renzini, B. Salmon, M. Salvato, V. Sommariva, M. Song, and E. Vanzella. The galaxy stellar mass function at 3.5 <z < 7.5 in the CANDELS/UDS, GOODS-South, and HUDF fields. A&A, 575:A96, Mar. 2015.

[57] C. Gruppioni, F. Pozzi, G. Rodighiero, I. Delvecchio, S. Berta, L. Pozzetti, G. Zamorani, P. Andreani, A. Cimatti, O. Ilbert, E. Le Floc'h, D. Lutz, B. Magnelli, L. Marchetti, P. Monaco, R. Nordon, S. Oliver, P. Popesso, L. Riguccini, I. Roseboom, D. J. Rosario, M. Sargent, M. Vaccari, B. Altieri, H. Aussel, A. Bongiovanni, J. Cepa, E. Daddi, H. Domínguez-Sánchez, D. Elbaz, N. Förster Schreiber, R. Genzel, A. Iribarrem, M. Magliocchetti, R. Maiolino, A. Poglitsch, A. Pérez García, M. Sanchez-Portal, E. Sturm, L. Tacconi, I. Valtchanov, A. Amblard, V. Arumugam, M. Bethermin, J. Bock, A. Boselli, V. Buat, D. Burgarella, N. Castro-Rodríguez, A. Cava, P. Chanial, D. L. Clements, A. Conley, A. Cooray, C. D. Dowell, E. Dwek, S. Eales, A. Franceschini, J. Glenn, M. Griffin, E. Hatziminaoglou, E. Ibar, K. Isaak, R. J. Ivison, G. Lagache, L. Levenson, N. Lu, S. Madden, B. Maffei, G. Mainetti, H. T. Nguyen, B. O'Halloran, M. J. Page, P. Panuzzo, A. Papageorgiou, C. P. Pearson, I. Pérez-Fournon, M. Pohlen, D. Rigopoulou, M. Rowan-Robinson, B. Schulz, D. Scott, N. Seymour, D. L. Shupe, A. J. Smith, J. A. Stevens, M. Symeonidis, M. Trichas, K. E. Tugwell, L. Vigroux, L. Wang, G. Wright, C. K. Xu, M. Zemcov, S. Bardelli, M. Carollo, T. Contini, O. Le Févre, S. Lilly, V. Mainieri, A. Renzini, M. Scodeggio, and E. Zucca. The Herschel PEP/HerMES luminosity function - I. Probing the evolution of PACS selected Galaxies to z = 4. MNRAS, 432:23–52, June 2013.

[58] A. Guérou, D. Krajnović, B. Epinat, T. Contini, E. Emsellem, N. Bouché, R. Bacon, L. Michel-Dansac, J. Richard, P. M. Weilbacher, J. Schaye, R. A. Marino, M. den Brok, and S. Erroz-Ferrer. The MUSE Hubble Ultra Deep Field Survey. V. Spatially resolved stellar kinematics of galaxies at redshift 0.2< z < 0.8. A&A, 608:A5, Nov. 2017.

[59] Q. Guo and S. D. M. White. Galaxy growth in the concordance lambdaCDM cosmology. MNRAS, 384:2–10, Feb. 2008.

[60] T. Hashimoto, T. Garel, B. Guiderdoni, A. B. Drake, R. Bacon, J. Blaizot, J. Richard, F. Leclercq, H. Inami, A. Verhamme, R. Bouwens, J. Brinchmann, S. Cantalupo, M. Carollo, J. Caruana, E. C. Herenz, J. Kerutt, R. A. Marino, P. Mitchell, and J. Schaye. The MUSE Hubble Ultra Deep Field Survey. X. Lyα equivalent widths at 2.9 < z < 6.6. A&A, 608:A10, Nov. 2017.

[61] E. C. Herenz and L. Wisotzki. LSDCat: Detection and cataloguing of emission-line sources in integral-field spectroscopy datacubes. A&A, 602:A111, June 2017.

[62] E. C. Herenz and L. Wistozki. LSDCat: Line Source Detection and Cataloguing Tool. Astrophysics Source Code Library, Dec. 2016.

[63] S. R. Hinton, T. M. Davis, C. Lidman, K. Glazebrook, and G. F. Lewis. MARZ: Manual and automatic redshifting software. *Astronomy and Computing*, 15:61–71, Apr. 2016.

[64] P. F. Hopkins, K. Bundy, D. Croton, L. Hernquist, D. Keres, S. Khochfar, K. Stewart, A. Wetzel, and J. D. Younger. Mergers and Bulge Formation in lambdaCDM: Which Mergers Matter? ApJ, 715:202–229, May 2010.

[65] G. D. Illingworth, D. Magee, P. A. Oesch, R. J. Bouwens, I. Labbé, M. Stiavelli, P. G. van Dokkum, M. Franx, M. Trenti, C. M. Carollo, and V. Gonzalez. The HST eXtreme Deep Field (XDF): Combining All ACS and WFC3/IR Data on the HUDF Region into the Deepest Field Ever. ApJS, 209:6, Nov. 2013.

[66] H. Inami, R. Bacon, J. Brinchmann, J. Richard, T. Contini, S. Conseil, S. Hamer, M. Akhlaghi, N. Bouché, B. Clément, G. Desprez, A. B. Drake, T. Hashimoto, F. Leclercq, M. Maseda, L. Michel-Dansac, M. Paalvast, L. Tresse, E. Ventou, W. Kollatschny, L. A. Boogaard, H. Finley, R. A. Marino, J. Schaye, and L. Wisotzki. The MUSE Hubble Ultra Deep Field Survey. II. Spectroscopic redshifts and comparisons to color selections of high-redshift galaxies. A&A, 608:A2, Nov. 2017.

[67] M. Jauzac, J. Richard, E. Jullo, B. Clément, M. Limousin, J.-P. Kneib, H. Ebeling, P. Natarajan, S. Rodney, H. Atek, R. Massey, D. Eckert, E. Egami, and M. Rexroth. Hubble Frontier Fields: a high-precision strong-lensing analysis of the massive galaxy cluster Abell 2744 using 180 multiple images. MNRAS, 452:1437–1446, Sept. 2015.

[68] H.-Y. Jian, L. Lin, and T. Chiueh. Environmental Dependence of the Galaxy Merger Rate in a ΛCDM Universe. ApJ, 754:26, July 2012.

[69] C. Y. Jiang, Y. P. Jing, A. Faltenbacher, W. P. Lin, and C. Li. A Fitting Formula for the Merger Timescale of Galaxies in Hierarchical Clustering. ApJ, 675:1095–1105, Mar. 2008.

[70] C. Y. Jiang, Y. P. Jing, and J. Han. A Scaling Relation between Merger Rate of Galaxies and Their Close Pair Count. ApJ, 790:7, July 2014.

[71] R. D. Joseph and G. S. Wright. Recent star formation in interacting galaxies. II - Super starburst in merging galaxies. MNRAS, 214:87–95, May 1985.

[72] P. Kampczyk, S. J. Lilly, C. M. Carollo, C. Scarlata, R. Feldmann, A. Koekemoer, A. Leauthaud, M. T. Sargent, Y. Taniguchi, and P. Capak. Simulating the Cosmos: The Fraction of Merging Galaxies at High Redshift. ApJS, 172:329–340, Sept. 2007.

[73] J. S. Kartaltepe, D. B. Sanders, N. Z. Scoville, D. Calzetti, P. Capak, A. Koekemoer, B. Mobasher, T. Murayama, M. Salvato, S. S. Sasaki, and Y. Taniguchi. Evolution of the Frequency of Luminous ($<=L^*_V$) Close Galaxy Pairs at $z < 1.2$ in the COSMOS Field. ApJS, 172:320–328, Sept. 2007.

[74] A. Katsianis, G. Blanc, C. P. Lagos, N. Tejos, R. G. Bower, A. Alavi, V. Gonzalez, T. Theuns, M. Schaller, and S. Lopez. The evolution of the star formation rate function in the EAGLE simulations: a comparison with UV, IR and Hα observations from $z = 8$ to $z = 0$. MNRAS, 472:919–939, Nov. 2017.

[75] S. Kaviraj. The significant contribution of minor mergers to the cosmic star formation budget. MNRAS, 437:L41–L45, Jan. 2014.

[76] S. Kaviraj, S. H. Cohen, R. A. Windhorst, J. I. Silk, R. S. Ellis, A. Dekel, and W. Science Organising Committee. The insignificance of major mergers in the early Universe. In *American Astronomical Society Meeting Abstracts #223*, volume 223 of *American Astronomical Society Meeting Abstracts*, page 310.07, Jan. 2014.

[77] S. Kaviraj, J. Devriendt, Y. Dubois, A. Slyz, C. Welker, C. Pichon, S. Peirani, and D. Le Borgne. Galaxy merger histories and the role of merging in driving star formation at z >1. MNRAS, 452:2845–2850, Sept. 2015.

[78] R. C. Keenan, S. Foucaud, R. De Propris, B. C. Hsieh, L. Lin, R. C. Y. Chou, S. Huang, J. H. Lin, and K. H. Chang. Evolution of the Major Merger Galaxy Pair Fraction at z $<$ 1. ApJ, 795:157, Nov. 2014.

[79] R. C. Kennicutt, Jr. Star Formation in Galaxies Along the Hubble Sequence. ARA&A, 36:189–232, 1998.

[80] R. C. Kennicutt, Jr. The Global Schmidt Law in Star-forming Galaxies. ApJ, 498:541–552, May 1998.

[81] D. Kereš, N. Katz, D. H. Weinberg, and R. Davé. How do galaxies get their gas? MNRAS, 363:2–28, Oct. 2005.

[82] M. G. Kitzbichler and S. D. M. White. A calibration of the relation between the abundance of close galaxy pairs and the rate of galaxy mergers. MNRAS, 391:1489–1498, Dec. 2008.

[83] C. Knobel, S. J. Lilly, A. Iovino, K. Kovač, T. J. Bschorr, V. Presotto, P. A. Oesch, P. Kampczyk, C. M. Carollo, T. Contini, J.-P. Kneib, O. Le Fevre, V. Mainieri, A. Renzini, M. Scodeggio, G. Zamorani, S. Bardelli, M. Bolzonella, A. Bongiorno, K. Caputi, O. Cucciati, S. de la Torre, L. de Ravel, P. Franzetti, B. Garilli, F. Lamareille, J.-F. Le Borgne, V. Le Brun, C. Maier, M. Mignoli, R. Pello, Y. Peng, E. Perez Montero, J. Silverman, M. Tanaka, L. Tasca, L. Tresse, D. Vergani, E. Zucca, L. Barnes, R. Bordoloi, A. Cappi, A. Cimatti, G. Coppa, A. M. Koekemoer, C. López-Sanjuan, H. J. McCracken, M. Moresco, P. Nair, L. Pozzetti, and N. Welikala. The zCOSMOS 20k Group Catalog. ApJ, 753:121, July 2012.

[84] C. Lacey and S. Cole. Merger rates in hierarchical models of galaxy formation. MNRAS, 262:627–649, June 1993.

[85] D. J. Lagattuta, J. Richard, B. Clément, G. Mahler, V. Patrício, R. Pelló, G. Soucail, K. B. Schmidt, L. Wisotzki, J. Martinez, and D. Bina. Lens modelling Abell 370: crowning the final frontier field with MUSE. MNRAS, 469:3946–3964, Aug. 2017.

[86] C. d. P. Lagos, A. R. H. Stevens, R. G. Bower, T. A. Davis, S. Contreras, N. D. Padilla, D. Obreschkow, D. Croton, J. W. Trayford, C. Welker, and T. Theuns. The catastrophic effect of mergers on the angular momentum and morphology of galaxies in EAGLE. *ArXiv e-prints*, Jan. 2017.

[87] C. Laigle, H. J. McCracken, O. Ilbert, B. C. Hsieh, I. Davidzon, P. Capak, G. Hasinger, J. D. Silverman, C. Pichon, J. Coupon, H. Aussel, D. Le Borgne, K. Caputi, P. Cassata, Y.-Y. Chang, F. Civano, J. Dunlop, J. Fynbo, J. S.

Kartaltepe, A. Koekemoer, O. Le Fèvre, E. Le Floc'h, A. Leauthaud, S. Lilly, L. Lin, S. Marchesi, B. Milvang-Jensen, M. Salvato, D. B. Sanders, N. Scoville, V. Smolcic, M. Stockmann, Y. Taniguchi, L. Tasca, S. Toft, M. Vaccari, and J. Zabl. The COSMOS2015 Catalog: Exploring the $1 < z < 6$ Universe with Half a Million Galaxies. ApJS, 224:24, June 2016.

[88] D. Lam, T. Broadhurst, J. M. Diego, J. Lim, D. Coe, H. C. Ford, and W. Zheng. A Rigorous Free-form Lens Model of A2744 to Meet the Hubble Frontier Fields Challenge. ApJ, 797:98, Dec. 2014.

[89] N. Laporte, A. Streblyanska, B. Clement, I. Pérez-Fournon, D. Schaerer, H. Atek, F. Boone, J.-P. Kneib, E. Egami, P. Martínez-Navajas, R. Marques-Chaves, R. Pelló, and J. Richard. The first Frontier Fields cluster: 4.5 μm excess in a z ˜ 8 galaxy candidate in Abell 2744. A&A, 562:L8, Feb. 2014.

[90] O. Le Fèvre, R. Abraham, S. J. Lilly, R. S. Ellis, J. Brinchmann, D. Schade, L. Tresse, M. Colless, D. Crampton, K. Glazebrook, F. Hammer, and T. Broadhurst. Hubble Space Telescope imaging of the CFRS and LDSS redshift surveys - IV. Influence of mergers in the evolution of faint field galaxies from z=1. MNRAS, 311:565–575, Jan. 2000.

[91] O. Le Fèvre, L. A. M. Tasca, P. Cassata, B. Garilli, V. Le Brun, D. Maccagni, L. Pentericci, R. Thomas, E. Vanzella, G. Zamorani, E. Zucca, R. Amorin, S. Bardelli, P. Capak, L. Cassarà, M. Castellano, A. Cimatti, J. G. Cuby, O. Cucciati, S. de la Torre, A. Durkalec, A. Fontana, M. Giavalisco, A. Grazian, N. P. Hathi, O. Ilbert, B. C. Lemaux, C. Moreau, S. Paltani, B. Ribeiro, M. Salvato, D. Schaerer, M. Scodeggio, V. Sommariva, M. Talia, Y. Taniguchi, L. Tresse, D. Vergani, P. W. Wang, S. Charlot, T. Contini, S. Fotopoulou, C. López-Sanjuan, Y. Mellier, and N. Scoville. The VIMOS Ultra-Deep Survey: 10 000 galaxies with spectroscopic redshifts to study galaxy assembly at early epochs $2 < z = 6$. A&A, 576:A79, Apr. 2015.

[92] F. Leclercq, R. Bacon, L. Wisotzki, P. Mitchell, T. Garel, A. Verhamme, J. Blaizot, T. Hashimoto, E. C. Herenz, S. Conseil, S. Cantalupo, H. Inami, T. Contini, J. Richard, M. Maseda, J. Schaye, R. A. Marino, M. Akhlaghi, J. Brinchmann, and M. Carollo. The MUSE Hubble Ultra Deep Field Survey. VIII. Extended Lyman-α haloes around high-z star-forming galaxies. A&A, 608:A8, Nov. 2017.

[93] B. L'Huillier, F. Combes, and B. Semelin. Mass assembly of galaxies. Smooth accretion versus mergers. A&A, 544:A68, Aug. 2012.

[94] S. J. Lilly, O. L. Fevre, A. Renzini, G. Zamorani, M. Scodeggio, T. Contini, C. M. Carollo, G. Hasinger, J.-P. Kneib, A. Iovino, V. Le Brun, C. Maier, V. Mainieri, M. Mignoli, J. Silverman, L. A. M. Tasca, M. Bolzonella, A. Bongiorno, D. Bottini, P. Capak, K. Caputi, A. Cimatti, O. Cucciati, E. Daddi, R. Feldmann, P. Franzetti, B. Garilli, L. Guzzo, O. Ilbert, P. Kampczyk, K. Kovac, F. Lamareille, A. Leauthaud, J.-F. Le Borgne, H. J. McCracken, C. Marinoni, R. Pello, E. Ricciardelli, C. Scarlata, D. Vergani, D. B. Sanders, E. Schinnerer, N. Scoville, Y. Taniguchi, S. Arnouts, H. Aussel, S. Bardelli, M. Brusa, A. Cappi, P. Ciliegi, A. Finoguenov, S. Foucaud, R. Franceschini, C. Halliday, C. Impey, C. Knobel, A. Koekemoer, J. Kurk, D. Maccagni, S. Maddox, B. Marano, G. Marconi, B. Meneux, B. Mobasher, C. Moreau, J. A. Peacock, C. Porciani, L. Pozzetti, R. Scaramella, D. Schiminovich, P. Shopbell, I. Smail, D. Thompson, L. Tresse, G. Vettolani, A. Zanichelli, and E. Zucca. VizieR Online Data Catalog: zCOSMOS-bright catalog (Lilly+, 2007). *VizieR Online Data Catalog*, 217, Feb. 2009.

[95] S. J. Lilly, O. Le Fèvre, A. Renzini, G. Zamorani, M. Scodeggio, T. Contini, C. M. Carollo, G. Hasinger, J.-P. Kneib, A. Iovino, V. Le Brun, C. Maier, V. Mainieri, M. Mignoli, J. Silverman, L. A. M. Tasca, M. Bolzonella, A. Bongiorno, D. Bottini, P. Capak, K. Caputi, A. Cimatti, O. Cucciati, E. Daddi, R. Feldmann, P. Franzetti, B. Garilli, L. Guzzo, O. Ilbert, P. Kampczyk, K. Kovac, F. Lamareille, A. Leauthaud, J.-F. Le Borgne, H. J. McCracken, C. Marinoni, R. Pello, E. Ricciardelli, C. Scarlata, D. Vergani, D. B. Sanders, E. Schinnerer, N. Scoville, Y. Taniguchi, S. Arnouts, H. Aussel, S. Bardelli, M. Brusa, A. Cappi, P. Ciliegi, A. Finoguenov, S. Foucaud, A. Franceschini, C. Halliday, C. Impey, C. Knobel, A. Koekemoer, J. Kurk, D. Maccagni, S. Maddox, B. Marano, G. Marconi, B. Meneux, B. Mobasher, C. Moreau, J. A. Peacock, C. Porciani, L. Pozzetti, R. Scaramella, D. Schiminovich, P. Shopbell, I. Smail, D. Thompson, L. Tresse, G. Vettolani, A. Zanichelli, and E. Zucca. zCOSMOS: A Large VLT/VIMOS Redshift Survey Covering 0 $<$ z $<$ 3 in the COSMOS Field. ApJS, 172:70–85, Sept. 2007.

[96] L. Lin, M. C. Cooper, H.-Y. Jian, D. C. Koo, D. R. Patton, R. Yan, C. N. A. Willmer, A. L. Coil, T. Chiueh, D. J. Croton, B. F. Gerke, J. Lotz, P. Guhathakurta, and J. A. Newman. Where do Wet, Dry, and Mixed Galaxy Mergers Occur? A Study of the Environments of Close Galaxy Pairs in the DEEP2 Galaxy Redshift Survey. ApJ, 718:1158–1170, Aug. 2010.

[97] L. Lin, D. R. Patton, D. C. Koo, K. Casteels, C. J. Conselice, S. M. Faber, J. Lotz, C. N. A. Willmer, B. C. Hsieh, T. Chiueh, J. A. Newman, G. S. Novak, B. J. Weiner, and M. C. Cooper. The Redshift Evolution of Wet, Dry, and Mixed Galaxy Mergers from Close Galaxy Pairs in the DEEP2 Galaxy Redshift Survey. ApJ, 681:232–243, July 2008.

[98] C. López-Sanjuan, O. Le Fèvre, L. de Ravel, O. Cucciati, O. Ilbert, L. Tresse, S. Bardelli, M. Bolzonella, T. Contini, B. Garilli, L. Guzzo, D. Maccagni, H. J. McCracken, Y. Mellier, A. Pollo, D. Vergani, and E. Zucca. The VIMOS VLT Deep Survey. The contribution of minor mergers to the growth of LB = LB* galaxies since z=1 from spectroscopically identified pairs. A&A, 530:A20, June 2011.

[99] C. López-Sanjuan, O. Le Fèvre, O. Ilbert, L. A. M. Tasca, C. Bridge, O. Cucciati, P. Kampczyk, L. Pozzetti, C. K. Xu, C. M. Carollo, T. Contini, J.-P. Kneib, S. J. Lilly, V. Mainieri, A. Renzini, D. Sanders, M. Scodeggio, N. Z. Scoville, Y. Taniguchi, G. Zamorani, H. Aussel, S. Bardelli, M. Bolzonella, A. Bongiorno, P. Capak, K. Caputi, S. de la Torre, L. de Ravel, P. Franzetti, B. Garilli, A. Iovino, C. Knobel, K. Kovač, F. Lamareille, J.-F. Le Borgne, V. Le Brun, E. Le Floc'h, C. Maier, H. J. McCracken, M. Mignoli, R. Pelló, Y. Peng, E. Pérez-Montero, V. Presotto, E. Ricciardelli, M. Salvato, J. D. Silverman, M. Tanaka, L. Tresse, D. Vergani, E. Zucca, L. Barnes, R. Bordoloi, A. Cappi, A. Cimatti, G. Coppa, A. Koekemoer, C. T. Liu, M. Moresco, P. Nair, P. Oesch, K. Schawinski, and N. Welikala. The dominant role of mergers in the size evolution of massive early-type galaxies since z = 1. A&A, 548:A7, Dec. 2012.

[100] C. López-Sanjuan, O. Le Fèvre, L. A. M. Tasca, B. Epinat, P. Amram, T. Contini, B. Garilli, M. Kissler-Patig, J. Moultaka, L. Paioro, V. Perret, J. Queyrel, L. Tresse, D. Vergani, and C. Divoy. MASSIV: Mass Assembly Survey with SINFONI in VVDS. V. The major merger rate of star-forming galaxies at 0.9 $<$ z $<$ 1.8 from IFS-based close pairs. A&A, 553:A78, May 2013.

[101] J. M. Lotz, P. Jonsson, T. J. Cox, D. Croton, J. R. Primack, R. S. Somerville, and K. Stewart. The Major and Minor Galaxy Merger Rates at z < 1.5. ApJ, 742:103, Dec. 2011.

[102] J. M. Lotz, P. Jonsson, T. J. Cox, and J. R. Primack. Galaxy merger morphologies and time-scales from simulations of equal-mass gas-rich disc mergers. MNRAS, 391:1137–1162, Dec. 2008.

[103] J. M. Lotz, P. Jonsson, T. J. Cox, and J. R. Primack. The effect of mass ratio on the morphology and time-scales of disc galaxy mergers. MNRAS, 404:575–589, May 2010.

[104] J. M. Lotz, A. Koekemoer, D. Coe, N. Grogin, P. Capak, J. Mack, J. Anderson, R. Avila, E. A. Barker, D. Borncamp, G. Brammer, M. Durbin, H. Gunning, B. Hilbert, H. Jenkner, H. Khandrika, Z. Levay, R. A. Lucas, J. MacKenty, S. Ogaz, B. Porterfield, N. Reid, M. Robberto, P. Royle, L. J. Smith, L. J. Storrie-Lombardi, B. Sunnquist, J. Surace, D. C. Taylor, R. Williams, J. Bullock, M. Dickinson, S. Finkelstein, P. Natarajan, J. Richard, B. Robertson, J. Tumlinson, A. Zitrin, K. Flanagan, K. Sembach, B. T. Soifer, and M. Mountain. The Frontier Fields: Survey Design and Initial Results. ApJ, 837:97, Mar. 2017.

[105] J. M. Lotz, P. Madau, M. Giavalisco, J. Primack, and H. C. Ferguson. The Rest-Frame Far-Ultraviolet Morphologies of Star-forming Galaxies at z ˜ 1.5 and 4. ApJ, 636:592–609, Jan. 2006.

[106] J. M. Lotz, J. Primack, and P. Madau. A New Nonparametric Approach to Galaxy Morphological Classification. AJ, 128:163–182, July 2004.

[107] B. Luo, W. N. Brandt, Y. Q. Xue, B. Lehmer, D. M. Alexander, F. E. Bauer, F. Vito, G. Yang, A. R. Basu-Zych, A. Comastri, R. Gilli, Q.-S. Gu, A. E. Hornschemeier, A. Koekemoer, T. Liu, V. Mainieri, M. Paolillo, P. Ranalli, P. Rosati, D. P. Schneider, O. Shemmer, I. Smail, M. Sun, P. Tozzi, C. Vignali, and J.-X. Wang. The Chandra Deep Field-South Survey: 7 Ms Source Catalogs. ApJS, 228:2, Jan. 2017.

[108] P. Madau and M. Dickinson. Cosmic Star-Formation History. ARA&A, 52:415–486, Aug. 2014.

[109] B. Magnelli, D. Elbaz, R. R. Chary, M. Dickinson, D. Le Borgne, D. T. Frayer, and C. N. A. Willmer. Evolution of the dusty infrared luminosity function from z = 0 to z = 2.3 using observations from Spitzer. A&A, 528:A35, Apr. 2011.

[110] B. Magnelli, P. Popesso, S. Berta, F. Pozzi, D. Elbaz, D. Lutz, M. Dickinson, B. Altieri, P. Andreani, H. Aussel, M. Béthermin, A. Bongiovanni, J. Cepa, V. Charmandaris, R.-R. Chary, A. Cimatti, E. Daddi, N. M. Förster Schreiber, R. Genzel, C. Gruppioni, M. Harwit, H. S. Hwang, R. J. Ivison, G. Magdis, R. Maiolino, E. Murphy, R. Nordon, M. Pannella, A. Pérez García, A. Poglitsch, D. Rosario, M. Sanchez-Portal, P. Santini, D. Scott, E. Sturm, L. J. Tacconi, and I. Valtchanov. The deepest Herschel-PACS far-infrared survey: number counts and infrared luminosity functions from combined PEP/GOODS-H observations. A&A, 553:A132, May 2013.

[111] G. Mahler, J. Richard, B. Clément, D. Lagattuta, K. Schmidt, V. Patrício, G. Soucail, R. Bacon, R. Pello, R. Bouwens, M. Maseda, J. Martinez, M. Carollo, H. Inami, F. Leclercq, and L. Wisotzki. Strong-lensing analysis of

A2744 with MUSE and Hubble Frontier Fields images. MNRAS, 473:663–692, Jan. 2018.

[112] A. W. S. Man, S. Toft, A. W. Zirm, S. Wuyts, and A. van der Wel. The Pair Fraction of Massive Galaxies at 0 <= z <= 3. ApJ, 744:85, Jan. 2012.

[113] A. W. S. Man, A. W. Zirm, and S. Toft. Resolving the Discrepancy of Galaxy Merger Fraction Measurements at z = 0-3. ApJ, 830:89, Oct. 2016.

[114] K. B. Mantha, D. H. McIntosh, R. Brennan, H. C. Ferguson, D. Kodra, J. A. Newman, M. Rafelski, R. S. Somerville, C. J. Conselice, J. S. Cook, N. P. Hathi, D. C. Koo, J. M. Lotz, B. D. Simmons, A. N. Straughn, G. F. Snyder, S. Wuyts, E. F. Bell, A. Dekel, J. Kartaltepe, D. D. Kocevski, A. M. Koekemoer, S.-K. Lee, R. A. Lucas, C. Pacifici, M. A. Peth, G. Barro, T. Dahlen, S. L. Finkelstein, A. Fontana, A. Galametz, N. A. Grogin, Y. Guo, B. Mobasher, H. Nayyeri, P. G. Pérez-González, J. Pforr, P. Santini, M. Stefanon, and T. Wiklind. Major merging history in CANDELS. I. Evolution of the incidence of massive galaxy-galaxy pairs from z = 3 to z = 0. MNRAS, 475:1549–1573, Apr. 2018.

[115] D. C. Martin, M. Matuszewski, P. Morrissey, J. D. Neill, A. Moore, S. Cantalupo, J. X. Prochaska, and D. Chang. A giant protogalactic disk linked to the cosmic web. Nature, 524:192–195, Aug. 2015.

[116] M. V. Maseda, J. Brinchmann, M. Franx, R. Bacon, R. J. Bouwens, K. B. Schmidt, L. A. Boogaard, T. Contini, A. Feltre, H. Inami, W. Kollatschny, R. A. Marino, J. Richard, A. Verhamme, and L. Wisotzki. The MUSE Hubble Ultra Deep Field Survey. IV. Global properties of C III] emitters. A&A, 608:A4, Nov. 2017.

[117] T. McCavana, M. Micic, G. F. Lewis, M. Sinha, S. Sharma, K. Holley-Bockelmann, and J. Bland-Hawthorn. The lives of high-redshift mergers. MNRAS, 424:361–371, July 2012.

[118] R. J. McLure, L. Pentericci, A. Cimatti, J. S. Dunlop, D. Elbaz, A. Fontana, K. Nandra, R. Amorin, M. Bolzonella, A. Bongiorno, A. C. Carnall, M. Castellano, M. Cirasuolo, O. Cucciati, F. Cullen, S. De Barros, S. L. Finkelstein, F. Fontanot, P. Franzetti, M. Fumana, A. Gargiulo, B. Garilli, L. Guaita, W. G. Hartley, A. Iovino, M. J. Jarvis, S. Juneau, W. Karman, D. Maccagni, F. Marchi, E. Mármol-Queraltó, E. Pompei, L. Pozzetti, M. Scodeggio, V. Sommariva, M. Talia, O. Almaini, I. Balestra, S. Bardelli, E. F. Bell, N. Bourne, R. A. A. Bowler, M. Brusa, F. Buitrago, K. I. Caputi, P. Cassata, S. Charlot, A. Citro, G. Cresci, S. Cristiani, E. Curtis-Lake, M. Dickinson, G. G. Fazio, H. C. Ferguson, F. Fiore, M. Franco, J. P. U. Fynbo, A. Galametz, A. Georgakakis, M. Giavalisco, A. Grazian, N. P. Hathi, I. Jung, S. Kim, A. M. Koekemoer, Y. Khusanova, O. Le Fèvre, J. M. Lotz, F. Mannucci, D. T. Maltby, K. Matsuoka, D. J. McLeod, H. Mendez-Hernandez, J. Mendez-Abreu, M. Mignoli, M. Moresco, A. Mortlock, M. Nonino, M. Pannella, C. Papovich, P. Popesso, D. P. Rosario, M. Salvato, P. Santini, D. Schaerer, C. Schreiber, D. P. Stark, L. A. M. Tasca, R. Thomas, T. Treu, E. Vanzella, V. Wild, C. C. Williams, G. Zamorani, and E. Zucca. The VANDELS ESO public spectroscopic survey. MNRAS, 479:25–42, Sept. 2018.

[119] J. Merten, D. Coe, R. Dupke, R. Massey, A. Zitrin, E. S. Cypriano, N. Okabe, B. Frye, F. G. Braglia, Y. Jiménez-Teja, N. Benítez, T. Broadhurst, J. Rhodes, M. Meneghetti, L. A. Moustakas, L. Sodré, Jr., J. Krick, and J. N. Bregman. Creation of cosmic structure in the complex galaxy cluster merger Abell 2744. MNRAS, 417:333–347, Oct. 2011.

[120] J. C. Mihos and L. Hernquist. Dense stellar cores in merger remnants. ApJ, 437:L47–L50, Dec. 1994.

[121] J. Moreno, A. F. L. Bluck, S. L. Ellison, D. R. Patton, P. Torrey, and B. P. Moster. The dynamics of galaxy pairs in a cosmological setting. MNRAS, 436:1765–1786, Dec. 2013.

[122] A. Mortlock, C. J. Conselice, A. F. L. Bluck, A. E. Bauer, R. Grützbauch, F. Buitrago, and J. Ownsworth. A deep probe of the galaxy stellar mass functions at z= 1-3 with the GOODS NICMOS Survey. MNRAS, 413:2845–2859, June 2011.

[123] E. Neistein and A. Dekel. Merger rates of dark matter haloes. MNRAS, 388:1792–1802, Aug. 2008.

[124] A. B. Newman, R. S. Ellis, K. Bundy, and T. Treu. Can Minor Merging Account for the Size Growth of Quiescent Galaxies? New Results from the CANDELS Survey. ApJ, 746:162, Feb. 2012.

[125] P. A. Oesch, R. J. Bouwens, G. D. Illingworth, M. Franx, S. M. Ammons, P. G. van Dokkum, M. Trenti, and I. Labbé. First Frontier Field Constraints on the Cosmic Star Formation Rate Density at z = 10 The Impact of Lensing Shear on Completeness of High-redshift Galaxy Samples. ApJ, 808:104, July 2015.

[126] M. S. Owers, S. W. Randall, P. E. J. Nulsen, W. J. Couch, L. P. David, and J. C. Kempner. The Dissection of Abell 2744: A Rich Cluster Growing Through Major and Minor Mergers. ApJ, 728:27, Feb. 2011.

[127] B. E. J. Pagel and B. E. Patchett. Metal abundances in nearby stars and the chemical history of the solar neighborhood. MNRAS, 172:13–40, July 1975.

[128] V. Patrício, J. Richard, A. Verhamme, L. Wisotzki, J. Brinchmann, M. L. Turner, L. Christensen, P. M. Weilbacher, J. Blaizot, R. Bacon, T. Contini, D. Lagattuta, S. Cantalupo, B. Clément, and G. Soucail. A young star-forming galaxy at z = 3.5 with an extended Lyman α halo seen with MUSE. MNRAS, 456:4191–4208, Mar. 2016.

[129] D. R. Patton, R. G. Carlberg, R. O. Marzke, C. J. Pritchet, L. N. da Costa, and P. S. Pellegrini. New Techniques for Relating Dynamically Close Galaxy Pairs to Merger and Accretion Rates: Application to the Second Southern Sky Redshift Survey. ApJ, 536:153–172, June 2000.

[130] L. Pentericci, R. J. McLure, B. Garilli, O. Cucciati, P. Franzetti, A. Iovino, R. Amorin, M. Bolzonella, A. Bongiorno, A. C. Carnall, M. Castellano, A. Cimatti, M. Cirasuolo, F. Cullen, S. De Barros, J. S. Dunlop, D. Elbaz, S. L. Finkelstein, A. Fontana, F. Fontanot, M. Fumana, A. Gargiulo, L. Guaita, W. G. Hartley, M. J. Jarvis, S. Juneau, W. Karman, D. Maccagni, F. Marchi, E. Marmol-Queralto, K. Nandra, E. Pompei, L. Pozzetti, M. Scodeggio, V. Sommariva, M. Talia, O. Almaini, I. Balestra, S. Bardelli, E. F. Bell, N. Bourne, R. A. A. Bowler, M. Brusa, F. Buitrago, K. I. Caputi, P. Cassata, S. Charlot, A. Citro, G. Cresci, S. Cristiani, E. Curtis-Lake, M. Dickinson, G. G. Fazio, H. C. Ferguson, F. Fiore, M. Franco, J. P. U. Fynbo, A. Galametz, A. Georgakakis, M. Giavalisco, A. Grazian, N. P. Hathi, I. Jung, S. Kim, A. M. Koekemoer, Y. Khusanova, O. Le Fèvre, J. M. Lotz, F. Mannucci, D. T. Maltby, K. Matsuoka, D. J. McLeod, H. Mendez-Hernandez, J. Mendez-Abreu, M. Mignoli, M. Moresco, A. Mortlock, M. Nonino, M. Pannella, C. Papovich,

P. Popesso, D. P. Rosario, M. Salvato, P. Santini, D. Schaerer, C. Schreiber, D. P. Stark, L. A. M. Tasca, R. Thomas, T. Treu, E. Vanzella, V. Wild, C. C. Williams, G. Zamorani, and E. Zucca. The VANDELS ESO public spectroscopic survey: Observations and first data release. A&A, 616:A174, Sept. 2018.

[131] V. Perret, F. Renaud, B. Epinat, P. Amram, F. Bournaud, T. Contini, R. Teyssier, and J.-C. Lambert. Evolution of the mass, size, and star formation rate in high redshift merging galaxies. MIRAGE - A new sample of simulations with detailed stellar feedback. A&A, 562:A1, Feb. 2014.

[132] Planck Collaboration, N. Aghanim, Y. Akrami, M. Ashdown, J. Aumont, C. Baccigalupi, M. Ballardini, A. J. Banday, R. B. Barreiro, N. Bartolo, S. Basak, R. Battye, K. Benabed, J.-P. Bernard, M. Bersanelli, P. Bielewicz, J. J. Bock, J. R. Bond, J. Borrill, F. R. Bouchet, F. Boulanger, M. Bucher, C. Burigana, R. C. Butler, E. Calabrese, J.-F. Cardoso, J. Carron, A. Challinor, H. C. Chiang, J. Chluba, L. P. L. Colombo, C. Combet, D. Contreras, B. P. Crill, F. Cuttaia, P. de Bernardis, G. de Zotti, J. Delabrouille, J.-M. Delouis, E. Di Valentino, J. M. Diego, O. Doré, M. Douspis, A. Ducout, X. Dupac, S. Dusini, G. Efstathiou, F. Elsner, T. A. Enßlin, H. K. Eriksen, Y. Fantaye, M. Farhang, J. Fergusson, R. Fernandez-Cobos, F. Finelli, F. Forastieri, M. Frailis, E. Franceschi, A. Frolov, S. Galeotta, S. Galli, K. Ganga, R. T. Génova-Santos, M. Gerbino, T. Ghosh, J. González-Nuevo, K. M. Górski, S. Gratton, A. Gruppuso, J. E. Gudmundsson, J. Hamann, W. Handley, D. Herranz, E. Hivon, Z. Huang, A. H. Jaffe, W. C. Jones, A. Karakci, E. Keihänen, R. Keskitalo, K. Kiiveri, J. Kim, T. S. Kisner, L. Knox, N. Krachmalnicoff, M. Kunz, H. Kurki-Suonio, G. Lagache, J.-M. Lamarre, A. Lasenby, M. Lattanzi, C. R. Lawrence, M. Le Jeune, P. Lemos, J. Lesgourgues, F. Levrier, A. Lewis, M. Liguori, P. B. Lilje, M. Lilley, V. Lindholm, M. López-Caniego, P. M. Lubin, Y.-Z. Ma, J. F. Macías-Pérez, G. Maggio, D. Maino, N. Mandolesi, A. Mangilli, A. Marcos-Caballero, M. Maris, P. G. Martin, M. Martinelli, E. Martínez-González, S. Matarrese, N. Mauri, J. D. McEwen, P. R. Meinhold, A. Melchiorri, A. Mennella, M. Migliaccio, M. Millea, S. Mitra, M.-A. Miville-Deschênes, D. Molinari, L. Montier, G. Morgante, A. Moss, P. Natoli, H. U. Nørgaard-Nielsen, L. Pagano, D. Paoletti, B. Partridge, G. Patanchon, H. V. Peiris, F. Perrotta, V. Pettorino, F. Piacentini, L. Polastri, G. Polenta, J.-L. Puget, J. P. Rachen, M. Reinecke, M. Remazeilles, A. Renzi, G. Rocha, C. Rosset, G. Roudier, J. A. Rubiño-Martín, B. Ruiz-Granados, L. Salvati, M. Sandri, M. Savelainen, D. Scott, E. P. S. Shellard, C. Sirignano, G. Sirri, L. D. Spencer, R. Sunyaev, A.-S. Suur-Uski, J. A. Tauber, D. Tavagnacco, M. Tenti, L. Toffolatti, M. Tomasi, T. Trombetti, L. Valenziano, J. Valiviita, B. Van Tent, L. Vibert, P. Vielva, F. Villa, N. Vittorio, B. D. Wandelt, I. K. Wehus, M. White, S. D. M. White, A. Zacchei, and A. Zonca. Planck 2018 results. VI. Cosmological parameters. *ArXiv e-prints*, July 2018.

[133] Y. Qu, J. C. Helly, R. G. Bower, T. Theuns, R. A. Crain, C. S. Frenk, M. Furlong, S. McAlpine, M. Schaller, J. Schaye, and S. D. M. White. A chronicle of galaxy mass assembly in the EAGLE simulation. MNRAS, 464:1659–1675, Jan. 2017.

[134] M. Rafelski, H. I. Teplitz, J. P. Gardner, D. Coe, N. A. Bond, A. M. Koekemoer, N. Grogin, P. Kurczynski, E. J. McGrath, M. Bourque, H. Atek, T. M. Brown, J. W. Colbert, A. Codoreanu, H. C. Ferguson, S. L. Finkelstein, E. Gawiser, M. Giavalisco, C. Gronwall, D. J. Hanish, K.-S. Lee, V. Mehta, D. F. de Mello, S. Ravindranath, R. E. Ryan, C. Scarlata, B. Siana, E. Soto, and E. N.

Voyer. UVUDF: Ultraviolet Through Near-infrared Catalog and Photometric Redshifts of Galaxies in the Hubble Ultra Deep Field. AJ, 150:31, July 2015.

[135] N. A. Reddy and C. C. Steidel. A Steep Faint-End Slope of the UV Luminosity Function at z ˜ 2-3: Implications for the Global Stellar Mass Density and Star Formation in Low-Mass Halos. ApJ, 692:778–803, Feb. 2009.

[136] J. Richard, M. Jauzac, M. Limousin, E. Jullo, B. Clément, H. Ebeling, J.-P. Kneib, H. Atek, P. Natarajan, E. Egami, R. Livermore, and R. Bower. Mass and magnification maps for the Hubble Space Telescope Frontier Fields clusters: implications for high-redshift studies. MNRAS, 444:268–289, Oct. 2014.

[137] J. Richard, V. Patricio, J. Martinez, R. Bacon, B. Clément, P. Weilbacher, K. Soto, L. Wisotzki, J. Vernet, R. Pello, J. Schaye, M. Turner, and T. Martinsson. MUSE observations of the lensing cluster SMACSJ2031.8-4036: new constraints on the mass distribution in the cluster core. MNRAS, 446:L16–L20, Jan. 2015.

[138] A. S. G. Robotham and S. P. Driver. The GALEX-SDSS NUV and FUV flux density and local star formation rate. MNRAS, 413:2570–2582, June 2011.

[139] V. Rodriguez-Gomez, S. Genel, M. Vogelsberger, D. Sijacki, A. Pillepich, L. V. Sales, P. Torrey, G. Snyder, D. Nelson, V. Springel, C.-P. Ma, and L. Hernquist. The merger rate of galaxies in the Illustris simulation: a comparison with observations and semi-empirical models. MNRAS, 449:49–64, May 2015.

[140] V. Rodriguez-Gomez, A. Pillepich, L. V. Sales, S. Genel, M. Vogelsberger, Q. Zhu, S. Wellons, D. Nelson, P. Torrey, V. Springel, C.-P. Ma, and L. Hernquist. The stellar mass assembly of galaxies in the Illustris simulation: growth by mergers and the spatial distribution of accreted stars. MNRAS, 458:2371–2390, May 2016.

[141] R. Sancisi, F. Fraternali, T. Oosterloo, and T. van der Hulst. Cold gas accretion in galaxies. A&A Rev., 15:189–223, June 2008.

[142] R. Sancisi, F. Fraternali, T. Oosterloo, and T. van der Hulst. Cold gas accretion in galaxies. A&A Rev., 15:189–223, June 2008.

[143] D. B. Sanders, J. M. Mazzarella, D.-C. Kim, J. A. Surace, and B. T. Soifer. The IRAS Revised Bright Galaxy Sample. AJ, 126:1607–1664, Oct. 2003.

[144] P. Schechter. An analytic expression for the luminosity function for galaxies. ApJ, 203:297–306, Jan. 1976.

[145] M. A. Schenker, B. E. Robertson, R. S. Ellis, Y. Ono, R. J. McLure, J. S. Dunlop, A. Koekemoer, R. A. A. Bowler, M. Ouchi, E. Curtis-Lake, A. B. Rogers, E. Schneider, S. Charlot, D. P. Stark, S. R. Furlanetto, and M. Cirasuolo. The UV Luminosity Function of Star-forming Galaxies via Dropout Selection at Redshifts z = 7 and 8 from the 2012 Ultra Deep Field Campaign. ApJ, 768:196, May 2013.

[146] D. Schiminovich, O. Ilbert, S. Arnouts, B. Milliard, L. Tresse, O. Le Fèvre, M. Treyer, T. K. Wyder, T. Budavári, E. Zucca, G. Zamorani, D. C. Martin, C. Adami, M. Arnaboldi, S. Bardelli, T. Barlow, L. Bianchi, M. Bolzonella, D. Bottini, Y.-I. Byun, A. Cappi, T. Contini, S. Charlot, J. Donas, K. Forster,

S. Foucaud, P. Franzetti, P. G. Friedman, B. Garilli, I. Gavignaud, L. Guzzo, T. M. Heckman, C. Hoopes, A. Iovino, P. Jelinsky, V. Le Brun, Y.-W. Lee, D. Maccagni, B. F. Madore, R. Malina, B. Marano, C. Marinoni, H. J. McCracken, A. Mazure, B. Meneux, P. Morrissey, S. Neff, S. Paltani, R. Pellò, J. P. Picat, A. Pollo, L. Pozzetti, M. Radovich, R. M. Rich, R. Scaramella, M. Scodeggio, M. Seibert, O. Siegmund, T. Small, A. S. Szalay, G. Vettolani, B. Welsh, C. K. Xu, and A. Zanichelli. The GALEX-VVDS Measurement of the Evolution of the Far-Ultraviolet Luminosity Density and the Cosmic Star Formation Rate. ApJ, 619:L47–L50, Jan. 2005.

[147] M. Schmidt. The Rate of Star Formation. II. The Rate of Formation of Stars of Different Mass. ApJ, 137:758, Apr. 1963.

[148] N. Scoville, H. Aussel, M. Brusa, P. Capak, C. M. Carollo, M. Elvis, M. Giavalisco, L. Guzzo, G. Hasinger, C. Impey, J.-P. Kneib, O. LeFevre, S. J. Lilly, B. Mobasher, A. Renzini, R. M. Rich, D. B. Sanders, E. Schinnerer, D. Schminovich, P. Shopbell, Y. Taniguchi, and N. D. Tyson. The Cosmic Evolution Survey (COSMOS): Overview. ApJS, 172:1–8, Sept. 2007.

[149] B. Semelin and F. Combes. Formation and evolution of galactic disks with a multiphase numerical model. A&A, 388:826–841, June 2002.

[150] R. Smit, R. J. Bouwens, M. Franx, G. D. Illingworth, I. Labbé, P. A. Oesch, and P. G. van Dokkum. The Star Formation Rate Function for Redshift z =4-7 Galaxies: Evidence for a Uniform Buildup of Star-forming Galaxies during the First 3 Gyr of Cosmic Time. ApJ, 756:14, Sept. 2012.

[151] G. F. Snyder, J. M. Lotz, V. Rodriguez-Gomez, R. d. S. Guimarães, P. Torrey, and L. Hernquist. Massive close pairs measure rapid galaxy assembly in mergers at high redshift. MNRAS, 468:207–216, June 2017.

[152] J. M. Solanes, J. D. Perea, and G. Valentí-Rojas. Timescales of major mergers from simulations of isolated binary galaxy collisions. A&A, 614:A66, June 2018.

[153] K. R. Stewart, J. S. Bullock, E. J. Barton, and R. H. Wechsler. Galaxy Mergers and Dark Matter Halo Mergers in ΛCDM: Mass, Redshift, and Mass-Ratio Dependence. ApJ, 702:1005–1015, Sept. 2009.

[154] K. R. Stewart, T. Kaufmann, J. S. Bullock, E. J. Barton, A. H. Maller, J. Diemand, and J. Wadsley. Observing the End of Cold Flow Accretion Using Halo Absorption Systems. ApJ, 735:L1, July 2011.

[155] T. T. Takeuchi, K. Yoshikawa, and T. T. Ishii. The Luminosity Function of IRAS Point Source Catalog Redshift Survey Galaxies. ApJ, 587:L89–L92, Apr. 2003.

[156] L. A. M. Tasca, O. Le Fèvre, C. López-Sanjuan, P.-W. Wang, P. Cassata, B. Garilli, O. Ilbert, V. Le Brun, B. C. Lemaux, D. Maccagni, L. Tresse, S. Bardelli, T. Contini, S. Charlot, O. Cucciati, A. Fontana, M. Giavalisco, J.-P. Kneib, M. Salvato, Y. Taniguchi, D. Vergani, G. Zamorani, and E. Zucca. Evidence for major mergers of galaxies at $2 = z < 4$ in the VVDS and VUDS surveys. A&A, 565:A10, May 2014.

[157] H. I. Teplitz, M. Rafelski, P. Kurczynski, N. A. Bond, N. Grogin, A. M. Koekemoer, H. Atek, T. M. Brown, D. Coe, J. W. Colbert, H. C. Ferguson, S. L. Finkelstein, J. P. Gardner, E. Gawiser, M. Giavalisco, C. Gronwall, D. J.

Hanish, K.-S. Lee, D. F. de Mello, S. Ravindranath, R. E. Ryan, B. D. Siana, C. Scarlata, E. Soto, E. N. Voyer, and A. M. Wolfe. UVUDF: Ultraviolet Imaging of the Hubble Ultra Deep Field with Wide-Field Camera 3. AJ, 146:159, Dec. 2013.

[158] E. Ventou, T. Contini, N. Bouché, B. Epinat, J. Brinchmann, R. Bacon, H. Inami, D. Lam, A. Drake, T. Garel, L. Michel-Dansac, R. Pello, M. Steinmetz, P. M. Weilbacher, L. Wisotzki, and M. Carollo. The MUSE Hubble Ultra Deep Field Survey. IX. Evolution of galaxy merger fraction since z = 6. A&A, 608:A9, Nov. 2017.

[159] A. Verhamme, T. Garel, E. Ventou, T. Contini, N. Bouché, E. Herenz, J. Richard, R. Bacon, K. Schmidt, M. Maseda, R. Marino, J. Brinchmann, S. Cantalupo, J. Caruana, B. Clément, C. Diener, A. Drake, T. Hashimoto, H. Inami, J. Kerutt, W. Kollatschny, F. Leclercq, V. Patrício, J. Schaye, L. Wisotzki, and J. Zabl. Recovering the systemic redshift of galaxies from their Lyman alpha line profile. MNRAS, 478:L60–L65, July 2018.

[160] M. Vogelsberger, S. Genel, V. Springel, P. Torrey, D. Sijacki, D. Xu, G. Snyder, D. Nelson, and L. Hernquist. Introducing the Illustris Project: simulating the coevolution of dark and visible matter in the Universe. MNRAS, 444:1518–1547, Oct. 2014.

[161] P. M. Weilbacher, O. Streicher, T. Urrutia, A. Jarno, A. Pécontal-Rousset, R. Bacon, and P. Böhm. Design and capabilities of the MUSE data reduction software and pipeline. In *Software and Cyberinfrastructure for Astronomy II*, volume 8451 of Proc. SPIE, page 84510B, Sept. 2012.

[162] S. M. Wilkins, N. Trentham, and A. M. Hopkins. The evolution of stellar mass and the implied star formation history. MNRAS, 385:687–694, Apr. 2008.

[163] R. J. Williams, R. F. Quadri, and M. Franx. The Diminishing Importance of Major Galaxy Mergers at Higher Redshifts. ApJ, 738:L25, Sept. 2011.

[164] T. K. Wyder, M. A. Treyer, B. Milliard, D. Schiminovich, S. Arnouts, T. Budavári, T. A. Barlow, L. Bianchi, Y.-I. Byun, J. Donas, K. Forster, P. G. Friedman, T. M. Heckman, P. N. Jelinsky, Y.-W. Lee, B. F. Madore, R. F. Malina, D. C. Martin, P. Morrissey, S. G. Neff, R. M. Rich, O. H. W. Siegmund, T. Small, A. S. Szalay, and B. Y. Welsh. The Ultraviolet Galaxy Luminosity Function in the Local Universe from GALEX Data. ApJ, 619:L15–L18, Jan. 2005.

[165] C. K. Xu, Y. Zhao, N. Scoville, P. Capak, N. Drory, and Y. Gao. Major-merger Galaxy Pairs in the COSMOS Field Mass-dependent Merger Rate Evolution since z = 1. ApJ, 747:85, Mar. 2012.

[166] Y. Q. Xue, B. Luo, W. N. Brandt, F. E. Bauer, B. D. Lehmer, P. S. Broos, D. P. Schneider, D. M. Alexander, M. Brusa, A. Comastri, A. C. Fabian, R. Gilli, G. Hasinger, A. E. Hornschemeier, A. Koekemoer, T. Liu, V. Mainieri, M. Paolillo, D. A. Rafferty, P. Rosati, O. Shemmer, J. D. Silverman, I. Smail, P. Tozzi, and C. Vignali. The Chandra Deep Field-South Survey: 4 Ms Source Catalogs. ApJS, 195:10, July 2011.

[167] A. Zitrin, W. Zheng, T. Broadhurst, J. Moustakas, D. Lam, X. Shu, X. Huang, J. M. Diego, H. Ford, J. Lim, F. E. Bauer, L. Infante, D. D. Kelson, and A. Molino. A Geometrically Supported z ˜ 10 Candidate Multiply Imaged by the Hubble Frontier Fields Cluster A2744. ApJ, 793:L12, Sept. 2014.